A Thesis Submitted for the Degree of PhD at the University of Warwick

First Step of Verification of Li's Hypothesis: Identification of A New Vortex Structure Induced by Guide-Plate in Three Gorges Turbines

by

Ting Chen

Thesis

A thesis submitted in partial fulfillment of

the requirements for the degree of

Doctor of Philosophy

School of Engineering

July 2014

THE UNIVERSITY OF WARWICK

Contents

---

[1] Section 1.1 is basically following the frame work by Li on the phenomenon and hypothesis in [1, 2].

Chapter 4 Guide-Plate Induced Pressure Fluctuations 83

Chapter 5 New Vortex Structure Identified 111

List of Tables

List of Figures

---

[3] http://www.ctg.com.cn/en/introduction/introduction_a.php

Acknowledgments

I would like to take this opportunity to thank my research supervisor Professor Shengcai Li for his academic support towards this research, for his tireless moral and inspiring guidance, I have learned a lot from him for being a good researcher; Thanks also go to Mr. R. H. Edwards for his technical support and to my research fellows Dr Zhigang Zuo, Dr Yuning Zhang and Dr Qingxian Chen for their discussions and assistances with whom I have enjoyed the research together in our cavitation group.

Special thanks to my parents and all my good friends for their constant patience, support, and encouragement through all weathers.

The financial support from the Royal Academy of Engineers (RESCM 3021), the technical and financial support from the Three Gorges authority and the PhD studentship provided jointly by the Chinese Scholarship Council (CSC) and the School of Engineering (University of Warwick) are highly appreciated.

Declarations

This thesis is submitted in partial fulfilment for the degree of Doctor of Philosophy under the regulations set out by the Graduate School at the University of Warwick. This thesis is solely composed of research undertaken by Ting Chen under the supervision of Professor Shengcai Li. The research materials have not been submitted in any previous application for a higher degree. All sources of information are specifically acknowledged in the content.

Abstract

A new type of cavitation (damage) has been recently discovered from the Three Gorges turbines, that suggests a complicated inception mechanism involving the boundary-layer K-mode instability triggering cavitation nucleation. As one of the elements, the level of free-stream turbulence increased by wrongly designed guide-plate on the Three Gorges turbines could be a primary concern in the sense of receptivity and the transient growth of K-mode instability.

The investigation focuses on the flow analysis of the on-coming flow influenced by the guide plate in terms of flow structure(s) and turbulence level variation. Firstly, CFD has been performed to obtain the main flow features in the whole turbine passage with more detailed analysis on the free-stream pressure-fluctuations near the lower surface of the guide vanes. The unsteady flow characteristics, especially the pressure fluctuations of low-frequency spectrum have been studied that significantly alternate the turbulence intensities and spectrum in the free-stream flow. The results verify that the addition of the guide-plate increases the free-stream turbulence, particularly contributing to the occurrence of a strongest component of extremely low-frequency pressure-fluctuation (i.e. the 0.336 Hz for the case 2 with opening of 16°). These low-frequency fluctuations readily transmit throughout the entire flow passage of the turbine.

An extremely large-scale and united unsteady vortex structure that occupies the whole flow passage of a Francis turbine, has been identified for the first time. That is, a vortex-ring structure triggered by the guide-plate, through the connection of the vortices in the stay-vane and guide-vane channels plus those in the runner channels, further interacts with the helical vortex-rope in the draft tube at part-load conditions (e.g. 16° and 30°), forming such an united giant vortex structure. This extremely large-scale vortex structure is thus responsible for the components of extremely low-frequencies (i.e., 0.336 Hz for 16°, 0.15 Hz for 30°) which have been identified from two part-load conditions. These convincing results have proved how this wrongly designed guide-plate increases the free-stream turbulence by inducing extra unsteadiness with gust-like low-frequency and explained that the flow upstream the cone of draft-tube could affect the cone flow significantly, especially under part-load operation conditions.

Abbreviations

δ_{ij}	Kronecker Delta
ϵ	turbulent dissipation
τ_{ij}	Reynolds stress tensor
k	turbulent kinetic energy
S_{ij}	strain rate tensor
2-D	Two-Dimensional
3-D	Three-Dimensional
ALE	Arbitrary Lagrangian Eulerian
APG	Adverse Pressure Gradient
CFD	Computational Fluid Dynamics
CTGPC	China Three Gorges Project Corporation
CTGPC	China Three Gorges Project Corporation
DNS	Direct Numerical Simulation
FDM	Finite Difference Method

FE	Finite Element
FFT	Fast Fourier Transform
FPG	Favourable Pressure Gradient
FV	Finite Volume
K-mode	Klebanoff-mode
LES	Large-Eddy Simulation
LIC	Line-Integral Convolution
M & E	Mechanical and Engineering
M & E	Mechanical and Engineering
mm	millimeter
MW	Mega-Watt
N-S	Navier-Stokes
OSE	Orr-Sommerfeld Equation
PDE	Partial Differential Equation
PIV	Particle-Image Velocimetry
RANS	Reynolds time Averaged Navier-Stokes
RNG	Re-Normalisation Group
rpm	revolutions per minute
RSI	Rotor-Stator Interaction

SCS	Soliton-like Coherent Structure
SIMPLEC	SIMPLE-Consistent
TWh	Tera-Watt hour

Chapter 1

Introduction

Hydropower is the most widely used technology for producing renewable, non-polluting and industrial-scale energy with relatively low operation-cost. According to the new research published online by the Worldwatch Institute[1], the worldwide production of hydropower energy of $3,427\ TWh$ meets around 16 % of the world's entire electricity demand in 2010, which continues the rapid rate of increase experienced between 2003 and 2009. Increasing demand for clean energy is the key driver for the growth of giant hydropower schemes, such as the Three Gorges Project[2], see Figure 1.1.

1.1 Strange Cavitation (Damage) Newly Spotted on Three Gorges Turbines[3]

---

[1] http://www.worldwatch.org/use-and-capacity-global-hydropower-increases-0

[2] http://www.ctg.com.cn/en/introduction/introduction_a.php

[3] Section 1.1 is basically following the frame work by Li on the phenomenon and hypothesis in [1, 2].

Figure 1.1: Full view of Three Gorges Project[3]

The significance of the Three Gorges Project itself is obvious in terms of technology development and economic-social-environmental effects. The Three Gorges turbines are the world largest Francis turbines in terms of their capacity (710 MW) and geometric dimensions (9800 mm of runner diameter), representing the cutting edge of modern technologies of turbines. The powerhouse is shown by the model in Figure 1.2.

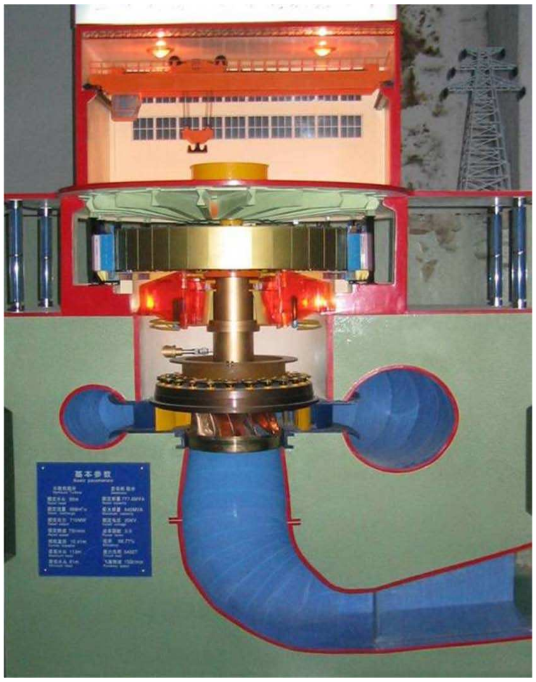

Figure 1.2: Cross-section of Three Gorges Plant model (Courtesy of Harbin Electric Works) [1]

Apart from producing electricity, the comprehensive Three Gorges scheme is also functional for other purposes, such as flood control and river transportation etc. The head variations at the initial stage and the final stage of the project construction are respectively 33 m and 42 m, which are among the largest variations in the world. In order to reduce the potential of flooding downstream by providing flood storage space in the reservoir, the turbines will, for 10 months in one year, operate at low head (i.e., below 80 m) over the flood period. While for non-flood period, the turbines should be operating at the head as high as possible for economic reasons. Owing to these demands, the Three Gorges turbines will inevitably operate for most of the time in off-design conditions.

Soon after the commissioning of the units in the left-bank plant, an unusual pattern of damage spotted on the guide-vanes of the 11F turbine and also on other units (e.g., 10F, 9F, 5F and 6F), during the repair to the torn guide-plate in the spiral casing in 2005. Prof Shengcai Li was invited by the Three Gorges authority to inspect the incident on the 11F[4] turbine, in particular the damage on the representative No 4 guide vane on 19th March 2006. Having done a multidisciplinary analysis, Li described it as a cavitation damage though its appearance is entirely different from the conventional sponge-like cavitation damage. He pointed out that this is presumably a new type of cavitation (damage) triggered by boundary-layer instability. This convincing hypothesis has drawn attention of the researchers all over the world, owing to the fact that the turbines in the left plant developed by the world leading manufacturers have all developed more or less the same pattern of damage though no cavitation was detected during their model tests and CFD simulations. **Therefore, it is not an isolated technical problem but a fundamental scientific challenge. A thorough investigation will benefit not only the power industry but also our scientific knowledge in general** [1, 14].

The resulting pioneering hypothesis about this new type of cavitation damage has been proposed [1,3,14–16] that serves well as the basis for this PhD

---

[4] 11F is following the abbreviation employed by the Three Gorges Power Station.

research and is thus named after Li. His description, analysis and hypothesis are briefly reviewed in the following subsections.

1.1.1 Damage Features

The *in-situ* investigation [1] has focused on the representative damages observed on the No. 4 guide vane surface of 11F turbine. The turbine has total 24 guide vanes and 24 stay vanes; and the guide vane is a positively curved hydrofoil, as shown in Figure 1.3. The damaged areas show the following features:

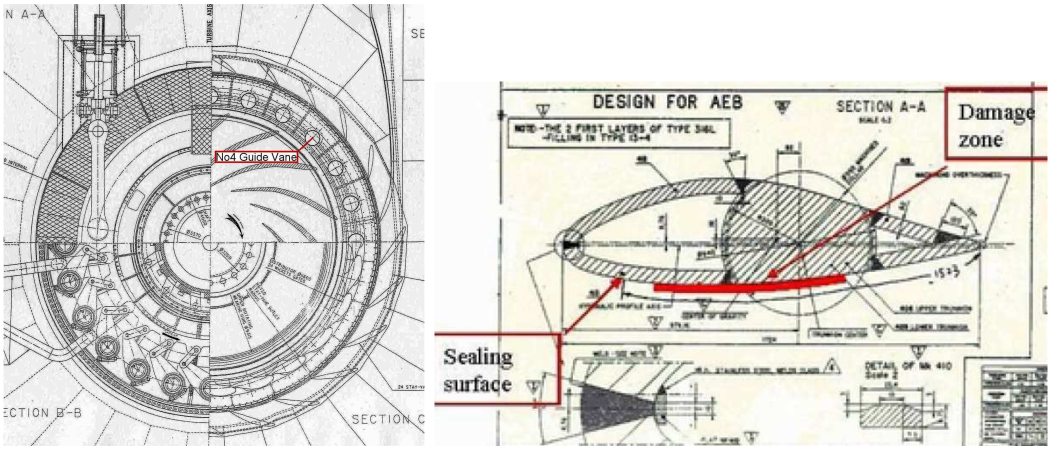

(a) (b)

Figure 1.3: (a) Plan view of 11F turbine; (b) Damage zone on No. 4 guide vane [1]

I: long and equal-width stream-wise damage-strips with span-wise regularity occur only on the foil's lower surface, starting from the favourable pressure gradient (FPG) zone extending into adverse pressure gradient (APG) zone, as shown in Figure 1.4. Based on the original data recorded by Li during the site inspection, 2-D and 3-D schematic diagrams of damages pattern on the surface of guide vane was redrawn by the author as shown in Figure 1.5;

(a) (b)

Figure 1.4: (a) Damages on the lower surfaces of all guide vanes showing nearly the same pattern; (b) No damage appeared on the upper surface [1]

II: wedged head always presents, see Figure 1.6 (a);

III: the depth of damage area is much less than 1 mm fully covered by corroded rough surface, see Figure 1.6 (b);

IV: heated sign on the top surface between guide vanes, see Figure 1.6 (c); and heated tail on the damaged surface, see Figure 1.6 (d).

1.1.2 Metallurgical analysis

The main types of cavitation in Francis turbines have been well described in [7,13]. Compared with the well-known sponge like cavitation erosion observed in Francis turbines (particularly those made of low-alloy steels before 1980's) as shown in Figure 1.7 [6], this damage appearance is distinguishly different.

Li [1,14] pointed out that corrosion is not the underlying cause responsible for this damage but a consequence of cavitation damage. The observed

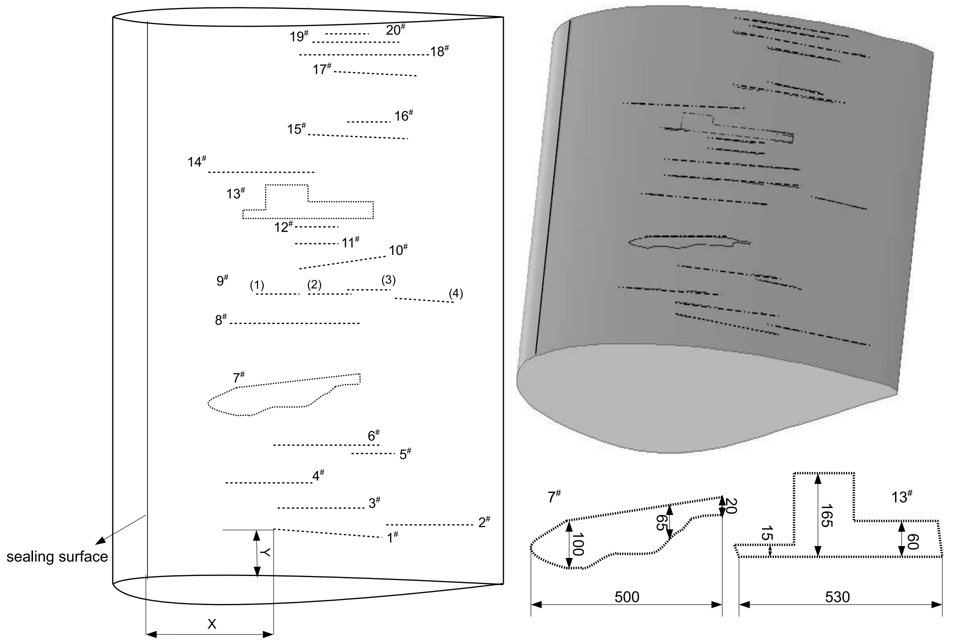

Figure 1.5: Schematic diagram of damages pattern on guide vane (Redraw by the author according to the private file from [5]

heated (blue and other) color zone at the tails of damaged areas indicates a temperature of 250℃ − 600℃ (termed as 'bluing' in heat-treatment[5]). The only possible hydrodynamic mechanism involved in a Francis turbine capable of generating temperatures at or above this range is cavitation. Metallurgical analysis [1, 14] explains that the heated zone itself indicates a relatively weak cavitation attacking on a relatively high cavitation-resistant material (martensitic stainless steel). Because the erosion rate (much less than 1 *mm* over 10,000 hours) is very low; and the narrow and shallow attributions of damage strips also suggest that the damage is not caused by large cavitating structures in the main flow directly striking on the guide vane surface, but possibly caused by a delicate-flow structures in the boundary-layer (for details

---

[5] Bluing: coating steels with a thin, even film of coloured oxide from bluish-black to purple brown shade, obtained by exposure to an atmosphere of dry steam or air, at certain temperature subject to the material as well as the color.

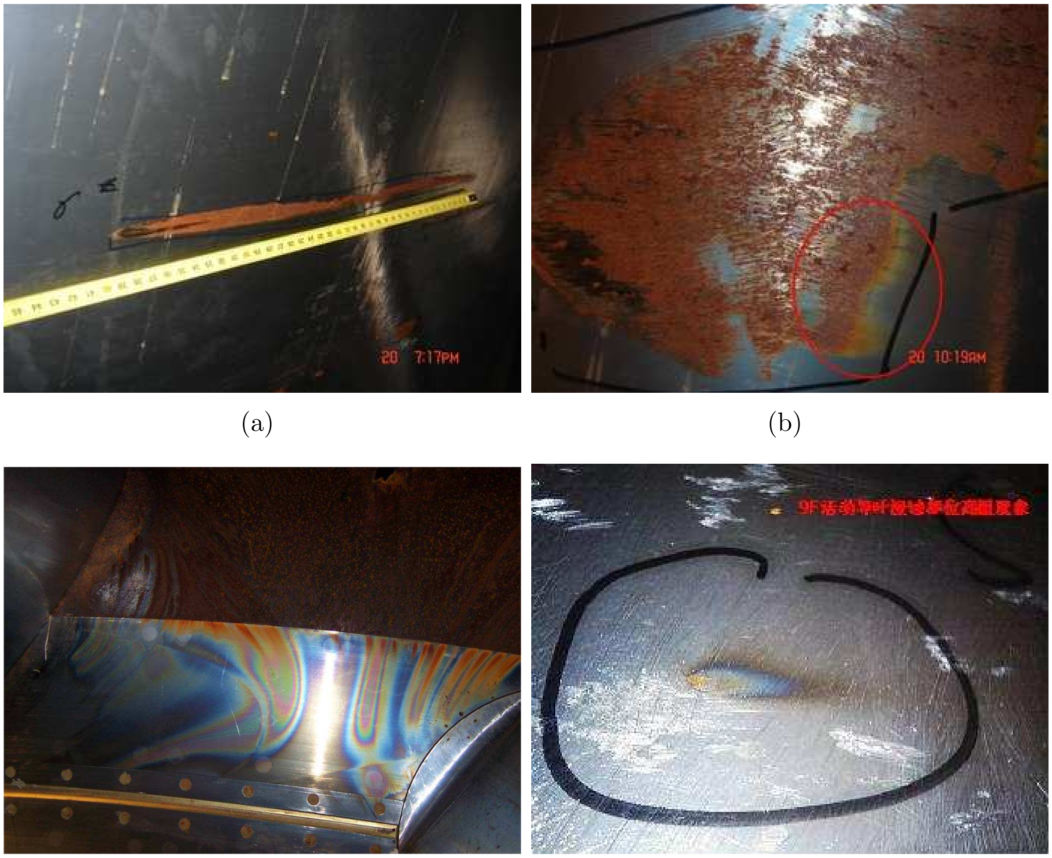

(a) (b)

(c) (d)

Figure 1.6: Damages features: (a) wedged head; (b) corroded rough surface; (c) heated sign on the top surface between guide vanes; (d) heated tail [1]

see the next subsection).

Inter-granular corrosion is also a potential problem to martensitic stainless steels which is the material used in this case. Experiments (e.g. [17]) show a trend that the maximum susceptibility to inter-granular corrosion was observed in the condition tempered at 500℃ to 550℃. Accordingly, the blue color on the heated tail of damage area represents a similar heat treatment, creating an ideal environment for sensitization, leading to inter-granular corrosion. This explains the reason for the corrosion appearance of the damage area after cavitation attack.

Figure 1.7: Typical sponge-like erosion pattern caused by a leading-edge cavitation attack after 4000 hour operation [6]

1.1.3 Fluid dynamics analysis

The wedged head of damage strips indicates that this cavitation damage is most likely related to the turbulent spots generated during boundary layer transition to turbulence. Li [1] further emphasized that the cavitation inception is most likely related to boundary layer's streaks and presumably induced by turbulent production during the transition process. Two aspects have been further analyzed: (1) to examine the conditions required to enable nuclei in boundary layers to cavitate; and (2) to determine how the boundary-layer providing such conditions through its transition process.

Daily and Johnson [18] first demonstrated that the lowest mean pressure across the boundary layer is the location where the turbulence level is the highest. Owing to the minimum value of mean pressure and the maximum value of instant pressure drop, bubbles at this particular location have the highest probability to cavitate. Besides, the magnitude and time scale of turbulence also play important roles for cavitation inception [19]. If the frequency of nuclear bubble (corresponding to the characteristic time scale of the bubble) is higher than the highest frequency of turbulence, the entire spectrum of turbulence may contribute to bubble growth. Therefore, long enough negative pressure drop generated in the boundary-layer is essential; The process of laminar streak breakdown into turbulent spots may provide an ideal flow structure for creating such conditions for nuclei to cavitate if the free-stream pressure there is also low enough (but not necessarily lower than the vapor pressure). However, transition from laminar to turbulent flow remains an unsolved challenge for fluid mechanics despite it has attracted numerous investigations for more than 100 years. Even for flows over a flat plate, the transition process is still not fully understood yet because of a variety of influences limiting the precise prediction of the transition Reynolds number, such as free-stream turbulence, surface roughness. Particularly, very limited understanding on the details of the later stages of transition and the knowledge of breakdown mechanism being initial condition dependent [20]. Recently, the soliton-like coherent structure (SCS) has been proposed by Lee [21, 22], presenting a much clearer picture of the low-speed streak formation and its breakdown. For details, see Ref. [23].

The damage pattern on the guide vane suggests that it is virtually a 2D flow. The resulting perturbed flows are span-wise-dependent but essentially unidirectional, i.e. the transverse velocity components are much smaller than the stream-wise component. The instability of such transversely sheared flows appears to be related to various aspects of the transition process, such as secondary instabilities and by-pass transition. Many factors [24] can cause three-dimensional steady and unsteady distortions in the form of stream-wise or longitudinal vortices. These include small steady or unsteady perturbations[6] superimposed on the oncoming flow, imperfections at the leading edge[7], cross-flow instability, and vortices induced by surface curvature, as well as certain excitation devices[8].

Free-stream turbulence initiates three distinct motions within the boundary layer, as summarised by Saric et al [20]. The first motion is a sustained, streaky and high amplitude motion, which is probably due to stretching of the ingested free-stream vorticity and the growth of transient modes (i.e. the Klebanoff mode). Klebanoff (K) modes are flow structures in the form of streamwise streaks that appear to be caused by freestream turbulence. They were first observed by Klebanoff [25]. His basic findings have been confirmed by many subsequent authors. Currently we only have limited understanding about the instability of Klabenoff mode and its role in the transition owing to the random nature of both the free-stream disturbances and the Klebanoff motion. Most studies so far investigate steady distortions, induced in a controlled manner through the receptivity at leading edge only [21]. The maximum growth of this K-mode distortion is a function of Reynolds number and wave number, e.g. as demonstrated by Anderson et al [26].

The turbulence in free-stream is one of the key factors for triggering cavitation inception in boundary layer since it alters boundary-layer instabilities (e.g. the growth of Klebanoff-streaks) through receptivity mechanism (see [24,27,28] for details). Span-wise distortions (modulations) is induced by various free-stream disturbances, e.g., small low-frequency three-dimensional

---

[6] Such as the perturbation caused by the guide plate prior to the entrance of stay-vanes, which will be discussed later.

[7] The sealing surface on the guide vane is such an imperfection in our case.

[8] The guide plate may serve well as an excitation device.

perturbations in the free stream can produce significant distortion within the boundary layer, leading to alternating span-wise thickening and thinning [27]. Steady disturbances (e.g. artificial roughness, vortices) can also cause a similar type of span-wise modulation. These distortions are all in the form of elongated streaks named as Klebanoff-mode or K-mode [25,29,30]. Li has predicted that this cavitation inception is triggered by boundary-layer turbulence-production. Thus the damaged (roughened) spot in turn triggers subsequent cavitation (damage) immediately downstream [1,14]. The dynamic behaviour progresses stream-wise, resulting in such a horizontal damage strip with a wedged head and heated tail.

The wedged head of damage strips highly resembles the turbulent spots caused by K-mode streak transient growth and breakdown in a Blasius boundary-layer, it also creates a turbulent wedge. Watmuff [31] demonstrated the evolution of a turbulent wedge from stream-wise streak. Experiments by Matsubara et al. [32] show that the growth of near-wall streaks is a key factor triggering the bypass transition that leads to breakdown and turbulent production. According to Lee [21, 22], the generation of the high frequency vortices, i.e., the chain of ring vortices is caused by the interaction of the secondly closed vortex with the Λ-vortex. This kind of vortices has high possibilities of creating a favorite environment for nuclei to grow. Earlier, other investigators also observed the existence of turbulence spots during the transition process [33].

Li pointed out that for extremely large turbines, the scale effect makes the free-stream turbulence level of prototype turbine much higher than model turbine (i.e. Reynolds number is usually higher by the order of 10^2). The large turbines are thus more susceptible to this type of cavitation inception developed in the boundary-layer through the receptivity mechanism. For detailed similarity analysis, see [1]. Also, there is absolutely no boundary-layer similarity for model and prototype. Li's analysis explains well that even no cavitation observed during model tests does not guarantee the Three Gorges turbines free from cavitation inception in boundary-layer and subsequent erosion damage.

Li has predicted that for turbines in the left-power plant, the flow in the guide-vane passages was subject to a high level of free-stream turbulence, owing to a structure named as guide-plate[9] in the spiral casing prior to the entrance of the stay-vane passage. This device was mainly for reducing the unit size[10]. As an evidence of high free-stream turbulence generated by this device, the premature damage of the guide plate (a piece torn off) accompanying by severe pressure-fluctuation and machine-vibration was reported after commissioning. Besides, the 3-D damage on the fillet of stay-vane immediately down stream of the guide-plate could also indicate the disturbances introduced by the guide plate. In addition, the units was operating at low head conditions ($61 - 72\ m$) in the initial stage of operation [4]. Under such condition, the circumferential velocity at the runner inlet reduced as the result of the reduced inlet circulation, the incidence angle of the incoming flow changed the direction which consequently made the pressure surface (the lower surface), instead of the suction surface, of the guide vane (hydrofoil) more vulnerable to cavitation.

---

[9] The sketch drawing of guide-plate can be seen in Figure 1.2 and also in Chapter 3.

[10] For high and medium specific speed turbine-generator units, spiral casing is often the crucial component that determines the overall size of plant. Therefore, reduction of spiral casing has a significant impact on the hydro scheme's economic feasibility. This is why manufacturers often take high risks to reduce the size of spiral casing in order to win the bidding. No doubt, the idea of using guide plate, which has already caused a break-down event, has to be justified technically and economically. In the March of 2006, Prof Li has made a suggestion to the M & E department of CTGPC about the feasibilities of employing oval cross-section spiral casing for the size reduction [1], which is now implemented in the turbine designed for Xi Luo Du power station by Hydro Power Generation of Voith-Siemens in late 2008.

To conclude his hypothesis, Li [1, 14] examined whether the span-wise spacing of the damage strips($\approx 0.1\ m$) complies with the span-wise distribution of K-mode streak breakdown and turbulence production. As the results, all the evidences are supportive to the hypothesis he proposed.

1.1.4 Li's Hypothesis

In order to understand Li's explanation about this phenomenon, a logical chart has been drawn as shown by Figure 1.9. The hypothesis proposed by Li can be stated as follows.

This is a non-conventional turbine cavitation. Its inception is likely triggered by the breakdown of the boundary layer K-mode streaks during their transition process. The resultant damage patterns reflect well the features of the turbulent production from the breakdown of these streaks. The metallurgical and fluid dynamic analysis support this hypothesis well. The covering corrosion is not the cause but a consequence of the cavitation attack on the martensitic stainless steel undergoing a sensitization process. Once the first damage spot created, a dynamics process follows: The first damage spot will serves well as a roughness spot creating a subsequent cavitation (damage) immediate downstream. This dynamic and sustainable process progresses stream-wise, resulting in such a horizontal and equal width damage-strip with a wedged head. Their span-wise distribution is thus a reflection of the span-wise stochastic characteristics of the K-mode streak breakdowns.

In order to understand this phenomenon, it is essential to see what conditions are required to enable the nuclei in the boundary-layer to cavitate and how the boundary-layer provides such conditions through its transition process. There must be a flow structure in the boundary-layer capable of creating such negative pressure drops lasting long enough time for nuclei to cavitate. More attentions should be paid to the K-mode involvement that responds to the free-stream turbulence [1].

In particular, the increased level of free-stream turbulence by the wrongly designed guide-plate for the Three Gorges turbines could be a primary concern in the sense of possessing a higher receptivity and promoting the boundary-layer K-mode instability. Therefore, it is the first element of Li's Hypothesis that should be verified as indicated in Figure 1.8. This has thus constituted the main objective of this PhD project. The phenomenon is extracted from a technology development that opens up a new scientific topic in the multidisciplinary domain for the cross fertilization of sciences.

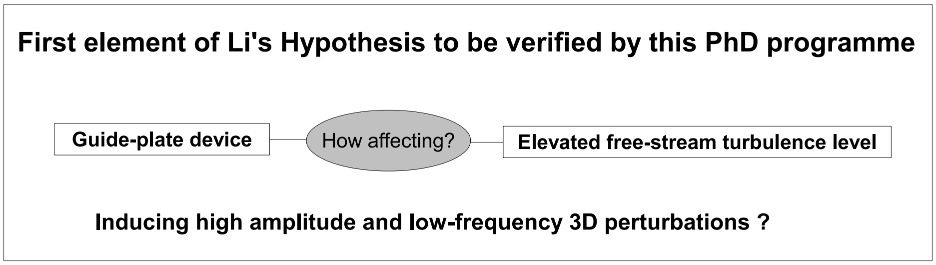

Figure 1.8: The first element of Li's Hypothesis to be verified by this PhD programme

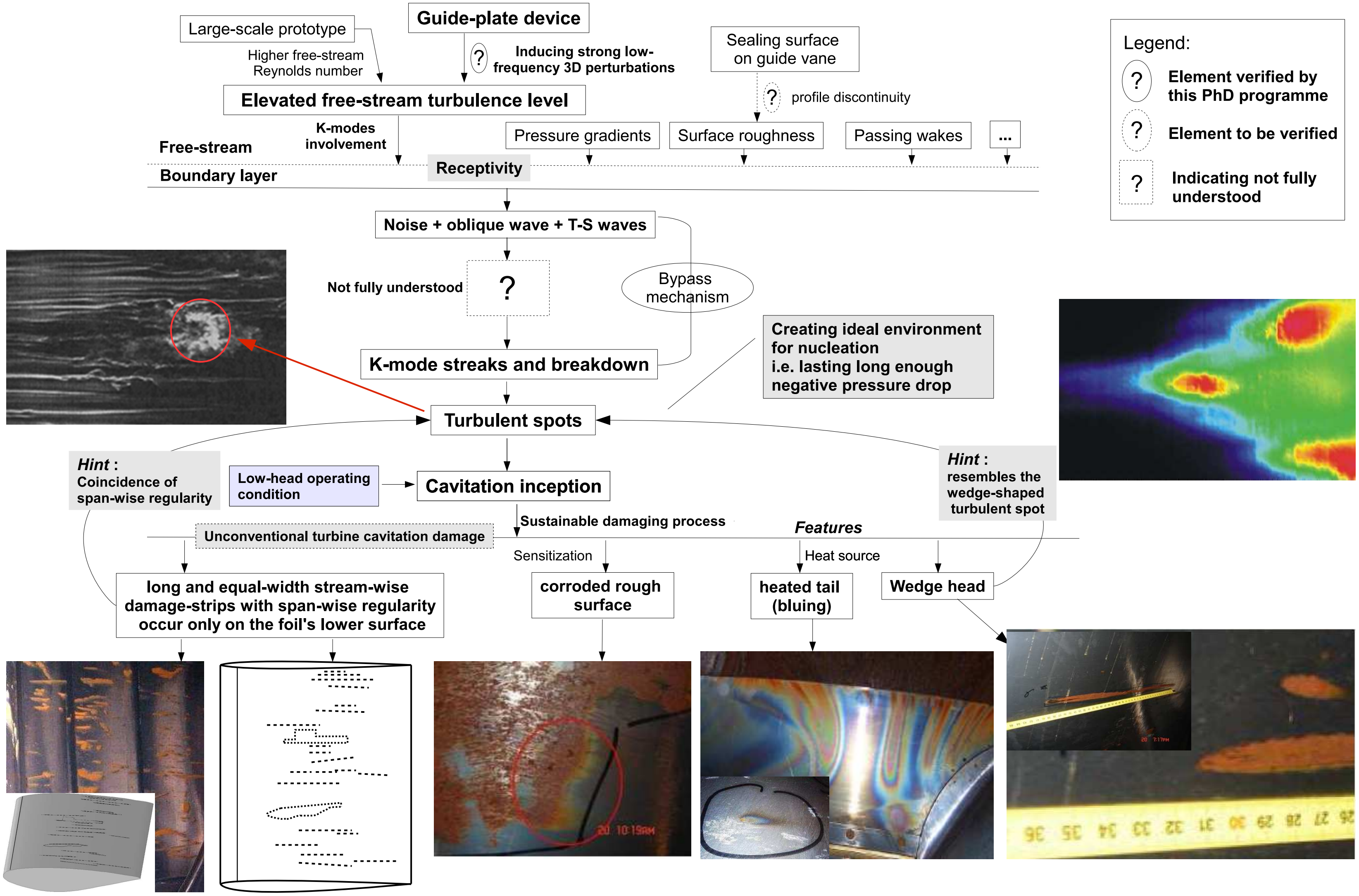

Figure 1.9: Logical chart of Li's Hypothesis

1.2 The Objectives of PhD Programme and Research Route

This PhD programme is the first step to prove Li's Hypothesis as explained before. The turbulence in particular the gust-like low-frequency pressure fluctuation component has the highest possibility of entering the boundary-layer and triggering the streak breakdown and consequently the cavitation inception. Verifying this hypothesis requires the recreation of this phenomenon under controllable conditions for thorough investigations. Such a follow-up programme is being carefully devised and conducted. The envisaged cavitation inception triggering process involves complicated multidisciplinary theories which needs to be verified step by step. The first step of verification of this hypothesis is to examine the low-frequency fluctuation components in the flow-passages of the turbine system, in particular the possibilities of the guide-plate induced ones as predicted in the hypothesis. Therefore, this thesis focuses on flow analysis of the oncoming flow affected unfavorably by the guide plate in terms of flow structure(s) and turbulence-level variation. This guide-plate could induce various modes of pressure fluctuations including extremely low-frequency ones. These low-frequency modes in the free-stream as mentioned before, have high possibilities to enter into the boundary-layer and thus make the K-mode instability much more prone to grow and breakdown. The investigations are conducted as follows.

Firstly, a 3-D flow investigation of the prototype is essential for providing whole-flow-field information in the turbine passage with more details on the free-stream pressure-fluctuations near the surface of the guide vanes. The unsteady flow characteristics, especially the pressure fluctuations in the prototype have been studied in details.

After analyzing the whole-flow-field characteristics, pressure-fluctuation characteristics for three different models have been compared, which clearly shows how the free-stream turbulence level has been unfavorably affected by the addition of guide-plate. Furthermore, unsteady vortex structures in the whole turbine passage have been numerically captured, giving a fuller explanation about the negative influence of the guide-plate. Convincing results obtained from this PhD programme thus successfully verified one of the elements in Li's Hypothesis [1].

All those calculations were performed in parallel on the high-performance computers at the Cavitation Research Group of Warwick University.

1.3 Thesis Structure

This thesis is organized in six chapters, of which Chapters 3, 4 and 5 present the novel and original contributions from this PhD research programme, as structured as follows.

Chapter 2 gives a brief introduction to the techniques of fluid transients modelling which is the theoretical basis of later numerical investigations. Of abundant modern Computational Fluid Dynamics (CFD) techniques, the turbulent models chosen for simulations have been given careful considerations.

Chapter 3 introduces the specifications of prototype turbine and the computation strategy. Then the details of building geometric models, meshing the models, as well as the validation of the numerical methods and simulation parameters are presented.

Chapter 4 presents the numerical studies on the main flow features in the whole turbine passage with detailed analysis on the free-stream pressure-fluctuations near the surface of the guide vanes. The influences of the addition of guide-plate on the free-stream turbulence level (in particular the low-frequency gust type) as proposed in previous studies [1, 14] has been verified. These results presenting in this chapter have been published [10] and cited in [11].

Chapter 5 provides further information on the flow pattern around the guide-plate, showing influences on the whole flow field of the turbine. Unsteady sources caused by a large complex vortex structure in the turbine flow field has been for the first time identified. The results presenting in this chapter have also been published [10] and cited in [11].

Chapter 6 concludes the main results and contributions of this PhD research programme and outlines some ideas for possible future work.

Chapter 2

Background Knowledge

2.1 Fundamentals of Hydraulic Turbine

2.1.1 Principle of Energy Conversion

The hydraulic turbine is a machine that converts the energy of an elevated water supply into the mechanical energy of a rotating shaft. The amount of energy stored in water depends on the volume and the difference in height between the source and the water's outflow. This height difference is called the head. The amount of potential energy in water is proportional to the head. Francis type units cover a wide head range, from 20 meters to 700 meters and their output varies from a few kilowatts to 1,000 megawatts [11]. Except for electrical production, they can also be utilized for pumped water storage. The Francis turbine is identified as reaction-type turbine, located between the high pressure water source and the low pressure water exit, usually at the base of a dam. The water enters a spiral casing forming a certain inlet circulation that will be further tuned by the stay vanes and guide vanes creating an ideal flow condition[1] for the water energy[2] to be firstly exploited through the rotating runner at highest efficiency and lowest risks of cavitation and other unfavorable phenomena[3]. Then the water runs through a diffusive draft tube consisting of three segments: a cone, an elbow and nearly horizontal outlets for further exploitation of the remaining kinetic and potential energy at lowest risks of inducing pressure surges and other unwanted flow structures such as vortex rope, cavitating flow and etc. The guide vanes are adjustable to allow turbine operating efficiently under different flow conditions. Large Francis turbines are individually designed for each site to optimize its operational efficiency, typically over 90%. More details can be found in [11].

2.1.2 General Hydraulic Excitations

Flows in hydraulic turbines are always unsteady due to the system rotation, flow instabilities and mutual interactions between rotating and stationary parts. Flow instabilities are mostly viscous phenomena such as boundary layer transition and vortex shedding that produce small amplitude pressure fluctuations at relatively low frequencies. The flow induced unsteadiness is a key issue because it leads to power fluctuation and affects efficiency. Interaction between runner blades and guide vanes produces pressure fluctuations of relatively high frequency and large amplitude. This phenomenon is more closely related to compressibility than viscosity. It is important because it may cause structural vibration and noise. The most common types of hydraulic excitations in hydraulic turbines are concluded from [11] and briefly described below.

---

[1] Subject to head and flow rate to be utilized.

[2] That is the kinetic and potential energies.

[3] Such as vibration, etc.

(1) Owing to the unevenly distributed structure of the spiral casing or the changes of the guide vane opening, the asymmetrical flow in front of the runner will induce pressure pulsations in the runner with different frequencies[4] There are a) runner blade rotating frequency (Hz): $f_b = \frac{nZ_b}{60}$, (b) guide vane passing frequency (Hz): $f_g = \frac{nZ_g}{60}$ and (c) stay vane passing frequency (Hz): $f_s = \frac{nZ_s}{60}$, here n is the rotating speed of runner (rpm), Z_b, Z_g and Z_s is the blade number, guide vane number and stay vane number, respectively.

(2) Pressure pulsations induced by vortices, e.g., the Karman vortex street from the trailing edge of runner blades or guide vanes; and/or the vortices shedding from blades and vanes, as well as channel vortices.

(3) Under part-load operation, the circulation flow at the runner exit rotates in the same direction as that of the runner rotation, which forms a low pressure region at the runner's exit section, producing a back-flow in the axial direction. Any asymmetrical distribution of this back-flow would cause instability in the vortex rope to develop into a helical vortex in the draft tube.

(4) Hydraulic vibration caused by transient flows in the penstock.

(5) Self-excitation vibration: the periodic motion of water and other fluids as well as other mechanical components may lead to the resonances of turbine structure. More details can be found in [11].

2.1.3 Off-Design Operation

Escaler, et al. (2006) [7] produced a simple sketch for explaining the adjustable process that a Francis turbine operates under a range of water flow conditions as shown in Figure 2.1.

---

[4] These frequencies may be also detected in other parts of the flow field, e.g., spiral casing, guide vanes, or even draft tube.

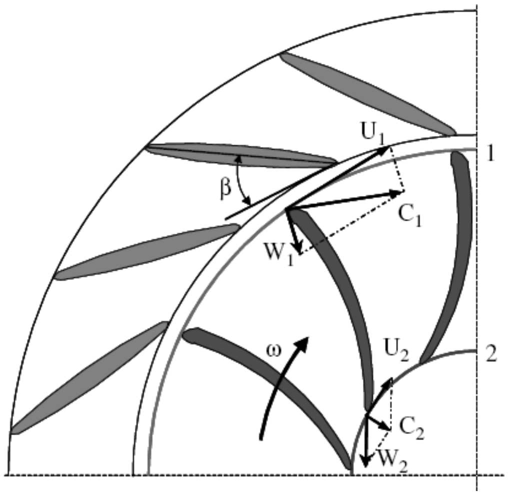

Figure 2.1: Velocity triangles for Francis turbine runner [7].

For a typical Francis turbine, the adjustable guide vanes are the only device available to control the flow rate and thus the power output of turbine by changing the opening angle, β. C, W, U respectively designate the absolute velocity (fixed reference), the relative velocity (rotating reference) and the tangential velocity[5]. The incidence angle of the incoming flow is the angle between W and the tangent to the blade at the leading edge. For a fixed guide vane angle, when increasing the head the absolute fluid velocity C_1 will grow and the incidence angle that for the optimum condition is almost close to zero, will become positive. At the same time, these velocity components at the outlet are also modified if the inlet conditions change, e.g., the absolute velocity C_2 will change the direction[6] and leave a residual circumferential component affecting the draft tube flow. The adverse pressure gradient imparts to the swirling flow at the runner outlet which further expanded in the cone segment of draft tube[7], inducing a vortex precession in the draft tube. As a consequence

---

[5] Subscripts 1 and 2 designate values at runner inlet and outlet.

[6] Under the optimum condition, the absolute velocity C_2 has a radial direction.

[7] It is briefly named cone, located just downstream of the turbine runner, upstream of

the entire power plant can show large pressure pulsations and severe vibrations, leading to restrictions of the safe operation range of a Francis turbine. For more details, readers are referred to [7, 11].

2.1.4 Operation range and pressure pulsation in draft tube

Figure 2.2 shows the operation ranges of Francis turbines with respect to the pressure pulsation in draft tube by Jacob and Prenat (1996) [8]. The stability of Francis turbine is highly related to the eigen frequency of the water in the draft tube. When any frequencies of pressure pulsations are close to this frequency, serious resonance would be prone to occur.

The graph on the left of Figure 2.2 is the operation curve of a model turbine in which the abscissa is the flow rate coefficient, and the ordinate indicates energy coefficient. For a given rotating speed, the required efficiency contour and guide vane opening contour curves can be deduced from the model characteristics chart in this figure. Turbine characteristics are specified by the unit energy a and the unit flow rate b at BOP (Best Operation Point). But the rated turbine characteristics of a hydro power project is specified by unit energy c and unit flow rate h at the rated point of the station, which are usually different from those at BOP. The continuous operation range of the turbine is restricted by the following factors: the minimum of guide vane opening d, the maximum of guide vane opening e, the maximum and minimum unit energy coefficients f and g of the hydro-project and the maximum power h of the generator used in the station.

---

the elbow segment.

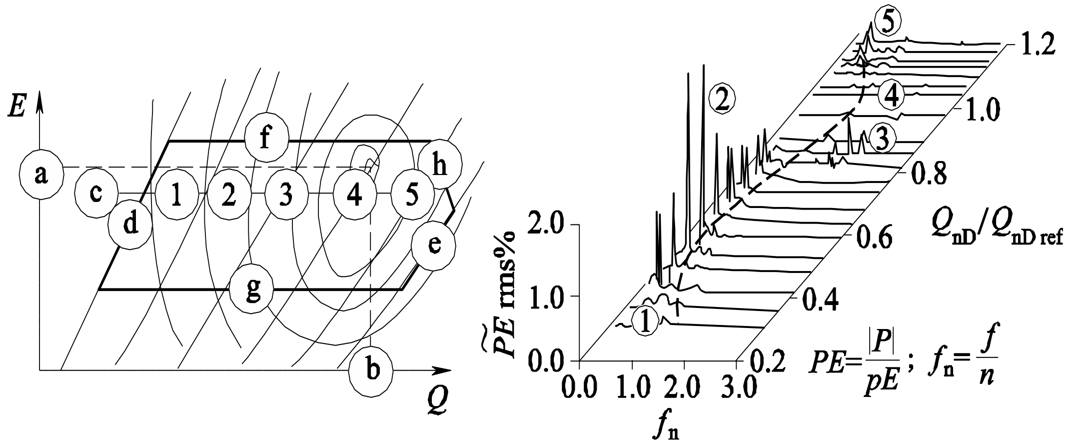

Figure 2.2: Francis turbines operation range with a pressure pulsation water fall graph in draft tube [8].

The graph on the right of Figure 2.2 shows variation of pressure pulsation amplitudes in the draft tube from minimum to maximum of guide vane openings under the rated energy unit c condition. In this figure, the dimensionless amplitude is the function of dimensionless flow rate and frequency. The turbine operation cases are ① very low flow rate, ② part load, ③ high part load, ④ high efficiency (optimized operation zone), and ⑤ full load.

I. Helical vortex rope precession at part load: ② indicates the pressure pulsation zone with the precession of a helical vortex rope in draft tube. The vortex rope rotates around its center with angular speed Ω. The precession is a rotation movement of a rotating center of the vortex rope around another fixed axis (central axis of the conical part) with another angular speed ω. In the case of a part load, the combined effect of the conical diffuser and the elbow causes the flow at the runner exit with a positive circulation to have a precession movement around the axis of the conical part of draft-tube. Consequently, the Tomas cavitation number may be down to critical level and cavitation occur at the low pressure center of the vortex rope, referred as the cavity vortex precession.

The precession will produce an asymmetric rotating velocity field in the draft tube and pressure pulsation in the conical part. The pressure pulsation with the precession frequency will mainly occur in the elbow. Although precession frequency varies greatly from turbine to turbine, the dimensionless precession frequency in most Francis turbines can be deduced through similarly laws: $Z_t = \frac{f_p}{f_n} \approx 0.26 \pm 20\%$, where Z_t equals to the ratio of the precession frequency (f_p) to the rated frequency of turbine (f_n). Some hydraulic turbines has been improved by designing to achieve that $Z_t = 0.4$.

The amplitude of pressure pulsation caused by the precession in part load is affected by either the dynamic response of the prototype flow system or the testing conduit of the model turbine. Precession synchronic frequencies also appear in the spectrum, but their contribution to the pulsation amplitude is small enough to be ignored. The multiple precession sometimes emerges in case ① with very low flow rate and induces weak amplitude pulsations.

II. The natural vibration of water flow in draft tube: owing to the undeveloped vortices and low pressure, cavitation bubbles accumulate in the middle of the runner's exit section, entering the draft tube with the fluid flow from runner which invoke vibration of the water body. In the draft tube system there exists the characteristic elements that are the water inertia I and the 'cavitation compliance /stiffness (flexible capacitance)' [8]. The dashed line in Figure 2.2 indicates the natural vibration frequency of the draft-tube system.

---

[8] Apart from the passive model of 'compliance', the cavitation cloud itself can also behave as a (pressure fluctuation) exciter with its own characteristic frequency and stimulate a particular low-frequency component in the whole turbine system through a double-oscillator mechanism. This is often referred as cavitation resonance which was firstly identified in the Ventari flow by Li et al. (1983, 1986) [34, 35]. For a systematic description of this phenomenon, see Li et al. (2009) [36].

When the cavity bubble approaches its maximum volume, the natural vibration frequency is close to the precession frequency of the vortex rope under part load conditions, causing a resonance in the draft tube and thus a strong pressure pulsation.

III. Instability in 'higher part load' case: ③ indicates the pressure pulsation zone caused by higher part load instability in Francis turbine. This zone is located at a flow rate between 70% $\sim$ 90% of the optimum. This instability will lead to strong pressure pulsation in the draft tube and spiral casing.

IV. Self excitation: ⑤ indicates the pressure pulsation zone at full load. The damping of natural vibration in the draft tube will be small and consequently it may transmit to the turbine conduit and cause resonance.

2.2 Transient Modeling for Hydraulic Turbines

2.2.1 Unsteady Turbine Flow Simulation

Computational Fluid Dynamics (CFD) is widely used in the field of hydraulic machinery for research and product development (e.g. see [37–39]). Generally the Reynolds Averaged Navier-Stokes (RANS) equations together with turbulence model (usually the $k - \epsilon$ model) is often employed. It is a common practice to apply steady state simulations, and the unsteadiness is simply treated as the consequence of the rotor-stator interactions by using averaging procedures. However, due to the geometrical complexities of Francis turbine together with the rotation of the turbine runner provide an extremely complicated flow environment characterized by various unsteadiness, large-scale vortices, intense turbulence breakdown, pockets of highly shear/reversal flow, collapsing cavitation bubbles, etc. Even under optimum design condition, organized unsteadiness is still prevailing throughout the whole flow field, the situation becomes especially pronounced in off-design operation. Investigation of these phenomena requires transient simulations and special numerical treatments to the interface between the components. The flow modeling of the machine is complicated because of the fact that the stator and runner have different numbers of blades. This difference restricts the use of geometrical periodicity within simulations so the entire region of stator and runner has to be simulated. It requires such an enormous computational effort in terms of memory and CPU time that only modern high performance computers can do the job.

The unsteady problems in the turbine flow systems can divided as two major types [40]. The first one is imposed by an externally forced unsteadiness, such as the unsteady boundary conditions or the temporary geometry variations. A typical example is the rotor-stator interactions[9]. The other is the self-excited unsteadiness, e.g. turbulent motion, vortex shedding (Karman vortex street) or unsteady vortex[10]. Here the unsteadiness is not caused by temporary variations of boundary conditions or geometries. Some problems might be a combination of both types, such as flow induced vibrations and geometry changes caused by vortex shedding. These are all common phenomena encountered and should be treated by using unsteady procedures other than steady-state simulations.

---

[9] Other examples such as the closure of a valve and the change of the flow domain.

[10] A common example is vortex-rope precession in draft tube at partial load.

2.2.2 Basic Equations

The Reynolds Averaged Navier-Stokes equations for incompressible flows are most common applied. Compared to the steady state the momentum equations contain an additional term $\frac{\partial U_i}{\partial t}$ prescribing the unsteady change:

$$\frac{\partial U_i}{\partial t} + U_j \frac{\partial U_i}{\partial x_j} = -\frac{1}{\rho}\frac{\partial P}{\partial x_i} + \frac{\partial}{\partial x_j}\left(\nu\left(\frac{\partial U_i}{\partial x_j} + \frac{\partial U_j}{\partial x_i}\right) - \tau_{ij}^{'}\right). \tag{2.1}$$

Here, $\tau_{ij}^{'}$ are the Reynolds stresses, which are calculated from the turbulence model. The continuity equation for incompressible flow does not possess a time depending term, can be described as [40]:

$$\frac{\partial U_i}{\partial x_i} = 0. \tag{2.2}$$

Equations above show elliptic behavior in space, requiring boundary conditions on all surfaces. Generally, the discretization method is solved out in different way in time and space. For spatial discretization, Finite Volume (FV) or Finite Element (FE) approximation is applied for different cases according to the requirements. While for time discretization, the Finite Difference method (FDM) has the most applications. The explicit methods require a restriction of the time step according to stability criteria, which depend on the local velocities and the local grid size. However, the implicit methods, are always stable, there is no strict restriction on the choice of the time step, proper time step can be chosen according to the physical requirements. 2^{nd} order is the least requirement for both the time discretization and the spatial discretization to get accurate results. Otherwise the restrictions on time step could become much more strict (i.e., extremely small time step required).

More details refer to [41].

Eulerian method can be used for unsteady boundary condition problems such as the first type of problems as discussed above. However, if the problem involves moving geometries in Eulerian coordinates this will be a bit more difficult. Thus, Lagrangian method is by nature having more advantageous for moving boundary problems owing to the fluid particles can be traced by this method. Consequently, combining these advantageous of two methods, Arbitrary Lagrangian Eulerian (ALE) method is developed for solving the problems with moving boundaries. In the ALE method the reference coordinates can be chosen arbitrary, as described as

$$\frac{\partial f\left(x_i^L, t\right)}{\partial t} = \frac{\partial f\left(x_i^R, t\right)}{\partial t} + \left(U_j - W_j\right)\frac{\partial f\left(x_i^E, t\right)}{\partial x_j} \tag{2.3}$$

with the coordinates x_i^L: Lagrangian coordinates; x_i^R: referential coordinates; x_i^E: Eulerian coordinates; U_i: reference velocity.

The momentum equations in the ALE formulation can be written as follows

$$\frac{\partial U_i}{\partial t} + \left(U_j - W_j\right)\frac{\partial U_i}{\partial x_j} + \frac{1}{\rho}\frac{\partial P}{\partial x_i} - \frac{\partial}{\partial x_j}\left(\nu\left(\frac{\partial U_i}{\partial x_j} + \frac{\partial U_j}{\partial x_i}\right) - \tilde{\tau_{ij}}\right) = 0 \tag{2.4}$$

The moving of the reference system W_i can be chosen according to practical needs. If W_i is equal to zero the Eulerian description works, on the other hand, if W_i is equal to the velocity of the fluid particle the Lagrangian formulation is used. The convective term in the transport equations for scalar quantities changes in the same way as in the momentum equations [40].

The governing equations are discretized into algebraic equations with the finite volume method in spatial domain at each time step. They are also discretized in temporal domain following a second-order implicit formula and integrated within one time step. The discretized equations reflect flow field parameters at each time step. The algebra equations obtained through discretization in spatial domain are solved with a sub-relaxation method. Frequency analyses of time-dependent results of unsteady flow are carried out with the Fast Fourier Transform (FFT) method. Figure 2.3 shows the calculated algorithm in the work which is based on the Fluent software 6.3.

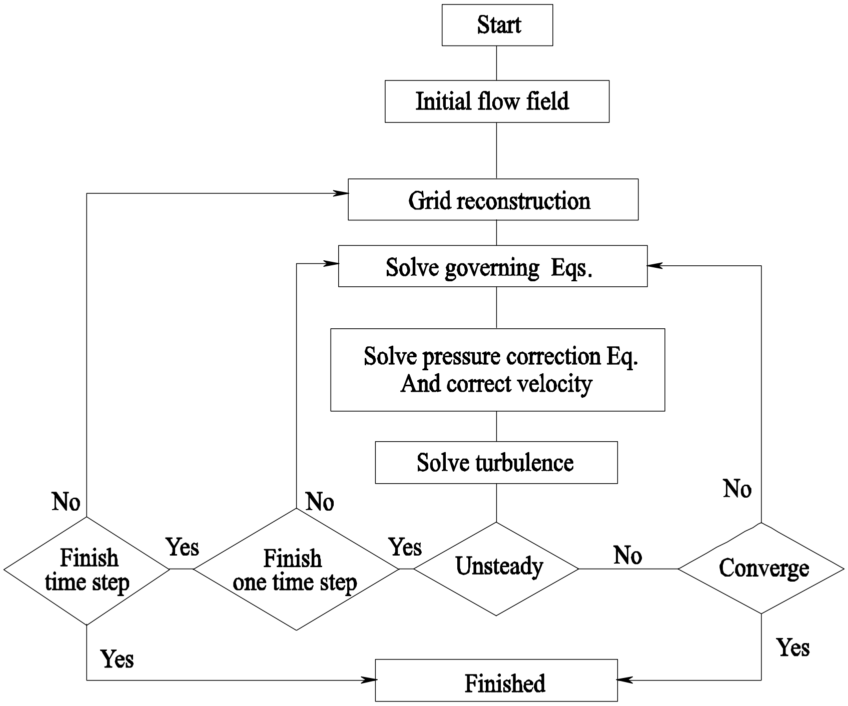

Figure 2.3: Simulation algorithm

2.2.3 Turbulence Model

The prediction of turbulent flows in complex flow passages such as turbomachinery is a great challenge due to the influence of the complex geometry of the passage. To achieve the objective of prediction, the accuracy of the turbulence model employed is a key issue in the numerical simulation of the flow field [42, 43]. This section is not aiming to cover all turbulence models, more attentions is given on the turbulence model that has been utilized in our numerical studies. The materials cited here are mainly from Launder & Spalding (1972) [44] and Wilcox (1998) [45].

Turbulent flows is strictly governed by the Navier-Stokes equations. In practice, it is usually solved by the Reynolds-averaged Navier-Stokes equations together with a proper turbulence models. A turbulence model is defined as a series of equations (algebraic or differential) which determine the turbulent transport terms in the mean flow equations and thus close the system of equations. Complexity of different turbulence models strongly depends on the information what one wants to achieve and also on the nature of Navier-Stokes equation (i.e. the $N-S$ equation) which is inherently nonlinear, time-dependent, three-dimensional PDE. Turbulence models are all based on hypotheses about the turbulent processes and to some extent rely on empirical formula; they do not resolve the details of the turbulent motion, but only the effect of turbulence on the mean flow behavior. Therefore, the concept of Reynolds averaging is the basis of turbulence modeling. **For modeling very complex phenomena, one of the most important issue is how to obtain the useful information by using a model as simple as possible**. Generally, the simulation methods can be classified by Figure 2.4[11].

Most extensive work has been done by Daly and Harlow (1970) [46] and Launder and Spalding (1972) [44] on two-equation turbulence model. $k-\epsilon$ model is the most common used two-equation turbulence model, although it

---

[11] Summary of current approaches by the author

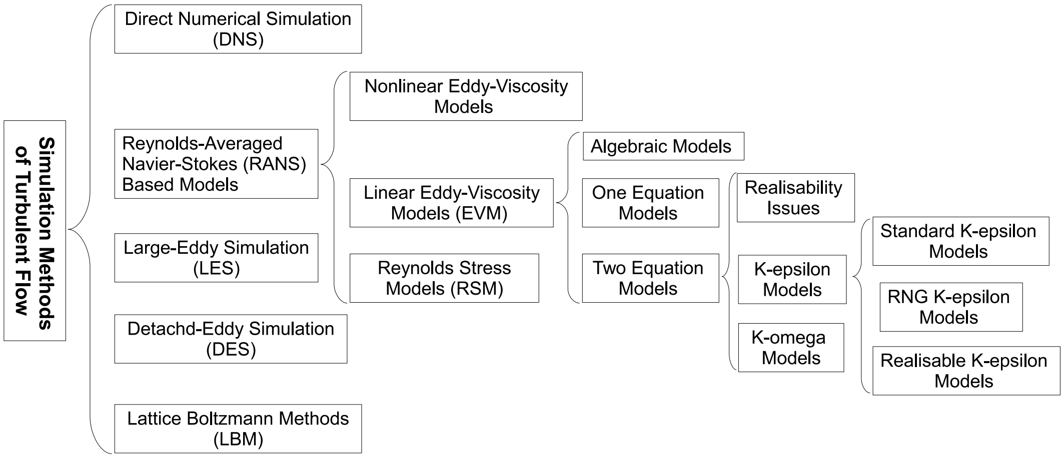

Figure 2.4: Classification of simulation methods of turbulent flow

does not perform very well in the flow with large adverse pressure gradients. It has two extra transport equations to represent the turbulent properties of the flow, allowing a two equation model to account for history effects like convection and diffusion of turbulent energy.

The first transported variable is turbulent kinetic energy, k. The second transported variable in this case is the turbulent dissipation, ϵ, which determines the scale of the turbulence.

The basis for all two equation models is the Boussinesq eddy viscosity assumption, which postulates that the Reynolds stress tensor, τ_{ij}, is proportional to the mean strain rate tensor, S_{ij}, and can be written in the following way:

$$\tau_{ij} = 2\mu_t S_{ij} + \frac{2}{3}\rho k \delta_{ij} \tag{2.5}$$

Where μ_t is a scalar property called the eddy viscosity which is normally computed from the two transported variables. The last term is included for modeling incompressible flow to ensure that the definition of turbulence kinetic energy is obeyed: $k = \frac{1}{2}\overline{u_i' u_i'}$. And

$$S_{ij} = \left(\frac{\partial \overline{u_i}}{\partial x_j} + \frac{\partial \overline{u_j}}{\partial x_i} \right) \tag{2.6}$$

Where δ_{ij} is the symbol of 'Kronecker delta' (when $i = j$, $\delta_{ij} = 1$; when $i \neq j$, $\delta_{ij} = 0$.

There are varieties of two-equation turbulence models, such as Standard $k - \epsilon$ model, Realisable $k - \epsilon$ model, RNG $k - \epsilon$ model, $k - \omega$ model, Wilcox's $k - \omega$ model, Wilcox's modified $k - \omega$ model, and SST $k - \omega$ model. For unsteady turbulent flow calculations, RNG $k - \epsilon$ model and SST $k - \omega$ model are widely used [11].

RNG $k - \epsilon$ model

The RNG model was developed using a rigorous statistical technique (called Renormalization Group (RNG) theory) by Yakhot et al. [47] to renormalise the Navier-Stokes equations to account for low-Reynolds-number effects. In the standard $k - \epsilon$ model the eddy viscosity is determined from a single turbulence length scale, so that the calculated turbulent diffusion is only for the specified scale, whereas in reality all scales of motion will contribute to the turbulent diffusion. The RNG model has an additional term in its ϵ equation, accounting for the different scales of motion, which significantly improves the accuracy for rapidly strained flows. Besides, the effect of swirl on turbulence is included in the RNG model, enhancing accuracy for swirling flows. An analytical formula for turbulent Prandtl numbers was applied, while only user-specified, constant values was used in Standard $k - \epsilon$ model [48]. These features make the RNG $k - \epsilon$ model more accurate and reliable for a wider class of flows[12] than Standard

---

[12] For example, high streamline curvature and strain rate; transitional flows; wall heat and mass transfer.

$k - \epsilon$ model. But it still lacks the accuracy for predicting the spreading of a round jet.

The momentum equation is

$$\rho \frac{\partial \overline{u_i}}{\partial t} + \rho \overline{u_j} \frac{\partial \overline{u_i}}{\partial x_j} = \rho F_i - \frac{\partial \bar{p}}{\partial x_i} + \mu \frac{\partial^2 \overline{u_i}}{\partial x_j \partial x_j} - \rho \frac{\partial}{\partial x_j} \left(\overline{u_i^{'} u_j^{'}} \right). \tag{2.7}$$

Here, $-\rho \overline{u_i^{'} u_j^{'}}$ is the Reynolds stress of turbulent flow as shown in Eqn. (**??**); $\bar{p}$ is the averaged pressure; ρ is the fluid density; and F is the body force acting on the unit volume fluid.

The transport equations for turbulent kinetic energy k are

$$\rho \frac{Dk}{Dt} = \frac{\partial}{\partial x_j} \left(\alpha_k \mu_{eff} \frac{\partial k}{\partial x_j} \right) + 2 \mu_t \overline{S_{ij}} \frac{\partial \overline{u_i}}{\partial \overline{x_j}} - \rho \varepsilon \tag{2.8}$$

and for dissipation rate ϵ are

$$\rho \frac{D\varepsilon}{Dt} = \frac{\partial}{\partial x_j} \left(\alpha_\varepsilon \mu_{eff} \frac{\partial \varepsilon}{\partial x_j} \right) + 2 C_{1\varepsilon} \frac{\varepsilon}{k} \mu_t \overline{S_{ij}} \frac{\partial \overline{u_i}}{\partial \overline{x_j}} - C_{2\varepsilon} \rho \frac{\varepsilon^2}{k} - R. \tag{2.9}$$

Here, the strain tensor components: $\overline{S_{ij}} = \left(\frac{\partial \overline{u_i}}{\partial \overline{x_j}} + \frac{\partial \overline{u_j}}{\partial \overline{x_i}} \right)$; the effective viscosity $\mu_{eff} = \mu_t + \mu$, where the eddy viscosity is $\mu_t = \rho C_\mu \frac{k^2}{\varepsilon}$ and μ is the molecular viscosity of fluid; and the additional term $R = \frac{C_\mu \eta^3 (1 - \eta / \eta_0)}{1 + \beta \eta^3} \frac{\varepsilon^2}{k}$ with $\eta = S \frac{k}{\varepsilon}$. The coefficients above are evaluated as $\eta_0 = 4.38$, $C_\mu = 0.0845$, $\beta = 0.012$, $C_{1\varepsilon} = 1.42$, $C_{2\varepsilon} = 1.68$, $\alpha_k = 1.0$ and $\alpha_\varepsilon = 0.769$ [47, 49].

SST $k - \omega$ model

The $k - \omega$ model is one of the most common turbulence models, which is a two-equation eddy-viscosity model. The first transported variable is turbulent kinetic energy, k. The second transported variable in this case is the specific dissipation frequency, ω. It is the variable that determines the scale of the turbulence, whereas the first variable, k, determines the energy in the turbulence. This allows a two equation model to account for history effects like convection and diffusion of turbulent energy. The $k-\omega$ based Shear-Stress-Transport (SST) model was originally used for aeronautic applications, providing highly accurate predictions of the onset and the amount of flow separation under adverse pressure gradients by the inclusion of transport effects into the formulation of the eddy-viscosity. This results in a major improvement in terms of flow separation predictions [50]. It becomes an industrial, commercial and research codes which has been widely applied to accurate computations of flows with pressure induced separation far beyond aerodynamics.

The use of a $k-\omega$ formulation in the inner parts of the boundary layer makes the model directly usable all the way down to the wall through the viscous sub-layer, hence the SST $k-\omega$ model can be used as a Low-Re turbulence model without any extra damping functions. The SST formulation also switches to a $k-\omega$ behaviour in the free-stream and thereby avoids the common $k-\omega$ problem that the model is too sensitive to the inlet free-stream turbulence properties. The SST $k-\omega$ model does produce a bit too large turbulence levels in regions with large normal strain, like stagnation regions and regions with strong acceleration. This tendency is much less pronounced than with a normal $k-\omega$ model though.

2.2.4 Comparison of DNS, LES with RANS methods

The concept of turbulence scale should be firstly introduced before better understanding these three modeling frameworks (i.e. DNS, LES and RANS).

Turbulent flows are characterized by a wide range of length scales. It's a better way to treat turbulence as vortex dynamics [51]. Flow can be considered as a collection of eddies of different sizes. The largest 'energy containing' eddies are of the order of the length scale of the object that generated turbulence in the first place[13]. The smallest eddies are the ones where the energy is dissipated. Generally speaking, there exists a 'cascade' of energy from the large scale to the smallest scales, owing to the random stretching of large eddies which interact with each other and eventually breakdown into smaller eddies. Three typical turbulence scales, as shown in Figure 2.5, are summarized as follows.

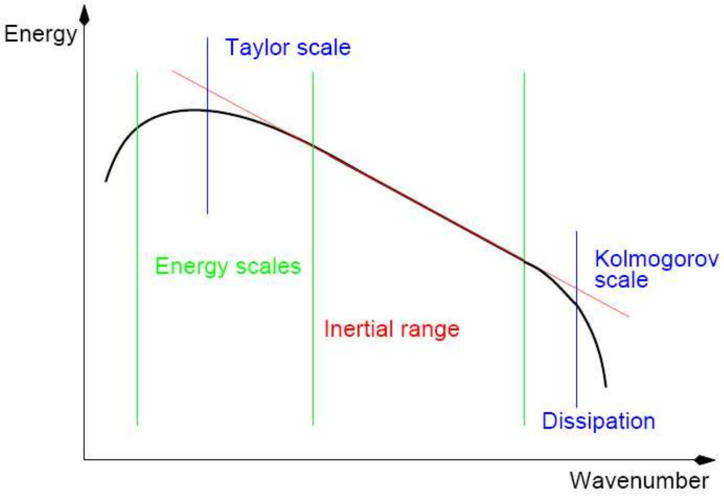

Figure 2.5: Scales of turbulence

Taylor scale: energy-containing vortices, which contain the highest part of the turbulent kinetic energy;

Inertial scale: where vortex stretching can be described by inertial effects of vortex breakup. Viscous effects are negligible;

Kolmogorov scale: the smallest scales, where the Reynolds number is small enough that viscous effects become dominant and the energy is dissi-

---

[13] For example, vortex shedding from a cylinder

pated.

Strictly speaking, DNS is not a turbulence model which solves the complete N-S and continuity equation on a computational grid without any approximations or averaging except the inherent approximations made in numerical discretization of the governing equations. All length and time scales of interest can be simulated in a well-resolved transient mode with sufficient spatial and temporal resolution [52]. For a successful simulation one basically needs to obtain the flow information of the smallest length, time and velocity scales of interest in advance. This is crucial for setting up space grid and time steps of adequate scales [53]. These data can be acquired by applying Kolmogorov turbulence theory, and thus the necessary number of grid point and time steps can be also extracted. All flow parameters are calculated at each grid point and then plot the flow parameter using those grid points. As shown in Figure 2.6, more details captured by more number of measurements. The biggest advantage regarding DNS is capable to 'capture' all the details of the flow, which however consequently requires your grid resolution should be fine enough to capture the 'smallest' flow structure. This demands the immense computer resource required in a sense of both processor's speed and memory size for storing intermediate results. For now DNS is unrealistically expensive for flows of engineering applications, however it still serves as very powerful research tool for gathering wealth of detailed information, particularly for model evaluation and fundamental understanding of all kinds of transition (e.g. natural, bypass, separated flow). As an alternative research method of experiments, the superiority of DNS is the reliable and complete data which can be correlated and visualized according to the needs. Gilbert (1988) [54], Gilbert & Kleiser (1990) [55] firstly modelled the flow from laminar to fully turbulent state by using DNS. The first DNS investigation of bypass transition was performed by Jacobs & Durbin [56] who found good overall agreement with the experiments by Roach & Brierley [57]. For more references see the book by Schmid & Henningson [58] and the recent review by Durbin & Wu [59].

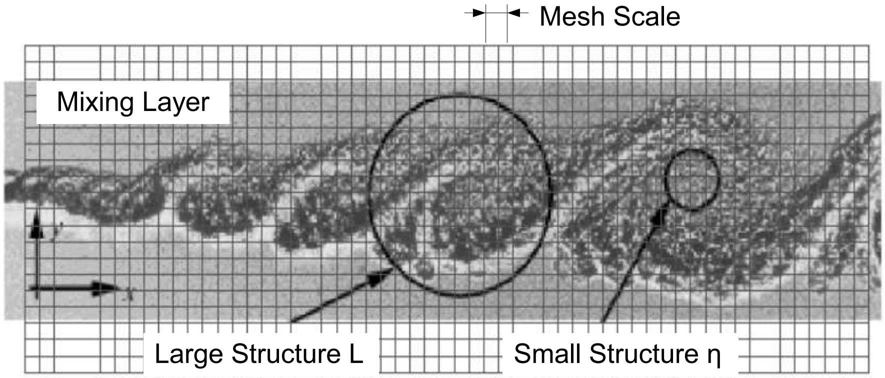

Figure 2.6: Detailed flow structure captured vs Number of grid points

Large-eddy simulation (LES) provides an alternative approach between DNS and RANS, in which large eddies are explicitly computed (resolved) in a time-dependent simulation using the 'filtered' Navier-Stokes equations. The first simulation has successfully performed by Deardorff (1970) [60], based on the eddy-viscosity model proposed earlier by Smagorinsky (1963) [61]. For new progress on this technique, see reviews [62]. In this method, the eddies (turbulent vortices) above a certain size are computed directly while the effect of smaller scales are modeled. This feature compared with DNS and RANS is pictorially shown by Figure 2.7. Its space grid and time steps is much longer than in DNS, and thus the required computational power of LES is much more economical than that of DNS.

The idea underlying LES is so called convergent evolution. Behavior of the large-scale eddies are strongly flow-dependent, owing to its dependence on the forces acting on the flow and on initial boundary conditions (geome-

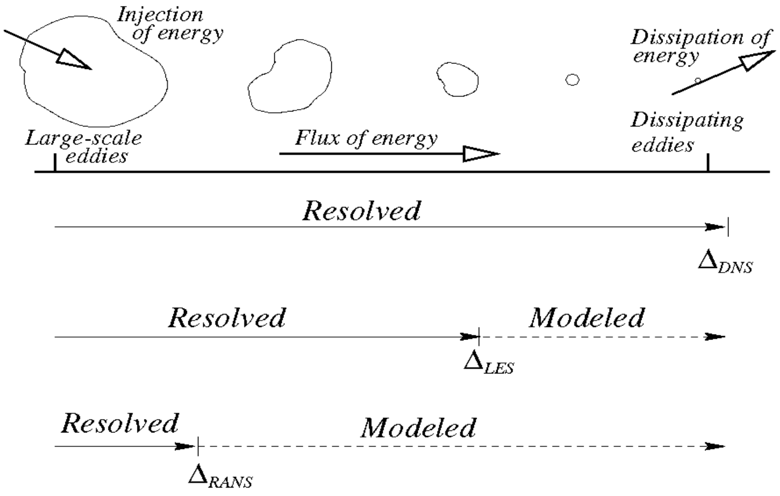

Figure 2.7: Modeling extend for different turbulent models

try, inflow, etc.). While for the small-scale eddies, they are coming from the dynamic activities of the larger scales and more homogeneous and isotropic than the large ones. They are flow-independent. Thus in LES, small eddies are generally supposed to be easier modelled owing to its self-similarity [63]. Another principal operation regarding LES is low-pass filtering, aiming to eliminate sub-grid fluctuations from resolving and reduce the computational cost of the simulation. Subgrid-scale models are those such as the Smagorinsky model [61], the Algebraic Dynamic model [64], the Dynamic Global-Coefficient model [65], the Localized Dynamic model [66], the Wall-Adapting Local Eddy viscosity model [67] and etc.

2.2.5 Why choose RANS model

No single turbulence model is universally accepted as being superior for all kinds of problems. In practice, the selection of turbulence model depends on many factors, such as the physical model of a specific flow, the level of accuracy required for a practical problem, the available computational capacity and the amount of time available for the simulation. In order to make the most appropriate choice, one needs to know what the most desired flow information are in the simulation. Besides, understanding the capabilities and limitations of the various optional models is also essential. For reference, see [41, 45, 48].

Why do we choose RANS model for our case? RANS equations govern the transport of the averaged flow quantities, which are mostly employed for turbine-flow modeling. They do not allow differentiation of the complete turbulent spectrum, unlike DNS and LES, which in turn require enormous computational resources. However this is not the main reason for choosing it. We should pay more attentions to the nature of time averaging since this is inherent in RANS formulations. The rationale for Reynolds averaging is that we are not interested in the entire spectrum of turbulence scales, thus some part of flow solution of small-scale turbulent fluctuations is to be ignored. We are tackling the high Reynolds numbers and determining the resolution based on required engineering accuracy. In other words, averaging intrinsically results in a loss of some detailed information. However the lost details by averaging is not essential information for achieving the main objective in this case.

The effect can be further seen from Figure 2.7. Compared to the models solving RANS equations, the models based on DNS and LES method computing fluctuation quantities resolve smaller length scales. Hence, if the small-scale flow field fluctuations are desired objectives of the predictions (e.g. modeling wall-bounded flows), then the negative effects of RNAS method cannot be ignored. In other words, without proper empirical correlations (which are generally not sufficiently reliable), the averaging-effect of RANS is absolutely not suitable for studying short-scale fluctuation quantities of some flows (e.g. flow transition). However for our case, we are looking for the possible low-frequency pressure fluctuations in the free-stream, for which large-scale vortex structures[14] at the scale of main turbine passage are responsible. Thus, transient RANS method is particular suitable and thus chosen for our targeted problem[15], while enjoying robust, economical advantages.

2.3 Literature Review on CFD Simulation of Francis Turbine

The undesirable effects of draft-tube pressure surge associated with a processing helical vortex are well known. Rheingans [68] was the first person who proposed an empirical equation to estimate the characteristic frequency f_n of the vortex rope in the draft tube. First attempts to investigate the physical nature of the draft tube vortex at part load by means of Computational Fluid Dynamics (CFD) have been published since 1999. For early examples, see Ruprecht et al. [69] and Sick et al. [70].

Extensive experimental and numerical investigations of the draft tube vortex rope have been done with predictions of the frequencies and pressure pulse amplitudes caused by the vortex rope precession as well as system resonance ([71]). Measurements on high head Francis turbines have shown that the pressure pulse frequency can reach up to $13f_n$ in the vaneless space and spread to the turbine [72]. Low-frequency pressure pulsations ($f_{pulsations} < f_n$)

---

[14] That is, unsteady vortex structures triggered by the guide-plate device as proposed, swirling vortex in the runner passage and vortex-rope in the draft tube.

[15] That is for predicting the large-scale vortex fluctuations in the entire flow field.

can cause fatigue cracks in the runner blades, whereas high-frequency pressure pulsations may limit the operating range of the turbine. High-amplitude pressure oscillations and a RSI frequency near the runner natural frequency can also produce resonance in the system [73]. Serial studies by Wang and Zhou (e.g., [74, 75]) relate the pressure oscillations caused by vortex ropes with the operating conditions. Paik et al. [76] simulated the swirl flow in the draft tube using an unsteady statistical turbulence model. Zhang, et al. [12] well explained the physical origin and control strategy of this spontaneous unsteady vortical flow. Two types of vortex ropes have been introduced in their work. The first one is a spiral-type vortex rope which is generally detected at the 'part-load condition[16]'. Its strong unsteady motions are always associated with severe low-frequency pressure fluctuations that often threat the turbine's operation and even the safety of the whole power station. The other one is a bubble-type vortex rope which occurs typically at the so-called 'higher part-load condition[17]', whose spiral tails also cause pressure fluctuations with relatively smaller amplitudes, therefore, sometimes named as vortex core.

Numerical simulations have investigated the flow field inside the turbine under different operating conditions. The latest research by Trivedi et al. [77] briefly reviewed the techniques and models that have been used to simulate hydraulic turbines to date. Owing to the limitations in computational resources, most studies simulated each component of the turbine separately. However, as discussed in above section, unsteady simulation on the entire turbine flow passage is essential for the accurate prediction and analysis. Tang et al. [78] predicted the pressure pulse characteristics with experiments in a

---

[16] Under 60% of the full load or so

[17] At $60 - 85\%$ of the full load

Three Gorges turbine, and investigated the relationships between prototype and model turbines. Liu et al. [79] numerically investigated the pressure pulse in an entire Three Gorges turbine and compared the results with model test data. The emphasis of later paper by Liu et al. [80] was the pressure fluctuation in draft tube. Stability problems on the Three Gorges prototype have been thoroughly studied by unsteady numerical simulations and experimental investigations, owing to its importance for the safety of operation (e.g., [81,82]).

Instead of focusing only on the vortex rope, flow separation in the runner or unsteady rotor-stator interference, few studies included the predictions of the unsteady performance, pressure pulses and unsteady flow behaviour in the entire flow passage. Xiao et al. [83] predicted the characteristics of the dominant unsteady flow frequencies in different parts of the turbine for various guide vane openings at the highest head. This numerical study investigated the unsteady flow patterns including the blade channel vortex in the runner and vortex rope in the draft tube in order to partition the turbine operating regions and identify safe operating regions. Besides, Xiao et al. [84] also analysed the flow characteristics in the whole flow passage with emphases on the pressure pulses at three low heads by the experimental and numerical investigations.

Owing to this flow phenomena mainly dominated by vortex structures, an accurate CFD prediction of the draft tube vortex requires great care with respect to the turbulence model [70, 79, 85, 86]. The standard $k-\epsilon$ model and the Reynolds stress model are compared for simulating the swirling flow in a conical diffuser. Although flow patterns are well predicted by both turbulence models, Sick et al. [70] concluded that the Reynolds stress model is physically better justified but more computationally expensive. Results obtained by the standard $k-\epsilon$ model indicated that turbulent dissipation is over modelled; as a result, vortices cannot fully develop in the shear layer. This well-known weakness of the standard $k-\epsilon$ turbulence model can be overcome by a modification which takes into account the stabilizing effect of stream line curvature. For example, RNG $k-\epsilon$ turbulence model are broadly applied in the 3D unsteady turbulent flow in Francis turbine model. It was reported as a reliable and effective turbulence model for parametric studies to optimize the hydraulic design, predicting characteristics and for stability research of hydraulic turbines [75,81,87]. Owing to a better performance in adverse pressure gradients and separating flow, SST $k-\omega$ mode shows more popularity in recent studies on unsteady simulation of turbine flow [77, 79]. However, it has a tendency to produce too large turbulence levels in regions with large normal strain, like stagnation regions and regions with strong acceleration. While for the $k-\epsilon$ models, this tendency is much less pronounced [48]. Liao [82] has studied and compared both RNG $k-\epsilon$ and SST $k-\omega$ in her PhD thesis, showing that there is no significant difference between these two turbulence models when predicting the pressure fluctuations in the large Francis turbine; especially the ability to capture low-frequency-component pressure fluctuation is almost the same.

Furthermore, the computational grid is of major importance for a realistic prediction of the vortex and the related pressure drop toward the vortex core, as reported by Stein [88]. A good general rule says that the vortex core should be resolved by at least 20 grid cells. If this condition is not fulfilled both the velocity gradients and the pressure drop are under-predicted. Validation of predicted results versus experimental data obtained in a model test shows that single-phase flow simulations give very good results of the frequency as well as the amplitude of the pressure pulsations. The CFD simulation reported in [88] gives a frequency prediction within 2% accuracy compared to the measurements because very high grid resolution was used (overall 35 million nodes). For coarser computational grids, which are more common in industrial applications, the error in frequency prediction may be up to 20%.

Generally speaking, studying the draft-tube flow one can simply ignore the upstream disturbances and work on much simpler sole draft-tube flow. It is because the upstream disturbances to the draft-tube flow are on much smaller time scales[18] and do not resonate with the low-frequency modes of vortex ropes [80]. However, this simplification cannot apply for the case in this thesis. Our previous results showed that the unsteadiness caused by the guide-plate are also dominated by low frequency motions, resonating well with the vortex rope instabilities in the draft-tube, which will be further proved by more results in the following chapters.

---

[18] i.e., higher frequencies

Chapter 3

Computational Strategy and Validation

3.1 Experimental Test of Prototype Turbine

The physical model in the thesis was built according to the prototype turbine of 11F unit in the left power house. The cross section of this Three Gorges unit together with the guide-plate is shown in Figure 3.1. The specifications of the 11F turbine are presented in Table 3.1.

Table 3.1: Specifications of 11F turbine [3]

Rated power	710 MW
Max efficiency guaranteed	96.26%
Rated head	80.6 m
Min head	61.0 m
Max head	113.0 m
Rated speed	75 rpm
Run away speed	< 150 rpm

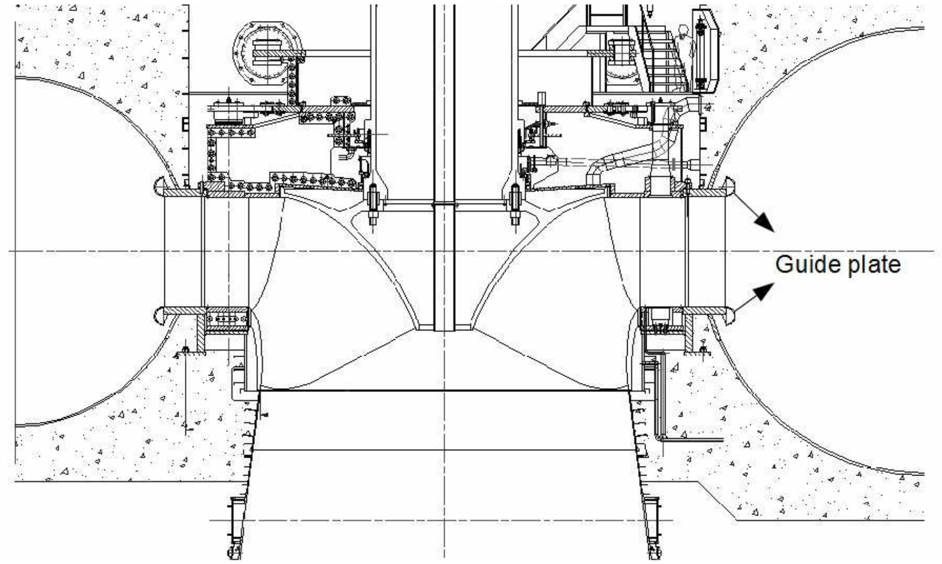

Figure 3.1: Cross section of the Three-Gorges unit with the guide-plate equipped in the spiral casing [4]

3.1.1 Monitoring System

An *in-situ* monitoring and analysis system has been employed to measure the fluctuating pressures, cavitation noise and air entrainment etc, for studying the hydraulic instability of the turbines in the left power plant that all equipped with the guide-plate device [11].

Position of Measuring Points

The selection and arrangement of measuring points is essential in the acquisition of vibration signal. The reasonable location and the number of measuring points in the monitoring system rest with several factors, such as the unit's operation performance and the hydroelectric equipment's structural characteristics, has great influence on the authenticity of the signal to be obtained and thus the diagnosis and analysis of the whole system.

For the Francis unit, it is essential to monitor its structural vibration, pressure pulsation and shaft swing. Particularly, the vibration caused by the unstable vortex-rope in the draft-tube is the most serious issue. Accordingly, measuring points for their vibration were arranged as below:

1. Two points along $X-$ and $Y-$ directions at three bearings, i.e., upper guide bearings (UGB), lower guide bearing (LGB), and turbine guide bearing (TGB) for shaft swings;

2. Three points along $X-$, $Y-$ and $Z-$ directions at the upper rack, the lower rack, and the head cover of the turbine for vibration monitoring, respectively. Owing to the upper rack subject to the weight of rotation components in the hydraulic thrust during the unit's run-time, two points are arranged along $X-$ and $Y-$ directions perpendicular to the vertical direction for vibration monitoring;

3. Two measuring points in the horizontal direction are arranged at stator core shell at 90° angles to each other in order to monitor the stator core vibration; In the vertical direction, one measuring point is arranged at the stator tooth plate. The monitoring and analysis of pressure fluctuations is essential at each turbine flow section.

The main measuring points for pressure fluctuations have been arranged at the spiral casing inlet, the draft tube inlet, and on inner surface of head cover. The pressure pulse at the draft tube inlet is monitored at the section below its inlet of $(0.4 \sim 0.5)$ D5 (D5 is the draft tube inlet diameter) on the downstream side. Typical arrangement of these measuring points is shown in Figure 3.2.

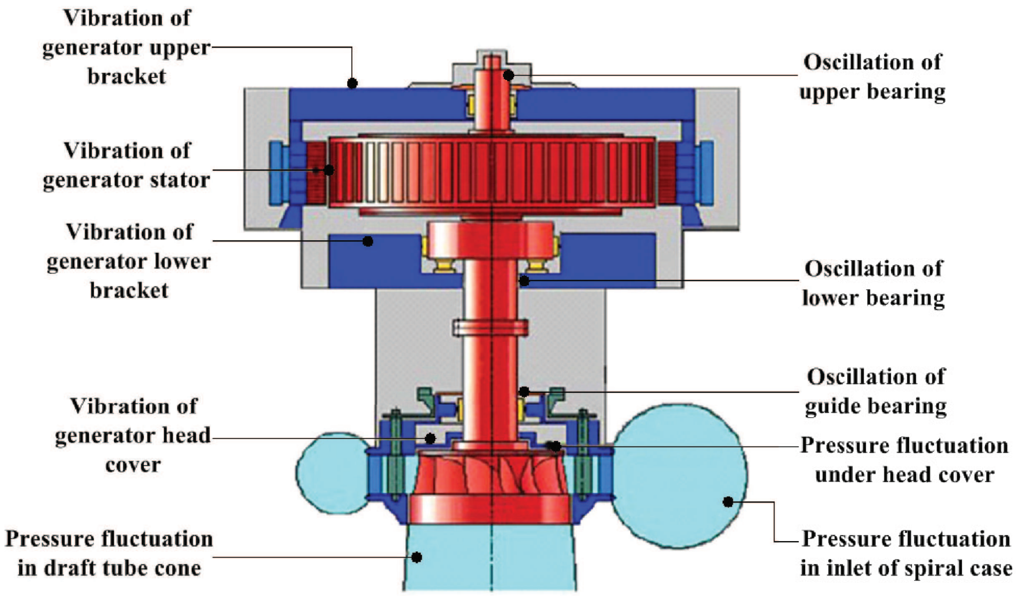

Figure 3.2: Arrangement of measuring points and experiment apparatus [4]

Sensors

As the inherent characteristic of Francis turbine units, low-frequency vibration measurements require a special attention. Recording the vortex-induced vibration requires a sensor with a suitable range. The velocity sensors are conventionally chosen for measuring the vibrations. The technical parameters are: Sensitivity, 8 $V/mm \pm 5\%$; Working frequency range, $0.3 \sim 150$ Hz; Range, ± 1000 μm; Amplitude linearity, $< 5\%$; Operating temperature, $-30 \sim +60$℃.

Monitoring and analyzing the pressure fluctuations on every flow section of the turbine aims to obtain the hydraulic characteristics of the hydro turbine for guiding the unit operating safely and effectively. There are 5 pressure transmitters in each unit, two are located under the turbine head cover, two are close to the inlet of draft tube, and one at the inlet of spiral casing. The ROSEMOUNT 3051 series transmitter is adopted and the pressure transmitter mode is 3051G. The technical parameters are: Accuracy, ±0.075%; Dynamic performance, delay time (Td), 45 ms; Refresh rate, 22 $times/s$; Zero and range, zero with the range value can be set arbitrarily within the range limit; Output, $4 \sim 20$ mA; Damping, User settings; Measuring range, user-defined with the threshold of 2.0 MPa; Temperature limit, $-40 \sim 121$℃ and Humidity limits, $0 \sim 100\%$ of relative value.

3.1.2 Analysis on Experimental Results

The *in-situ* investigations have been carried out since the Three Gorges turbines were put into operation in April 2005. The experimental data about the unsteady operating parameters, such as pressure fluctuation, shaft-torsional oscillation and structure vibration, have been collected and translated into both time- and frequency-spectrum results. Particularly, the characteristic frequencies and its behind mechanism of these unstable dynamic behaviors have been studied based on the obtained results.

Results at unstable operation zone

A single signal only tells the vibration characteristics of the unit at a single moment, a specific speed or a specific operating condition. Instead, the waterfall chart is able to present various frequency components with amplitudes at different loads. A three-dimensional spectrum diagram composed of a group of frequency spectra is obtained by recording continuous data in certain time-domain. Under normal circumstances, it is used to analyze the vibration characteristics under different operating conditions. According to the experimental investigations [4, 81, 82, 89], the power range of $280 - 410$ MW has been found to be the main unstable zone, presenting all types of unsteady flows (particularly the vortex rope in the draft tube). Turbine operating at part load is characterized by low flow rates with small guide-vane opening-angles, causing a high angle of attack on the fixed runner-blades. As a result, severe abnormal signals often occur at this operation-condition zone, particu-

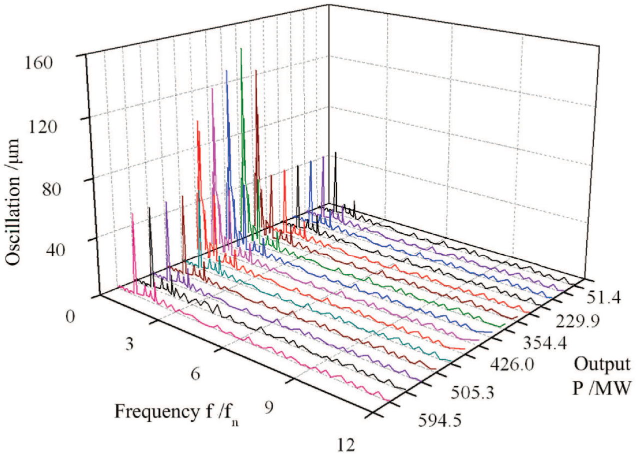

(a)

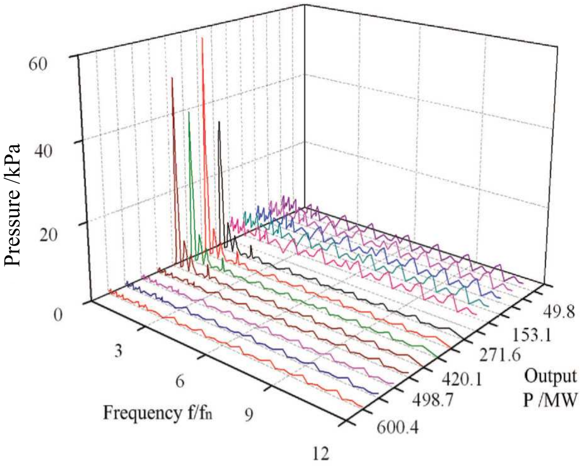

(b)

Figure 3.3: The waterfall charts indicate the unstable operation zone: (a) Shaft-torsional oscillations in the $X-$ direction at guide bearing; (b) Pressure fluctuation in the draft tube [4]

larly for the large-scale Francis turbines [90]. As presented in the 3-D waterfall charts of Figure 3.3, the shaft torsional oscillation and pressure fluctuation have been chosen as the typical parameters for indicating the unstable operation zone of the investigated turbine. In which X is designated as the dimensionless frequency f/f_n[1], Y as the amplitude of oscillation and Z as the output ranging from 51.4 MW to 594.5 MW, shows the measured shaft-torsional oscillations in the $X-$ direction at guide bearing over the ranged operation-condition. It clearly indicates more violent oscillations within the unstable zone of 280 $MW-420$ MW. The pressure in the draft tube fluctuates strongly within a certain range of frequencies. The situation becomes severer while operating within the unstable zone, referring to Figure 3.3(b). It can be seen that the dominant frequency within this range is the low-frequency component at approximate $0.3f_n$ with the relatively large amplitude of pressure fluctuation. The frequency of 1.25 Hz dominates the other operation conditions.

To study this unsteady behavior in detail, the shaft-torsional oscillation in the $X-$ direction at guide bearing under typical operation condition of 350 MW is shown in Figure 3.4 (a). The first strongest frequency is 0.31 Hz with the corresponding amplitude of $148\mu m$, referring to Figure 3.4 (b). Similar oscillation shows in the $Y-$ direction and it has the same strongest frequency (0.31 Hz), as shown in Figure 3.4 (c) and (d).

Shaft-torsional oscillation has important effect on the stability of a large Francis turbine operating within this load range. Experimental investigations (e.g., [90, 91]) pointed out that pressure fluctuations with the low-frequency components of $0.2f_n - 0.5f_n$ induced by the vortex rope in the draft tube,

---

[1] f_n is the runner rotating frequency, 1.25 Hz, at the running speed of 75 r/min

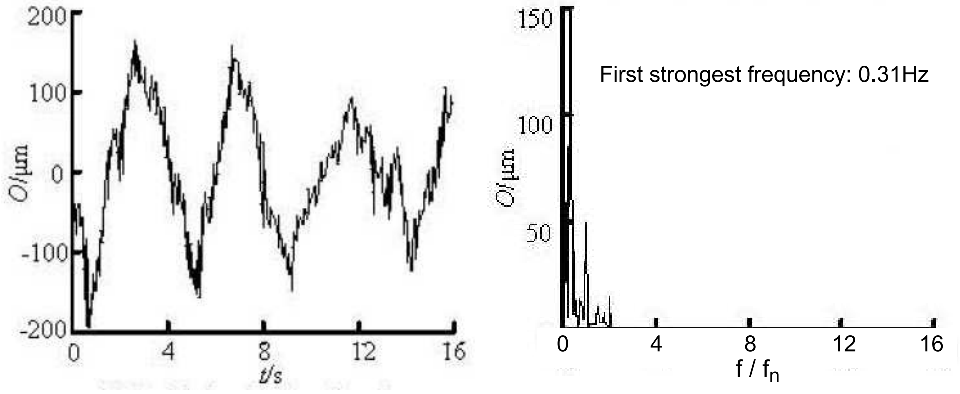

(a) $X-$ direction (b) $X-$ direction

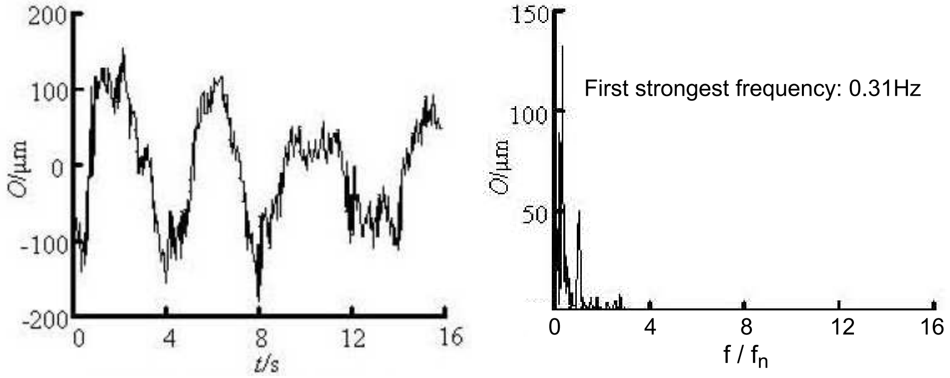

(c) $Y-$ direction (d) $Y-$ direction

Figure 3.4: Shaft-torsional oscillations at guide bearing at load of 350 MW: (a), (c) Oscillations in time domain; (b), (d) Frequency spectrum of oscillations [4].

usually exist under part-load conditions. It may also cause the shaft-torsional oscillation or the structure vibration. The pressure fluctuation in the draft tube at load of 350 MW verifies this viewpoint. As shown in Figure 3.5 (a), the periodicity of pressure fluctuation is obvious. The first strongest frequency of this pressure fluctuation is 0.31 Hz, as same as the characteristic frequency of shaft oscillation, referring to Figure 3.5 (b).

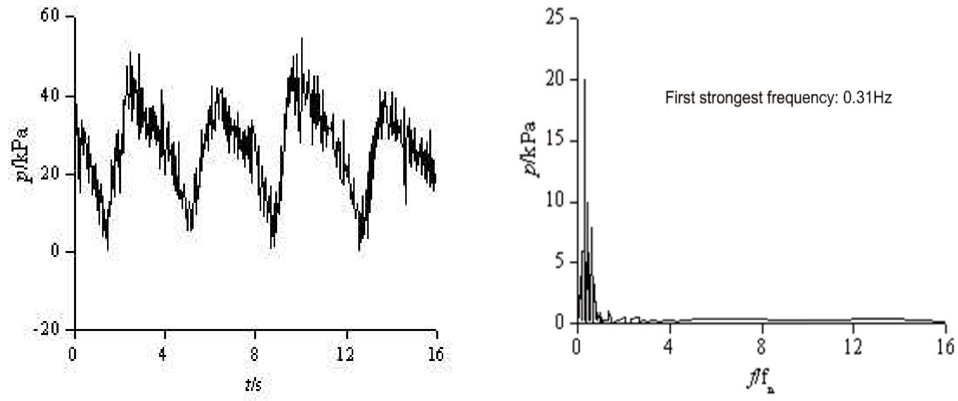

(a) (b)

Figure 3.5: Pressure fluctuations in the draft tube at load of 350 MW:(a): Pressure fluctuations against time; (b): Pressure fluctuations against frequency [4]

Results in special operating conditions

Many researchers have been puzzled by this special operating conditions in which this special vibration or oscillation takes place. This unsteady feature presents a significant threat to the safe operation of the units. These special vibration or oscillation have neither found in model tests nor in any numerical studies, therefore the *in situ* investigation is the only opportunity to analyze this problem.

Table 3.2 presents the recorded vibrations at different measuring points under the specific operating conditions (head: 68.3 m; range of load: 491 $MW-$ 556 $MW)$. It is noticed that the amplitude of the vertical vibration recorded at head cover exceeds the critical value within the load range of 531 $MW -$ 545 MW (Highlighted), although the horizontal vibrations for the measuring points during this range are far less than the critical value.

The details of the head cover vibration at a load of approximate 540 MW are shown in Figure 3.6. Comparing the horizontal vibration and vertical

Table 3.2: Peak to peak amplitude of vibration (μm) [4]

Load (MW)	491	510	531	540	545	550	556	Critical
Upper bracket (horizontal)	48.7	47.3	55.5	51	41.4	42	42.2	110
Upper bracket (vertical)	11.6	13.3	17.7	16	18.8	15.1	13.9	80
Low bracket (horizontal)	6.5	6.3	16.3	18	17.5	9.4	8.5	110
Low bracket (vertical)	19.6	22.3	33.8	33	39.3	26.7	20	80
Head cover (horizontal)	37.4	37.1	43.7	43	38.1	39	35.3	120
Head cover (vertical)	70.9	71.5	**178.6**	**165**	**154**	68.9	66.1	120

vibration in the same time domain, as shown in Figure 3.6 (a) and (c), it is clear that the vertical vibration is much stronger. This vibration value (peak-to-peak amplitudes of vibration) is as large as $165\mu m$, and exceeds the level-2 allowed value $120\mu m$ [92]. A frequency component at 5.7 Hz with the strongest amplitude of $84\mu m$, as regarded as 'special frequency', is revealed as the dominant one in the vibration spectrum as shown in Figure 3.6 (d). This special vibration frequency was confirmed in the *in situ* study at the load of 530 $MW - 545$ MW. It has also been observed in the vibration spectra for upper and low brackets, particular for horizontal vibration results although its level is not high.

The pressure transducers located at the inlet of spiral case indicated that the inlet flow is in good condition regardless the load is low or high. Figure 3.7 presents the pressure fluctuation at the inlet of spiral case at the load of 540.6 MW, showing very low pressure fluctuations. The pressure fluctuation under the head cover also exhibits similar features, as shown in Figure 3.8.

The amplitude is much less than 1 kPa at this special load. No noticeable dominant frequency with large fluctuation level was found for the pressure

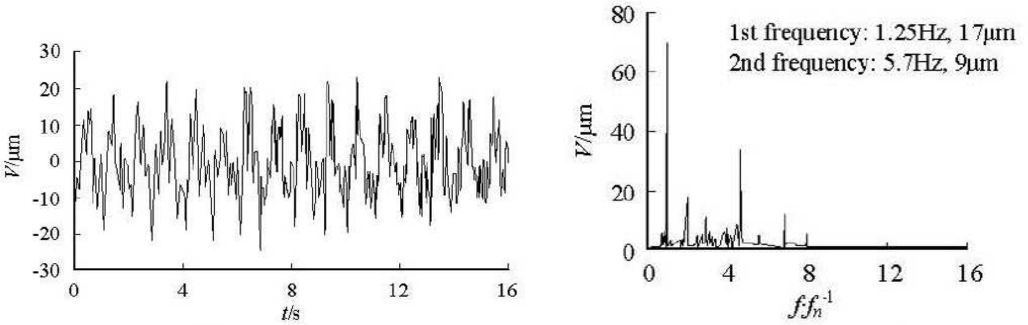

(a) Horizontal direction (b) Horizontal direction

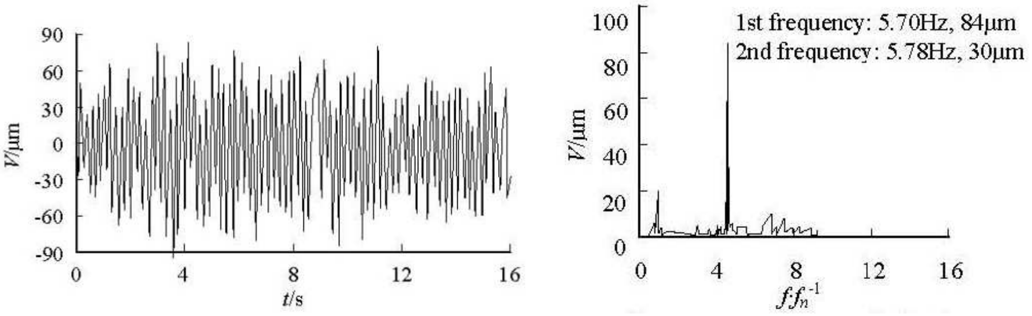

(c) Vertical direction (d) Vertical direction

Figure 3.6: Vibration of head cover at load of 540.6 MW: (a), (c) Vibration in time domain; (b), (d) Frequency spectrum of vibration. [4]

fluctuation. However, the pressure fluctuation in draft tube revealed a different frequency spectrum, as shown in Figure 3.9. There is a dominant frequency (5.70 Hz) in the frequency spectrum in this operating condition. The amplitude of pressure fluctuation at this frequency is 13 kPa. This frequency corresponds to the one at which a strong vibration of head cover exists.

Therefore, the numerical simulations for this PhD programme have been performed on typical operation points covering the full range of load for the initial study. Then three representative cases are selected and presented in this thesis: one with guide vane opening of 16° at 350 MW operates within the unstable operation zone; another with guide vane opening of 35° at 540 MW operates within the steady operation zone. The third case with the guide-vane

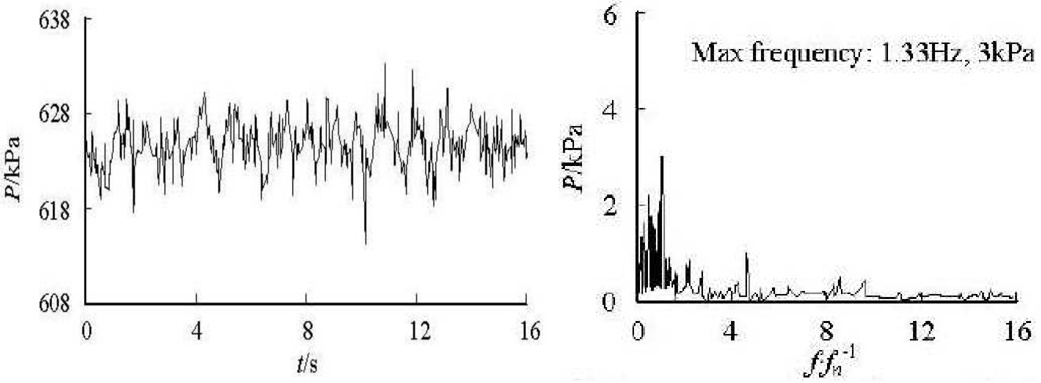

(a) (b)

Figure 3.7: Pressure fluctuation at inlet of spiral casing at load of 540.6 MW (a) Pressure fluctuation in the time domain; (b) Frequency spectrum of pressure fluctuation [4].

opening of 30° has been calculated as the comparison for the other two cases.

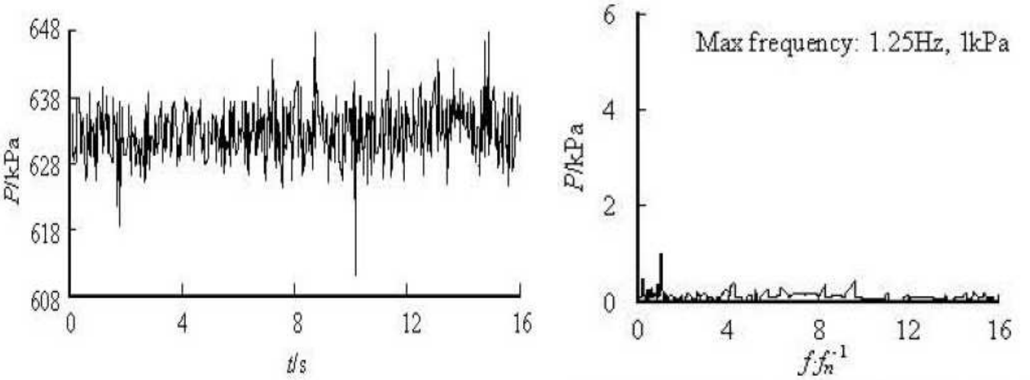

(a) (b)

Figure 3.8: Pressure fluctuation under head cover at load of 540.6 MW (a) Pressure fluctuation in the time domain; (b) Frequency spectrum of pressure fluctuation [4].

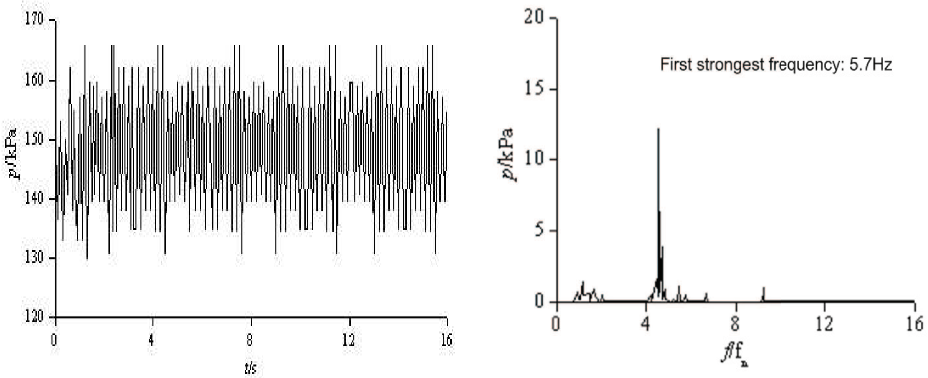

(a) (b)

Figure 3.9: Pressure fluctuation under in the draft-tube cone at load of 540.6 MW (a) Pressure fluctuation in the time domain; (b) Frequency spectrum of pressure fluctuation [4].

3.2 Geometric Modelling of Prototype Turbine

Solving CFD problem usually consists of four main steps: building-up a physical model, generating geometry and grid, solving and post-processing. Though theories are available for generating computational domain and grid, computing the equations and dealing with data etc, it is always a tricky task for modelling complex phenomena with a simple chosen model. An ideal model should introduce the minimum complexity but capable of capturing the essence of physics. Following this principle, the numerical model has been thus carefully built up for this PhD programme.

3.2.1 Numerical Models

The geometrical parameters of turbine model is presented in Table 3.3. The entire calculation domain is divided into five components: spiral casing, stay

Table 3.3: Parameters of turbine model

Name	Parameter preferences
runner diameter	$D_1 = 9.8\ m$
runner throat diameter	$D_{th} = 9.257\ m$
runner blade number	$Z_B = 15$
blade inlet angle	$\beta_1 = 53.3°$
blade outlet angle	$\beta_2 = 20.1°$
runner blade style	X style blade
nose angle of spiral casing	$\Phi = 345°$
entrance diameter of spiral casing	$D_{in} = 12.21\ m$
stay vane number	$Z_c = 24$
stay vane circle diameter	$D_c = 1.51D_1$
guide vane number	$Z_0 = 24$
guide vane height	$B_0 = 0.3D_1$
guide vane circle diameter	$D_0 = 1.19D1$
draft tube depth	$H_0 = 2.64D_1$
draft tube length	$L = 5.62D_1$
draft tube style	elbow draft tube with two piers

vanes, guide vanes, runner, and draft tube (including cone, elbow and outlet segments), referring to Figure 3.10 (a). The geometric models of runner and X style blade are showed in Figure 3.10 (b-c).

Our numerical simulation aims to investigate the effect of guide-plate on the free-stream turbulence for the entire flow passage of the turbine (in particular near the damage surface of the guide vanes). Two physical models for comparison have been employed. That is, *case 1*: without the guide-plate; *case 2*: with the guide-plate only. The axial cross-sections of these two geometric models are shown by Figure 3.11. In Figure 3.12, 3-D model of the guide-plate is plotted in the spiral case. Other geometrical dimensions for both models remain identical for comparability.

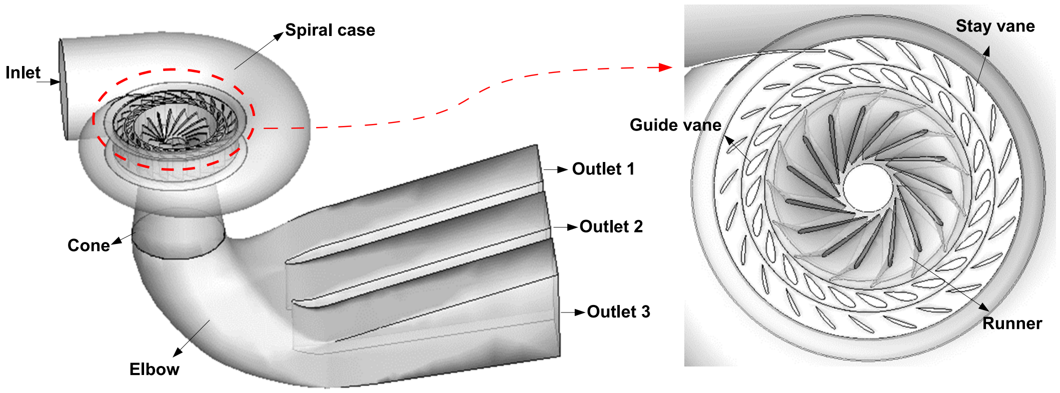

(a) Turbine model

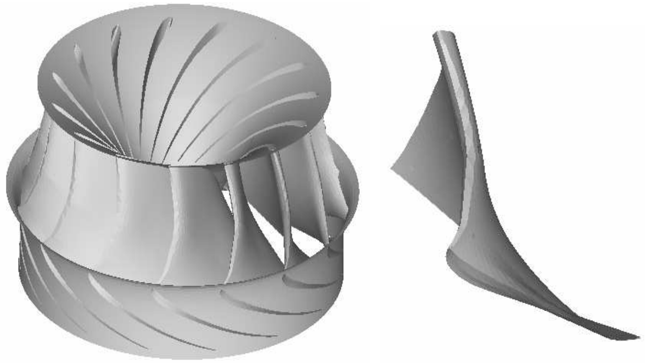

(b) Runner (c) X style blade

Figure 3.10: Geometric model: (a) Entire calculation domain; (b) Runner; (c) X style blade

3.3 Performance prediction

The overall efficiency of the Francis turbine is calculated based on the fundamental equation, i.e. ratio of output power from the turbine to input power supplied to the turbine. When it comes to the hydraulic losses in power generation, the hydraulic efficiency (η_h) is considered as the definition as the ratio of power developed by the turbine runner to power supplied by the water at entrance of the turbine. It can be calculated with the following equation,

$$\eta_h = \frac{H_e}{H} \tag{3.1}$$

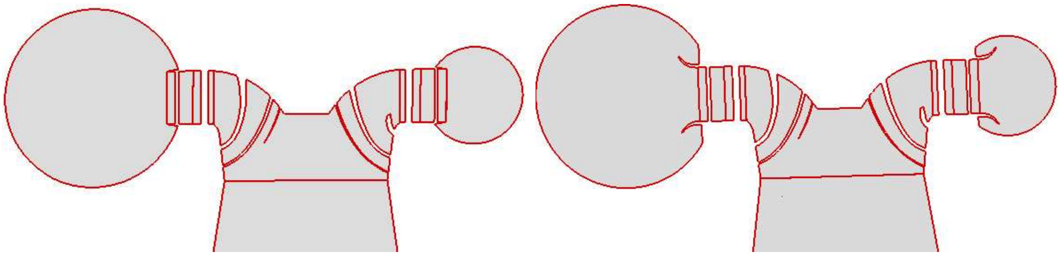

(a) Without Guide-Plate (b) With Guide-Plate

Figure 3.11: Axial cross-sections of two comparison models

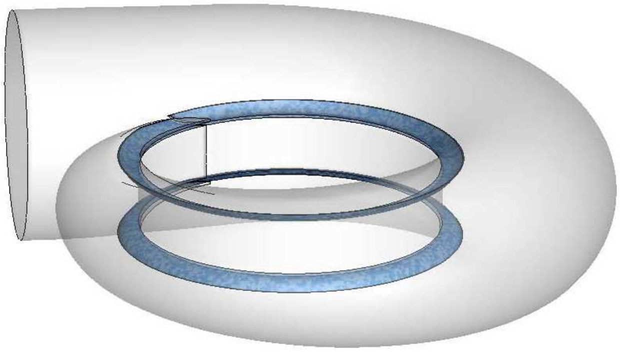

Figure 3.12: 3D model of the guide-plate in the spiral case

where H is the working head on the turbine and H_e is called 'Euler head' or 'Runner head' which represents the energy transfer per unit weight of water.

The working head H on the turbine is defined as:

$$H = H_{in} - H_{out} = H_{in} - [\left(\frac{p}{\rho g} + z\right)_{out} + \frac{(Q/A)^2_{out}}{2g}], \tag{3.2}$$

where p is the static pressure, ρ is the fluid density, z is the vertical ordinate. The subscripts *in* and *out* express the inlet of spiral casing and the outlet of draft tube, respectively.

The Euler head H_e is defined as:

$$H_e = \frac{1}{gQ}[(\int\int_{A_{ri}} u v_n v_u dA)_{ri} - (\int\int_{A_{ro}} u v_n v_u dA)_{ro}] \tag{3.3}$$

and Q is the discharge through turbine (m^3/s) given by

$$Q = \int\int_{A_{in}} \upsilon_n dA = \int\int_{A_{out}} \upsilon_n dA \tag{3.4}$$

Here, υ_n is the velocity normal to the boundaries at the inlet and the outlet, υ_u is the circumferential component of the absolute velocity, u is the rotation speed, g is the gravitational acceleration. The subscripts ri and ro denote the inlet and outlet sections of the runner respectively. The subscripts A_{in} and A_{out} are the areas of the spiral casing inlet and the draft tube outlet, respectively. The Euler head is obtained from the Euler equation for turbomachinery and all hydraulic losses in the three-dimensional turbulent flow through whole flow passage have been considered.

In Fluent, the hydraulic efficiency of the turbine is calculated by equation,

$$\eta_h = \frac{M\omega}{\rho g Q H} = \frac{M\omega}{Q(P_{ti} - P_{to})} \tag{3.5}$$

In above equation, M is the net hydraulic torque acting on the runner (N/m), ω is the angular speed (rad), P_{ti} is total pressure at the inlet of spiral casing (Pa) and P_{to} is the total pressure at the exit of draft tube (Pa).

The net hydraulic torque M as a resultant of pressure and viscous moments is calculated by taking surface integral of cross product of stress tensor and radius vector.

$$M = \int (\vec{r} \times (\tau \bullet n) dS) \bullet a \tag{3.6}$$

As the output parameters generated by Fluent, the volume flow rate Q is calculated based on the mass fluxes entering and leaving the turbine; the torque M acting on the turbine is calculated based on the total moment acting on the rotating runner. Both parameters can be read in Fluent post-processing report directly.

The output[2] of Francis turbine can be calculated by

$$p = \rho g Q H \eta_h \tag{3.7}$$

In unsteady flow simulation, at each time step of the computation, the flow rate and the torque of the turbine are recorded and the hydraulic efficiency and the output of the turbine can be calculated by Eqn. (3.5) and Eqn. (3.7), respectively.

3.4 Validation of Numerical Approach

3.4.1 Grid Independence

Unstructured meshes have been employed for this calculation owning to the complex shape of the computational domain. The flow is considered to be incompressible. For each geometric component, different computational grids have been generated manually according to the flow patterns and details sought, as shown by Figure 3.13. The grid independence has been firstly investigated within the range of grid numbers adopted by previous numerical studies.

For case 1, the physical model of the Three Gorges prototype turbine without the guide-plate, reported in numerical studies (e.g. Refs [9, 79, 81])

---

[2] Here only the hydraulic loss is counted. In practice the leaking and mechanical losses should also be counted to deduce the output for turbine runner.

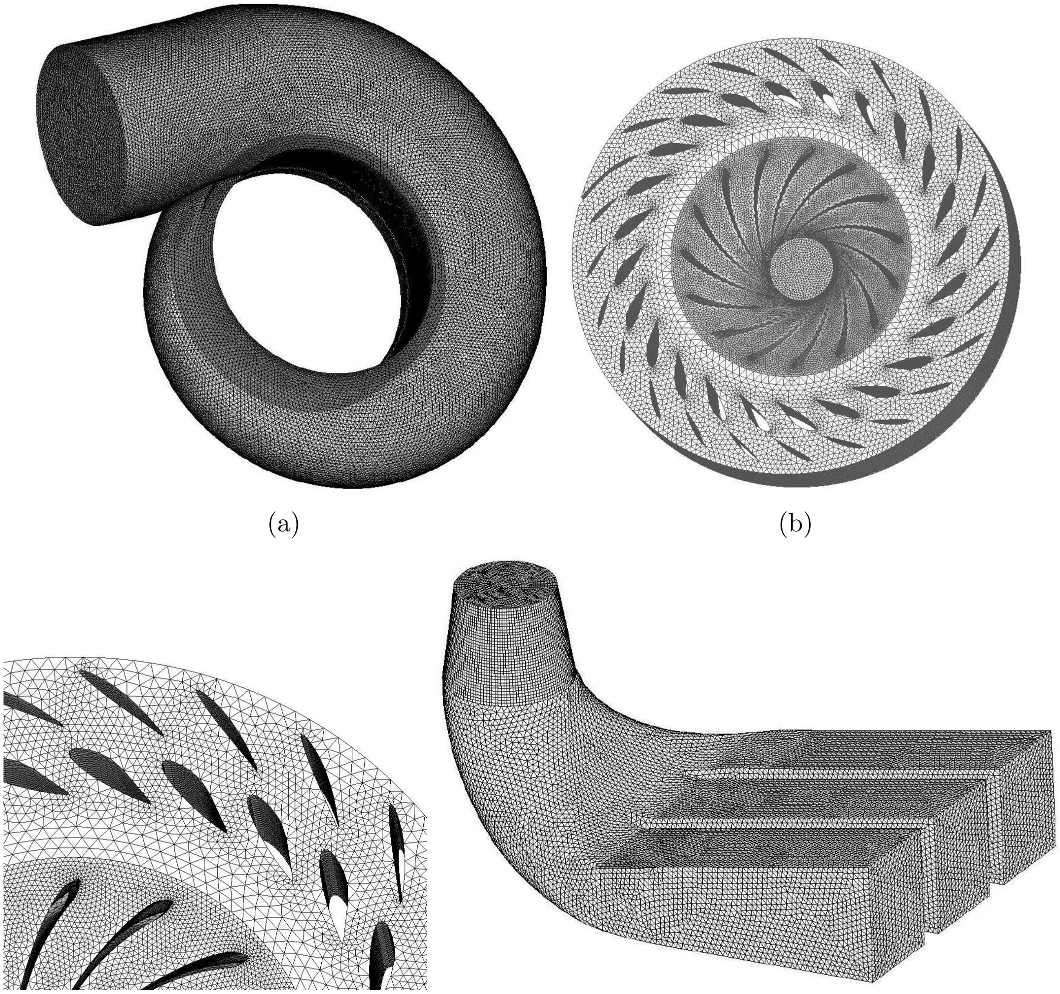
(a) (b) (c) (d)

Figure 3.13: Mesh model for each component

have done unsteady turbulent simulations by using similar models to investigate the hydraulic instability of the Three Gorges turbine. For simulations on the entire turbine flow passage, 350,000-550,000 nodes have been well accepted for obtaining reasonable results. For example, Liao [9] presented the curves for efficiency against unit discharge, $\eta - Q_{11}$, by using steady simulations with 360,000 nodes and 540,000 nodes for the comparison with experiment results. Both the calculated and the measured curves have similar trends except for the calculated value being lower. Efficiency calculated by the denser mesh model is closer to the experiment result, i.e., improved 0.56% by RNG $k-\epsilon$ turbulent model and 0.58% by SST $k-\omega$ turbulent model, as shown in Figure 3.14 [9].

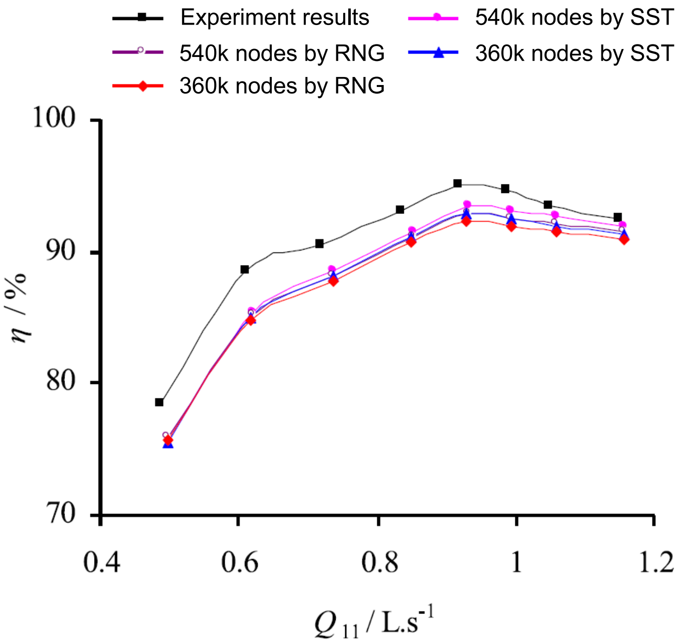

Figure 3.14: Efficiency-unit discharge curve ($\eta - Q_{11}$) [9]

In searching for part-load oscillating mechanism and control strategy of unsteady swirling flow in the draft tube, an SDTF (Sole Draft-Tube Flow) model has been employed by Zhang et al. [12], showing that 1.0×10^6 nodes are enough for predicting global performances of vortex rope in draft-tube under partial load operation, although their grid spacing is too coarse for investigating the flows in turbulent boundary layers and their separations. However, the coarse grid does not affect capturing the fundamental features of large-scale structures correctly. The dominant frequencies caused by large-scale vortex structures captured by coarse grid is almost the same as those captured by denser grid which is capable of obtaining more relatively small-scale URANS vortex structures in the turbulent boundary layers.

Therefore, for case 1 (without guide-plate) the final grid number of the whole turbine passage is approximate 5.84×10^5 nodes (1.96×10^6 elements) whose validity is already verified by other numerical studies of the Three Gorges prototype turbine as discussed above. Among them there are 211,010 nodes in the spiral case, 109,155 nodes in the stay vane, 86,200-88,000 nodes in the guide vanes subject to operation conditions, 46,804 nodes in the runner, 130,830 nodes in the draft tube. Further refining of mesh size has been tested in this study showing no improvement in the observed vortex structure but only increasing calculation time.

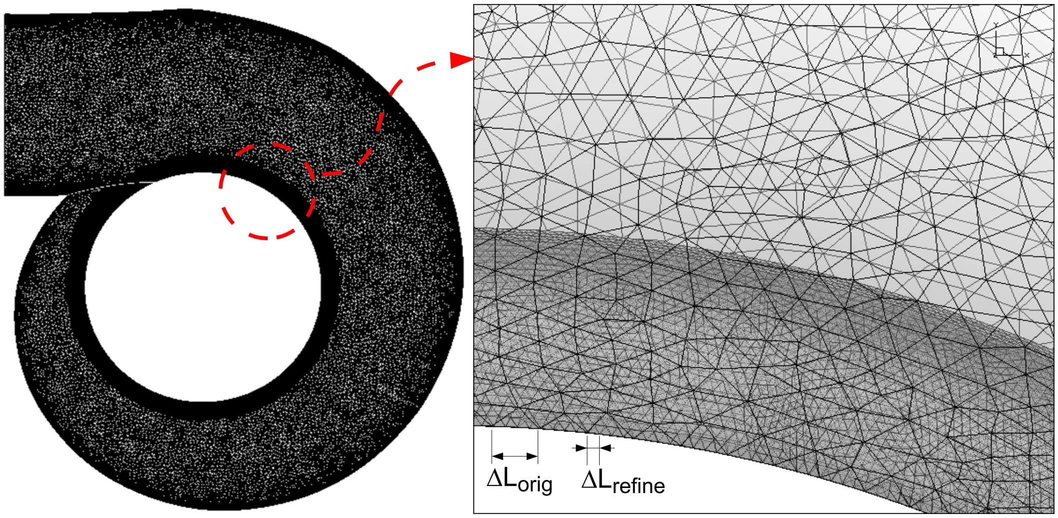

Figure 3.15: Refine the mesh of guide-plate; Original mesh size: ΔL_{orig}; Refined mesh size: ΔL_{refine}

After understanding the ranges of grid numbers for both the whole turbine model and the draft tube[3]. A series of numerical tests have been employed to further examine the influence of grid number and its distribution on the computed flow field according to the interests of this research. The damage

---

[3] It is a crucial component for studying large-scale unsteady vortex structures in Francis turbines particularly.

occurred on the pressure surface of guide-vane, therefore certain requirements have been satisfied in order to capture the detailed flow information on the objective area. For the standard wall function, each wall-adjacent cell's centroid in a RANS simulation should be located within the log-law layer with $30 < y^+ < 300$, preferably with y^+ close to its lower bound 30 [48]. Besides, in order to capture the delicate vortex structures around the guide-plate inside the spiral casing, a further refinement of the grid size around the guide-plate for case 2 (with guide-plate) was implemented according to this requirement, as shown in Figure 3.15. For case 2, the grid numbers of other components have to be increased as well for balancing the grid distribution throughout the entire flow passage.

For case 2 (with guide-plate), three mesh models have been adopted for grid-independence test by both steady and unsteady calculation. First one (mesh model_a) has the same grid numbers as for case 1 (without the guide-plate) plus 10^5 nodes for the guide-plate structure, the total nodes number is 6.8×10^5; Second one (mesh model_b) has refined the grid size on stay vane and guide vane but employed coarser grid for draft tube, the total nodes number is 1.3×10^6; Third one (mesh model_c) has refined the grid size for draft tube (as same grid size for draft tube as the first model), retaining the same grid sizes for stay vane and guide vane as the second model, the total nodes number is 1.4×10^6.

For all three mesh models, approximate 1000 checking points have been selected on the guide-plate and guide-vane surface for recording the values of average pressure in the steady simulation. The grid number sensitivity has been validated firstly by steady calculation. Recorded the number of checking points (n_1) comply the requirement:

$$\left|\frac{P_{i+1}-P_i}{P_i}\times 100\%\right| \leq 5\% \;\; (i=0,1) \tag{3.8}$$

and the number of checking points (n_2) comply the requirement:

$$\left|\frac{P_{i+1}-P_i}{P_i}\times 100\%\right| \leq 10\% \;\; (i=0,1) \tag{3.9}$$

where P_0, P_1, P_2 is the average pressure on certain checking point of three mesh models ($685k$, $1350k$, $1443k$) respectively. The difference between first two mesh models satisfied $n_2/1000 > 85\%$. For mesh models of $1350k$ and $1443k$, the difference is slight, strictly satisfying that $n_1/1000 > 80\%$ and $n_2/1000 > 90\%$. The total grid number of $1350k$ is good enough for steady calculation.

For unsteady calculation, further validating the influence of grid numbers on capturing the pressure fluctuations (especially the low-frequency components) is also necessary. Pressure fluctuations against frequency at runner, draft-tube and guide-vane have been recorded for these three mesh models. Results for mesh model_a and mesh model_c were compared and presented in Figure 3.16. No significant difference was found within the frequency-spectrum range of $0-20\ Hz$. Therefore, mesh model_b (total nodes number: 1350k) was selected for studying the case 2 (with guide-plate).

3.4.2 Turbulence Model and Boundary Conditions

RNG $k-\epsilon$ and SST $k-\omega$ has been briefly introduced in the Chapter 2 and compared in the validation study. There is no significant difference between these

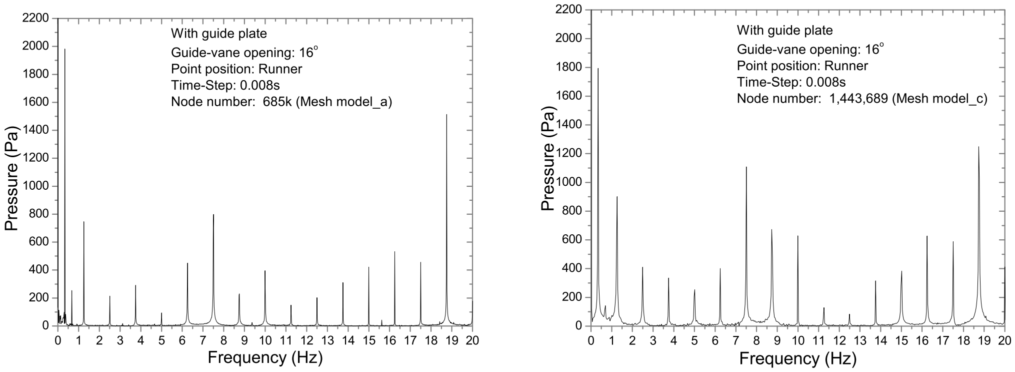

(a) Runner: $685k$

(b) Runner: $1443k$

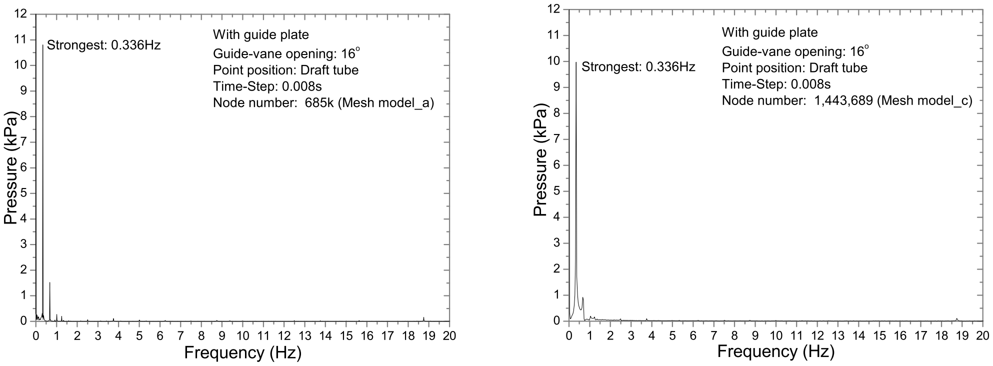

(c) Draft-tube: $685k$

(d) Draft-tube: $1443k$

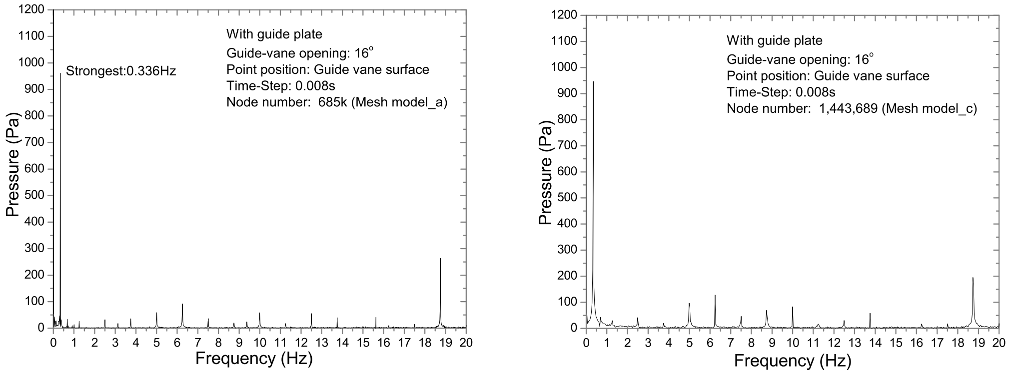

(e) Guide-vane: $685k$

(f) Guide-vane: $1443k$

Figure 3.16: Pressure fluctuations against frequency recorded at (a) Runner; (c) Draft-tube; (e) Guide-vane with notes number of 685k; (b) Runner; (d) Draft-tube; (f) Guide-vane with notes number of 1443k (Size of time-step: 0.008s; Guide-vane opening: 16°; Case with the guide-plate;)

two turbulence models when predicting the pressure fluctuation information in the large Francis turbine, especially the ability to capture low-frequency-component pressure fluctuation is almost the same. However the SST $k-\omega$ model takes longer time than the RNG $k-\epsilon$ model in the comparison test (approximate 1.4 times), as shown in Table 3.4.

Among four available Pressure-Velocity Coupling Algorithms in ANSYS Fluent, SIMPLEC is the most common used algorithm in unsteady simulation of complicated flow field. PISO is also recommended for transient calculations. These two algorithms were compared showing that PISO captures higher-frequency pressure fluctuations, while the periodic characteristics of the lower-frequency pressure fluctuations captured by SIMPLEC is more visible. Therefore, for mainly investigating the low-frequency behaviors SIMPLEC has been chosen for this case.

Table 3.4: Calculation Steps in 10 hours by different turbulence models and algorithms

	Calculated steps in 10 hours
RNG $k-\epsilon$, SIMPLEC	1000
RNG $k-\epsilon$, PISO	780
SST $k-\omega$, SIMPLEC	560
SST $k-\omega$, PISO	485

Therefore, RNG $k-\epsilon$ turbulence model has been employed to close the governing equations. A second order fully implicit scheme is applied for time discretization[4], central difference for the diffusion term and second order upwind scheme for the convective term. The SIMPLEC algorithm is used for the discretized equations. The total pressure and the turbulence was set at the inlet of the spiral casing with the velocity direction defined for the

---

[4] To ease the restriction in the size of time-step.

steady flow simulations. At the draft tube outlet, the average static pressure condition was calculated based on the water level. The sliding mesh model is used to obtain time-accurate solutions of the strong rotor-stator interactions at the interfaces of runner-guide vanes and runner-draft tube. The upstream variables were passed to the downstream locations by interpolation at the interfaces. The initial condition for the unsteady flow computation was based on the preliminary steady flow computation. In the steady flow computations, it took approximate 5000 iterations to allow the residual errors in the entire flow passage becoming sufficiently small ($\leq 10^{-5}$). The flow pattern after 5000 steady flow iterations was then specified as the initial boundary conditions for the unsteady flow computation. All simulations have been performed by using ANSYS FLUENT 13.0.

3.4.3 Size of Time-step

Though theoretically there is no strict requirement on the size of each time step when fully implicit scheme is applied for time discretization, it is still important to choose appropriate size of time-step, otherwise the computation could be vulnerable in terms of divergence and instability. Generally, the time-step size should be in the same order as the smallest characteristic time Δt_c:

$$\Delta t_c = \min\left(\frac{\Delta L}{U}, \frac{\rho \Delta L^2}{\Gamma}\right) \tag{3.10}$$

Here, U is the characteristic velocity, ΔL is the averaged mesh size, Γ is the dissipation term. The criterion of $\Delta t \leq 50\Delta t_c$ can be used for limiting the proper range of time-step [9].

Another practical guideline is the Courant number which is defined as:

$$Co = \frac{|\vec{v}|\,\Delta t}{l} \tag{3.11}$$

Here, $\vec{v}$, l are both the characteristic velocity and length respectively. If it is based on mesh size, $\vec{v}$ is estimated velocity, l is the averaged mesh size, the Courant number should not excess 100; If it is based on geometric size of the flow field, $\vec{v}$ is estimated averaged velocity of the whole flow field, l is the characteristic size of the geometric model, the Courant number should be in the range of $100 - 500$ [48].

According to Eqn. (3.11), when the Courant number has been set, time-step size is proportional to the mesh size since the average characteristic-velocity in given physical model is fixed[5]. It means that the time-step size is supposed to be larger for coarser mesh size, and smaller for denser mesh size. By striking a balance between the risk of divergence (and/or instability) and computation time, a right time step must be chosen between these two extreme cases.

The choice of time-step size is also highly dependent on the specific physical object and the turbulence level of the phenomena. Referring to the latest unsteady simulations of large Francis turbine [11], the range of time-step size is between 1/60 to 1/200 of runner rotation. In each time step, the convergence criterion is that the residuals of all the variables reach below 10^{-5}. After the calculation of one time-step finished, the computational mesh of the runner will turn to a new circumferential position according to the rotating speed. Thus, the computation for another time-step will be started. Moving

---

[5] Generally, the average characteristic-velocity is chosen as the average value of the maximum velocity and minimum velocity

meshes are adopted for the runner domain. The runner rotation speed is 75 r/min ($\omega = 7.854\ rad/s$), the time-step sizes of 0.008 s, 0.004 s and 0.002 s corresponding to 1/100, 1/200 and 1/400 of runner rotation (i.e. the sliding angles of interfaces are 3.6°, 1.8° and 0.9° respectively) have been compared in order to obtain the proper time-step size fine enough to predict the dominant frequencies of pressure fluctuations in the prototype of Francis turbine.

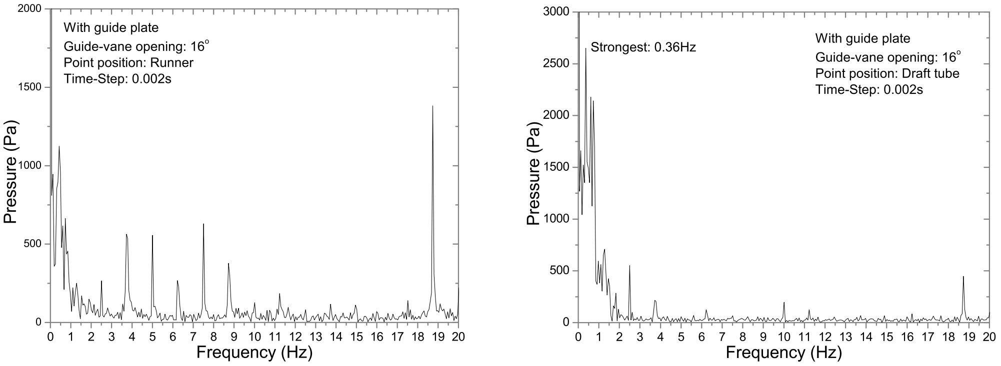

(a) Runner: FFT

(b) Draft-tube: FFT

Figure 3.17: Pressure fluctuations against frequency recorded at (a) Runner; (b) Draft-tube; (Size of time-step: 0.002 s; Guide-vane opening: 16°; Case with the guide-plate;)

There is no significant difference in FFT results by using these three different time-step size. The extremely low-frequency component has been captured in all cases as the strongest frequency, only their values are slightly different. As shown in Figure 4.19, the strongest frequency for case with time-step size of 0.008 s is 0.336 Hz, while for case with time-step size of 0.004 s and 0.002 s are 0.306 Hz and 0.36 Hz, referring to Figure 3.19 and Figure 3.17 respectively. By comparing the results of 0.004 s and 0.008 s, it is noticeable that smaller time-step size can capture more high-frequency fluctuations, e.g., the peak at 12.5 Hz is captured as a strong signal for the time-step size of

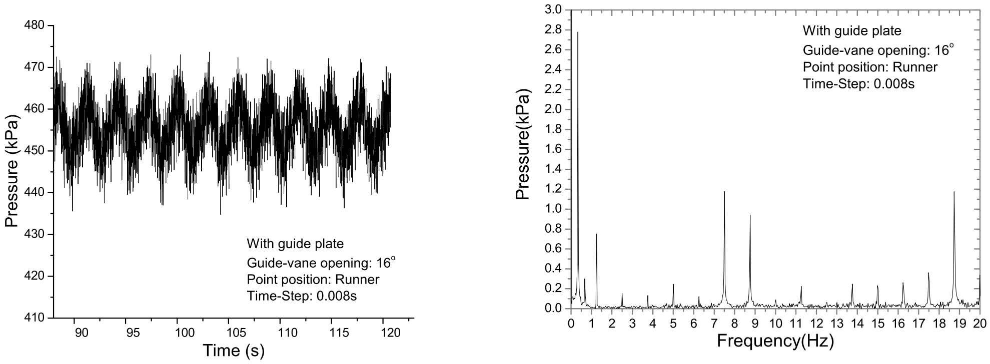

(a) Runner: $P-T$

(b) Runner: FFT

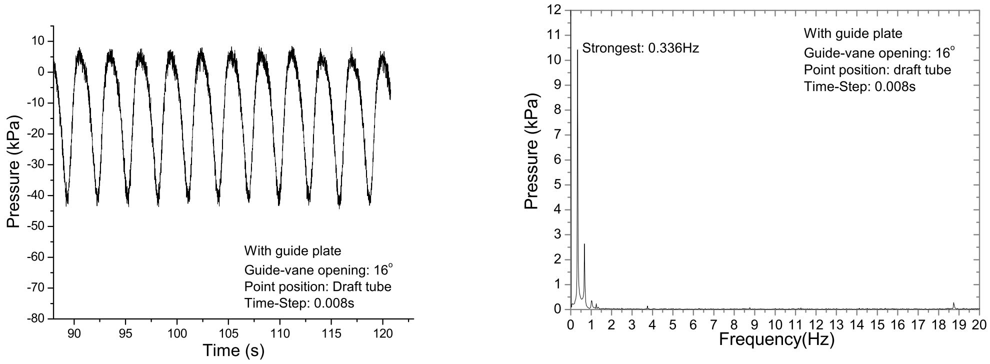

(c) Draft-tube: $P-T$

(d) Draft-tube: FFT

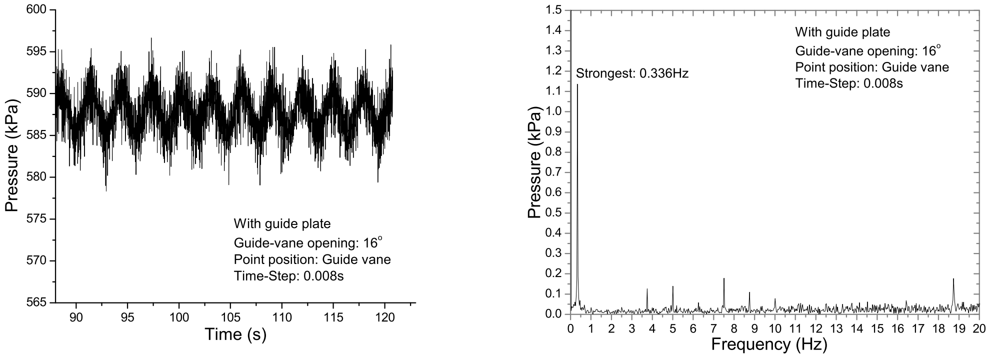

(e) Guide-vane: $P-T$

(f) Guide-vane: FFT

Figure 3.18: $P-T$ result: Pressure fluctuations against time recorded at (a) Runner; (c) Draft-tube; (e) Guide-vane; FFT result: Pressure fluctuations against frequency recorded at (b) Runner; (d) Draft-tube; (f) Guide-vane (Size of time-step: 0.008 s; Guide-vane opening: 16°; Case with the guide-plate;)

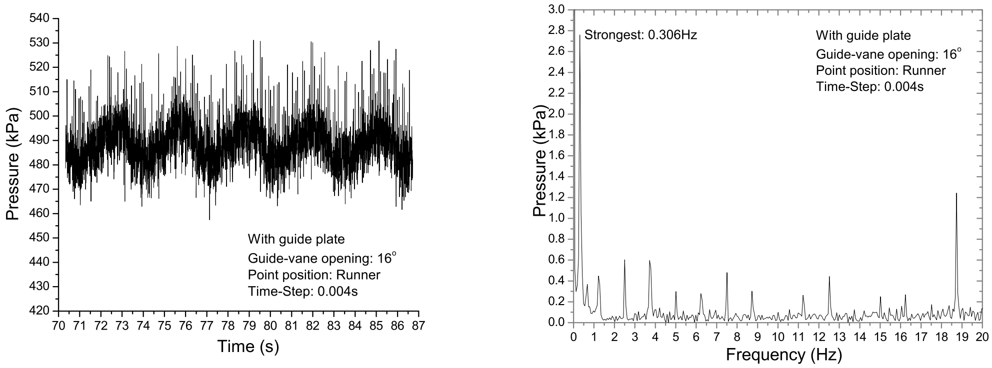

(a) Runner: $P-T$

(b) Runner: FFT

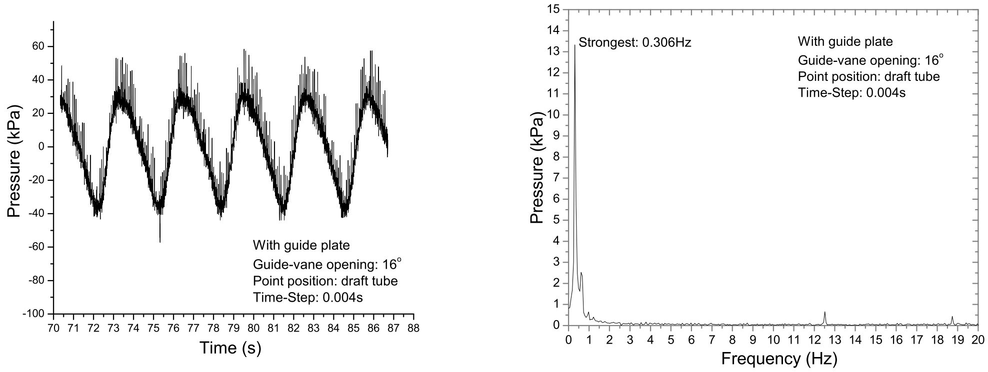

(c) Draft-tube: $P-T$

(d) Draft-tube: FFT

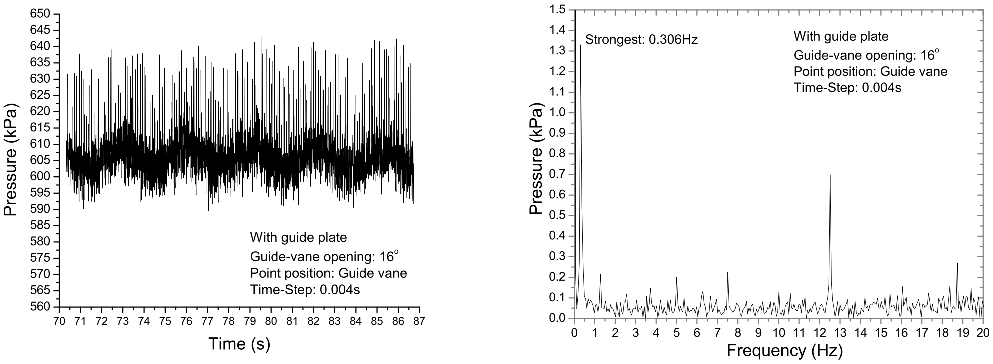

(e) Guide-vane: $P-T$

(f) Guide-vane: FFT

Figure 3.19: $P-T$ result: Pressure fluctuations against time recorded at (a) Runner; (c) Draft-tube; (e) Guide-vane; FFT result: Pressure fluctuations against frequency recorded at (b) Runner; (d) Draft-tube; (f) Guide-vane (Size of time-step: 0.004 s; Guide-vane opening: 16°; Case with the guide-plate;)

0.004 Hz, while not showing in the case with the time-step size of 0.008 s nor the case with the time-step size of 0.002 s. However, the finer time-step size will exponentially increase the computational time and require finer grid size. According to the analysis on the results, there is no necessity to choose the finest time-step size (0.002 s) unless we aim at looking for high-frequency fluctuations.

In this study, low-frequency pressure fluctuations are the main target. In the case with guide vane opening of 16°, low-frequency pressure fluctuation signal is very strong, allowing us to use the time step of 0.008 s. While for the case with guide vane opening of 35°, the time step of 0.004 s is adopted to obtain wider spectrum of pressure fluctuations.

3.4.4 Total Calculated Time Matters

The pressure fluctuations by nature are stationary oscillations though the numerically transient trip takes quite a while to fade out, owing to the complex nested loops in the code for solving the unsteady flows including the rotor-stator interactions for whole complex flow-passages of the turbine. As demonstrated in Figure 3.20, it takes long runner rotating time[6] (at least over 235 s) allowing the simulations to reach the status of stationary oscillations completely. The effective sampling interval for different operating conditions has to be determined upon the transient oscillation becoming a completed stationary oscillation. Otherwise in the FFT results false (numerical) frequency spikes (or white noise like) will also present even over shed the real spikes. This is particular true for the case of 35° that weaker oscillation signals hide in the numerical calculation noise (virtual signals) before the calculation time reach-

---

[6] That is the calculation time of runner rotation.

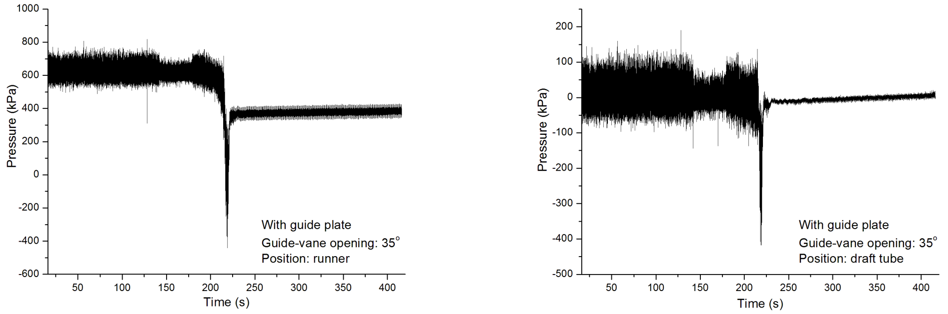

(a) Runner

(b) Draft-tube

Figure 3.20: Pressure fluctuations against time recorded at (a) Runner; (b) Draft-tube; (Time-span: $16s \sim 419s$; Size of time-step: $0.004s$; Guide-vane opening: 35°; Case with the guide-plate;)

ing certain threshold values for the real spikes to emerge. It can be further explained as follows.

For the case with guide vane opening of 35°, the numerically effective sampling period of $258\ s \sim 389\ s$ (2^{15} calculation steps) has been selected and the corresponding P-T results are showed in Figure 3.21 (a) and (c). The corresponding FFT results reveal very clear peaks as showed in Figure 3.21 (b) and (d). For the recording point in the runner, the strongest frequency component 18.75 Hz is the blade passing frequency[7]. All the significant components having harmonic frequencies of the rotation frequency (e.g. 2.5 Hz, 7.5 Hz and 10 Hz) indicate the rotor-stator interactions [93] being main instabilities at this operating condition. For the recording point in the draft tube, the strongest frequency component is 2.5 Hz and the second one is 1.25 Hz, the amplitudes of these two components are almost the same as those in the runner (see Figure 3.21(b)). However, the amplitude of peak at 18.75 Hz is much smaller than that in the runner. This is because the low frequency

---

[7] i.e. The number of blades, 15 times the rotation frequency 1.25 Hz, resulting in 18.75 Hz.

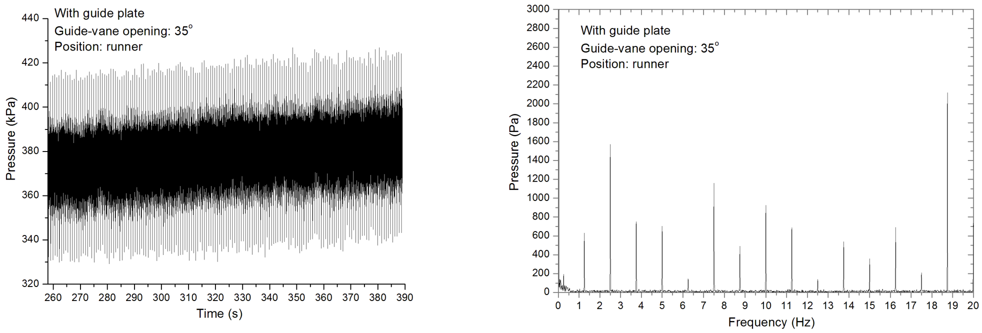

(a) Runner: $P-T$ (b) Runner: FFT

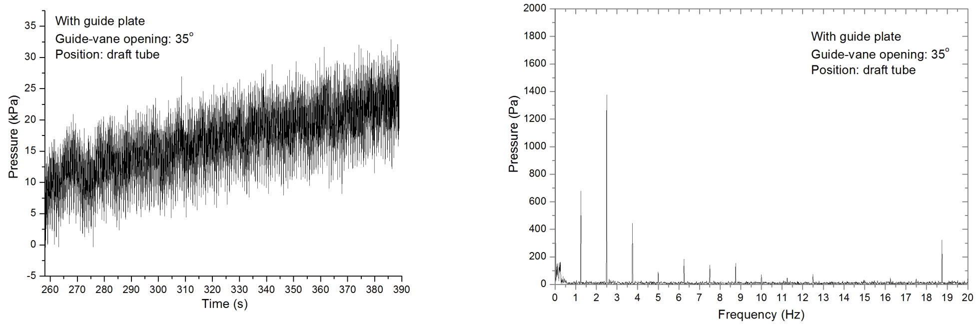

(c) Draft-tube: $P-T$ (d) Draft-tube: FFT

Figure 3.21: $P-T$ result: Pressure fluctuations against time recorded at (a) Runner; (c) Draft-tube; FFT result: Pressure fluctuations against frequency recorded at (b) Runner; (d) Draft-tube; (Time-span: $258s \sim 389s$; Size of time-step: $0.004s$; Guide-vane opening: 35°; Case with the guide-plate;)

components are transmitted throughout the whole passage, owing to its low-rate of dampness. While for the high frequency components, their amplitudes attenuate quickly while being transmitted from runner to draft-tube.

Allowing enough total calculation time is particularly crucial for the case with guide vane opening of 35°. As demonstrated by Figure 3.22 (a) and (c), FFT results for the sampling period of 16 $s \sim 147$ s at the recording point in the draft tube look like white noise, for the recording point in the runner, only the signal of 18.75 Hz shows its peak. While for the sampling period of

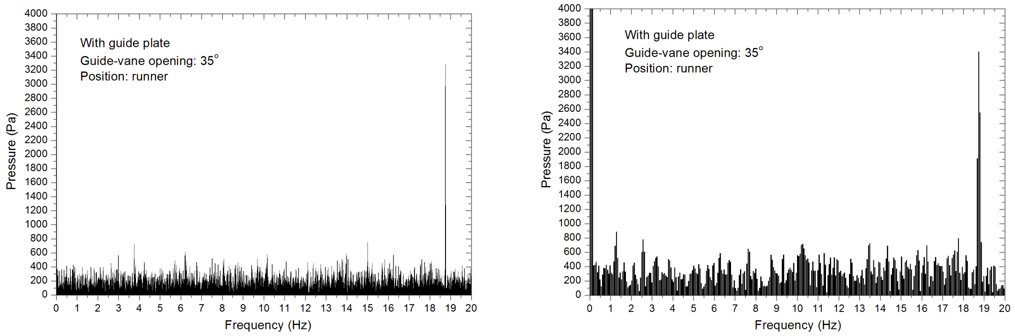

(a) Runner: $16s \sim 147s$

(b) Runner: $147s \sim 163s$

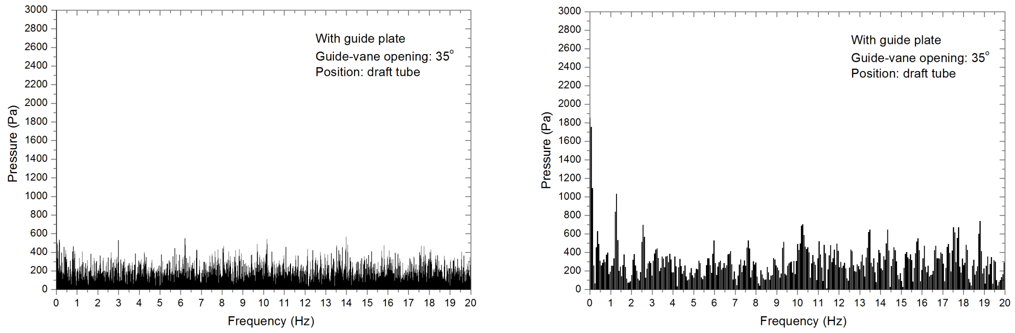

(c) Draft-tube: $16s \sim 147s$

(d) Draft-tube: $147s \sim 163s$

Figure 3.22: Pressure fluctuations against frequency recorded at (a) Runner; (c) Draft-tube with time-span: $16s \sim 147s$; (b) Runner; (d) Draft-tube with time-span: $147s \sim 163s$; (Size of time-step: $0.004s$; Guide-vane opening: 35°; Case with the guide-plate;)

$147\ s \sim 163\ s$, as shown in Figure 3.22 (b) and (d), some peaks (e.g. 1.25 Hz, 2.5 Hz, 18.75 Hz and 10 Hz) start to appear though not distinct enough for proper analysis. This is a phenomenon of numerical simulation particular for large and complex geometry with moving parts like the Francis turbine in this case. It can be explained as below. The numerical calculation noise (virtual signals) needs long time to die out before the real and weak oscillation signals (particular for the case of 35°) can be seen. Otherwise, they are hidden in the virtual noise. It is a similar scenario for the case without guide plate at the opening of 35°.

For the case of 16°, the oscillation signals of flow field are much stronger than the numerical noises, as shown in Figure 3.23, therefore the total calculation time can be shortened for an effective frequency-spectra analysis. The total calculated time of 200 s is more than enough for both cases with and without guide plate at the guide vane opening of 16°.

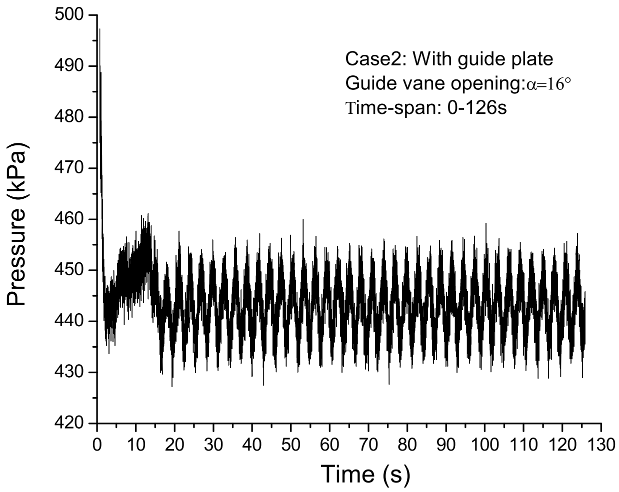

Figure 3.23: Pressure fluctuations against time recorded at guide-vane. Time-span: $0 \sim 126s$; Size of time-step: $0.008s$; Guide-vane opening: 16°; Case with the guide-plate.

3.5 Concluding Remarks

The experimental results obtained from prototype *in situ* show strong unstable phenomena with low-frequency fluctuations under part-load operation condition. However, many physical limitations in the experimental test, e.g., the recording points, positions, accessibilities and etc. have made numerical simulations of the prototype turbine necessary for providing more required information for our investigations.

Geometric turbine model has been built based on the actual parameters of prototype turbine with some necessary simplification. Total grid numbers and its distribution have been discussed. Three mesh models for the case with guide-plate have been compared to elaborate the validation of grid independence. Grid sizes around the guide-plate and the guide vane have been refined according to the requirements of this study (in the RANS sense). The choice of turbulence model and other numerical methods have been examined through theoretical analysis and comparison. RNG $k-\epsilon$ turbulence model and SIMPLEC algorithm have been thus chosen for this study. Although the size of time-step for simulating hydraulic machinery is conventionally available, a validation study comparing three time-step sizes has been done in order to select the most rational one for the objective in this thesis. Finally, it has been demonstrated that the total calculation time is very important. If the selected sampling period is before the oscillation process becoming fully stationary, the FFT results would show false signals. Both the size of time-step and total calculation time have to be chosen according to the specific flow problem.

Chapter 4

Guide-Plate Induced Pressure Fluctuations

The premature damage of the guide-plate accompanying severe pressure-fluctuations and machine-vibration has been paid particular attention during the *in-situ* inspection carried out by Li. As Li clearly stated [1], the guide-plate increased the free-stream turbulence is a primary concern in the sense of receptivity and the transient growth of K-mode instability. This instability may bypass the primary OSE mode and lead to early and random breakdown/turbulent spot although the flow in the first half of guide-vane passage is a highly accelerating flow[1]. In particular the receptivity to the vortical gust fluctuations (i.e. low frequency unsteadiness) is about four times that produced by an acoustic wave (high frequency unsteadiness) [94]. Therefore, these increases of turbulence level at the low-frequency end in the free-stream make the K-mode instability much more prone to grow and breakdown [3].

---

[1] That is, with strong favorable pressure gradient, which would have a prolong laminar boundary-layer until transition if the level of free-stream turbulence was low.

In this chapter, only brief introduction of Li's prediction and the numerical proof has been presented for the sake of conciseness. For details of Li's prediction on the introduction of the low-frequency fluctuation into the free-stream by the guide-plate, see the Appendix B [1]; And, for the evidence of this see Appendix C [10].

4.1 Recording Points for Pressure Prediction

For the purpose of verification, pressure fluctuations have been calculated at the same locations in the draft tube as those on the prototype *in situ* as shown in Figure 4.1 for comparison. This type of location is termed as recording point in this simulation. The recording points used for calculating the free-stream pressure-fluctuations on the guide vane are located within the damage area

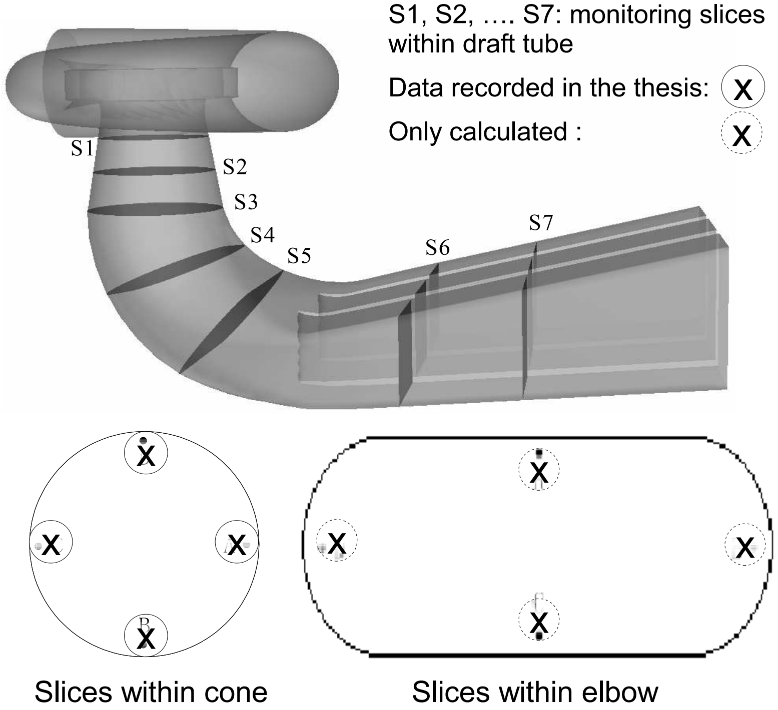

Figure 4.1: Typical monitoring points within draft tube

on its lower surface [2], see Figure 4.2. The pressure fluctuations in the flow passages of other turbine-components have also been calculated for an overall understanding of the flow situation in the turbine. These recording points employed in our simulation are shown in Figure 4.3.

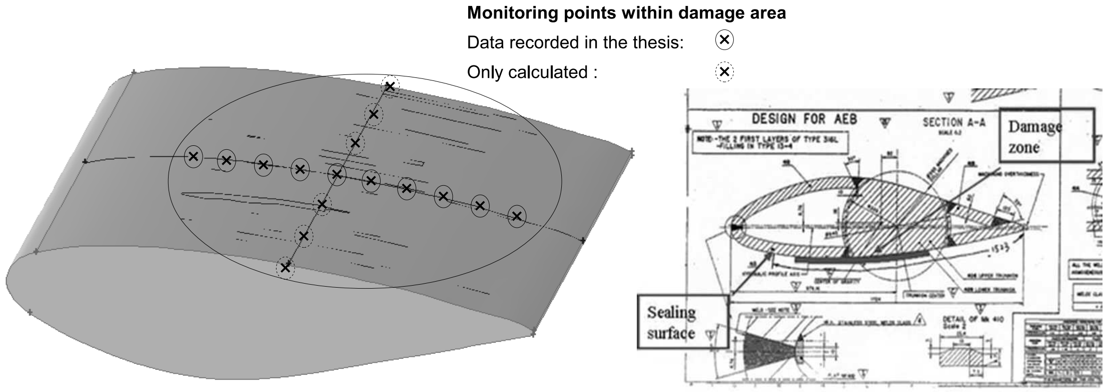

Figure 4.2: Monitoring points within damage area

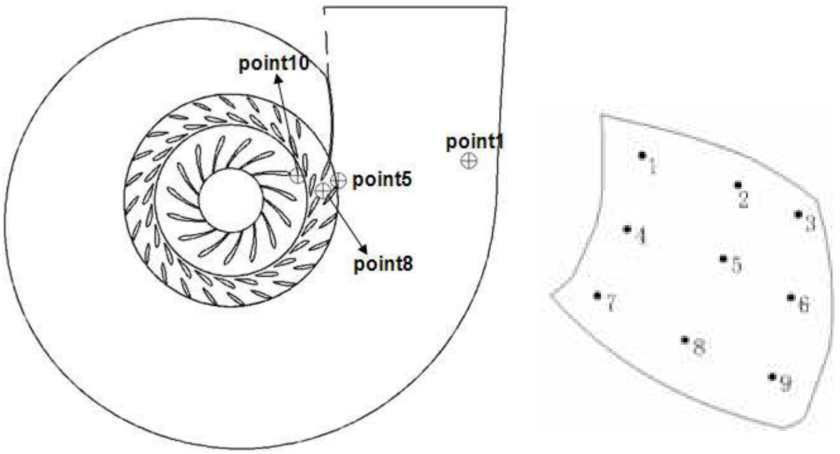

(a) (b)

Figure 4.3: (a) Other monitoring points throughout the flow passage: point1 (in the spiral casing), point5 (before the stay vane) point8 (before the guide vane) and point10 (before the runner); (b) monitoring points on the blade surface of runner

---

[2] To be exactly, in the free-stream just outside the edge of boundary-layer

4.2 Cases Without Guide-Plate

This section presents the results from the simulations of the prototype-turbine model without the guide-plate for the guide-vane opening of 16°, 30° and 35°. Previous numerical studies in the literature (e.g., Three Gorges turbine models) have adopted similar geometric model (i.e., without the guide-plate in the spiral casing) with various simplifications subject to their own needs.

4.2.1 Guide-vane opening: 16°

Spiral casing distributes the flow around the stay vane, water flowing into the stay-ring smoothly. Figure 4.4 shows the static pressure distribution (contour levels) on the radial and axial cross-sections of spiral casing. As shown in Figure 4.4 (b), the stream-straces distribution (solid lines) shows the flow entering into the stay-vane passages smoothly when the spiral casing is designed

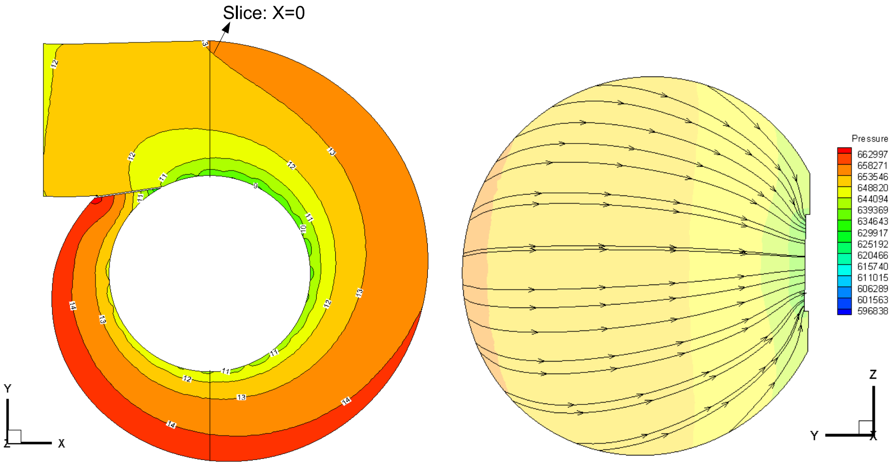

(a) radial section (Slice:Z=0) (b) axial section (Slice:X=0)

Figure 4.4: (a) Pressure distribution (contour levels) on the radial cross-section of spiral casing (Slice:Z=0); (b) Pressure distribution (contour levels) and Stream-traces distribution (solid lines) on the axial cross-section of spiral casing (Slice:X=0) (case without guide-plate, guide-vane opening of 16°)

without the guide-plate.

Operation with the guide-vane opening of 16° (Head=67 m) is within the main unstable zone ($280 \sim 410\ MW$); and among all types of instabilities, the pressure fluctuations caused by vortex rope in the draft tube are prominent. Figure 4.5 (a) presents the pressure distribution at different planes of the draft-tube and Figure 4.5 (b) reveals the instabilities in the draft tube by showing the velocity distribution at the axial cross-section (Y=0). The vortex structures in the draft tube move with time periodically, as a consequence, the precession will be responsible for the unstable operation of turbine, as well as the main

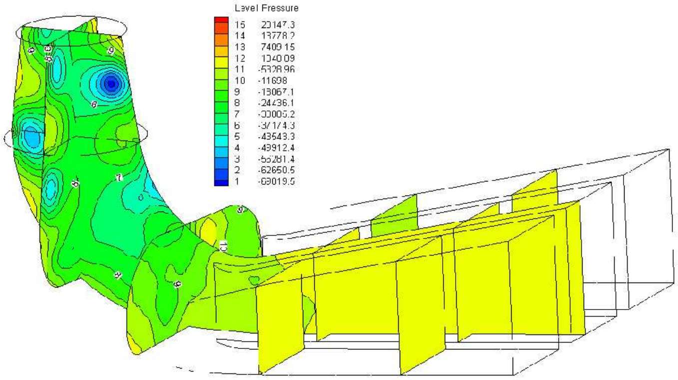

(a) Pressure distribution

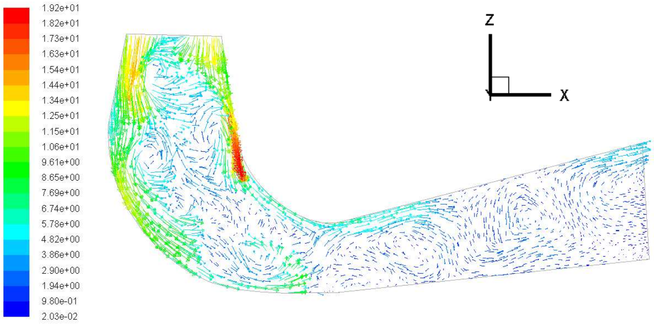

(b) Velocity distribution

Figure 4.5: Flow patterns in draft tube: (a) Pressure distribution at different planes; (b) Velocity distribution at the axial cross-section: Y=0 (case without guide-plate, guide-vane opening of 16°)

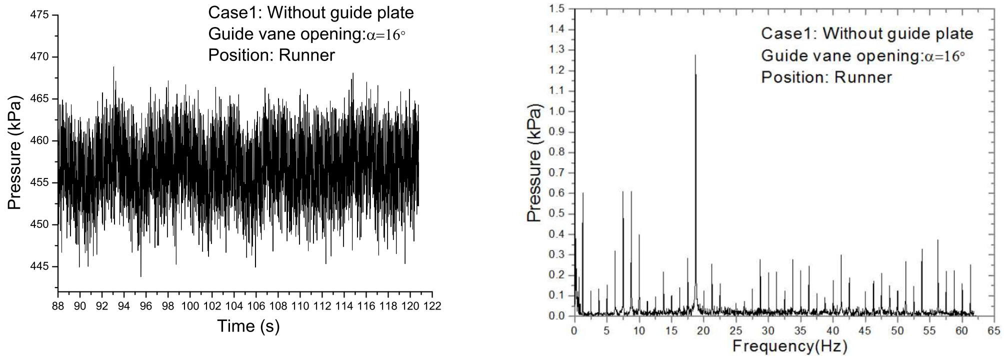

(a) Runner: $P-T$ (b) Runner: FFT

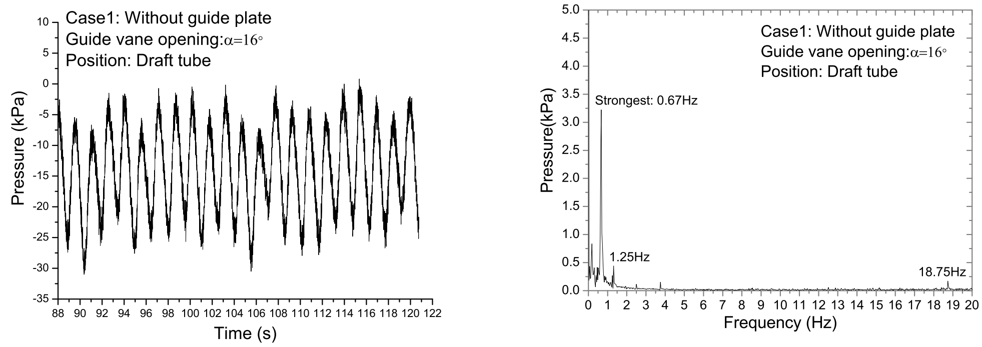

(c) Draft-tube: $P-T$ (d) Draft-tube: FFT

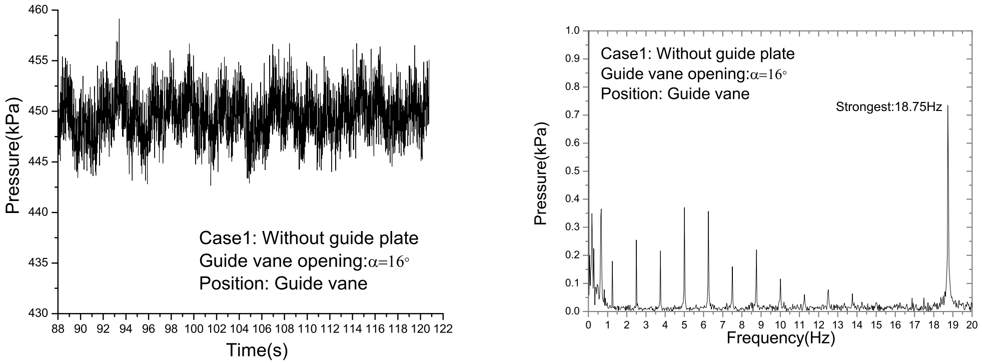

(e) Guide-vane: $P-T$ (f) Guide-vane: FFT

Figure 4.6: $P-T$ result: Pressure fluctuations against time recorded at (a) Runner; (c) Draft-tube; (e) Guide-vane; FFT result: Pressure fluctuations against frequency recorded at (b) Runner; (d) Draft-tube; (f) Guide-vane (Size of time-step: 0.008 s; Guide-vane opening: 16°; Case 1: without guide-plate;)

resource of vibrations.

As discussed in the previous chapter, the oscillation signals of flow field are much stronger than the numerical noises for the case with guide-vane opening of 16°, the effective period for numerical sampling is 88 $s \sim 121$ s (equivalent to 2^{12} calculation steps) has been employed and pressure fluctuations information was recorded at runner, draft-tube and guide-vane respectively. Their P-T and FFT results during this sampling period are showed in Figure 4.6 with clear peaks accordingly. For the recording point in the runner, the frequency component 18.75 Hz as the well-known blade passing frequency is the strongest within the entire frequency spectrum. Other significant components having harmonic frequencies of the rotation frequency (e.g. 7.5 Hz, 8.75 Hz and 1.25 Hz) indicate the rotor-stator interactions are main instabilities in the runner. For the recording point in the draft tube, the strongest frequency component is 0.67 Hz which is the Rheingans [68] pressure oscilla-

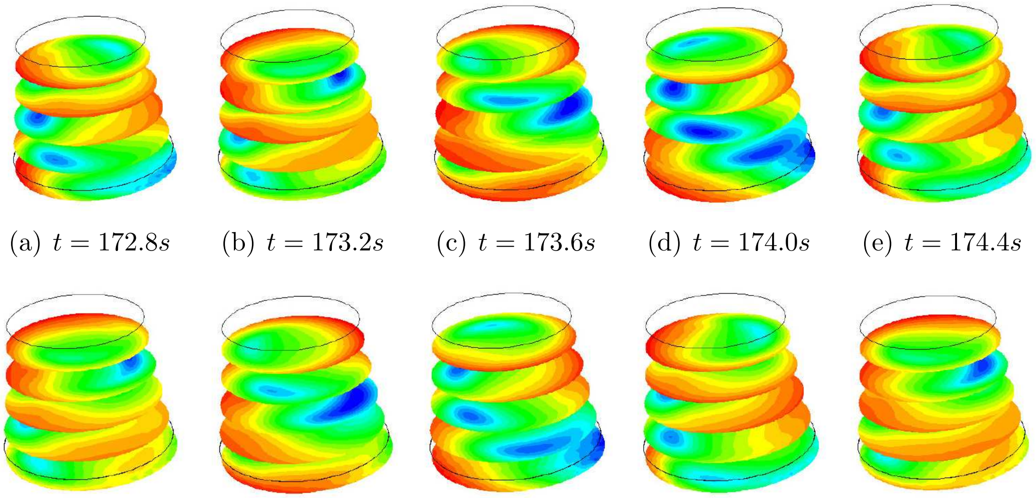

(a) $t = 172.8s$ (b) $t = 173.2s$ (c) $t = 173.6s$ (d) $t = 174.0s$ (e) $t = 174.4s$

(f) $t = 174.8s$ (g) $t = 175.2s$ (h) $t = 175.6s$ (i) $t = 176.0s$ (j) $t = 176.4s$

Figure 4.7: Calculated pressure distribution against time at fixed sections in the draft tube for Case 1 (Guide-vane opening: 16°) [10]

tion caused by the vortex rope in the draft tube during partial-load operations. The second one is 1.25 Hz and the third one is 18.75 which are the rotation frequency and the blade passing frequency respectively. However, the amplitude of peak at 18.75 Hz is much smaller than that appearing in the runner since the signal attenuates when it is transmitting from runner to draft-tube.

The flow variations against time in the draft tube are presented in Figs. 4.7, its period is 1.48 s, corresponding to the paramount frequency component of 0.67 Hz. It agrees well with the FFT results discussed above. As shown in Figure 4.6 (f), the strongest component on the guide-vane surface is 18.75 Hz, other than harmonic frequencies of the rotation frequency, though the component of 0.67 Hz is also appearing but with much less amplitude.

4.2.2 Guide-vane opening: 30°

For operating at 30°, the instabilities in the draft tube is smaller compared with the situation of operation at 16°. With the larger guide-vane opening, adverse flow patterns are also weaker in the runner blade surface. Figure 4.8 presents the velocity distribution at the axial cross-section of draft tube. There are still unstable vortex structures which contribute to the formation of smaller vortex rope with less instabilities.

The employed sampling period is 105 $s \sim 236$ s (2^{14} calculation steps). The corresponding P-T results and FFT results are showed in Figure 4.9. The dominant frequency component is also 18.75 Hz for runner and guide vane. For the draft tube, the strongest frequency component is 0.265 Hz which is a very low frequency signal but with small amplitude[3]. The pressure fluctuations in the draft tube at this operation point shows that the operation with guide-vane

---

[3] Note: different scales are used for Figure 4.6 (d) and Figure 4.9 (d)

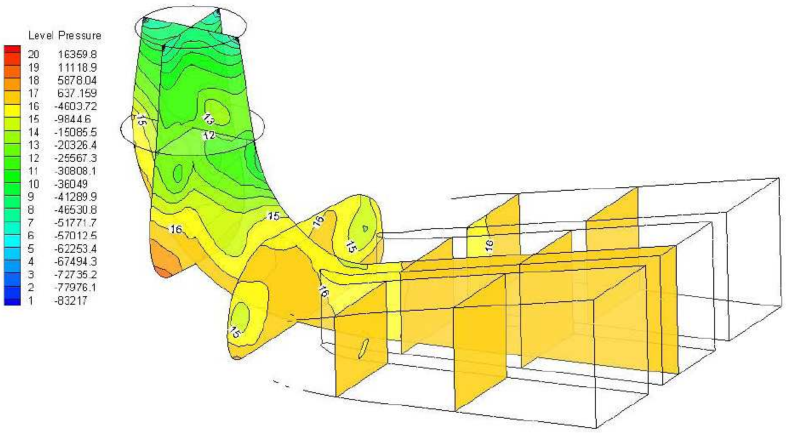

(a) Pressure distribution

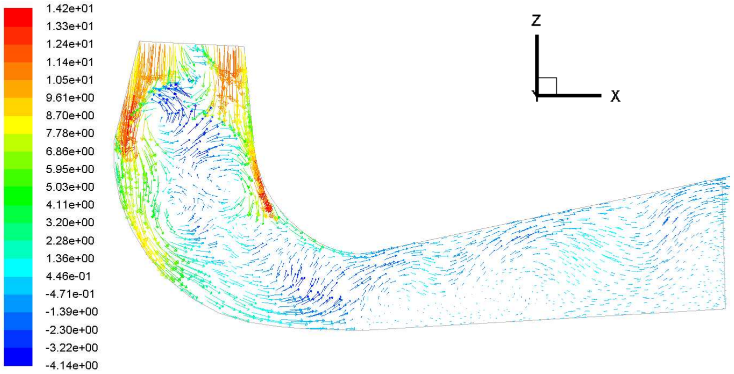

(b) Velocity distribution

Figure 4.8: Flow patterns in draft tube: (a) Pressure distribution at different planes; (b) Velocity distribution at the axial cross-section: Y=0 (case without guide-plate, guide-vane opening of 30°)

opening of 30° is relative stable, having no strong vibrations which would harm the safe operation. This component of 0.265 Hz transmitted hardly upstream to the guide vane surface, where it almost disappears in comparison with the blade passing frequency of 18.75 Hz. Owing to the amplitude of this vortex-rope precession being much smaller than that for the case of a typical part load (e.g., guide-vane opening of 16°), no major concerns have been reported against this frequency of 0.265 Hz yet though a fully and thoroughly investigation is still being conducted.

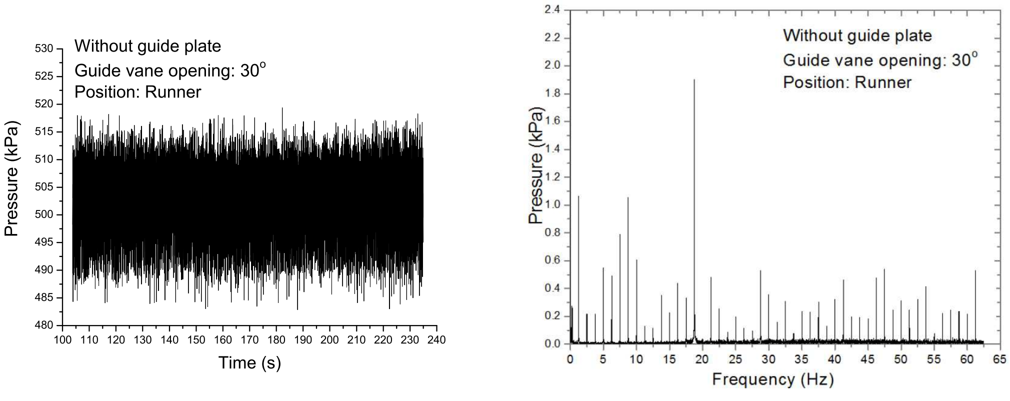

(a) Runner: $P-T$ (b) Runner: FFT

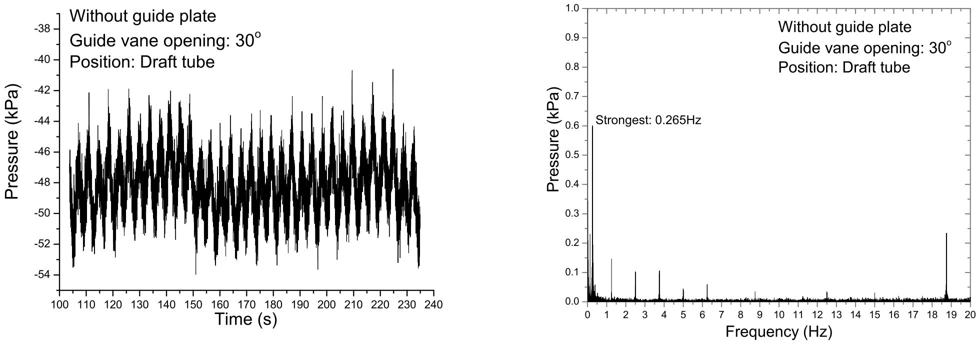

(c) Draft-tube: $P-T$ (d) Draft-tube: FFT

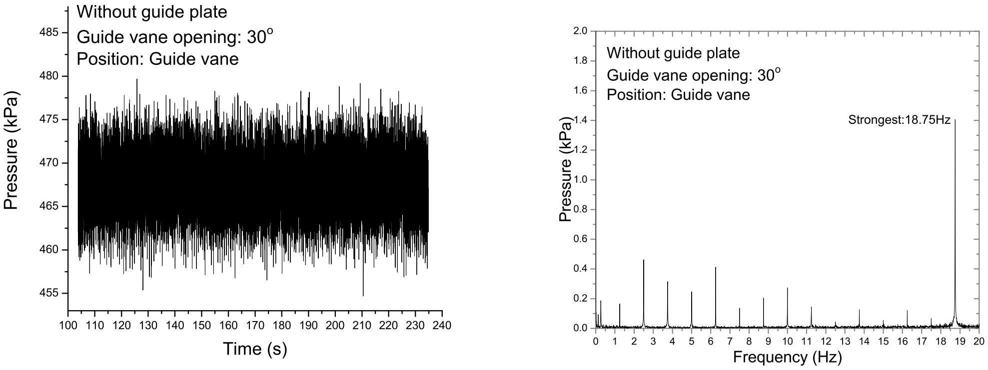

(e) Guide-vane: $P-T$ (f) Guide-vane: FFT

Figure 4.9: $P-T$ result: Pressure fluctuations against time recorded at (a) Runner; (c) Draft-tube; (e) Guide-vane; FFT result: Pressure fluctuations against frequency recorded at (b) Runner; (d) Draft-tube; (f) Guide-vane (Size of time-step: 0.008 s; Guide-vane opening: 30°; Case 1: without guide-plate;)

4.2.3 Guide-vane opening: 35°

For operating at 35° which is close to the optimum condition, the helical vortex rope in the draft tube no longer emerges. As a result any local disturbances will virtually not pollute the upstream flow. Figure 4.10 shows the pressure and velocity distributions at the axial cross-section of draft tube (Y=0). Figures 4.11 and 4.12 present the calculated pressure distribution against time at fixed sections of $S1$ and $S2$. The flow pattern in the cone section is quasi-stable, unsteady swirling vortex-structures obtained in the cases of part load (e.g., the openings of 16° and 30°) do not exist at this load. The 3-D flow pattern shown in Figure 4.13 clearly indicates a central cone flow pattern which is nearly a

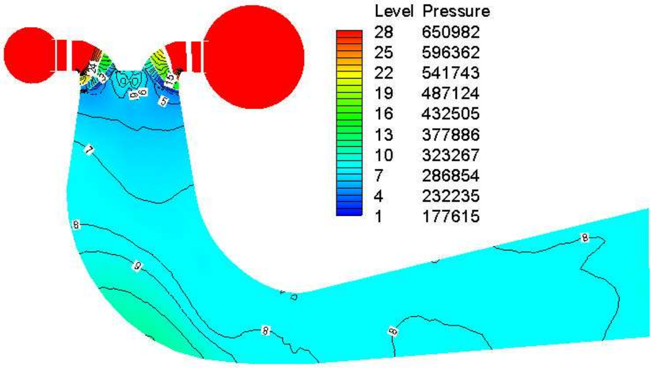

(a) Pressure distribution

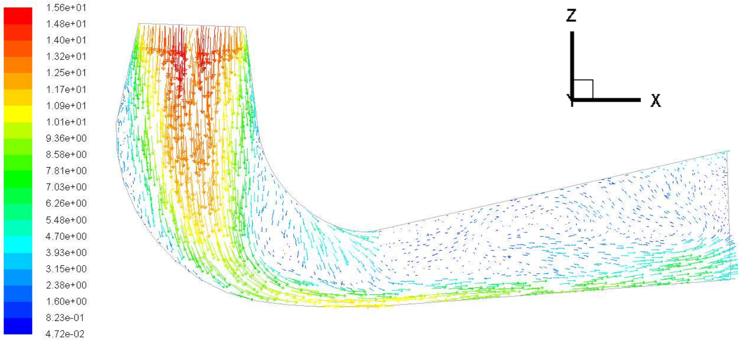

(b) Velocity distribution

Figure 4.10: (a) Pressure distribution; (b) Velocity distribution at the axial cross-section: Y=0 (case without guide-plate, guide-vane opening of 35°)

steady flow in the draft tube.

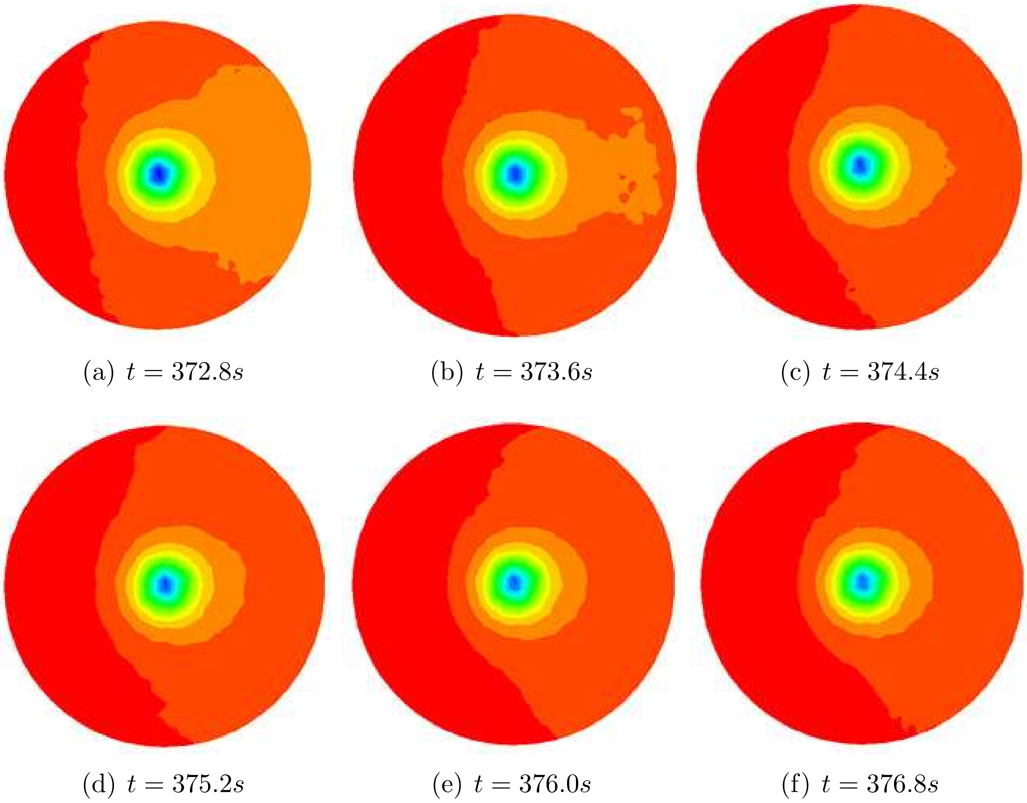
(a) $t = 372.8s$ (b) $t = 373.6s$ (c) $t = 374.4s$

(d) $t = 375.2s$ (e) $t = 376.0s$ (f) $t = 376.8s$

Figure 4.11: Calculated pressure distribution against time at fixed sections (S1) in the draft tube for Case 1 (Guide-vane opening: 35°)

The sampling period is 234 s ∼ 496 s (equivalent to 2^{16} calculation steps, the size of time-step is 0.004 s) was selected and the corresponding P-T results and FFT results at the recording points in the runner and draft-tube are presented in Figure 4.14. The pressure fluctuations in the runner are still having all the modes of the rotation frequency (the strongest component is 18.75 Hz). While for the recording point in the draft tube, the amplitude of all the frequency components are small which again indicates a stable flow pattern in the draft tube.

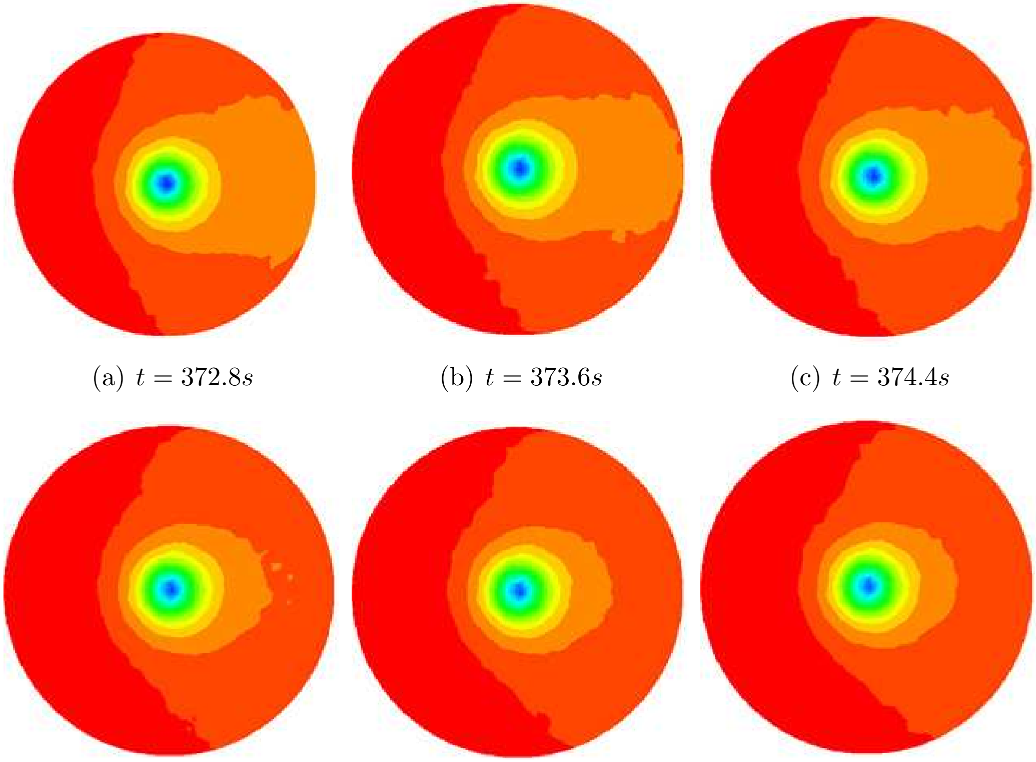

(a) $t = 372.8s$ (b) $t = 373.6s$ (c) $t = 374.4s$

(d) $t = 375.2s$ (e) $t = 376.0s$ (f) $t = 376.8s$

Figure 4.12: Calculated pressure distribution against time at fixed sections (S2) in the draft tube for Case 1 (Guide-vane opening: 35°)

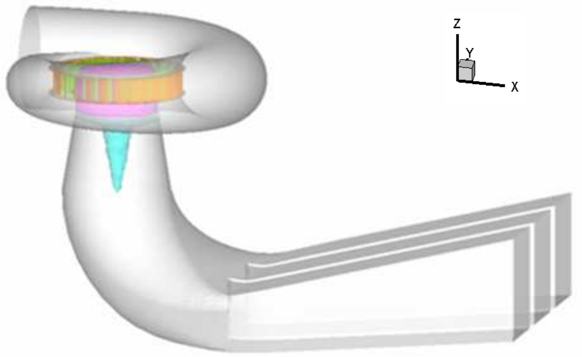

Figure 4.13: Vortex pattern in the draft tube with the guide-vane opening of 35° (case without guide-plate)

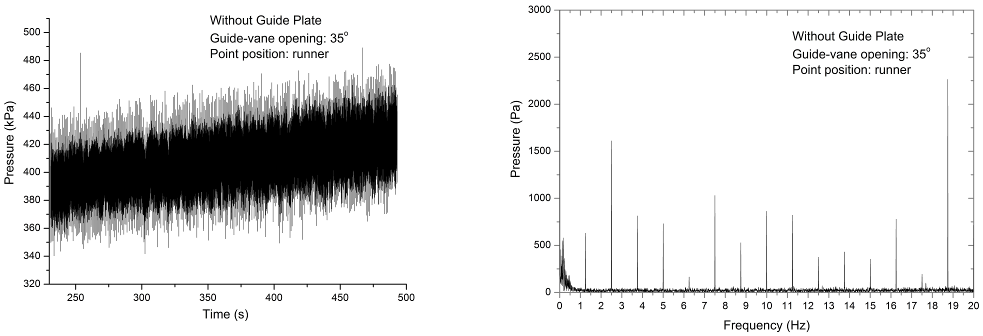

(a) Runner: $P-T$

(b) Runner: FFT

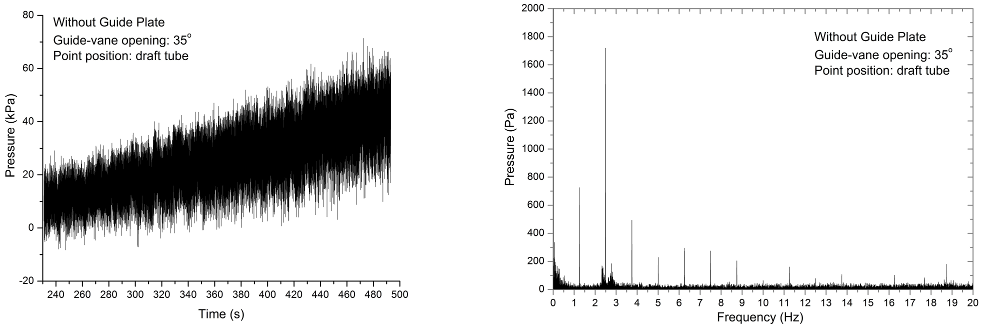

(c) Draft-tube: $P-T$

(d) Draft-tube: FFT

Figure 4.14: $P-T$ result: Pressure fluctuations against time recorded at (a) Runner; (c) Draft-tube; FFT result: Pressure fluctuations against frequency recorded at (b) Runner; (d) Draft-tube; (Time-span: 230 $s \sim 493$ s; Size of time-step: $0.004s$; Guide-vane opening: 35°; Case 1: without guide-plate;)

4.2.4 Dominant pressure fluctuation signals on other recording points

As introduced in the previous chapter, the pressure fluctuations information has been specially recorded on the guide-vane surface and in the draft-tube. Besides, the pressure fluctuations in the flow passages of other turbine-components have also been calculated for an overall understanding of the flow situation in the turbine. These recording points employed in our simulation are

Table 4.1: Dominant pressure-fluctuation frequency-components on other recording points for case without the guide-plate

recording points	16°	30°	35°
point1	0.67 Hz (30 Hz)	1.25 Hz (30 Hz)	18.75 Hz (10 Hz)
point5	0.67 Hz (30 Hz)	1.25 Hz (0.265 Hz)	18.75 Hz (10 Hz)
point8	18.75 Hz (0.67 Hz)	18.75 Hz (2.5 Hz)	18.75 Hz (30 Hz)
point10	18.75 Hz (1.25 Hz)	18.75 Hz (1.25 Hz)	18.75 Hz (2.5 Hz)

shown in Figure 4.3. Table 4.1 shows the first and second[4] strongest pressure-fluctuation frequency-components on other recording points for case without the guide-plate.

4.3 Comparative Analysis for Guide-Vane Opening of 16°

By comparing the pressure-fluctuation characteristics of two corresponding cases (i.e. with and without guide-plate) for the same operation condition (i.e. guide vane opening of 16°), the guide-plate effects on the generation of extremely low frequency fluctuation will be revealed clearly.

4.3.1 Basic description

Figure 4.15 shows the static pressure distribution (contour levels) and the stream-straces distribution (solid lines) on the axial cross-sections of spiral casing. It can be seen that the addition of guide-plate is not guiding the flow into the turbine runner smoothly by thus inducing reversed flow and vortex

---

[4] Values in bracket () is the second strongest frequency

instabilities around.

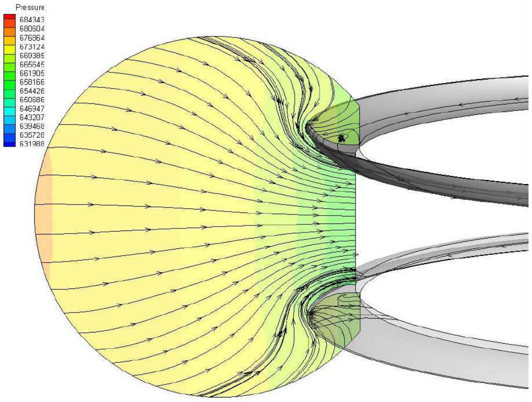

Figure 4.15: Pressure distribution (contour levels) and stream-traces distribution (solid lines) on the axial cross-section of spiral casing (Slice:X=0) (case with guide-plate, guide-vane opening of 16°)

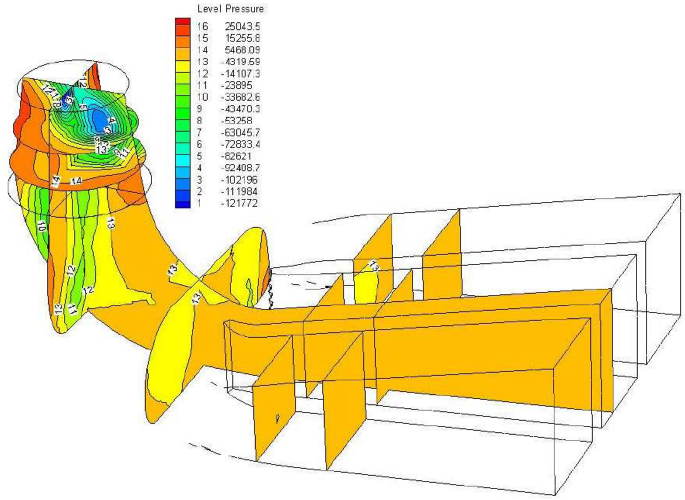

Figure 4.16: Pressure distribution at different planes (case with guide-plate, guide-vane opening of 16°)

4.3.2 Pressure Fluctuation in the draft tube

The comparison for the draft tube under the partial-load operation (i.e. 16°), referring to Figures 4.5(a) and 4.16. The FFT results presented in Figure 4.17

shows an extremely low frequency (0.336 Hz) with the strongest amplitude

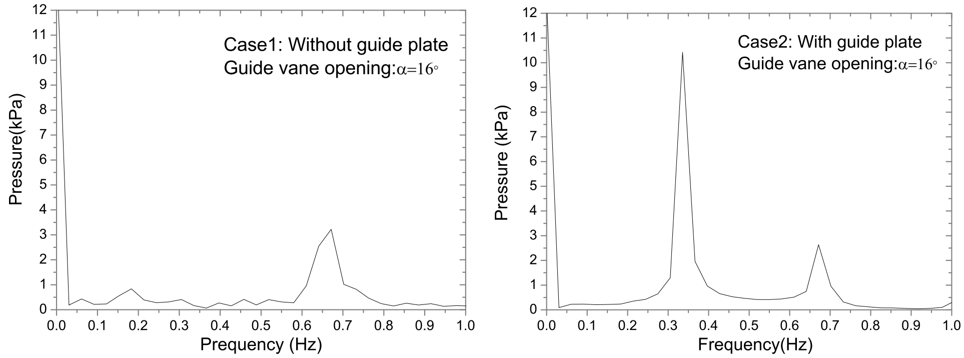

(a) Without guide-plate (b) With guide-plate

Figure 4.17: FFT results in the draft tube with the opening of 16°: (a) case 1 ; (b) case 2 [10]

distinguishingly appearing for the case with guide-plate. From numerical simulations, this component is also found being transmitted throughout the whole passage with little attenuation, owing to its low-rate of dampness.

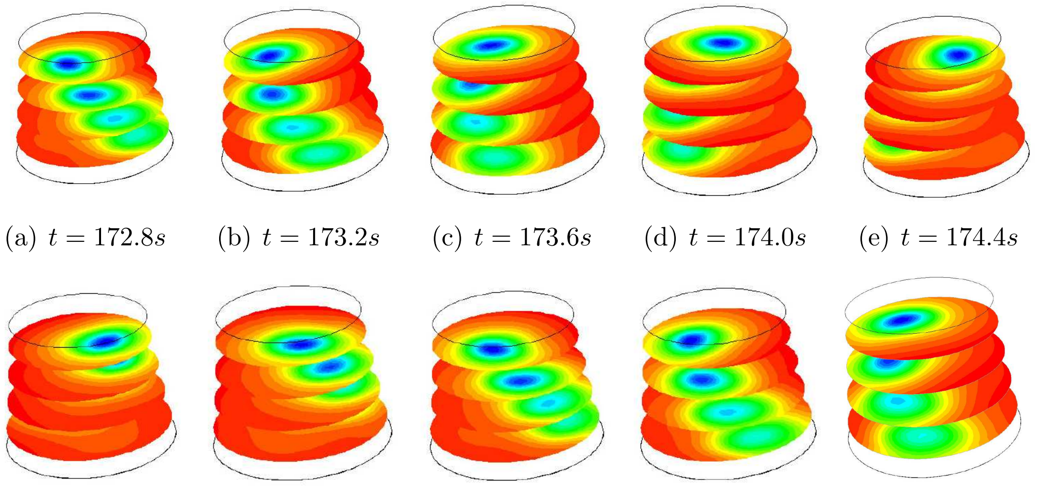

(a) $t = 172.8s$ (b) $t = 173.2s$ (c) $t = 173.6s$ (d) $t = 174.0s$ (e) $t = 174.4s$

(f) $t = 174.8s$ (g) $t = 175.2s$ (h) $t = 175.6s$ (i) $t = 176.0s$ (j) $t = 176.4s$

Figure 4.18: Calculated pressure distribution against time at fixed sections in the draft tube for Case 2 [10]

The flow variations against time in the draft tube are presented in Figure 4.18, showing an organized rotating vortex rope. The period is around

Table 4.2: Comparison of frequencies of pressure fluctuations on the guide vane for the opening of 16°

	Case 1	Case 2
Static Pressure	449757 Pa	443283 Pa
f1	18.75 Hz	**0.336** Hz
f2	5 Hz	18.75 Hz
f3	0.67 Hz	7.5 Hz
f4	6.25 Hz	5 Hz
f5	0.183 Hz	8.75 Hz
f6	2.5 Hz	3.75 Hz
f7	8.75 Hz	10 Hz

3 s, corresponding to the frequency of 0.336 Hz for case 2. It agrees well with the FFT results, as shown in Figure 4.19.

As presented in the last section, the pressure-fluctuation frequency component of 0.67 Hz has the largest amplitude in the draft tube for the case 1 (i.e. without the guide-plate). While for case 2 (i.e. with guide-plate), the component of 0.67 Hz also presents but with much smaller amplitude than that of 0.336 Hz. These two geometric models are all identical except for the structure of guide-plate in the spiral casing. The emergence of this component of 0.336 Hz is thus undoubtedly attributed to the addition of guide-plate in the spiral casing[5]. This dominant low-frequency component from our calculation agrees well with the measured one on the prototype *in situ* (0.31 Hz) which has been analyzed in Subsection 3.1.2.

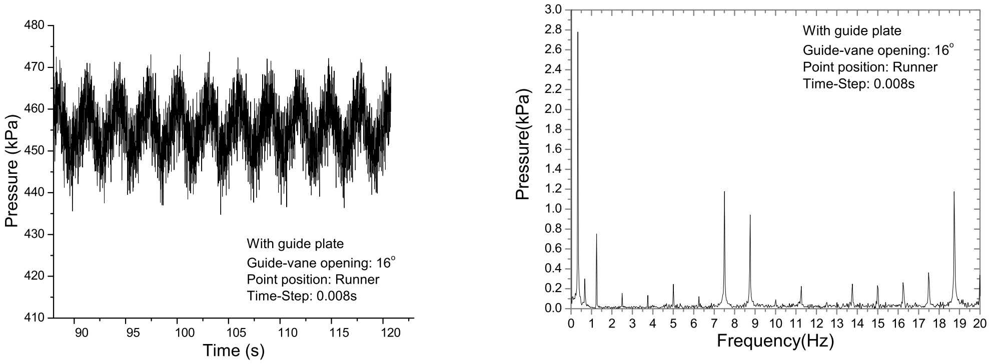

(a) Runner: $P-T$

(b) Runner: FFT

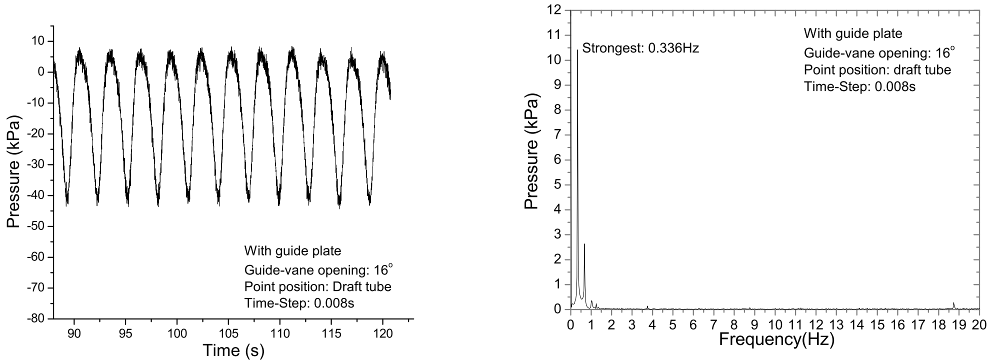

(c) Draft-tube: $P-T$

(d) Draft-tube: FFT

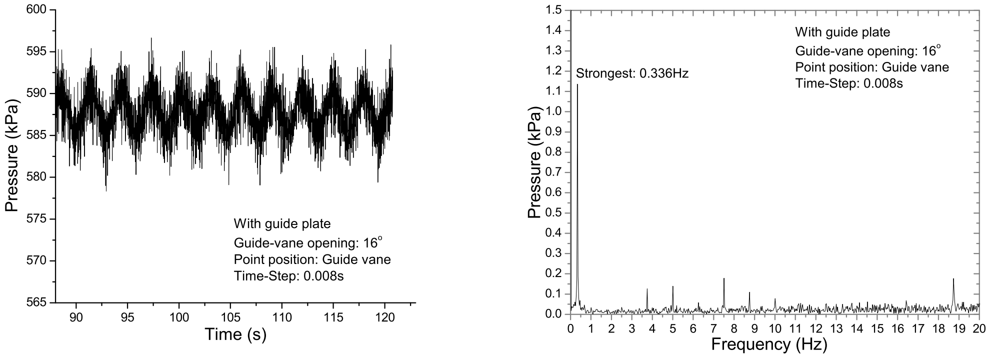

(e) Guide-vane: $P-T$

(f) Guide-vane: FFT

Figure 4.19: $P-T$ result: Pressure fluctuations against time recorded at (a) Runner; (c) Draft-tube; (e) Guide-vane; FFT result: Pressure fluctuations against frequency recorded at (b) Runner; (d) Draft-tube; (f) Guide-vane (Size of time-step: 0.008 s; Guide-vane opening: 16°; Case with the guide-plate;)

4.3.3 Pressure Fluctuation on the Guide Vane

Our FFT results show that the guide-plate significantly increases the turbulence level in the free stream over the entire spectrum in particular at the low-frequency end and also lowers the average static pressure on the lower surface of the guide vanes as shown in Table 4.2. Both effects have favorable contribution to the promotion of cavitation inception within boundary layer though the local average pressure in the main flow is not below the vapor pressure. Among those increased fluctuation components the extremely low-frequency (0.336 Hz) component is the strongest for cases 2, but disappears for case 1. This numerical result explains well Li's concern that the guide-plate introduces low-frequency fluctuations in the incoming free-stream that may promote the K-mode instability and its transition through the boundary-layer's receptivity mechanism.

4.3.4 Instabilities caused by the guide-plate

In order to further verify the origin of this low-frequency component (0.336 Hz) in the case 2, the flow field in the spiral case has to be carefully examined in the first place. Figure 4.20 shows the helicity distribution around the guide-plate on the axial cross-section of spiral casing (X=0) with the opening of 16°. Vortex structures around the guide-plate is clearly presented, which has not been found in the case 1. These instabilities are thus triggered by this extra guide-plate in the spiral casing that will inevitably affect the downstream flow.

Figure 4.21 showing the turbulent kinetic energy distribution at four perpendicular slices along the circumferential direction of the spiral case, in-

---

[5] This will be further verified by analyzing the flow pattern around the guide-plate in the later part of the thesis.

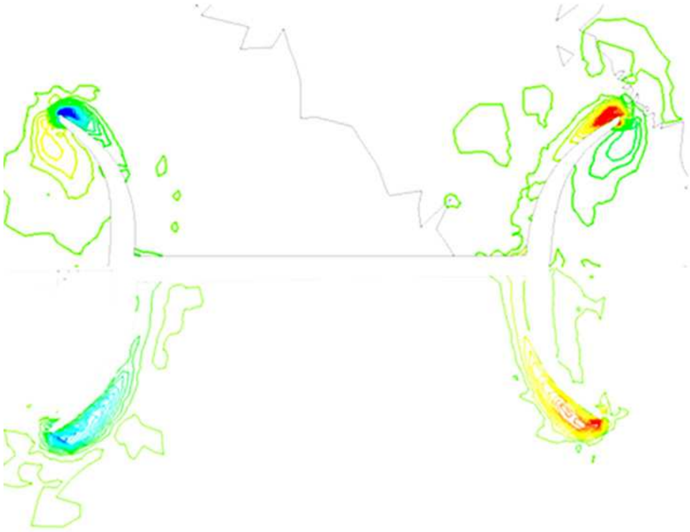

Figure 4.20: Helicity distribution around the guide-plate in spiral casing with the opening of 16° (spiral casing: x=0)

dicates that the highest turbulent kinetic energy exists near the guide-plate. That means the induced unsteadiness by the addition of guide-plate device also causing unnecessary energy loss in the spiral case.

This again proves the prediction that the addition of guide-plate induces high instabilities in the free-stream. The space distribution of these vortices changes along the circumferential direction of the spiral casing, which is further clearly demonstrated in Figure 4.22 and Figure 4.23, by visualizing the stream-traces distribution and the velocity distribution in the different slices of the spiral casing. The circumferentially uneven distribution in space of the vortex around the guide-plate indicates the possible vortex precession in the circumferential direction.

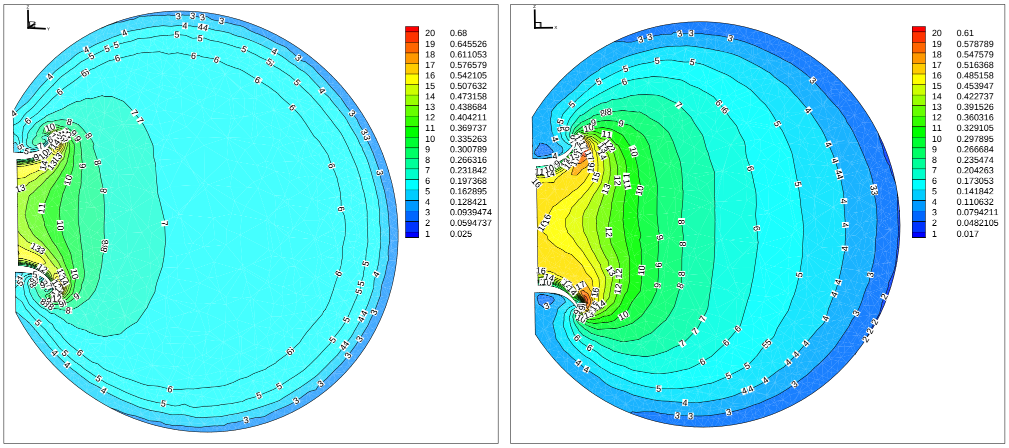

(a) *Slice_0* (b) *Slice_90*

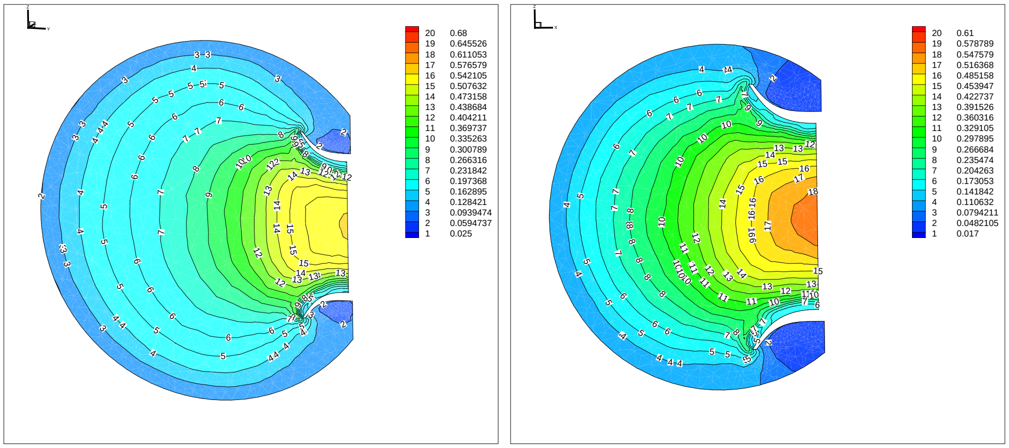

(c) *Slice_180* (d) *Slice_270*

Figure 4.21: Visualization of Vortex instabilities around the guide-plate: turbulent kinetic energy distribution at different slices of the spiral casing

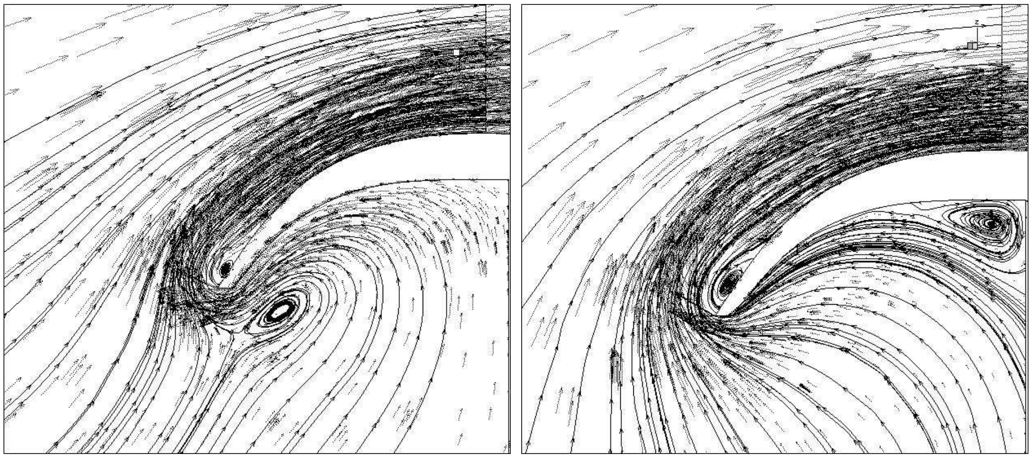

(a) $Slice\_0$ (b) $Slice\_45$

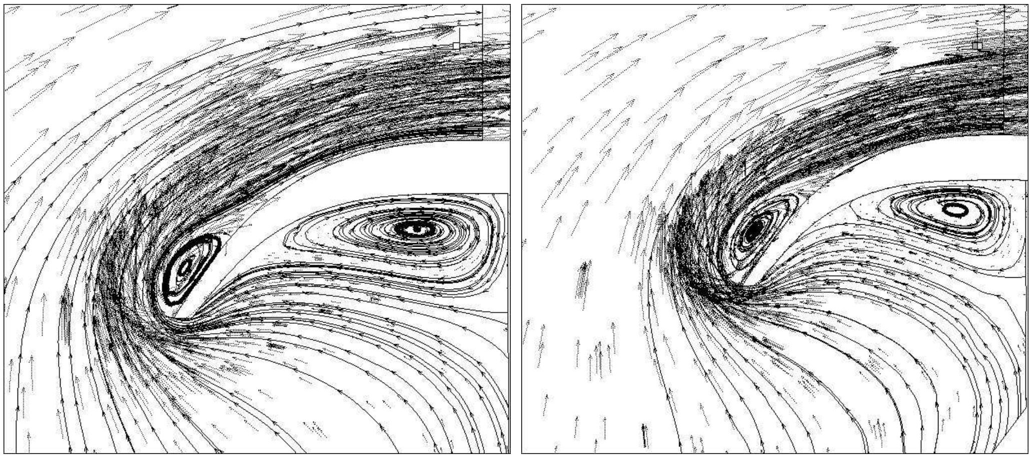

(c) $Slice\_90$ (d) $Slice\_135$

Figure 4.22: Visualization of Vortex formation around the guide-plate: streamtraces distribution(solid lines) and velocity distribution (dotted lines) at different slices of the spiral casing

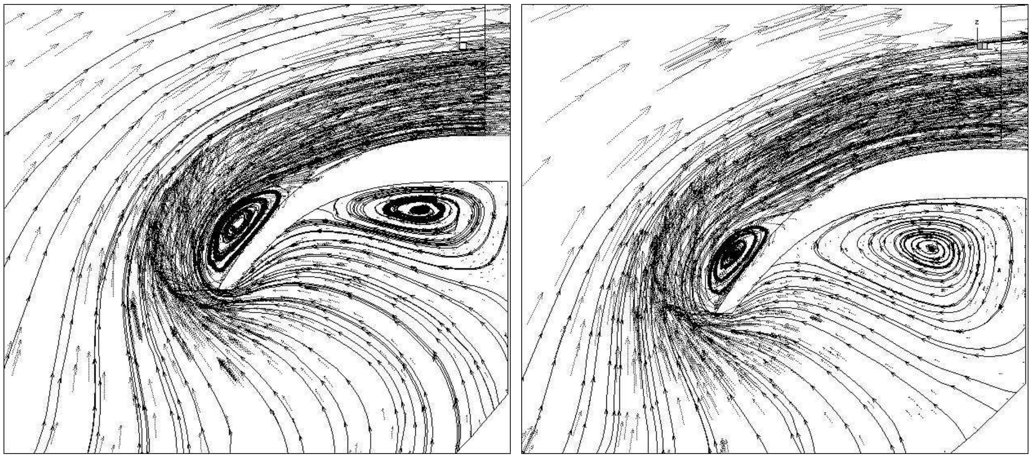

(a) *Slice*_180 (b) *Slice*_225

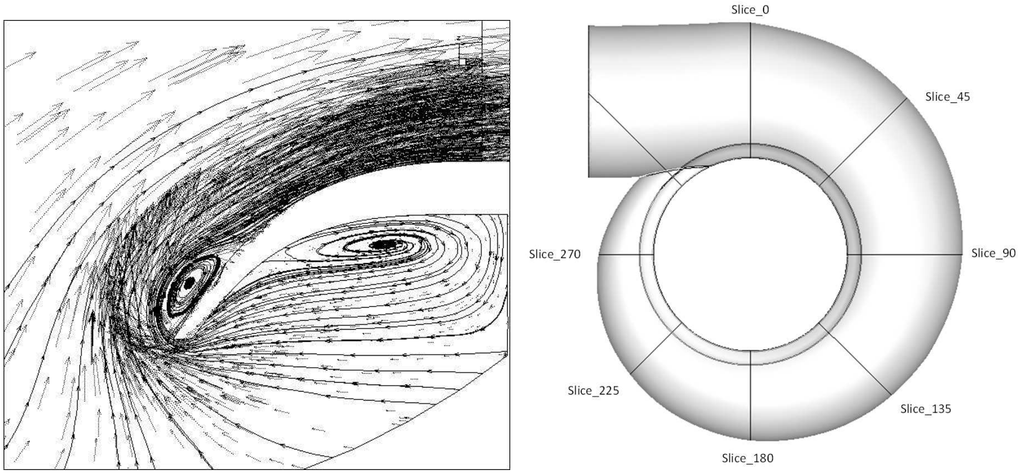

(c) *Slice*_270 (d) Distribution of slices in the spiral casing

Figure 4.23: (Continued) Visualization of Vortex instabilities around the guide-plate: stream-traces distribution (solid lines) and velocity distribution (dotted lines) at different slices of the spiral casing

4.4 Comparative Analysis for Guide-Vane Openings of 30° and 35°

As discussed in the Section 4.2, pressure fluctuations in the draft tube is relatively less unstable for the guide-vane opening of 30° and 35°. The extremely unstable helical vortex-rope does not emerge in these two operation conditions for either case 1 and case 2, despite that for the opening of 30°, in case 1 (i.e. without guide-plate) there is a very weak vortex-rope precession in the draft tube inducing a negligible pressure-fluctuation component of 0.265 Hz. Figure 4.24 shows the P-T results and FFT results for the opening of 30°. Though the strongest component in the draft tube for case 2 (i.e. with guide-plate) has an even lower frequency of 0.15 Hz, but with a negligible amplitude. For the opening of 35°, similar results obtained for case 2 as those shown in case 1[6]. There are no strong pressure-fluctuations with the frequencies lower than 1.25 Hz being detected.

The strongest peak at 5.7 Hz measured from the prototype tests *in situ* at load 540 $MW - 542$ MW is referred by all investigators as a special frequency[7] because it has never been matched from their numerical studies [11, 79–82] as well as from this PhD study. This is very common situation for FFT analysis of the pressure fluctuations on such a complex and large flow system that any geometrical or operational condition discrepancies between the simulation and the physical models will lead to one or two spikes not matching among those many spikes of harmonics and super- and sub-harmonics. For our

---

[6] These results have already presented in Chapter 2, are not included here for the conciseness.

[7] According to the experimental investigation, this special frequency only exists at the head of 68.3 m; when the head exceeds 68.3 m, it disappears.

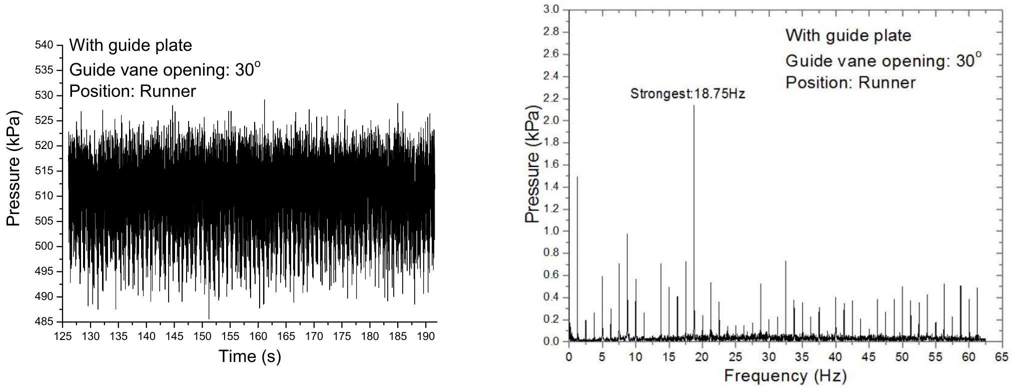

(a) Runner: $P-T$ (b) Runner: FFT

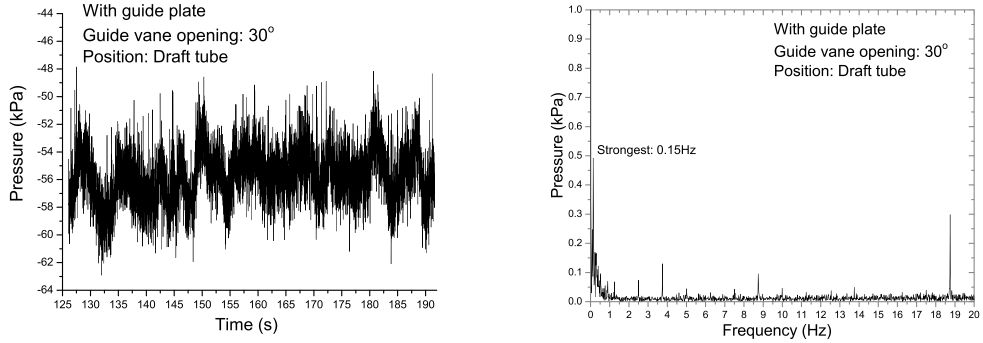

(c) Draft-tube: $P-T$ (d) Draft-tube: FFT

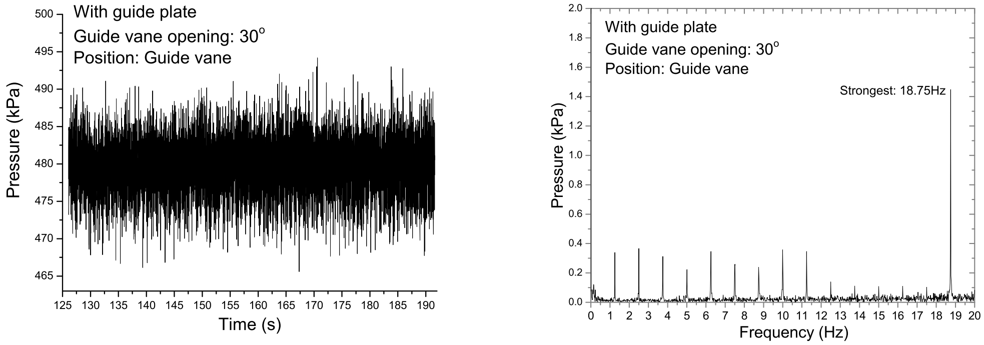

(e) Guide-vane: $P-T$ (f) Guide-vane: FFT

Figure 4.24: $P-T$ result: Pressure fluctuations against time recorded at (a) Runner; (c) Draft-tube; (e) Guide-vane; FFT result: Pressure fluctuations against frequency recorded at (b) Runner; (d) Draft-tube; (f) Guide-vane (Size of time-step: 0.008 s; Guide-vane opening: 30°; Case 2: with guide-plate;)

case, this frequency is far above the targeted extremely low frequencies such as 0.15 Hz, 0.26 Hz and 0.3 Hz etc. Therefore, it is a negligible discrepancy for this study and is therefore ignored for this study. Of course the physical mechanism behind this discrepancy needs to be further investigated in the future studies[8].

4.5 Concluding Remarks

The guide-plate causes an extremely low frequency component with high intensity in the free stream identified from our numerical studies was not predicted by the manufactures though it has been detected from the *in situ* measurements. This 0.336 Hz component plays a significant role in promoting the growth of K-mode instability and its early breakdown. This is exactly the reason for examining the pressure variations particularly the low-frequency spectrum in the free stream.

Li [1] firstly pointed out that the increased free-stream turbulence introduced by the guide-plate structure should be a primary concern. The studies have numerically verified:

(1) The addition of the guide-plate increases the free-stream turbulence and particularly introduces a component of extremely low-frequency pressure-fluctuation. This particular component is highly likely the one of the sources entering the boundary-layer and promoting the growth of Klabenoff-streaks and their transition, which in turn triggers the cavitation inception in the boundary-layer of the guide vane;

(2) The guide-plate also significantly lowers the average static pressure

---

[8] It might be simply attributed to a particularly geometry discrepancy of the prototype that has been tested in *in situ*

in the free-stream near the lower surface of the guide vanes, contributing to the promotion of the cavitation inception as well;

(3) The guide-plate is not guiding the flow into the turbine runner smoothly but adding extremely low frequency fluctuations and preventing the flow from entering the turbine smoothly.

Chapter 5

New Vortex Structure Identified

In the previous chapter we have simulated the whole flow field in the prototype turbine, verifying that the device of guide-plate is mainly responsible for a component of extremely low-frequency pressure-fluctuation of 0.336 Hz and increases significantly the free-stream turbulence under partial-load operation conditions. However, the information of the spectra about pressure fluctuations only is not enough for a satisfactory understanding of the nature of this component. Therefore, in order to find out the root of this problem, we have investigated the details of the flow around the guide-plate and how it influences the whole-flow-field of the prototype turbine. Some interesting findings will be presented here.

5.1 Preliminary knowledge

Some numerical techniques used for detecting and identifying the vortex structure induced by the addition of the guide-plate are briefly introduced in this section.

5.1.1 Vortex Detection Method

Modeling the swirling feature in flow field, commonly referred to as a vortex, needs a generally acceptable definition of a vortex though precise definition does not exist. Most of definitions are consistent with visual observations, depicting a vortex in terms of closed or spiraling streamlines or path-lines, local pressure minima, and iso-vorticity contours and surfaces. However, the shortcoming is that spiraling streamlines or path-lines are obtained just for an observer moving with the vortex to be identified (self-referential); And the existence of a local pressure minimum is neither sufficient nor necessary condition for guarantee the existence of a vortex, owing to unsteady irrotational straining, which can create a pressure minimum in the absence of a vortex, and viscous effects, which can eliminate the pressure minimum within a vortex.

Jiang et al. [95] presented an overview of nine existing detection methods covering a widely range of relevant issues. The detection algorithm can be classified based on how it defines a vortex, whether it is Galilean invariant, and the local or global nature of its identification process. Vorticity tensor, as a Galilean invariant quantity[1] expressing an average angular velocity of fluid elements, is one of the most natural choices for a vortex identification criteria. Here we just briefly introduce λ_2 method proposed by Jeong & Hussain (1995) [96] which has been adopted for visualizing vortices in our research. This method is based on the premise that a pressure minimum is not sufficient as a detection criterion. To remove the interfering effects such as straining and viscous effects, the velocity gradient tensor J is decomposed into its symmetric part, the rate of deformation or strain-rate tensor S, and antisymmetric part,

---

[1] i.e. independent of the translational velocity of an observer

the spin tensor Ω, and consider only the contribution from $S^2 + \Omega^2$,

$$S = \frac{J + J^T}{2} \quad \Omega = \frac{J - J^T}{2}\,. \tag{5.1}$$

They define a vortex as a connected region where $S^2 + \Omega^2$ has two negative eigenvalues. Because $S^2+\Omega^2$ is real and symmetric, it has only real eigenvalues. Let λ_1, λ_2 and λ_3 be the eigenvalues such that $\lambda_1 \geq \lambda_2 \geq \lambda_3$. The λ_2 criterion is: if

$$\lambda_2 < 0, \tag{5.2}$$

i.e., λ_2 is negative at a point, then that point belongs to a vortex core. Compared to other vortex detection methods [95], the effectiveness of the λ_2 criterion is distinct. However, under conditions when several vortices exist, it can be difficult for this method to distinguish individual vortices apart.

5.1.2 Visualization of Vortices

Methods used for visualizing vortices are closely related to the way in which the vortices are identified. Generally, results produced by line-based algorithms would be better visualized as line segments. While for those generated by region-type algorithms, visualization methods such as color-maps or iso-surfaces are preferred. There are many techniques (manually or automatically) used for verifying the accuracy of detected results. For example, one popular technique is by seeding streamlines into the flow-field, the swirling patterns of these streamlines that are generally associated with vortices can be visualized directly. Another broadly used technique is by adopting the cutting plane. The dataset is demonstrated on a sample slice by cutting plane along the commanded path, and the visualization method can be iso-contours of a scalar quantity or line-integral convolution (LIC) of velocity vectors [97].

In our case, for visualizing vortices in 3-D flow, we adopt vortex-core extraction technique in the post-processing applied by the software Tecplot 360 [98]. The default vortex-core extraction method is based on λ_2 method, extracting vortex cores which are depicted as lines. This algorithm then finds lines that run through the center of the region of negative λ_2. However, only the extracted vortex cores cannot provide us enough information about vortex size and thus pose difficulty in high-quality visualization. To solve these problems we can look at iso-surfaces[2] of λ_2 instead. It can be done in the software by using specific equations to compute the symmetric and antisymmetric parts of the velocity gradient tensor and the inclusion of an add-on to compute the eigenvalues of a tensor [98]. The computation mainly involves the following steps, that is:

(i) Compute the velocity gradient tensor J;

(ii) Compute $S^2 + \Omega^2$ from the velocity gradient tensor;

(iii) Compute the eigenvalues of the new tensor of $S^2 + \Omega^2$;

(iv) Compute the trace of $S^2 + \Omega^2$ by summing three eigenvalues;

(v) Turn on iso-surfaces, using EgnVal 2 as the iso-surface variable.

5.1.3 Characteristics of the Draft-Tube Flow in Part-Load Francis Turbine

The geometrical complexities of Francis turbine together with the rotation of the turbine runner provide an extremely complicated flow environment charac-

---

[2] In 3-D volume data, an iso-surface is the surface that has the same value of a variable (the iso-surface variable).

terized by various unsteadiness, large-scale vortices, intense turbulence breakdown, pockets of highly shear/reversal flow, collapsing cavitation bubbles, etc. Even under optimum design condition, organized unsteadiness is still prevailing throughout the whole flow field, as discussed in the former chapter, the situation becomes especially pronounced in off-design operation.

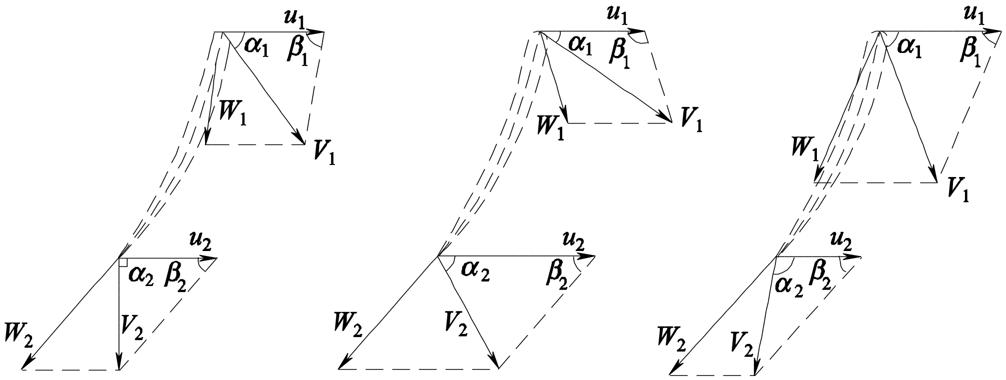

Figure 5.1: Runner blade inlet, outlet flow velocity triangles: (a) optimum condition (b) small guide vane angle (c) big guide vane angle [11]

Under certain off-design conditions, strongly unstable vortices may occur in the draft tube. Figure 5.1 schematically shows velocity triangles at both the inlet and the outlet of runner for different opening angles. In part load cases with the velocity triangles as shown in Figure 5.1 (b), there is an attack angle[3] $\Delta\beta_1 = \beta_1 - \beta_{1a} > 0$, here β_{1a} is the angle of blade leading edge. At the runner exit, the absolute velocity V_2 has a positive circumferential component $V_2 \cos\alpha_2$ caused by a flow with a positive attack angle passing through the blade-blade channel to the exit. That means V_{u_2} $(= V_2 \cos\alpha_2)$ is in the same direction as u_2 (the runner rotation direction). This positive V_{u_2} results in the formation of a helical vortex rope in the draft tube at part load[4], leading to severe pressure pulsation that often threat the turbine's operation and even

---

[3] That is, the attack angle $\Delta\beta_1$ of the relative velocity W_1 at inlet.

[4] Under 60% of the full load or so

the safety of the whole power station. This spiral-type vortex rope is shown in Figure 5.2 (a).

For the cases when the attack angle $\Delta\beta_1 = \beta_1 - \beta_{1a} < 0$, at the runner exit, the absolute velocity V_2 has a negative circumferential component $V_2 \cos\alpha_2$ caused by the flow of this negative attack angle flowing through the blade-blade channel to the exit. That is, V_{u_2} $(= V_2 \cos\alpha_2)$ is in the reverse direction as u_2 (the runner rotation direction). This negative V_{u_2} results in an onion-shaped vortex rope in the draft tube, as shown in Figure 5.2 (b), whose spiral tails also cause pressure fluctuations with relatively smaller amplitudes, therefore, sometimes named as vortex core.

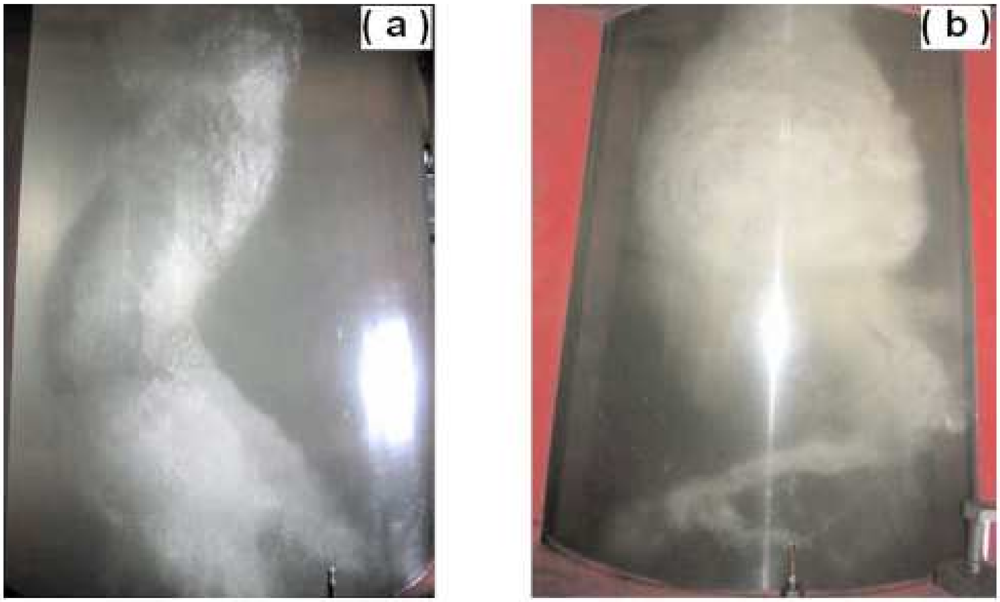

Figure 5.2: Typical vortex ropes in the draft-tube cone of a Francis turbine model, (photos taken at Harbin Electric Machinery Co. by Q. D. Cai) (a) spiral-type vortex rope and (b) bubble-type vortex rope [11]

Generally speaking, for studying the draft-tube flow, one can simply ignore the upstream disturbances and work on much simpler sole draft tube flow. This is because the upstream disturbances to the draft-tube flow are on much smaller time scales[5] and do not resonate with the low-frequency modes of vortex ropes [80]. However, this simplification cannot apply for our case. Results in the former chapter have already shown that the unsteadiness caused by the guide-plate are also dominated by low frequency motions, resonating well with the vortex rope instabilities in the draft-tube, which will be further convinced by more results in the following section.

5.2 Vortex Pattern in Turbine at Partial Load

5.2.1 Comparative analysis on vortex-rope pattern in draft tube

In order to understand the physical mechanism of the vortex-rope formation, firstly the flow unsteadiness of the swirling flow at partial load (i.e. Guide-vane opening: 16°) can be demonstrated by some selected instantaneous stream-traces distribution in the draft tube, along with the contours of pressure distribution (in color), referring to Figure 5.3. The runner blades are designed at the optimal operating condition to rectify the rotating fluid[6] toward the axial direction. But under off-design conditions, since the azimuthal velocity of the flow at the guide vanes reduces while the runners rotational speed remains the same. Inevitably, the flow downstream the runner acquires an azimuthal velocity to form a swirl flow in the cone (draft tube).

From Figures 5.4 and 5.5, one can see how complicated the elbow flow is. The reversed flow occurs in the core region of the swirling vortex, and the forward streams go through the outer region. In the elbow space of middle and

---

[5] i.e., higher frequencies

[6] That is, to make it virtually swirl-free in the cone

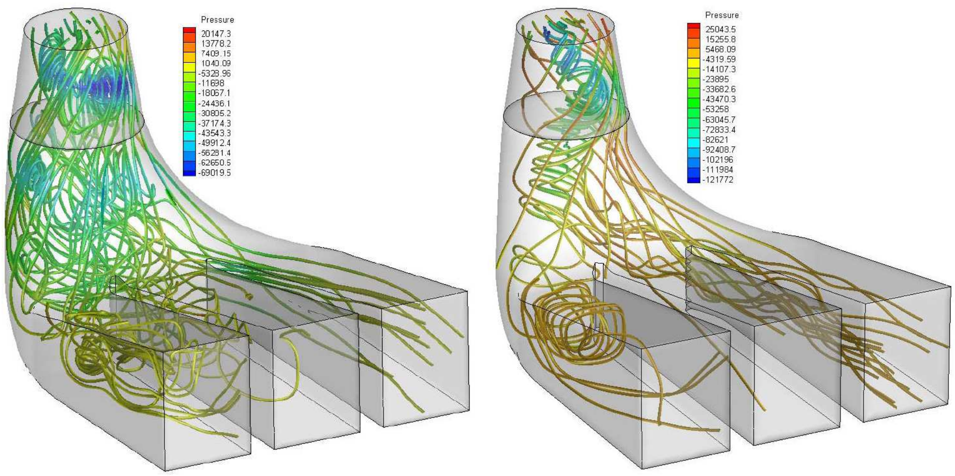

(a) (b)

Figure 5.3: Vortex rope in the draft tube: stream-traces distribution (format: volume rod, color indicate pressure contour) with guide-vane opening of 16°: (a) case 1 ; (b) case 2

left part (from the view of readers), the low-speed, reversed flow contributes to this chaotic flow pattern. And the forward stream is always concentrated on the right part of the elbow (from the view of readers), rather than switching back and forth among the three outlets as the vortex-rope spirals. Consequently, almost the entire flow (mass flux) runs only through the right outlet at high speed. In the previous experimental and numerical study by many scholars [12,99], a similar uneven partition of the mass flux has been reported.

By comparing the swirling flow pattern in the cone for case 1 and case 2, the swirling vorticity of vortex-rope precession for case 2 is even stronger with a smaller radius of vortex-rope. Recall that the pressure-fluctuation frequency component caused by vortex-rope for case 1 and case 2 is 0.67 Hz and 0.336 Hz respectively. It is supposed to see the vortex-rope precession for case 2 slower. For further investigating this flow pattern in the draft tube, the vortex-rope precession is thus visualized by vortex cores and EgnVal 2 iso-surfaces (λ_2

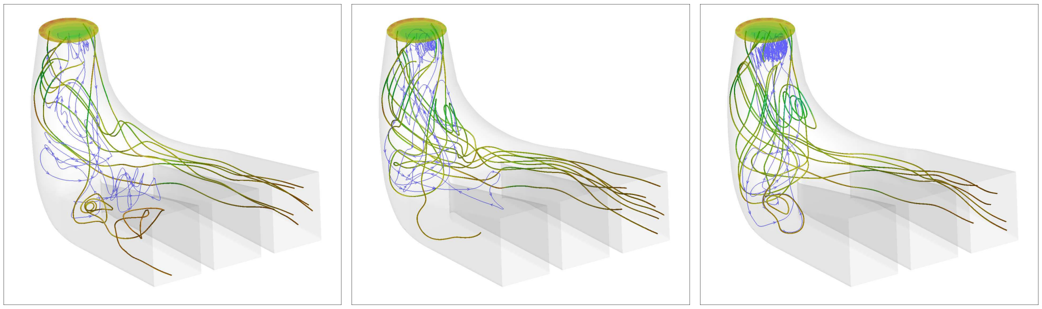

(a) $t = 143.68s$ (b) $t = 145.28s$ (c) $t = 146.88s$

Figure 5.4: Instantaneous streamlines at different time, pressure contours at the inlet for case 1, Volume rods (color indicate pressure contour) indicate forward streams and blue lines with arrowheads indicate reversed streams, respectively. (Guide-vane opening of 16°)

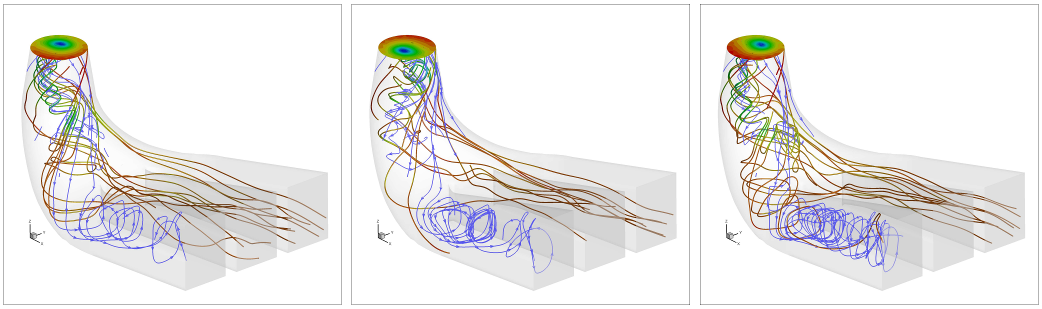

(a) $t = 143.68s$ (b) $t = 145.28s$ (c) $t = 146.88s$

Figure 5.5: Instantaneous streamlines at different time, pressure contours at the inlet for case 2, Volume rods (color indicate pressure contour) indicate forward streams and blue lines with arrowheads indicate reversed streams, respectively. (Guide-vane opening of 16°)

method).

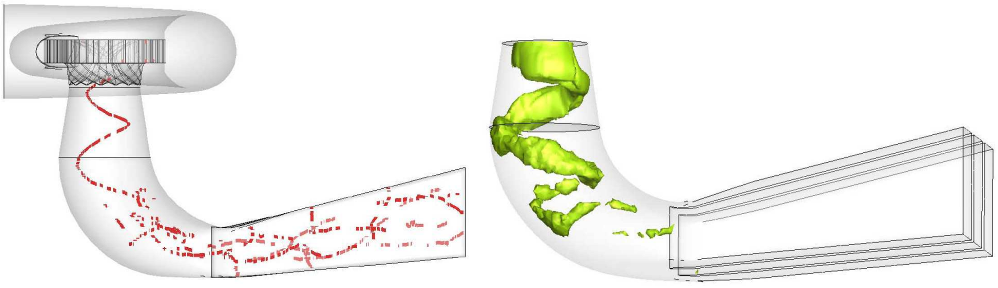
(a) (b)

Figure 5.6: Vortex rope in the draft tube for case 1 with guide-vane opening of 16°: (a) vortex cores; (b) vortex-rope pattern

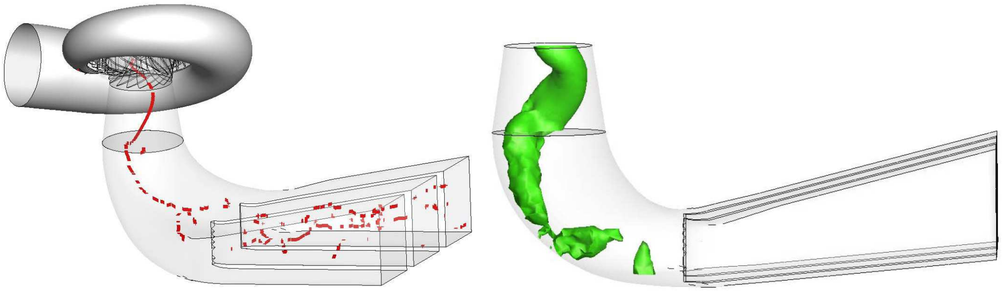
(a) (b)

Figure 5.7: Vortex rope in the draft tube for case 2 with guide-vane opening of 16°: (a) vortex cores; (b) vortex-rope pattern

Figure 5.6 (a) and Figure 5.7 (a) show the vortex cores in the draft tube for case 1 and 2. Apart from the swirling flow in the core, the flow downstream the cone is also very complicated consisting of unsteadiness, flow separation and locally reversed flow (depends on the flow conditions) that all have influences on the cone flow. The swirling flow pattern visualized by λ_2 method for both cases are clearly shown in the right-side figures. It presents reasonably well vortex-rope formation under partial load (by comparing with Figure 5.2 (a)) and Figure 5.9 predicted in previous numerical studies (without guide-plate, similar to Case1) [12] while ignoring the unsteadiness in the elbow part (low strength vortex structures). This is also a validation of the λ_2 method employed for this case.

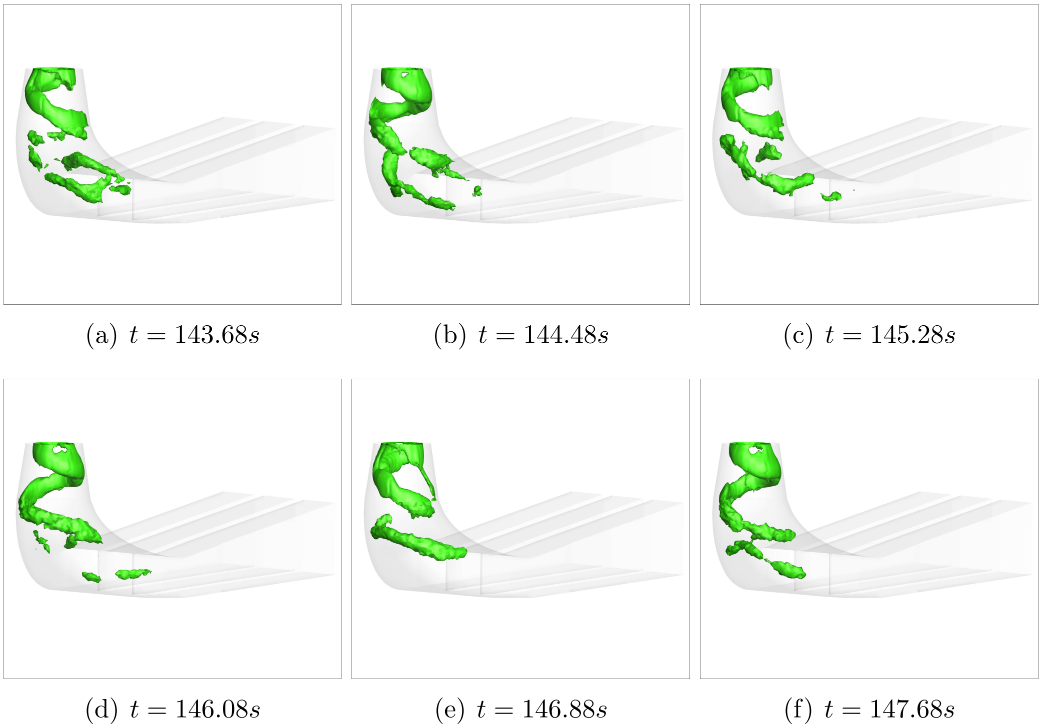
(a) $t = 143.68s$ (b) $t = 144.48s$ (c) $t = 145.28s$

(d) $t = 146.08s$ (e) $t = 146.88s$ (f) $t = 147.68s$

Figure 5.8: Vortex-rope precession in the draft tube for case 1 changes with time (Guide-vane opening of 16°)

In search for the periodic behavior of this swirling vortex-rope in the draft tube, Figure 5.8 and Figure 5.10 compare the vortex-rope pattern moving with time for both cases. The same time points have been selected for comparability. The total time slot is 4 s and with the time interval of 0.8 s (100 computation steps) for each frame. It is noticeable that the period of the swirling flow pattern for case 1 and case 2 is around 1.8 s and 3 s, corresponding to frequency of 0.67 Hz and 0.336 Hz respectively. It agrees well with the FFT results reported in the previous chapter.

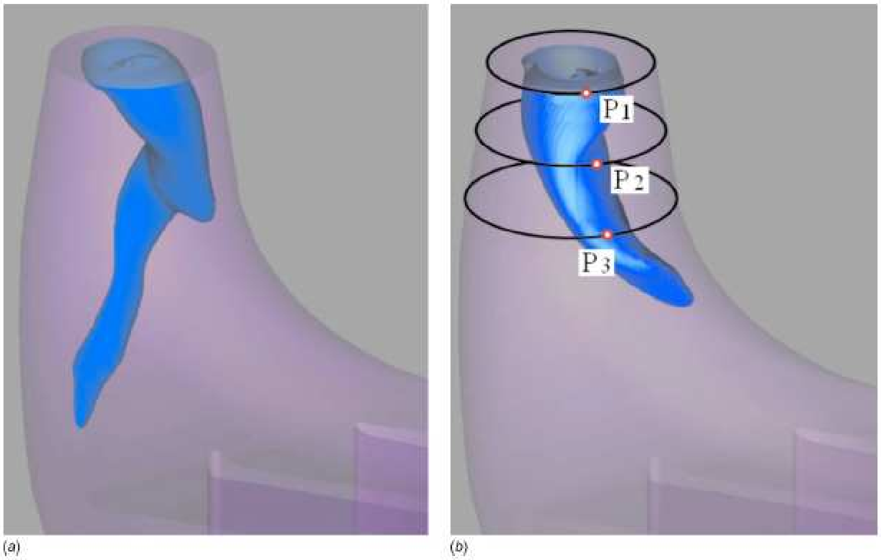

Figure 5.9: Vortex rope at part load by using the rational Δ-criteria: (a) t = 11.52; (b) t = 13.39 [12]

5.2.2 New vortex structure induced by guide-plate

For the case with guide-plate in spiral casing, the strong vorticity not only occur in the draft-tube swirling flow. A new structure of vortex flow has been identified from numerical studies. That is, an unsteady vortex ring firstly appears around the guide-plate as shown by Figure 5.11. It again proves the prediction that the addition of guide-plate induces unstable large vortex structure in the free-stream flow. As already discussed in the previous chapter, the space distribution of these vortices changes along the circumferential direction of the spiral case. Figure 5.11 (a) shows the entire guide-plate surrounded by the ring-shape vortex structure that has thus advanced the formation of strong vorticity well before the runner. In Figure 5.11 (b), apart from the vortex ring around the guide-plate, commonly known vortices are also shown such as blade-blade vortex in the stay vanes and guide vanes and the strong swirling flow at the outlet of runner by λ_2 method.

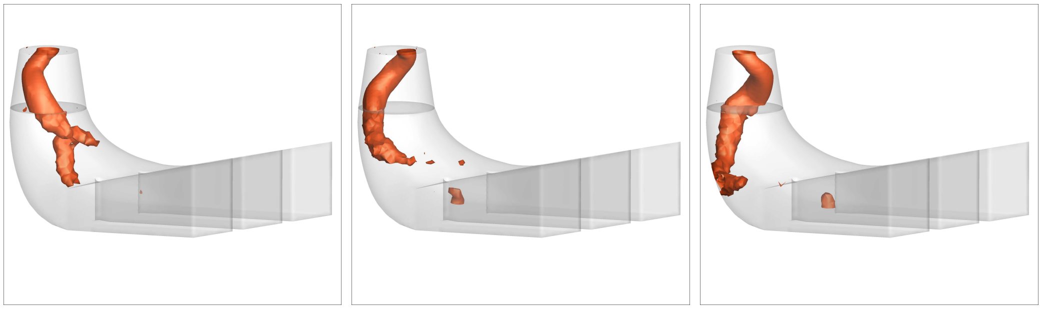

(a) $t = 143.68s$ (b) $t = 144.48s$ (c) $t = 145.28s$

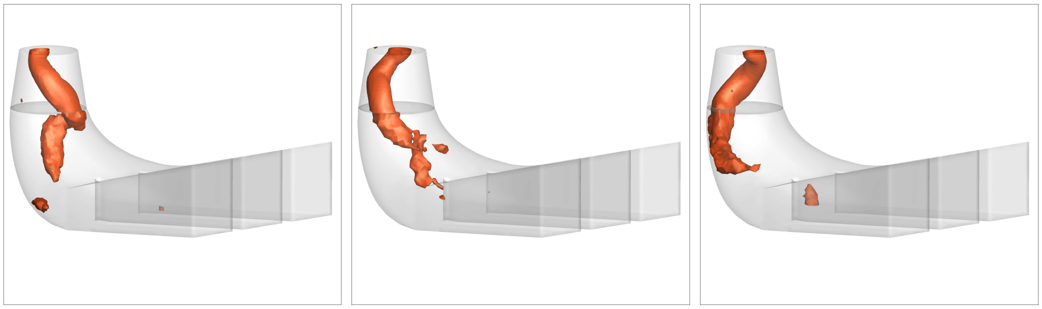

(d) $t = 146.08s$ (e) $t = 146.88s$ (f) $t = 147.68s$

Figure 5.10: Vortex-rope precession in the draft tube for case 2 changes with time (Guide-vane opening of 16°)

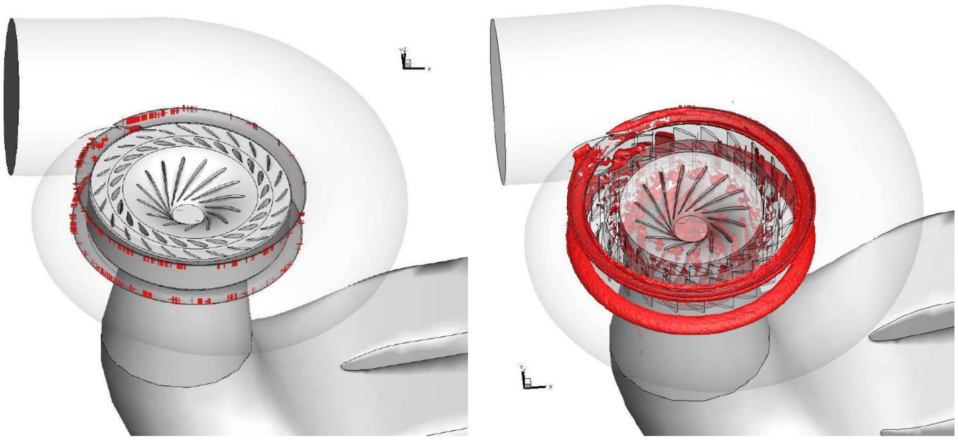
(a) (b)

Figure 5.11: Vortex in spiral case for case 2 with guide-vane opening of 16°: (a) vortex cores; (b) vortex-ring pattern

For cases under different operation conditions, the detailed structure of this vortex ring is very different. For 35° it consists of many small vortices, like a complete vortex-ring breaking into small pieces shown in Figure 5.12. Whereas for 16°, it is almost a complete ring around the guide-plate. This structure difference is attributed to the difference of main flow in the spiral-case for 16° and 35° guide-vane openings. The fact of broken small pieces of vortices in the ring for the opening of 35° explains well the reason why the addition of guide-plate produces less low-frequency components whereas promotes more high-frequency components in contrast to the opening of 16°[7].

5.2.3 Vortex interaction

Figure 5.13 shows the vortex cores and other unsteady vortices in the whole flow field for case 2 with guide-vane opening of 30°. It should be noticed

---

[7] Note: The frequency of pressure-fluctuation varies inversely with the scale of vortex.

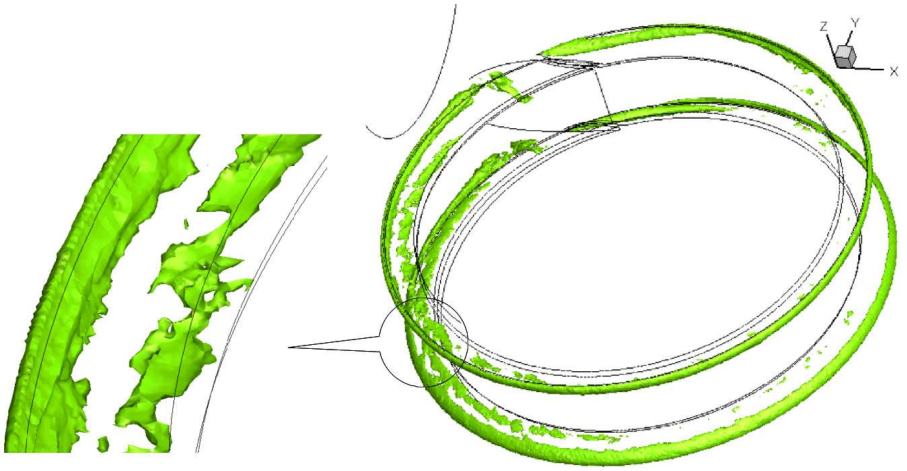

Figure 5.12: The structure of vortex ring at openings of 35°

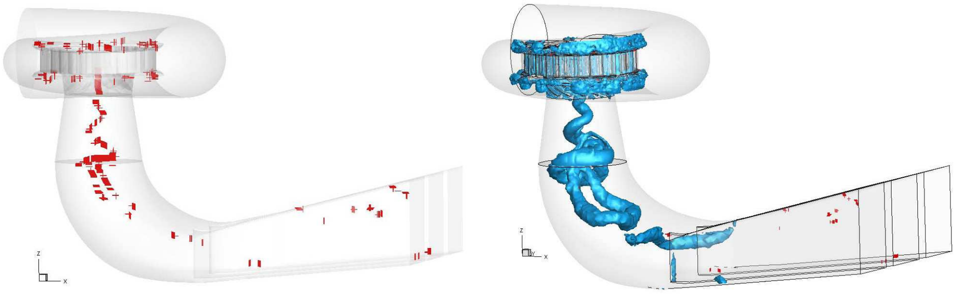

(a)

(b)

Figure 5.13: Vortex in the whole flow passage for case 2 with guide-vane opening of 30°: (a) vortex cores; (b) vortex pattern

that the vortex cores of vortex-ring in the spiral casing are connected[8] with the vortex cores of vortex-rope in draft tube while for case 1 there are no vortex cores existing before the runner blade-blade passage. This reflects the interaction mechanism between these vortex structures in different parts of whole turbine passage. That is, they act together, forming an extremely large and complicated structure of vortex possessing the entire flow passage of the turbine. The two vortex-structures (i.e. both the vortex-ring at the guide-

---

[8] This connection is established through the runner blade-blade vortices. A typical case is shown in Figure 5.11 (b).

plate and the vortex-rope in the draft-tube) have been connected through the vortex structure in the runner as a single giant and complex vortex-structure throughout the whole passage as shown in Figure 5.13 (b). Such an extremely large-scale and unsteady structure is thus for the first time identified from this PhD programme.

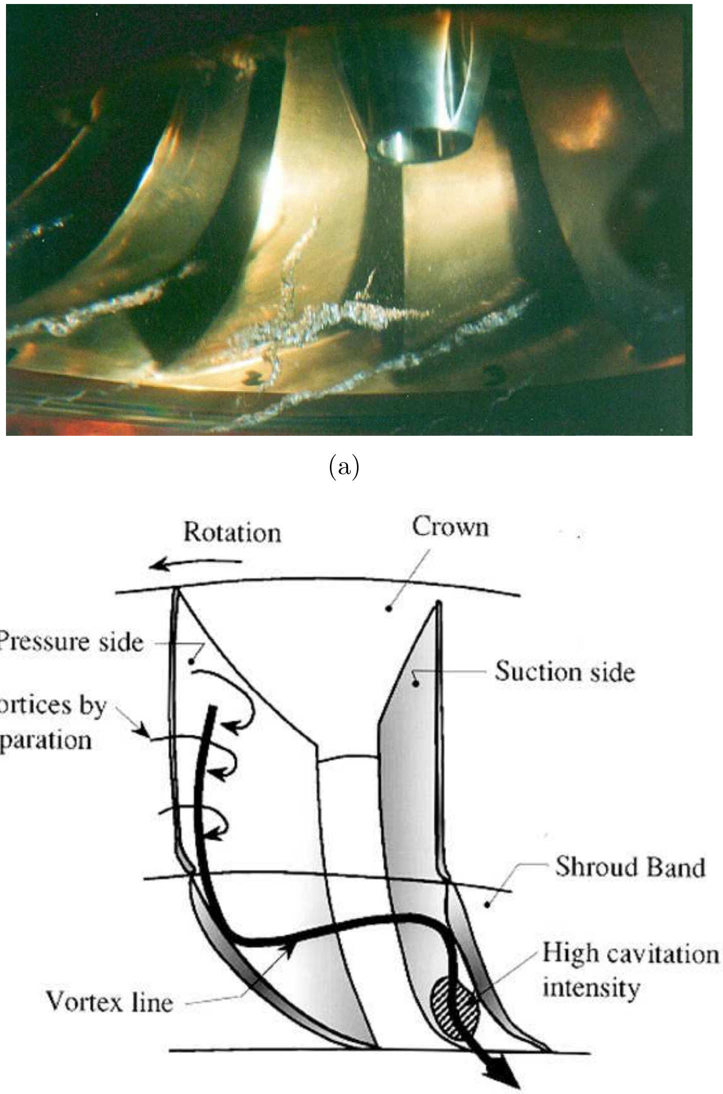

(a)

(b)

Figure 5.14: (a) Runner induced vortices; (b) Vortex line at low head [13]

Along the vortex cores from the spiral casing extending to the draft tube, vortex patterns in different component are shown in Figure 5.15. It

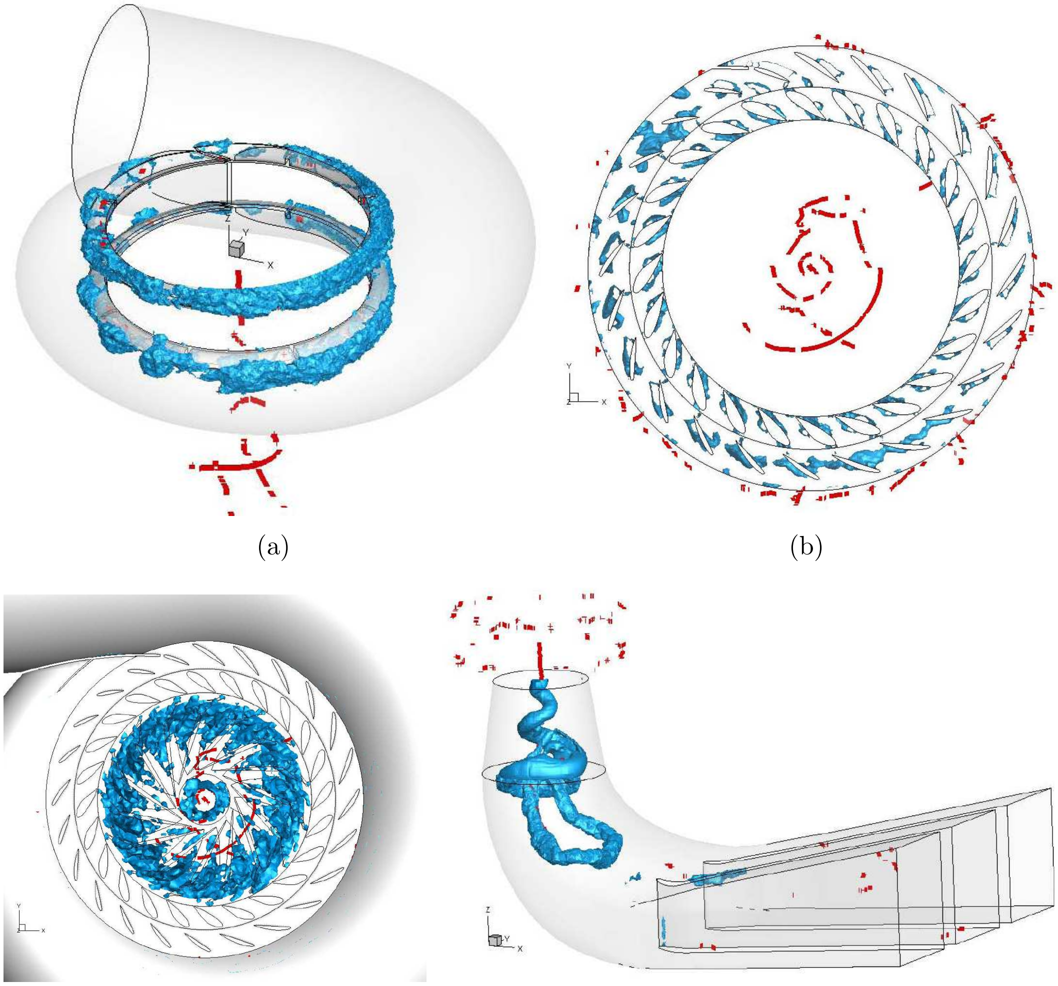

(a)

(b)

(c)

(d)

Figure 5.15: Vortex pattern for case 2 with guide-vane opening of 30° in (a) spiral case; (b) stay vanes and guide vanes; (c) runner; (d) draft tube

makes us easier to visualize that the ring-shape vortex structure in the spiral casing moves and precesses with the flow periodically, and breaking into smaller pieces of vortices while entering the blade-blade passages of stay vane and guide vane. More vortices produced by the moving runner[9] and a swirling

---

[9] Runner induced vortices is a well-known phenomenon. A typical case for Francis turbine operating at off design is skeptically presented by Figure 5.14 [13].

flow formed at the outlet of runner, enters into the cone region, through the complicated self and mutual inductions, eventually leading to a highly unstable swirling vortex-rope precession in the draft tube.

Figure 5.16 presents the dynamic behavior of this united vortex-structure throughout the whole flow field moving with time under the operation condition of 30° opening. The total time slot is 12.8 s with the time interval of 1.6 s (200 computation steps).

By comparing this vortex-rope with the case of 16°, referring to Figure 5.10, their vortex-rope formations are very different. For the case of 30°, the orientation is much less organized than that of 16°, which is well organized with a stronger vortex-core rotating (precessing) uniformly. The nine frames almost elapse two periods, the vortex-rope precession swirls with time while its radius and orientation change dramatically. The vortex ring in the spiral casing also contributes to this dynamic behavior that has a characteristic time T of approximate 6.6 s. Consequently, this large unsteady vortex structure occupying the whole system will thus induce an even lower frequency pressure-fluctuation component (0.15 Hz) than the 0.265 Hz induced by the vortex-rope in the draft-tube for case 1. However, their amplitudes are all much smaller than that of 0.336 Hz for case 2 at 16°.

5.3 Vortex Pattern in Turbine With Guide-Vane Opening of 35°

Figure 5.17 shows the calculated vortex pattern in the whole flow passage for case 2 at the opening of 35°. In contrary to cases with guide-vane opening of

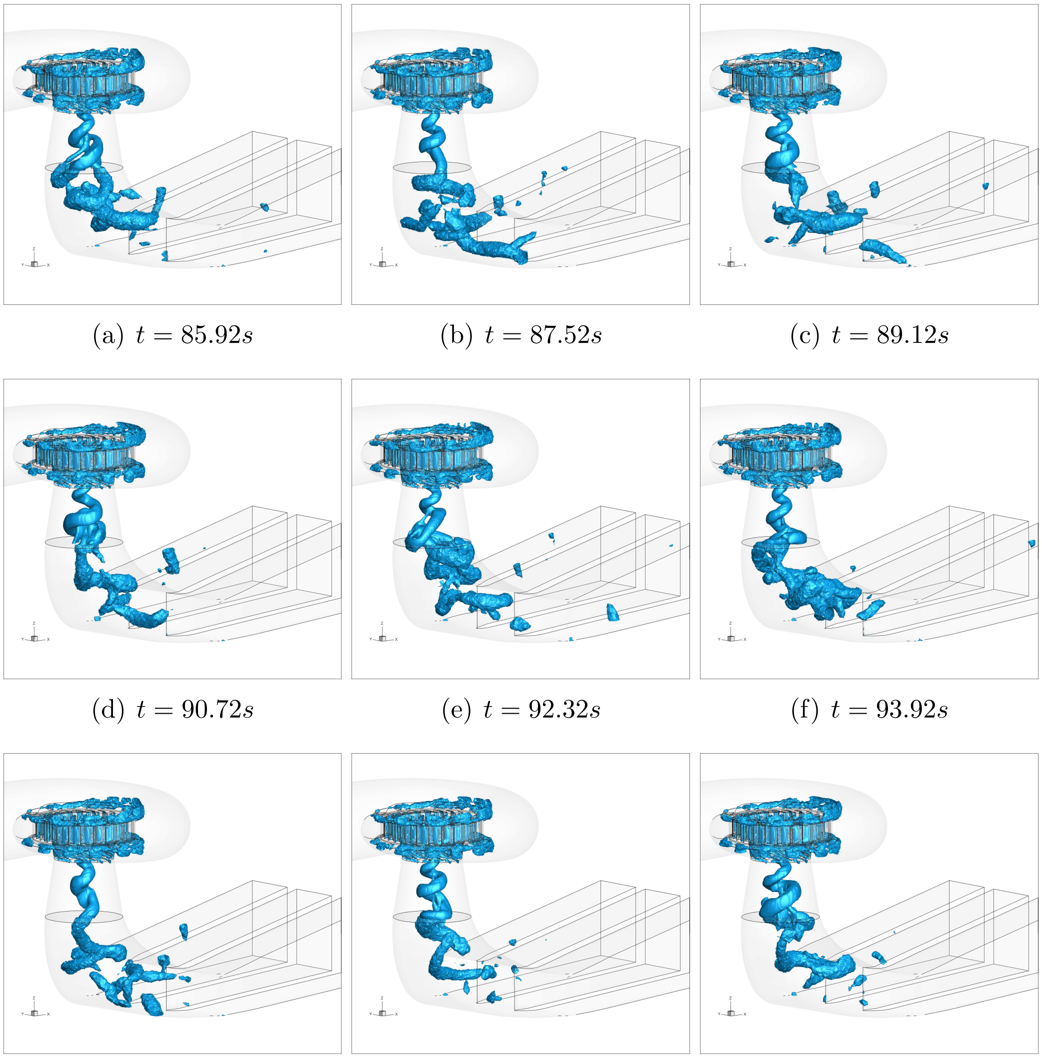
(a) $t = 85.92s$ (b) $t = 87.52s$ (c) $t = 89.12s$

(d) $t = 90.72s$ (e) $t = 92.32s$ (f) $t = 93.92s$

(g) $t = 95.52s$ (h) $t = 97.12s$ (i) $t = 98.72s$

Figure 5.16: Vortex precession in the whole flow field for case 2 (Guide-vane opening of 30°)

16° and 30°, at the opening of 35°, owing to the operation condition close to the optimum the flow in the draft-tube does not have a spiral vortex rope but a weak and nearly steady vortex-core. This feature has also been predicted by previous studies [12], referring to Figure 5.18. The flow quasi-steadiness indicated by the vortex pattern in the draft tube for case 1 has already been analyzed in the previous chapter. Even for the case with guide-plate, since V_{u_2} at runner outlet is very small, the formation of a helical vortex rope in the draft tube is no longer the case. Therefore, although the ring-shape vortex structures still exists and affects the flow pattern throughout the whole turbine passage, without the swirling vortex-rope in the draft tube, a giant and single vortex-structure starting from the spiral casing extending to the draft tube is not possible to be formed, leaving virtually no difference on the pressure-fluctuation within the low-frequency range of the spectrum for case 1 and case 2. This physical mechanism explains well why case 2 (with guide-plate) didn't show pressure-fluctuation frequency lower than 1.25 Hz when operating at the opening of 35° in the previous FFT analysis.

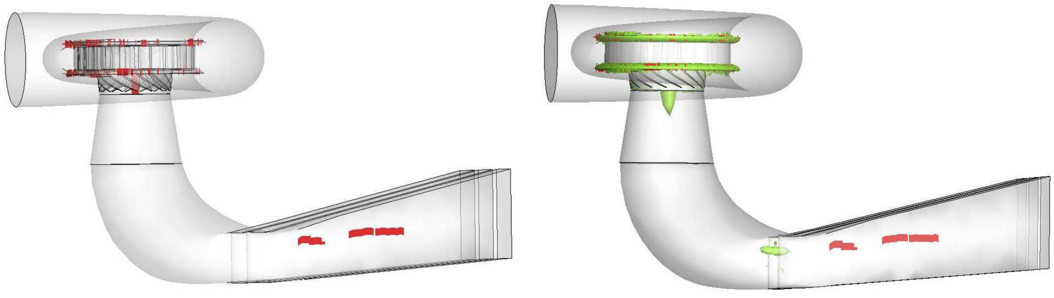

(a) (b)

Figure 5.17: (a) Vortex cores; (b) Vortex pattern in the whole flow passage of turbine at the opening of 35°

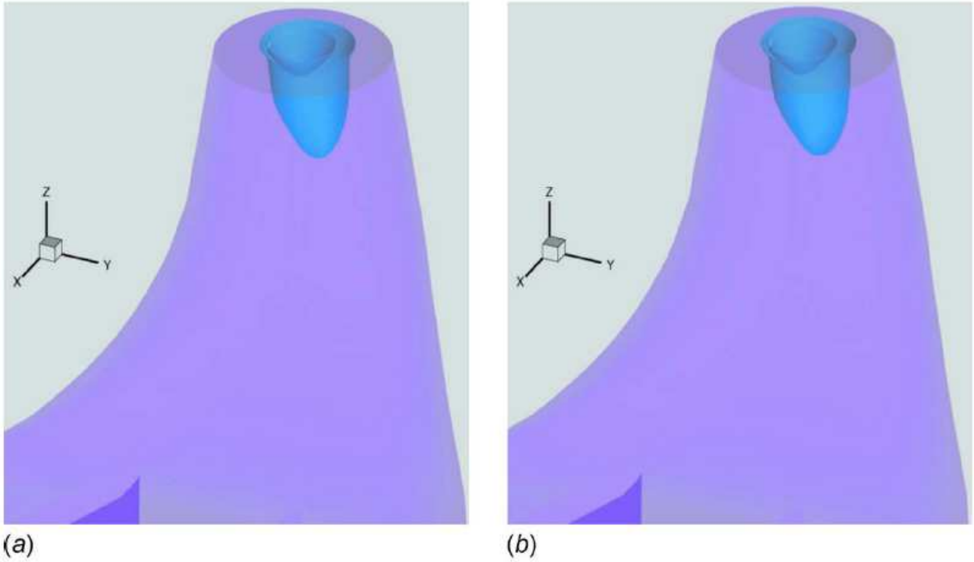

Figure 5.18: Vortex rope at full load by using the rational Δ-criteria: (a) t = 2.13; (b) t = 2.66 [12]

5.4 Solutions to the problem

The formation of a vortex-ring structure around the guide-plate has been for the first time identified. Investigations indicate that it interacts with other vortices, contributing to the formation of an extremely large-scale and very unstable vortex structure throughout the whole turbine system. It is responsible for the extremely low-frequency of 0.336 Hz with the highest amplitude induced in the whole passage under partial-load operation conditions (e.g. 16°), and for the other and even lower frequency pressure fluctuations at lower amplitudes at other partial-load conditions. This particular frequency of 0.336 Hz is even lower than the traditionally primary unsteady sources of the vortex rope in the draft-tube. It thus imposes a significant threat to the hydraulic instability of the system. The introduction of the so-called device of guide-plate for reducing the unit size is therefore not justified because it indeed is harmful to the turbine system in particular during the partial-load operation.

This guide-plate device has now been redesigned or simply removed from the Three Gorges turbines at the right-power plant following the advice given by Li in 2006 [1]. However, for the high and medium specific speed turbine-generator units, spiral casing is often the crucial component that determines the overall size of plant. Therefore, the size reduction of spiral casing has a significant impact on the hydro scheme's economic feasibility. This is why manufacturers thus take high risks to reduce the size of spiral casing in order to win the bidding. The idea of using guide plate, which has already experienced a torn-off accident within one year since commissioned at the left power house of the Three Gorges project, is further scrutinized with negative results in our study. The feasibilities of employing oval cross-section spiral casing for the size reduction was suggested[10]. This suggestion has been employed in the new turbines designed for Xi Luo Du power station by Hydro Power Generation of Voith-Siemens in late 2008. And, the newly designed turbines for large hydro projects in China are all following these trends, modifying their designs as well. Some results will be presented later.

Apart from the redesign of the spiral casing, the key problem causing this global instability is this united giant vortex structure in the whole flow passage of the turbine. The flow upstream the cone will affect the cone flow significantly, especially under part-load operation condition. The swirling flow in the cone is absolutely unstable, leading to a strong and robust helical vortex-rope as the source of severe low-frequency pressure fluctuations, and the addition of this guide-plate worsens this situation extremely. Since

---

[10] In the March of 2006, Prof Li has made a suggestion to the M & E department of CTGPC about the novel idea.

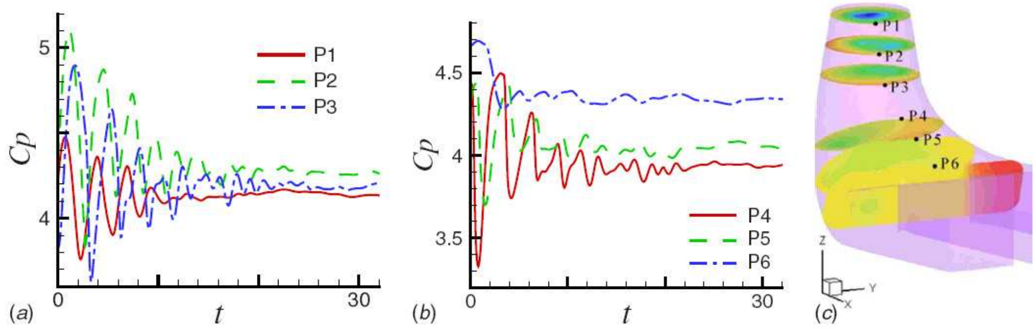

Figure 5.19: Pressure fluctuations of the controlled flow by jet injection: (a) and (b) are the pressure fluctuations on six check points, whose locations are marked in (c) [12]

operation under part-load condition is inevitable for hydro power generation, eliminating and/or mitigating the vortex rope is a feasible strategy for the suppression of pressure surges. Many investigations have been conducted by focusing on the control of the reversed axial flow through various means, e.g., referring to Figures 5.19 and 5.20 [12].

For a Francis turbine, if vibration occurs in the middle range of the load, three mitigating methods can be employed in engineering practice [11].

(a) Avoid operating within the zone where excessive vibration occurs. In this case, no corrective action is required. However, the flexibility of operation in an integrated grid system is limited;

(b) Inject air below the runner. Air admission will suppress the upward surges in draft tube, reducing vibration [100, 101];

(c) Modify the shape of the trailing edge of the runner blades. This is often the best method, yet it is more time-consuming. Furthermore, it has to be carried out by an expert hand otherwise it may aggravate the problem.

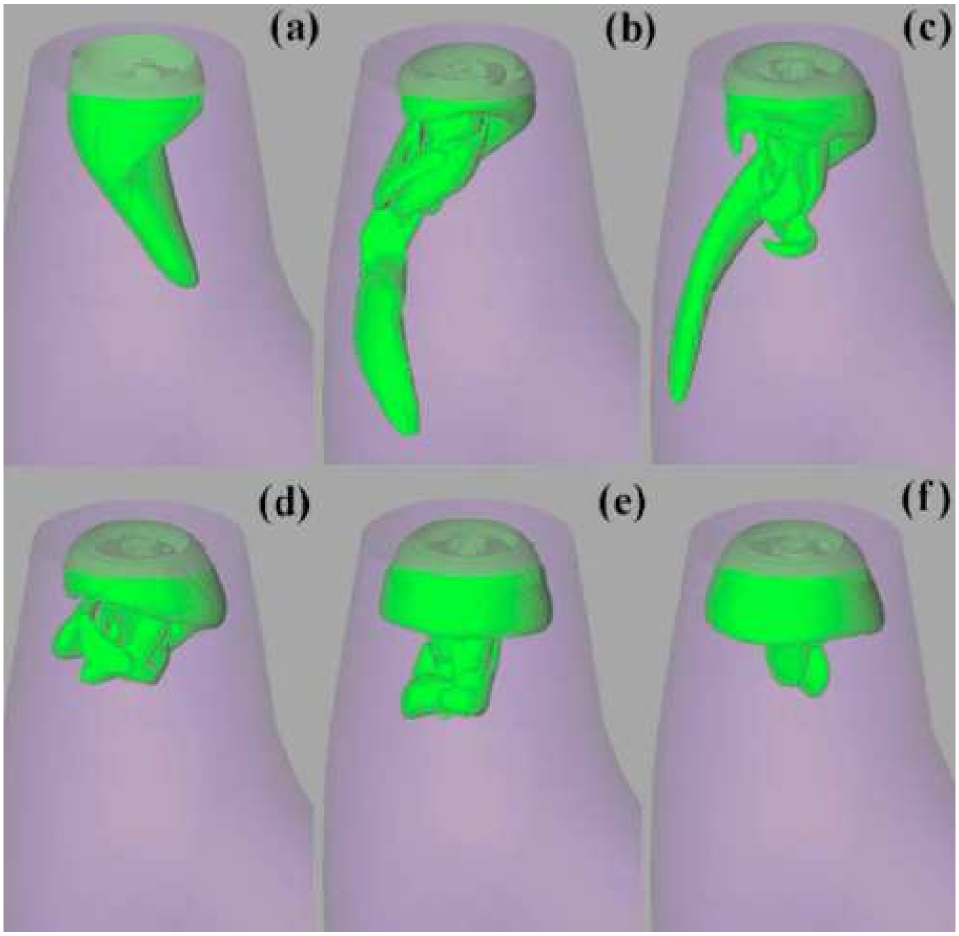

Figure 5.20: Isosurfaces of Δ of the controlled flow by jet injection. Starting from the onset of control, the dimensionless times in (a)-(f) are t=0, 3.60, 5.04, 7.92, 12.25, and 32.4, respectively. [12]

Chapter 6

Conclusion and Future Work

As the first-step development of proving Li's hypothesis, the motivation of this PhD programme is to verify that the wrongly designed guide-plate for the Three Gorges turbines of the left-power plant has increased the level of free-stream turbulence, particularly components of the gust-like low-frequency pressure-fluctuations.

6.1 Achievements

The main achievements from the PhD programme as presented in this thesis can be concluded as follows:

(1) A 3-D flow investigation of the prototype turbine is essential for providing a complete information in this research. Geometric turbine model has been built based on the actual parameters of prototype turbine with some necessary simplifications. As the first step of such a thorough investigation, numerical simulations have been performed to obtain the main flow features in the whole turbine passage with more detailed analysis on the free-stream

pressure-fluctuations near the lower surface of guide vanes. The unsteady flow characteristics, especially the pressure fluctuations of low-frequency spectrum have been studied that significantly alternate the turbulence intensities and spectrum in the free-stream flow.

(2) The studies have numerically verified that the addition of guide-plate increases the free-stream turbulence level and particularly contributes to the occurrence of a strongest component of extremely low-frequency pressure-fluctuation (i.e. the 0.336 Hz for the case 2 with the opening of 16°); while for the comparable case (without guide-plate) the strongest pressure-fluctuation component is weaker with higher frequency (i.e., 0.67 Hz) owing to the commonly known vortex rope in the draft-tube. For another part-load operation condition (i.e., the guide-vane opening: 30°), the strongest pressure-fluctuation frequency in the draft tube for case 2 (with guide-plate) is 0.15 Hz while for case 1 (without guide-plate) it is 0.265 Hz but with much smaller amplitudes. The addition of guide-plate induces extra unsteadiness with gust-like low-frequency at part-load condition that is even stronger than the most 'powerful' unsteady sources caused solely by the helical vortex-rope in the draft tube. These low-frequency fluctuations readily transmit throughout the entire flow passage of the turbine. Our calculation results agree well with the measured data particularly at guide-vane opening of 16° for this dominant low-frequency (i.e. 0.31 Hz) fluctuation component. It is very likely that this particular component is one of the sources entering the boundary-layer and promoting the growth of Klabenoff-streaks and their transition, which in turn triggers the cavitation inception in the boundary-layer of the guide vane.

(3) The studies have for the first time identified an extremely large-scale and single united unsteady vortex structure occupying the whole flow passage

of a Francis turbine. Firstly a vortex-ring structure around the guide-plate has been numerically spotted and visualized; through the connection of the vortices in the stay-vane and guide-vane channels and the runner channels it further interacts with the helical vortex-rope in the draft tube at part-load conditions, forming such an united giant vortex. This extremely large-scale vortex structure is thus responsible for the components of low-frequencies (i.e., 0.336 Hz for 16°, 0.15 Hz for 30°) identified from this PhD programme for two part-load operation conditions. It is not only responsible (in our opinion) for the cavitation inception and damage on the guide vane but also imposes a significant hydraulic instability on the hydro-electric units, even possible risks to the stability of the whole national grid. Figure 6.1 summarizes this first verification of Li's Hypothesis, from which we can clearly see how this wrongly designed guide-plate device increases the free-stream turbulence level.

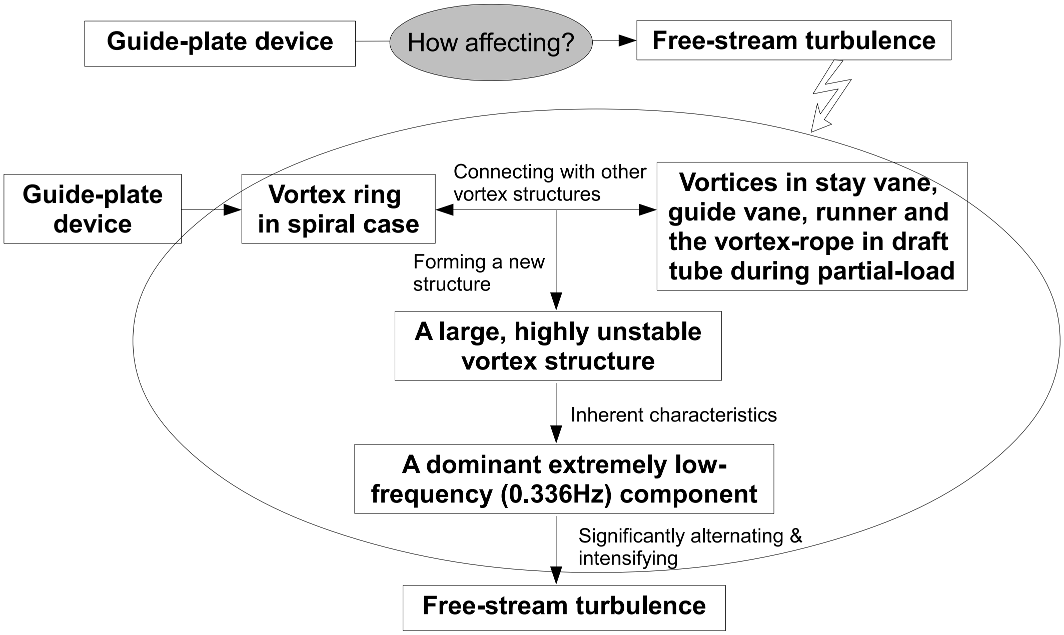

Figure 6.1: Conceptual sketch of the first element verification of Li's Hypothesis

(4) The study has successfully proven that the guide-plate device is harmful, especially for partial-load operation. It is not guiding the flow into the turbine runner smoothly but adding extremely low-frequency fluctuations and preventing the flow from entering the turbine smoothly. Also, it significantly lowers the average static pressure in the free-stream near the lower surface of the guide vanes, contributing to the promotion of cavitation inception as well. The results from this study have pointed out that the flow upstream the cone could affect the cone flow significantly, especially under part-load condition. Since the study initiated by Li in 2006 and followed by this PhD programme, it has become one of focal issue attracting the attentions from academic circle, manufacturing sectors and utility companies. Following the advice and outcomes from this study, these guide-plates have been completely removed from the units in the right-power plant of the Three Gorges project. And for new turbine designs, modifications have been done accordingly for huge hydro schemes such as WuDongDe and XiLuoDu, etc.

6.2 Future Work

Having successfully verified the first element of Li's Hypothesis, a full investigation[1] across multi-disciplinary subjects is to be carried out according to the suggestions proposed by Li [1]. Long-term commitment is necessary, in particular by experiment investigation to re-create this cavitation inception in the boundary-layer triggered by the K-mode breakdown.

---

[1] Motivating by Li's initial report on the discovery of this highly multi-disciplinary subject, investigations of measuring the temperature encountered by such possible hydrodynamic cavitation is already performed in Europe.

6.2.1 Proposed project: Cavitation inception control

Further verifying the hypothesis requires the recreation of this phenomenon under controllable conditions for thorough investigations. Such an experiment set-up is being carefully devised and conducted in the tunnel of the Warwicks cavitation lab. The test section is made transparent, enabling direct observation of the behavior of cavitation bubbles, as shown in Figure 6.2.

Figure 6.2: Test section of the Cavitation Rig

The parameters governing the inception process are extremely crucial for understanding its mechanism and reducing a correlation ship of this cavitation with flow conditions. However, the governing factors and their combinations are very complex and could lead to one or combination of (cavitation) inceptions. It would become a great challenge to maintain the occurred and required type of cavitation very stably within an allowed range under varying circumstance (perturbations) through controlling those governing factors.

Based on the findings in the PhD programme, the future research will target on the control mechanism of cavitation inception and subsequent types by building the experiment platform on the existing cavitation tunnel and conducting various experiment tests combined with numerical investigations. The frontier control theories and novel device will be adopted to realize the complicated and delicate control of cavitation inception. Furthermore, by using the modern control theories, the characteristics of the control target (i.e. the governing factors together with the flow system) can be identified quantitatively, thus clarifying the influences of individual variables on the inception of individual type of cavitation and their stable range. This will help to optimize the control by a methodical exploration of the available parameter space, making the control more accurate and stable. In turn, it will form a complementary approach from the control viewpoint to solve the elusive (challenging) area left by many fluid dynamic studies nowadays.

Once realizing the recreation of cavitation inception, it has to be closely examined if the turbulent spots concise with the cavitation inception. The initial experimental/numerical studies could be carried out on a flat-plate to acquire the information that how the streaks grow and breakdown under the influences from the free-stream low-frequency turbulences and the possibilities of inducing cavitation inception. With the information obtained from flat-plate, we may able to predict the trends about the streak formation, growth, interaction with T-S waves and breakdown on hydrofoil. Therefore, experiments on prototype turbine could be designed and conducted more effectively and predictably. It is essential to further examine if the stream-wise position and the span-wise variation of the breakdown (especially, the turbulent spot) does comply with the observed pattern of damage strips.

This future research is very challenging and highly multidisciplinary but feasible and meaningful. It will for the first time in the history bring together these two disciplines to solve the long lasting challenge in fluid mechanics by applying artificial control to cavitation inception. It is anticipated that new knowledge and technology to be obtained will be of great importance to both the obvious academic development mentioned above and the industrial sectors worldwide such as turbo-machinery and high-speed cavitating marine crafts etc., and will make economical and social impact.

6.2.2 Remarks on Possible Difficulties

Initial designs and trial tests are already on the way. However, there are several issues need careful considerations.

(1) The choice of flow visualization method

Precise near-wall measurement is a challenge for quantitatively capturing two extremely elusive phenomena within the boundary layer: streaks break-down and cavitation inception. In order to capture this dynamic process happening in a very short time period, the use of high-speed camera with high resolution is essential. Hydrogen-bubble technique and PIV (Particle-Image Velocimetry) are commonly useful tools for flow visualization, however both of them are not non-intrusive for cavitation detection because neither the hydrogen-bubbles nor the reflective particles are real 'non-intrusion' for the cavitated flow. The use of each of them will confuse us with detecting the nucleating bubbles, or inevitably change the nature of cavitation inception itself. Therefore novel experimental techniques should be sought for this extremely complicated problem.

(2) Limits on numerical techniques

Owing to the highly nonlinear nature of the dynamic process from the streaks breakdown to the turbulent spot formation, no numerical techniques (including DNS approach) can reproduce this whole process yet. However for the first half process of transition, the recently proposed scenario by Lee [23] provides a good opportunity to solve the near-wall transition problem, that is, one can only focus on a single flow structure called SCS and its time evolution to a long streak and breakdown. DNS approach is thus suggested for this physical model.

(3) How to introduce an extremely low-frequency disturbance into wall-bounded flow

All possible disturbances should be strictly controlled, such as pressure and temperature, etc. Besides, the design should be sensitive enough in responding to an extremely low-frequency disturbance introduced into the leading edge flow in order to advance the transition and sequentially to facilitate the cavitation inception. Further site experiments on the prototype will be necessary for verifying these numerical and experimental results.

6.2.3 Other Studies

Apart from above, other necessary studies should be done in the future work:

Laboratory study on the characteristics of this material damage is necessary for understanding the heating phenomenon/mechanism associated, which has never been studied before[2]. Theoretically, some unsolved theories of tran-

---

[2] Some trial tests on this have already been carried out recently by European scientist inspired by this research programme.

sition in wall-bounded flow (e.g., length and time scales of turbulence and scaling laws etc.) needs to be thoroughly investigated which is especially important for the development of huge turbines. Compared with small-scale turbines, the much higher Reynolds numbers of large turbines for free-stream flow and boundary-layer flow make the turbine is more vulnerable to this type of cavitation[3]. Therefore, for large turbines, while scaling cavitation data from model to prototype, the scaling effect due to the boundary-layer property difference must be investigated thoroughly and considered properly. Therefore, long-term efforts are needed to combat these problems. Furthermore, fundamental research as well as the development of novel design and manufacturing concepts should be a priority. Aiming to improve/replace the old design, novel design of elliptical spiral-casing model is being further developed for size reduction but better performance. A new wave of modifications to this part of turbines is already underway though a full understanding of this phenomenon is far from achieved yet.

In short, these findings pose new challenges but also provide new opportunities for the development of huge turbines as well as the advance of fundamental knowledge.

---

[3] For details, refer to [1].

Appendix A

Timetable of Events

Table A.1: Timetable of events on investigating this new type of cavitation.

Time	Events
Jun 2003-Sep 2005	14 units in the left-powerhouse commissioned successfully.
14 Oct 2005	Damage firstly found on 11F turbine incidentally during examining & repairing damaged guide-plate.
11 Dec 2005	Similar damage detected on 9F and other turbines (e.g. 5F and 6F).
27 Dec 2005	Similar damage detected on 10F turbine.
12-14 Mar 2006	This strange damage caught great attention from CTGPC authority. An inconclusive meeting at the Three Gorges site attended by research engineers, university academics and manufacturer representatives because of unknown damage never reported in the world literature, puzzling professionals.
19 Mar 2006	Prof Shengcai Li of Warwick University called by the Three Gorges authority, inspecting 11F turbine, in particular the representative No. 4 guide vane. Having searched for possible mechanism, Li diagnosed the problem: cavitation inception stems from boundary-layer instabilities.

Table A.2: (Continued) Timetable of events on investigating this new type of cavitation.

Time	Events
19 Mar 2006	In the presentation given *in-situ*, against all suggestions including those from the manufacturers [4], Li proposed a new type of cavitation (damage) possibly triggered by boundary-layer transition. This conceptual idea further developed into a hypothesis in late 2006 and presented by Li for the first time, and here named after him.
28 Mar 2006	Li's seminar at Peking University received positive responses from academics working on flow-transition in boundary-layer.
29 Mar 2006	Presentation and discussion with specialists at China National Research Institute of Hydro Power, Beijing.
27-29 Oct 2006	Li's plenary speech at 1st International Conference on Hydropower Technology & Key Equipment, revealing his findings by giving a systematic description of its features and a convincing hypothesis. The first paper (Ref [1]) on Li's Hypothesis (Appendix B).
2007	Journal paper "A new type of cavitation damage triggered by boundary-layer turbulent production" published (Ref [14]).
Oct 2008	Under Prof Shengcai Li's supervision, this PhD project under taken by Miss Chen started, aiming at verifying Li's Hypothesis step by step.
22-23 Oct 2009	Presentation "Cavitation (damage) Strips with Span-wise Regularity Identified from Three Gorges Turbines" (Ref [3]) at IEEE 'Electrical Power and Energy Conference', Canada,
26-27 May 2011	Presentation "Cavitation (Damage) Strips with Span-wise Regularity Caused by Cavitation: Observation and Envisaged Mechanism", SHF Conference on Cavitation and Hydraulic Machines, Lausanne, Switzerland (Ref [16]).
Jun 2011	Journal paper "Numerical investigation of guide-plate induced pressure fluctuations on guide vanes of Three Gorges turbines" published (Appendix C). The first paper on the verification of Li's Hypothesis (Ref [10]).
14-16 Aug 2012	Presentation "Cavitation (Damage) Strips with Span-wise Regularity Caused by Cavitation (Observation and Envisaged Mechanism)", the 8th Int. Symposium on Cavitation, Singapore (Ref [2]).

Appendix B

Li's first paper on this new type of cavitation

The 1st International Conference on Hydropower Technology & Key Equipment 2006
27-29 Oct 2006 Beijing

Plenary Lecture

CHALLENGE TO MODERN TURBINE TECHNOLOGIES
Analysis of Damage to Guide Vane Surface of Three Gorge Turbines

S.C. Li
Fluid Dynamics Research Centre, Warwick University
Coventry CV4 7AL, UK
S.Li@warwick.ac.uk

ABSTRACT

The Francis turbines (710 MW) of the Three Gorge Project are the world largest and even larger ones (1000MW) are to be developed for schemes on the upstream of the Yangtze River in China. The 14 units installed in the left-powerhouse have been all commissioned successfully during the period from June 2003 to September 2005, functioning as expected. However, all these turbines supplied by world leading manufacturers have developed a pattern of damage mainly on the guide-vanes, which is virtually span-wise dependent stream-wise strips. This type of damage has never been reported before. Is it an isolated issue or a fundamental phenomenon/challenge to huge turbines? Brief description of the damage is presented, together with analysis of possible causes. The preliminary study suggests that this is a phenomenon not fully understood yet, and it is a type of cavitation erosion induced by boundary layer turbulent spots. In other words, the turbulent spots serve as the cavitation inception points causing damage and then the damaged spots subsequently induce further cavitation and damage downstream. Thus a dynamic process forms producing these damage strips. According to the multidisciplinary nature of the phenomenon, the discussion presented in this article is developed from a wide view angle of metallurgical science as well as cavitation inception in boundary layer. It is emphasized that this is a new challenge to huge turbines. Further studies on both the fundamental mechanism of the damage and the novel turbine-design are essential for developing huge turbine.

1. INTRODUCTION

The turbines developed for the Three Gorge Project are the world largest Francis turbines in terms of their power (710 MW) and geometric dimensions (9800 mm of runner diameter). The 14 units installed in the left-powerhouse have been all commissioned successfully during the period from June 2003 to September 2005, generating electricity normally.

The damage was firstly found on the Number 11 turbine ('11F' will be used in the article, following the abbreviation employed at the Three Gorge Power Station) incidentally on 14th October 2005 (operated for 10,245.78 hours) when examining/repairing the damaged guide plate[1]. Later on similar damages were found on 10F on 27th December 2005 (11924.55 hours), on 9F on 11th December 2005 (2328.41 hours) and other units (e.g. 5F and 6F etc). The 14 machines in the left-powerhouse are supplied by two consortiums (Alstom + HEC, GE + Voith Siemens + DFEM) [31].

The significance of the Three Gorge Project itself is obvious in terms of technology development, economic-social-environmental effects. Further 12 similar turbines, in the right-powerhouse are being installed, and 6 additional similar machines in the underground-powerhouse will be purchased soon. Other hydro projects employing similar scale turbines are being developed by the China Yangtze Three Gorge Project Development Cooperation (CTGPC). For example, 18 turbines of 770 MW each for Xiluodu Project and 8 turbines of 750 MW each for Xiangjiaba are to be purchased late this year; 18 turbines of 825 MW each for Baihetan project and 10 units of 700 MW each for Wudongde project are at the feasibility study stage, total about 90 turbines. It is also under consideration to develop 1,000 MW turbine-generator units for hydro schemes. Under such a strategy for hydropower development, these damages, although their impact on the machine operation is

---

[1] A device employed on turbines for the first time. It will be discussed later.

insignificant[2], does catch the great attention from the top management team of CTGPC, and needs to be thoroughly investigated.

Questions immediately arise: (1) Is this a new phenomenon happened particularly to extremely large turbines? (2) Should new technologies be sought & developed for combating this problem? A special meeting was thus held at the Three Gorge site from 12 to 14 March 2006, attended by research engineers, university academics and manufacturer representatives. A few days later (19th March 2006), the author inspected the damages on 11F unit, in particular the damage on the representative No 4 guide vane. As an initial report of the *in situ* inspection, this article is thus also presented to the 1st International Conference on Hydropower Technology & Key Equipment 2006 for promoting further research in this direction. The outcome would benefit not only the power industry but also the advance of scientific knowledge in general.

2. BASIC INFORMATION

The powerhouse is shown by the model in Figure 1, and the specifications of the 11F turbine are as follows:

- Rated power 710 MW
- Max efficiency guaranteed, 96.26%
- Rated head 80.6 m
- Min head 61.0 m
- Max head 113.0 m
- Rated speed 75 rpm
- Run away speed <150 rpm

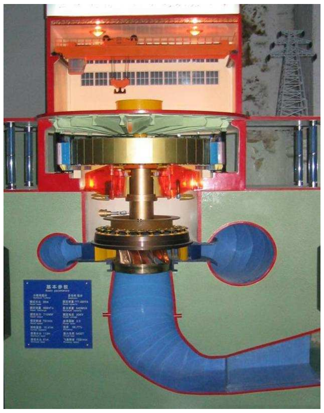

Figure 1 Cross-section of Three Gorge Plant model (Courtesy of Harbin Electric Works)

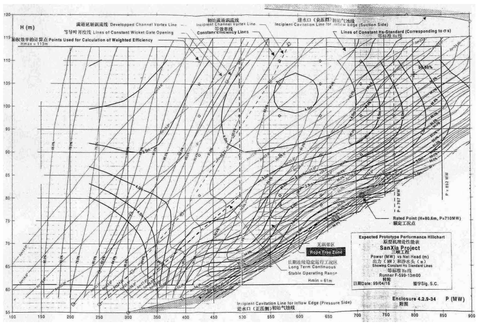

Figure 2 Expected prototype performance hill-chart for 11F by the supplier

The performance curve is shown by . For most times, the 11F unit has been operating under low head conditions (around and below 70 m).

3. DAMAGE OBSERVED

3.1 NO4 GUIDE VANE (11F)

The damage observed on the Number 4 guide vane of 11F turbine is representative for this particular pattern of damage. The guide vane is a positively curved hydrofoil as shown in Figure 3. The turbine has total 24 guide vanes and 24 stay vanes, referring to Figure 4.

---

[2] They do not require an immediate rectification/repairing at this stage because the damage does not affect the safety and effectiveness of operation.

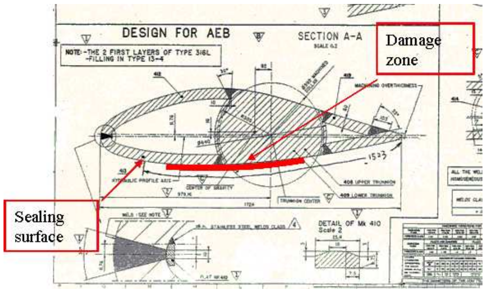

Figure 3 No 4 guide vane

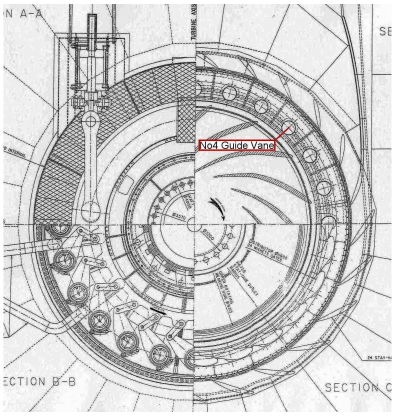

Figure 4 Plan view of 11F turbine

3.2 FEATURES

The damages occur only on the foil's lower surface[3] in the form of horizontal strips, starting from the favorable pressure gradient (FPG) zone extending into adverse pressure gradient (APG) zone as shown by Figure 5. The depth of most damaged area is much less than 1 mm fully covered by corroded rough surface as shown by Figure 8. Heated tail on damaged surface is observed (red-circled in Figure 8), which is another common feature. Figure 9 shows heated area at joints. However, it puzzles that the circled one (in Figure 9) is not similar to others that appear approximately at the main flow direction. This heated feature is also observed on other machines, e.g. photos from 9F are shown by Figure 7 and Figure 9. These damaged strips are approximately in the direction of flow there. Another feature is the wedged head which almost always presents[4]. Typical one is shown in Figure 10.

The damaged strips are distributed in span-wise, showing regularities, referring to Figure 5, with average span-wise spacing, $\lambda^*_{strip}\,(\approx 0.100\ \mathrm{m})$.

4 ANALYSIS AND CONSIDERATIONS

Such damages on the guide vane have not been reported before. In order to facilitate a thorough investigation, based on the information gathered through the *in situ* inspection, a preliminary analysis and considerations are presented herewith.

Among all possible factors, cavitation damage needs to be considered firstly although the observed damage appearance does not comply with conventional cavitation damages often observed on Francis turbines. However, following factors based on the considerations of both metallurgical and fluid dynamic sciences strongly suggest the possible cause of cavitation.

4.1 METALLURGICAL CONSIDERATIONS

4.1.1 HEATED TAIL

---

[3] Here, the lower surface refers to the pressure side of a foil if the angle of attack is positive as conventionally defined in aerofoil aerodynamics.

[4] The heads of No 1 & 18 has been sanded off by the representative of the manufacturer during the *in situ* meeting 12-14 March 2006.

Figure 5 Damages on the lower surface on all guide vanes showing nearly the same pattern

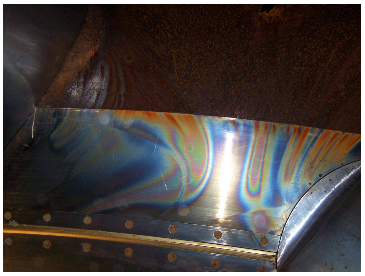

Figure 6 Heated sign on the top surface between guide vanes

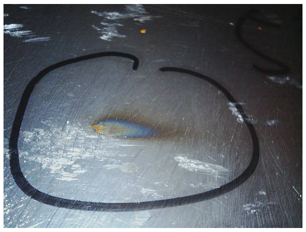

Figure 7 Heated tail on the guide vane (9F)

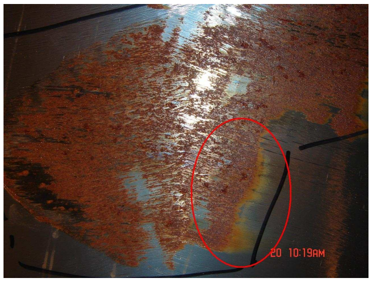

Figure 8 Damaged surface

Figure 9 Heated tails observed on the top ring (9F)

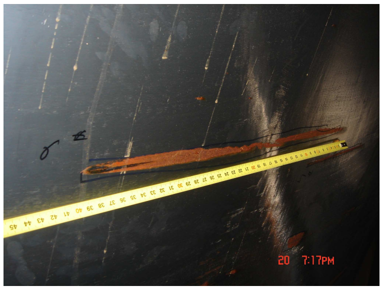

Figure 10 A representative damage-strip showing wedged head

The observed heated (blue and other) colour zone at the tails of the damaged areas suggests that this zone has encountered a temperature of $250^0C - 600^0C$ (termed as 'bluing' in heat-treatment[5]). As far as we know, the only hydrodynamic mechanism involved in Francis turbines that is able to provide/generate temperature at or above this range is cavitation. The experimentally proven temperature that a collapsing single bubble could generate is about $6000^0C - 7000^0C$ [6]. One may argue: 'why the damage compared with those often observed in Francis turbines, in particular those made of low-alloy steels before 1980's, are very different'. The following may provides the answer.

Figure 11 Typical sponge-like erosion pattern caused by a leading-edge cavitation attack (4000 hour operation) [18]

Typical cavitation damage is featured by sponge-like deep erosion, such as shown by Figure 11. Nowadays, materials with better cavitation resistance are used such as the martensitic stainless steel (containing 13% Cr and 4% Ni or 17% Cr and 7% Ni) replacing the low-Mn steel for fabricating machines. The material used for 11F is X3CrNiMo13-4 (EN-1088), which is close or equivalent to *CA6MN* (12.9% Cr, 4% Ni and 0.04% C), a commonly used martensitic stainless for turbine fabrications [20]. Whereas the striking force (i.e. cavitation attack) in this case is relatively weak owing to both the high overall pressure in the guide vane passage and the mechanism of cavitation[7]. The existence of this heated zone itself may also evidence a relative weak cavitation attack on a relatively high cavitation-resistance material. Why? We may put this argument in such a way: heating effect always presents during cavitation attack, but if damage rate is high, the heated portion of material is removed immediately/simultaneously by bubble strikes. Therefore, we can not see the heated zone afterwards. The heated part of material may remain to be seen if the cavitation erosion rate is low. The very low erosion rate (much less than 1 mm over 10,000 hours) of the damage in this case is consistence with the hypothesis proposed here.

4.1.2 CORROSION APPEARANCE

The existence of corrosion on all damaged area combined with the fact of very shallow damage depth (actually touch feeling only) readily tempts one to think that corrosion is the underlying cause responsible for the damage observed as some comments made at the meetings [21]. From the author's opinion, it might be more appropriate to assume the corrosion is a consequence of cavitation damage. The following arguments may provide clues for clearing the cloud over the nature of the corrosion appearance.

The material is a martensitic S S as suggested by its brand which is roughly equivalent[8] to *CA6MN* indicated by '*W*' in the Schaeffler diagram, referring to Figure 12.

It is well-known, for austenite S S, *sensitisation* is a phenomenon of heat effect that causes inter-granular corrosion and is a wide spread problem. The *stainless* character of stainless steels occurs when the concentration of chromium exceeds about 12 wt%. When an austenite S S is exposed to a temperature range between $620^0\ C$ to $676^0\ C$, subject to exposure-time as well as its own composition, the carbon will diffuse towards the grain boundaries where the high concentration of carbon ties up the chromium by forming chromium carbides $M_{23}C_6$ at grain boundaries, which leaves a zone of chromium depletion (below 12%) in the immediate area around the

---

[5] A simple heat-treatment method that coats steels with a thin, even film of coloured oxide from bluish-black to purple brown shade, obtained by exposure to an atmosphere of dry steam or air, at certain temperature subject to the material as well as the colour. A typical case of coating sheets with a thin, even film of bluish-black oxide is obtained by exposure to an atmosphere of dry steam or air, at a temperature of about 1000^0F (538^0C) done during box-annealing [29].

[6] Comparison with black body's spectra gives the temperature values, subject to bubble size, content and external pressure fields. Collapse of multi-bubble cloud can generate even higher temperature owing to bubble-bubble interaction.

[7] The mechanism will be addressed later.

[8] Accurate and detail analysis of chemical composition and metallurgical structures needs to be done.

grain boundary making this area less corrosion resistant than the bulk material and resulting in inter-granular corrosion. Such typical corrosion (on 304) is shown in Figure 13. The mechanism of sensitisation is conceptually shown by Figure 14.

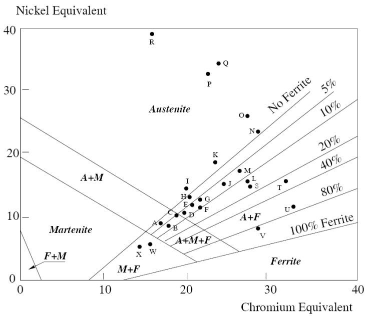

Figure 12 Schaeffler diagram [25]

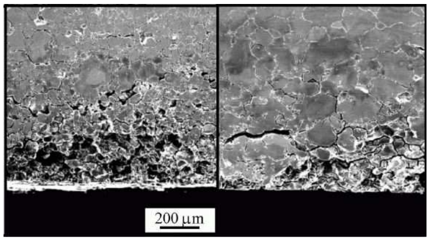

Figure 13 Grain decohesion due to intergranular corrosion [28]

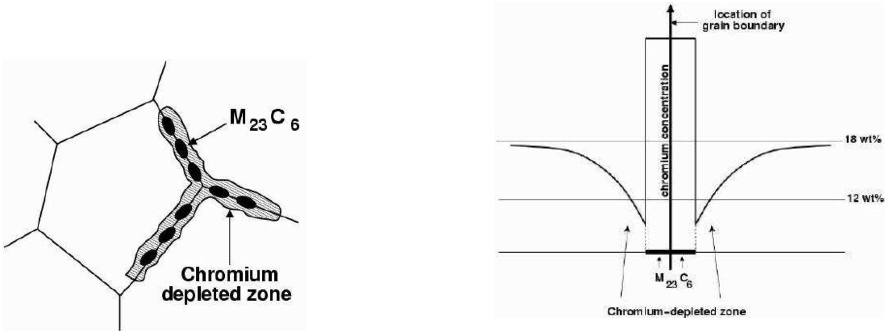

(a) (b)

Figure 14 Conceptual sketch of sensitisation. (a) Chromium depleted zone susceptible to inter-granular corrosion (b) Chromium distribution across grain boundary [30].

Most publications concerning inter-granular corrosion refer to austenitic steels. Study of inter-granular corrosion in martensitic stainless steels is not in current technical literature. Does that mean sensitization is irrelevant or insignificant to martensitic stainless steels? Actually, inter-granular corrosion is also a potential problem to martensitic S S because it is a Fe-Cr-C system and always used in tempered condition[9], in which carbides are precipitated. Recent investigations [e.g. 2], show a trend that the maximum susceptibility to inter-granular corrosion was observed in the condition tempered at $500^{0}C$ to $550^{0}C$, and a sensitized structure was detected. For lower tempering temperatures, it was less sensitized, or not at all, and for higher tempering temperatures, it was also less sensitized. A typical case (UNS S41000) is shown in Figure 15 ($550^{0}C$), and the

---

[9] Martensitic S S is often used for fabrication. Both strength and toughness are requested which is achieved through temper treatment. It is known: (1) at 350°C, higher strength and moderate toughness (2) at 650°C, moderate strength and high toughness (3) avoid 500°C, temper embrittlement (i.e. sensitisation) and minimum toughness.

characteristic value variations with temperature (for two hours) is shown in Figure 16. A zone of high sensitization-susceptibility is indicated clearly for temperature ranging from $500^0 C$ to $600^0 C$.

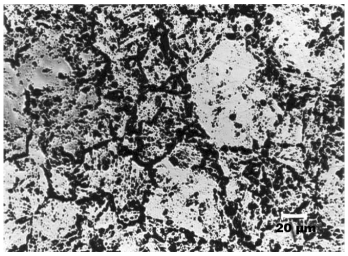

Figure 15 Optical micrographs of UNS S41000 steel specimens after oxalic acid etch test: tempered at $550^0 C$ [2]

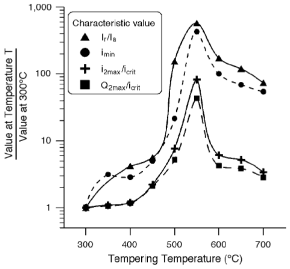

Figure 16 Comparison among electrochemical tests to discriminate degrees of sensitization for different tempering temperatures. Characteristic values are i_r / i_a for the DL-EPR, $i_{\min}$ for the potentiostatic test, and $i_{2\max} / i_{crit}$ and $Q_{2\max} / i_{crit}$ for the potentiokinetic polarization. To make different tests comparable, the ratio was plotted between the characteristic value for the material tempered at different temperatures and the same for the material tempered at $300^0 C$ [2].

Based on the analysis above for the heated sign left on the tail of damaged area, the blue colour (plus other spectra of colors) strongly suggests a similar heat treatment at the temperature range of $500^0 C$ to $600^0 C$ that creates an ideal environment for sensitization, leading to inter-granular corrosion. This explains why corrosion appearance is discovered on the damaged area of this martensitic stainless steel after cavitation attack.

4.2 FLUID DYNAMICS CONSIDERATION

The damage pattern does not suggest a large structure of cavitating flow-structure that directly strikes and causes the damage such as those shown by Figure 11, whereas the wedged head of damage strips gives us a hint: are there any links with the turbulent spots generated during boundary layer transition to turbulence that is also featured by wedge head?

Through the inspection *in situ*, a conjecture has been put forward by the author that this is a non-typical turbine cavitation, its inception and corresponding damages are relating to boundary layer's streaks and most likely induced by turbulent spots during the boundary layer transition process [21 & 22]. In order to understand this, it is essential to see what conditions are required to enable the nuclei in the boundary-layer to cavitate and how the boundary-layer can provide such conditions through its transition process.

4.2.1 CAVITATION INCEPTION

Cavitation inception is closely related with and strongly influenced by boundary layer transition. The main points can be summarized as follows [19].

For cavitation in the boundary shear layer, the statistical properties of bubbles are dominated by the pressure fluctuation field in terms of their intensity and duration. Therefore, the distribution of the turbulence level, which varies across the boundary layer, alters the statistical characteristics of the micro-bubbles' inception performance across the boundary layer. This phenomenon was firstly demonstrated by Daily & Johnson [9]. This relation indicates that the lowest mean pressure across the boundary layer is the location where the turbulence level is highest since (referring to Figure 17)

$$\overline{p} + \rho \overline{v'^2} = p_1(x)$$

where $p_1(x)$: pressure in the free flow region beyond the boundary layer where $\overline{v'^2}$ is negligible

$\overline{p}$: mean pressure

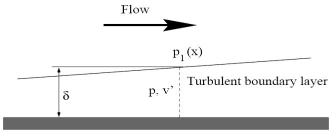

Figure 18 Conceptual sketch of (turbulent) boundary layer

It is obvious that bubbles at this particular location have the highest probability to cavitate owing to the minimum value of mean pressure and the maximum value of instant pressure drop.

The influences of magnitude and time scale of turbulence on cavitation inception were also demonstrated by many other studies on inception scale effect. For example as early as 1981, Arakari & Acosta [4] already emphasize the importance of time scale by postulating that the turbulent fluctuations may actually stall the local flow near the wall, leading to a brief period of separation or a turbulent burst with reverse flow. Then the nuclei within these regions may be exposed to a low pressure longer than would otherwise be the case, thereby promoting the growth of micro-bubbles. This is supported by their experiment that the frequency of the most unstable Tollmien-Schlichting wave in the laminar boundary layer just prior to transition is about 5 kHz equal to a reference time period of 0.2 msec for growth, which is about the same order as the bubble life-time (0.1 msec) observed in their experiments. The early work by Huang [12] also found that the inception is correlated with the spatial amplification ratio A through the mechanism of laminar to turbulent transition or laminar separation. For the tunnel with low level of free-stream turbulence, the inception is well correlated with the computed amplification ratio value of $A = e^{11}$; and, for higher levels of free-stream turbulence, it takes place in a region where the value of A is less than e^{11}, for say e^9 or even e^7.

As early as 1979, attempt by using the Kolmogorov theory for homogeneous and isotropic turbulence to relate the properties of the temporal pressure field to cavitation inception for both free turbulent shear flow and fully developed boundary layer flow has been made. For fully developed boundary layer flow, Arndt & George [5] suggested that if

$$\left(\frac{u_*^2}{\nu}\right) T_B < 1 \quad \text{for smooth wall;}$$

$$\left(\frac{u_*^2}{h}\right) T_B < 1 \quad \text{for rough wall,}$$

the nuclei in the flow will have enough time to respond to the entire spectrum. Otherwise only a fraction below the frequency of T_B is sensed by the micro-bubbles[10].

Therefore, for the nuclei to cavitate, long enough negative pressure drop generated by flow structures is essential.

4.2.2 FREE STREAM TURBULENCE & B L TRANSITION

Despite of studies over decades, the origins of turbulent flow and transition from laminar to turbulent flow still remains an unsolved challenge for fluid mechanics. Currently, even for flows over a flat plate, no mathematical model can precisely predict the transition Reynolds number because of variety of influences, such as free-stream turbulence, surface roughness, which are still not fully understood yet. Currently, owing to the availability of linear stability methods and the knowledge of breakdown mechanism being initial condition dependent, studies are aiming at understanding the source of initial disturbances rather than the details of the

---

[10] For turbulent boundary layer flow, the highest frequency in the flow is $\left(u_*^2/\nu\right)$ for smooth wall and $\left(u_*^2/h\right)$ for rough wall. Thus if the bubble frequency T_B is higher than the highest frequency, the entire spectrum may contribute to bubble growth.

later stages of transition [27]. Very recently, the discovery of Soliton-like Coherent Structure (SCS) by Lee [15 and 16] gives clearer picture of the low-speed streak formation and its breakdown, which helps to clarify the complex burst phenomena. As pointed out by Lee and Chen [17][11]: there are two different kinds of flow structures which have been referred to as stream-wise vortices by other researchers. One is the real stream-wise vortex. The other is the long streak containing several SCS, often referred as solitary quasi-stream-wise vortex. A long streak containing several SCS appears in the very near-wall region. The middle layer has two real stream-wise vortices which are the relatively long quasi-stream-wise vortices (often counter-rotating pairs). The interaction between the secondary closed vortex and the Λ-vortex produces the chain of ring vortices (i.e. high frequency vortices), leading to breakdown & turbulent spots. Figure 19 shows the evolutions from SCS to a long streak and its breakdown.

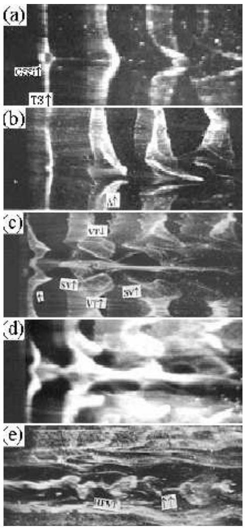

Figure 19 (a) T–S wave and CSS. The hydrogen bubble wire was at x = 250mm and y = 0.75mm; (b) The Λ-vortex structure. The wire was positioned at x = 300mm and y = 0.75mm; (c) Development of the Λ-vortex and the long streak. The wire was at x = 350mm and y = 0.75mm; (d) The long streak is composed of several CS-solitons and the wire was at x = 450mm and y = 0.5mm; (e) Breakdown of a long streak. The wire was at x = 550mm and y = 0.75 mm [17].

However, for turbines, owing to its complexities in geometry and off-design operation, much less is known [26]. For hydro turbines, the interplay of B L transition with cavitation inception is important but little study has been done. Despite of these difficulties, it is still possible to understand the phenomenon based on the knowledge gained from flat plate cases.

For 3D B L flows over (hydro) foil, cross-flow instability may dominate the breakdown while T-S waves act as generators of fundamental low-frequency secondary modes, but are neither important for their growth nor for breakdown [32]. For the problem on our hands, the damage pattern on guide vane gives us a clue that it is virtually a 2D flow. The resulting perturbed flows are span-wise-dependent but essentially unidirectional, i. e. the transverse velocity components are much smaller than the stream-wise component. The instability of such transversely sheared flows appears to be related to various aspects of the transition process, such as secondary instabilities and by-pass transition. Many factors [35] can cause three-dimensional steady/unsteady distortions in the form of stream-wise or longitudinal vortices. These include small steady or unsteady perturbations superimposed on the oncoming flow, imperfections at the leading edge[12], cross-flow instability, and Görtler vortices induced by surface curvature, as well as certain excitation devices[13]. Distortion of this kind also arises due to the nonlinear interaction between pairs of Tollmien-Schlichting waves.

Free-stream turbulence initiates three distinct motions within the boundary layer, as summarised by Saric et al [27]. The first motion is a sustained, streaky ($z \approx 2\delta$), high amplitude ($|u'| \approx 5-10\% U_\infty$) motion, which is probably due to stretching of the ingested free-stream vorticity and the growth of transient modes, i.e. the Klebanoff mode. The second is an outer-layer oscillation at T-S frequencies that grows weakly in the stream direction. The third is the usual T-S mode, which exhibits higher growth rates.

Currently we have very limited understanding about the instability of Klabenoff mode and its role in the transition owing to the random nature of both the free-stream disturbances and the Klebanoff motion. Most studies so far investigate steady distortions, induced in a controlled manner through the receptivity at leading

---

[11] For more details, please see the forthcoming publication by Lee & Chen [17].

[12] And the sealing surface in our case.

[13] The guide plate may serve well as an excitation device. This will be discussed later.

edge only[14]. The maximum growth of this K-mode distortion is a function of Reynolds number and wave number, e.g. as demonstrated by Anderson et al [3]. In Figure 20(I), $\bar{\beta}$ is span-wise wave number,

$$\bar{\beta} = \beta^{*} \nu / U = \beta / \sqrt{\mathrm{Re}}$$

with β^{*} is the dimensional span-wise wave number; β is the non-dimensional span-wise wave number valued as $\beta = 0.45$ for maximum transient growth.

The mechanism of the downstream response to upstream disturbance is visualized by Figure 20(II). The calculated initial disturbance at $x_0 = 0$ is outside the boundary layer, while its downstream response is inside the boundary layer. Thus, this numerical simulation demonstrate well the receptivity at the leading edge: the disturbances at the leading edge that cause the largest growth of stream-wise streaks inside the boundary layer are vortices aligned in the stream-wise direction outside the boundary layer.

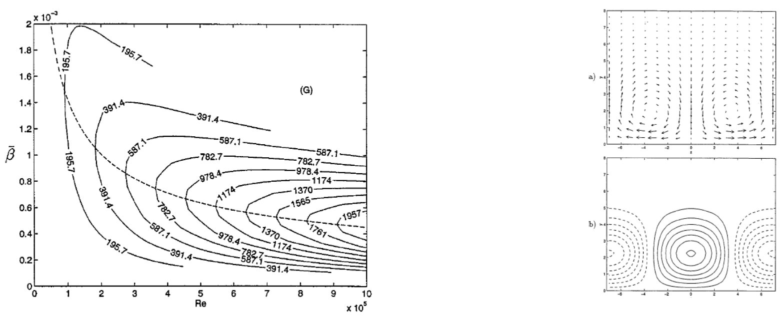

(I) (II)

Figure 20 (I) Contour plot of maximum transient growth vs. $\bar{\beta}$ and Reynolds number. The dashed line describes $\bar{\beta}$ for which the maximum transient growth occurs given a specific Reynolds number. Here $x_0 = 0$ [3]. (II) (a) Velocity vectors in the z – y plane of the optimal disturbance at $x = x_0$. Here $x_0 = 0$ and $\beta = 0.45$. The *u* component is zero. (b) Contours of constant stream-wise velocity representing the downstream response at $x = x_f = 1$ corresponding to the optimal disturbance shown in (I). The *v* and *w* components are zero. Here, the solid lines represent positive values and the dashed lines represent negative values [3].

As early as 1979, Gates & Acosta [11] have already shown that free-stream turbulence is an important factor for inception scaling; and that the mechanism through which this factor influences inception is the structural alteration of the boundary layer in terms of its separation and/or transition[15]. This is crucial for extremely large turbines, the difference of Reynolds number (based on main flow parameter, reflecting the status of free stream) between model and prototype is in the order of 10^2, which represents a significant difference on turbulence level[16], consequently its influence on cavitation inception.

The K-mode involvement (responding to the free-stream turbulence) should be further considered owing to following reasons.

Firstly, the guide plate increased free-stream turbulence is a primary concern in the sense of receptivity and the transient growth of K-mode instability, which may bypass the primary OSE[17] mode and lead to early and random breakdown/turbulent spot although the flow in the first half of guide-vane passage is a highly accelerating flow[18], i.e. with strong favourable pressure gradient, which would have a prolong laminar B L until transition if the level of free-stream turbulence was low.

---

[14] In reality, there is a continuous receptivity process along the stream-wise extent of the boundary layer, as in flow around the guide-vane.

[15] See, e.g. § 2.4 'Cavitation Nucleation and Inception' in *Cavitation of Hydraulic Machinery*, ICP, London.

[16] This will be discussed later.

[17] Orr-Summerfeld Equation

Secondly, the turbulences in the wake of stay vane is likely to possess span-wise structure (say span-wise distributed stream-wise vortices) comparable with the span-wise variation of observed damage strips, and thus the high receptivity occurs only associated with these structures, causing K-mode transient, bypass transition and breakdown to turbulence in such a pattern of strips.

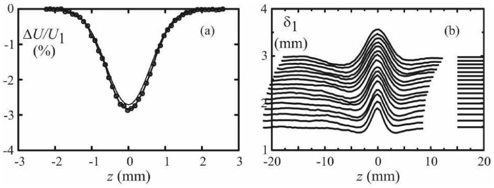

Figure 20 (a) Wake profile 63.5 mm upstream of leading edge. Z-relative to wire centreline. (b) Stream-wise growth of span-wise variation of displacement thickness, δ_1. Z-relative to the peak δ_1 values. Lines in range 15 < z < 20 are Blasius values, i.e. $\delta_1 = 1.7208\left(\nu x / U_1\right)^{1/2}$ [33].

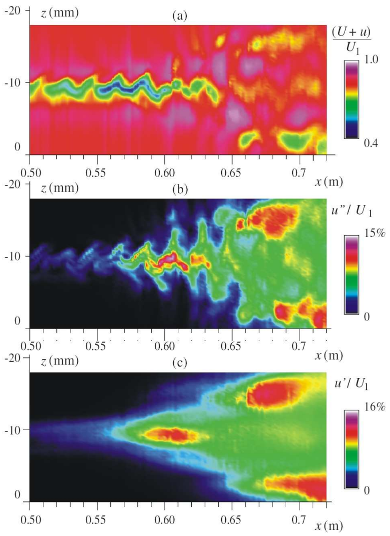

Figure 21 True spatial contours in plane, y=2mm (a) $\left(\overline{U} + u_\phi\right) / U_1$. (b) u''_ϕ / U_1. (c) Broadband unsteadiness, $\overline{u'} / U_1$ [33].

	Zero pressure gradient	Mild pressure gradient	Strong pressure gradient
SSLC	10.3^0	9.4^0	7.8^0
TSLC	5.5^0	4.1^0	2.5^0

Table 1 half angles of wedge spreading for zero, mild and strong favourable pressure gradients for SSLC and TSLC [8]

Figure 22 SSLC results for the turbulent wedge under zero, mild and strong (favourite) pressure gradients respectively [8] .

Thirdly, the wedged head of damage strips highly resembles the turbulent spots caused by such a streak (K-mode) transient growth and breakdown in a Blasius B L, which leads to a turbulent wedge. As an example, the work by Watmuff [] is worth mentioning here, which demonstrates the evolution of a turbulent wedge from

---

[18] Rough estimation shows that the average velocity increases from 12 m/s at the entrance to 25 m/s at the mid-chord, with a acceleration of $\left.\frac{dV}{dS}\right|_{average}$ 18 sec^{-1} .

stream-wise streak. In his study, a narrow low-speed streak (i.e. region of elevated thickness) is deliberately introduced into the Blasius boundary layer as a result of the interaction of a laminar wake with the leading edge of the flat plate. The wake is generated by stretching a fine wire across the full extent of the test section and it is aligned perpendicular to the free-stream and to the leading edge. The wire has a diameter of d=50.8 mm, located 184 mm upstream of the leading edge. Stream-wise development of the span-wise variation of displacement thickness resulting from interaction of the wake (referring to (a)) with the leading edge is shown in (b) for 16 stream-wise positions, ranging from x=0.3 to 1.8 m. The results clearly demonstrate the narrow region of elevated thickness, i.e. the low-speed streak. The final stages of growth and the ultimate breakdown of the streak are shown in (a-c). The breakdown on the centre-line and the formation of two regions of highly unsteady flow on either side of the streak are most clearly evident in the contours of the broadband unsteadiness shown in (c). It is evident that streak is responsible for introducing a new pair of streaks on either side via some instability mechanism, causing span-wise growth of the wedge since a span-wise succession of new streaks is observed in the early stages of its development.

Here, $\overline{U} + u_\phi$ is the total phase averaged stream-wise velocity; u' is the background (broad band) unsteadiness; and, u'' is the phase averaged unsteadiness.

The wedge-shaped turbulent spot can also be visualized by using both shear sensitive liquid crystal (SSLC) and temperature sensitive liquid crystals (TSLC). The results [8] show the dependency of wedge spreading angle on the level of flow acceleration, referring to Table 1 and Figure 21.

Lastly, as demonstrated by Matsubara *et al.* (2000) [23] experimentally that the growth of near-wall streaks is a key phenomenon triggering the bypass transition leading to breakdown & turbulent spots. The mechanism of breakdown postulated by Lee [15 & 16] suggests that the generation of the high frequency vortices, i.e. the chain of ring vortices is resulting from the interaction of the secondly closed vortex with the Λ-vortex. For our case, these vortices surely will create an favorite environment for nuclei to grow.

5. DISCUSSION

All these considerations above make us to think: if for this case (particular large turbines) the scale effect makes it happen[19] that the *turbulent spots* just generated at a right area where flow has a highest susceptivity to cavitation inception[20] and thus trigger the *cavitation-inception* there*,* In other words, both *turbulent spots* and *inception points* concise for prototype.

5.1 MODEL-PROTOTYPE SIMILARITY

5.1.1 FREE STREAM TURBULENCE

The free-stream turbulence level of prototype is much higher than that of model turbine, which makes the prototype, in particular for large turbines, more susceptible to the formation of low-speed streak and the transitional breakdown through the receptivity mechanism. For the Three Gorge turbines, if the similarity of free stream turbulence were required, by assuming a prototype-model scale of 28, the Reynolds number equality would have required

that is,

$$\frac{H_m}{H_p} = \left(\frac{D_{1,p}}{D_{1,m}} \right)^2 ,$$

$$\frac{H_m}{H_p} \approx 784, \ \text{ i.e. } \ H_m \approx 47,824 \text{💻} 88,592 \, m$$

In reality, this is impossible, and consequently the constraint of test rig makes us to use much smaller Reynolds number for models. For the Three Gorge turbines, the prototype's Reynolds number is

---

[19] On model tests, no cavitation observed within the allowable operating zone.

[20] At low head operating condition, the inlet circulation reduces which in turn makes the lower surface of guide vane become more susceptible for cavitation that the upper surface.

$\mathrm{Re}_{,p} \approx 4.6\times 10^{7}$ at $Q_{opt} = 718\, m^{3}/s$ approximately , while for models, it might be $10^{2} : 10^{3}$ smaller[21]. This implies that the free-stream turbulence level is much higher for prototype.

For the turbines in the left-plant, the flow in the guide-vane passages indeed is subject to a high level of free-stream turbulence owing to the reason below. For this turbine design, a guide plate is provided in the spiral case prior the entrance of stay-vane passage shown in Figure 23. Obviously, the designer intended to reduce the size of spiral case without sacrifice of cross-section area. However, the premature damage (a piece torn off) of the guide plate and subsequent severe pressure-fluctuation and machine-vibration gave us a clear clue: this device might have caused unusual free-stream disturbances in the oncoming flow (i.e. the wake flow of stay-vane) to the guide vane. Will these disturbances cause particular distortion in the boundary layer of guide vane? Researchers have demonstrated a type of span-wise distortion (modulation) induced by various free-stream disturbances. For example, it has been shown that small low-frequency three-dimensional perturbations in the free stream can produce significant distortion within the boundary layer, leading to alternating span-wise thickening and thinning [10]. Steady disturbances (e.g. artificial roughness, vortices etc) can also cause a similar type of span-wise modulation [e.g. 6]. And these distortions are all in the form of elongated streaks now named as *Klebanoff* mode [13, 34 and 14].

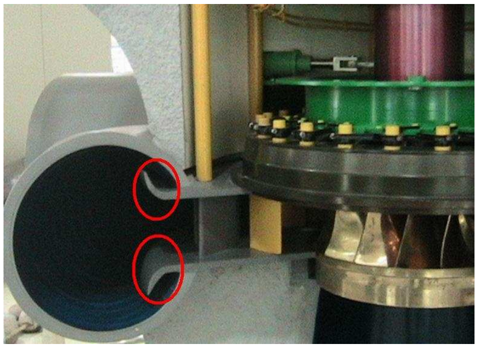

Figure 23 Guide-plate (circled) shown on the model of turbine

5.1.2 BOUNDARY-LAYER SIMILARITY

Boundary-layer similarity not only requires the similar free-stream conditions but also the equality of the boundary-layer based Reynolds number,

$$\mathrm{Re}_{l} = \frac{L\ U}{\nu}$$

Owing to the equality of Strouhal number (i.e. $n_1{}'$), this leads to

$$\frac{(\mathrm{Re}_{l})_{m}}{(\mathrm{Re}_{l})_{p}} = \left(\frac{D_{1,\,m}}{D_{1,\,p}}\right)\left(\frac{H_{m}}{H_{p}}\right)^{1/2} = 1$$

That is, for our case (i.e. the prototype-model ratio of 28) the boundary-layer similarity also requires

$$H_{m} = 784\, H_{p}$$

In reality, as mentioned before, it is impossible to use such high head for model tests. And this constraint condition makes the ratio of two boundary-layer based Reynolds numbers far away from unity, resulting in the range of

$$\frac{(\mathrm{Re}_{l})_{m}}{(\mathrm{Re}_{l})_{p}} = \frac{1}{28}\left(\frac{H_{m}}{H_{p}}\right)^{\frac{1}{2}}$$

Therefore, it is absolutely no boundary-layer similarity for model and prototype in respect of their boundary-layer dynamics, making the prototype much more susceptible to turbulent transition.

---

[21] The Reynolds number for prototype is obtained from Prof Wu Yu-Lin of Tsinghua University and for models it is estimated based on the current conditions of turbine test rigs around the world.

These two factors above explain well the fact that no cavitation observed during model tests does not guarantee the Three Gorge turbines free from cavitation attack.

5.2 ESTIMATION OF LAMINAR STREAKS AND TURBULENT SPOTS

The span-wise wave-length (spacing) of laminar streaks or Klebanoff wave, λ^*, can be estimated[22] as

$$\lambda^* = 10\,\delta^*$$

Here, δ^* is the displacement thickness,

$$\delta^* = \frac{1.7208\,L}{\sqrt{\mathrm{Re}_{,l}}}$$

From a typical damage strip observed, say $L = 0.550$ m, we have $\mathrm{Re}_{,l} = 5.2\times 10^6$ (based on $U_\infty \approx 12.4$ m/s), and $\delta^* = 0.43\ \ 10^{-3}$ m. This gives a span-wise wave length

$$\lambda^* \approx 4.3\times 10^{-3}\ \mathrm{m}$$

The transition region is characterised by a random appearance of turbulent spots, referring to Figure 24. Assuming a spot generated from 20-30 such streaks, the turbulent spot spacing λ^*_{spot} will be

$$\lambda^*_{spot} \approx 86\times 10^{-3} \sim 129\times 10^{-3}\ \mathrm{m}$$

It is approximately equivalent to the observed strip spacing $\lambda^*_{strip}(\approx 0.100\ \mathrm{m})$. This again strongly supports the conjecture that the damaged strips are caused by cavitation spots that incepts from turbulent spots.

Surprisingly, the features of turbulent-spot above are all supportive to the hypothesis that the cavitation inception points might coincide with the turbulent spots, or in other words, cavitation incepts from these turbulent points. Thus, a *dynamics process* follows: once the first cavitation damage spot is created at the turbulent spot, it will serves well as a roughness spot create a subsequent damage immediately downstream. This dynamic process progresses stream-wise, resulting in such a horizontal damage strip with a wedged head and heated tail. These span-wise distributed stream-wise damage strips thus become dominant pattern on the guide vane. This may provide a reasonable route for searching more detailed explanation and answer to the problem at hand.

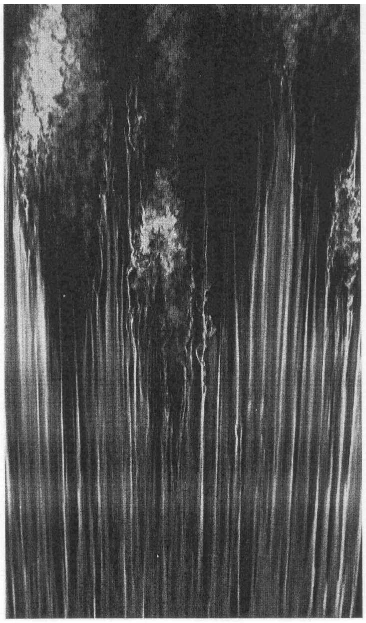

Figure 24 Streak structure observed through smoke visualisation in a laminar boundary layer subject to 2.2 % free-stream turbulence [1]

6. REMARKS

As this problem has just been discovered, apart from *in situ* inspection, no further studies have been conducted yet. Therefore, it is only a very preliminary report servicing as guidelines for further investigation and research proposal preparation. However, it does provide strong evidence about the cause of this type of damage that has never reported before.

---

[22] The results obtained from flat plate case, i.e. for pressure gradient $K = 0$, are used, where K is defined as $K = \frac{\nu}{U^2}\frac{dU}{dx}$. For the turbine guide vane, the average value at inlet (FPG) is about $K = 0.148\ \ 10^{-6}$.

1. Flow analysis of the oncoming flow influenced by the guide plate in terms of flow structure(s) and turbulence level variation is essential. The study should employ the fluid-structure interaction approach. The shape of the guide plate (thin and plateful geometry without stiffener owing to flow requirements) readily induces various vibrating modes including extremely low-frequency ones. These low-frequency modes are particular concern because their influences on the growth of boundary layer streaks as mentioned before. The studies may performed numerically first and then followed by experiment study on prototype and model turbines.
2. The information obtained from above flow analysis should facilitate the boundary layer studies[23]. It will look for possible streak formation, receptivity and transition mechanism (including the interaction with T-S waves). It is particular interesting to see if the stream-wise position and the span-wise variation of the breakdown (in particular, the turbulent spots) under such strong influences of the free-stream (flow-structures and turbulence level) agree with the observed pattern of strips. The study may be carried out firstly on flat-plate with added pressure gradients similar to those on the guide vane either numerically or experimentally[24]. As the most interesting issue we want to know is the spatial growth of streaks, a DNS approach in space domain is strongly suggested for numerical study. With the information obtained from flat-plate, we may able to predict the trends about the streak formation, growth, interaction with T-S waves and breakdown on hydrofoil. And, observation on prototype can be designed and carried more effectively and predictably.
3. The possibility that cavitation inception might occur right at the turbulent spots should be verified through experiments by testing on model foil and monitoring on the guide vane of prototype. Various approaches can be employed. For example, for prototype, SSLC mentioned before combined with high-speed photography through endoscope is a good choice.
4. The material undergoing this type of cavitation attack should be mimicked through laboratory study in order to understand the heating phenomenon/mechanism associated with this type of damage. It may uncover knowledge not known yet to us. Laboratory study using facilities such as cavitation tunnel or rotating device should be supported by metallurgical and chemical analyses.
5. Developments of novel turbine design/manufacture ideas are encouraged in order to respond to the challenges to extremely large turbines. For example, novel spiral case that has smaller size[25] and better flow conditions should be sought to replace the use of guide plate, which obviously disturbances flow significantly, resulting in high turbulence level in free-stream and consequent problems[26].
6. The B L behavior, such as transition length and scaling laws etc., should be investigated thoroughly. This is particularly important for huge turbines. The size of their components[27] and the high free-stream velocity[28] make the critical Reynolds number[29],

$$\mathrm{Re}_{crit} = \frac{Ux_{crit}}{\nu},$$

   to be reached in the FPG zone instead of APG zone, resulting in more susceptibility to cavitation inception compared with smaller turbines. Therefore, for large turbines, while scaling cavitation data from model to

---

[23] The sealing surface on the guide vane serves as a profile discontinuity which could be another source from generating boundary layer flow distortion. This needs to be considered in the analysis too. This is particularly true for this case because the sealing surface was machined on a bended stainless steel plate, very likely leaving the edge highly wavy pattern (not as expected straight lined edge).

[24] On scaled down model.

[25] As mentioned before, for high and medium specific speed turbine-generator units, spiral case is often the crucial component that determines the overall size of plant. Therefore, reduction of spiral case has a significant impact to the hydro scheme's economic feasibility. This is why manufacturers often take high risks to reduce the size of spiral case in order to win the bidding. No doubt, the idea of using guide plate, which has already caused a break down event, has to be justified technically and economically. In the March of 2006, the author has made a suggestion to the M & E department of CTGPC about the feasibilities of employing oval cross-section spiral case for the size reduction.

[26] The 3-D damage on the fillet of stay-vane immediately down stream of the guide-plate might be well explained by the disturbances introduced by the guide plate.

[27] Such as the chord lengths of both the stay vane and the guide vane, which are well over one metre.

[28] In the order of 20-30 m/sec.

[29] $3\times10^5 \sim 3\times10^6$ for flat plate at zero angle of attack, subject to free-stream turbulence level.

$$\mathrm{Re}_{crit} = \frac{Ux_{crit}}{\nu},$$

to be reached in the FPG zone instead of APG zone, resulting in more susceptibility to cavitation inception compared with smaller turbines. Therefore, for large turbines, while scaling cavitation data from model to prototype, the scaling effect due to the boundary-layer property difference must be investigated thoroughly and considered properly. Currently our knowledge about the transition length in turbines is fairly poor compared with that of flat plate B L case. For gas turbines, a correlation[30] is found through experiments. That is, the Reynolds number Re_{lT} calculated with the transition length l_T^* is a linear function of $\mathrm{Re}_{\theta T}^{5/4}$, where $\mathrm{Re}_{\theta T}$ designates the momentum thickness Reynolds number at the end of transition [e.g. 26]. But for hydraulic turbines, little work has been done yet neither theoretically nor experimentally.

7. The damage occurred on the turbines presents no urgent need for remedy action, and turbines can be put back into operation as usual. With the increase of reservoir water-level in the coming autumn, the operating head will gradually move into the optimum head zone and it is anticipated that the damage will also reduce or even disappear[31]. However, a continuous and comprehensive monitoring, recording and accumulating detail data about the machine operation is essential to the understanding of the phenomenon and the control of machine status.
8. The study on these fundamental issues will serve as a sound base for developing next generation of huge turbines (e.g. 1000 MW unit). An effort by multi-disciplinary team at international level is essential.

ACKNOWLEDGMENTS

The author would like to express his sincere thanks to the EPSRC's Warwick-IMRC for their long term financial support (R.ESCM.9001 and R.ESCM9004) on turbine technology and cavitation; and to the CTGPC for their financial & technical support during his visit to the Three Gorge Station from 19th to 20th of March 2006. Thanks also go to Prof Dai Jiang, the Deputy Director of Mech. & Elec. Division of CTGPC and Professor K Sen, the Indian Institute of Technology, New Delhi, for valuable discussions.

REFERENCES

1. Alfredsson P H and Matsubara M, 2000, 'Free-stream Turbulence, Streaky Structures and Transition in Boundary Layer Flows', Fluids 2000 Conference and Exhibit, Denver, CO, USA, 19-22 June 2000.
2. Alonso-Falleiros N, Magri M and Falleiros I G S, 1999, 'Intergranular Corrosion in a Martensitic Stainless Steel Detected by Electrochemical Tests', Corrosion, Vol55, No8.
3. Andersson P, Berggren M and Henningson D, 1999, 'Optimal disturbances and bypass transition in boundary layers', *Physics of Fluids*, 11(1), January 1999
4. Arakeri V H and Acosta A, 1981, 'Viscous Effects in the Inception of Cavitation', ASME J. Fluid Eng. 103, pp280-287.
5. Arndt R E A and George W K, 1979,'Pressure Fields and Cavitation in Turbulent Shear Flows', 12th Symp. Naval Hydrodynamics, Washington D. C., pp327-339.
6. Bradshaw P, 1965, 'The effect of wind-tunnel screens on nominally two-dimensional boundary layers', *J. Fluid Mech*. 22, 679-687.
7. Brandt L, Schlatter P and Henningson D., 2004, 'Transition in boundary layers subject to free-stream turbulence', *J. Fluid Mech.* (2004), vol. 517, pp. 167–198
8. Chong T, Zhong S and Hodson H, 2005, 'Visulization of Turbulent Wedges under Favourable Pressure Gradients using Shear Sensitive and Temperature-sensitive Liquid Crystals'.
9. Daily J W and Johnson V E, 1956, 'Turbulence and Boundary-Layer Effects on Cavitation Inception From Gas Nuclei', Transactions ASME , 78, pp1695-1706.
10. Dryden H L, 1936, 'Air flow in the boundary layer near a plate', *NACA Report* 562.
11. Gates E M and Acosta A, 1979, 'Some Effects of Several Freestream Factors on Cavitation Inception of Axisymmetric Bodies', 12th Symp. Naval Hydrodynamics, Washinfton D. C. pp86-112.
12. Huang T T, 1981, 'Cavitation Inception Observations on Six Axisymmetric Headforms', ASME J. Fluid Eng. 103, pp273-279.
13. Kendall, J. M. 1985 Experimental study of disturbances produced in pre-transitional laminar boundary layer by weak free stream turbulence. AIAA Paper 85-1695.
14. Klebanoff, P. S. 1971 'Effect of free-stream turbulence on a laminar boundary layer', *Bulletin. Am. Phys. Soc*. 16.

---

[30] Precisely the same correlation stems from processing experimental data for both smooth and rough surfaces.

[31] The increase of head will increase the inlet circulation, shifting the angle of attack from negative back to optimum value and increasing the pressure on the lower surface of guide vanes.

15. Lee C. B., ‘New feathers of CS-solitons and the formation of vortices’, *Phys. Lett*. A 247 (1998) 397–402.
16 Lee C. B., ‘Possible universal transitional scenario in a flat plate boundary layer: measurement and visualization’, *Phys. Rev*. E 62 (2000) 3659–3670.
17. Lee C B and Chen S Y, 2006, §2 ‘Dynamics of Transitional Boundary Layer’ in *Transition and Turbulent Control* (Editor Lai Fun), SPI-B320 (in press).
18. Li S C, 2000 §6.2 ‘Cavitation Damage in Turbines’, in *Cavitation of Hydraulic Machinery*, ICP, London
19. Li S C, 2000 §3.7.4 ‘Bubble-Flow Field Interaction’ in *Cavitation of Hydraulic Machinery*, ICP, London.
20. Li S C, 2000 §6.5 ‘High Resistance Materials’ in *Cavitation of Hydraulic Machinery*, ICP, London.
21. Li S C, 2006 ‘Cavitation Damage: Three Gorge Turbines (Phenomenon, Implication & Unknowns…)’, presentations at the Three gorge Power station (19 March 2006), the Beijing University (28 March 2006) and the National Research Institute of Hydro Power (29 March 2006)
22. Li S C, 2006, ‘Guide Vane Surface Damage to Three Gorge Turbines’, WIMRC FORUM06, 3rd July 2006, Warwick University, Coventry, UK
23. Matsubara *et al.,*2000, in Proc IUTAM Symposium on Laminar-Turbulent Transition (H Fasel & W Saric, eds), Springer.
24. Morkovin MV, Reshotko E, Herbert T, 1994, ‘Transition in open flow systems—a reassessment’, Bull. Am. Phys. Soc. 39:1882
25. Rao A S and Kung D, 1987, Metallic Overlay Materials for the Optimum Cavitation Performance of Hydraulic Turbines, Report for the Canadian Electric Association, CEA No.135 G273.
26. Ryzhov O S, 2005, ‘Transition length in turbine & compressor blade flows’, Proc. R. Soc. A, doi: 10.1098 / rspa. 2005. 1651.
27. Saric W S, Reed H L, and Kerschen E J, 2002, ’Boundary-layer Receptivity to Free-stream Disturbances’, Annu. Rev. Fluid Mech. 2002. 34:291–319.
28. Shimada M, Kokawa H, Wang Z J, Sato Y S and Karibe I, 2002, ‘Optimization of grain boundary character distribution for intergranular corrosion resistant 304 stainless steel by twin-induced grain boundary enngineering’, Acta Materialia, 50, pp2331-2341.
29. Simons Roll Forming Co, 2006, ‘Glossary of Metal Terms’, **www.rollformedshapes.com/metalterms.htm**.
30. Sourmail T and Bhadeshia H K D H, ‘Stainless steel’, **www.msm.cam.ac.uk/phase-trans/2005/Stainless_steels**
31. Three Gorge Power Station, 2006, ‘Damage of Guide Vane Surface (Left Powerhouse)’, Document for the *in situ* Investigation Meeting, 12-14 March 2006, Yi Chang, China.
32. Wassermann P and Kloker M, 2005, ‘Transition mechanisms in a three-dimensional boundary-layer flow with pressure-gradient changeover’, J. Fluid Mech. (2005), vol. 530, pp. 265–293.
33. Watmuff J H, 2004, ‘Evolution of a Turbulent Wedge from a Streamwise Streak’, 15th Australasian Fluid Mechanics Conference, The University of Sydney, Sydney, Australia, 13-17 December 2004.
34. Westin, K. J., Boiko, A.V., Klingmann, B. G. B, Kozlov, V. V. & Alfredsson, P. H. 1994 Experiments in a boundary layer subjected to free stream turbulence. Part I. Boundary layer structure and receptivity. *J. Fluid Mech*. 281, 193-218.
35. Wu X and Luo J, 2001, ‘Instability of Blasius boundary layer in the presence of steady streaks’, *Annual Research Briefs* 2001, Centre for Turbulence Research.

Appendix C

The first paper on verification of Li' Hypothesis

Numerical Investigation of Guide-Plate Induced Pressure Fluctuations on Guide Vanes of Three Gorges Turbines

Ting Chen

S. C. Li[1]
e-mail: S.Li@warwick.ac.uk

School of Engineering,
University of Warwick,
Coventry, UK, CV4 7AL

A new type of cavitation triggered by boundary-layer turbulence-production has been identified from the turbines of the Three Gorges Power Station. Our previous studies point out that the addition of the 'guide-plate' is responsible for the increase of the turbulence level (in particular the low-frequency mode) in the free-stream which in turn promotes the boundary-layer transition through receptivity mechanism. A new vortex structure identified from our numerical studies is revealed in this paper. It explains well how the free-stream turbulence is influenced by this new vortex structure which is created by the addition of this 'guide-plate'. These results support one of the claims in the hypothesis proposed in our previous studies. The other claims in the hypothesis about the triggering mechanism of this type of cavitation in the boundary-layer are being verified through our on-going (numerical and experimental) studies. The numerical studies reported here are performed by using CFD simulations of the entire flow passage of the prototype turbine. [DOI: 10.1115/1.4004257]

1 Introduction

Cavitation is an undesirable phenomenon in hydraulic machinery. The main types of cavitation in Francis turbines have been well described (e.g., [1,2]). The world largest Francis turbines developed for China's Three Gorges project represent the modern technologies of turbines. Their capacity (710 *MW*) and geometric dimensions (9800 *mm* of runner diameter) are all the largest. However, after $10^3 - 10^4$ hour operations, all these cutting edge turbines have developed a pattern of strange damage mainly on the lower surface of the guide-vanes as shown in Fig. 1 which has never been reported and studied before. The first investigation [3] was carried out in the March of 2006. The in situ inspection shows following features: (a) *long and equal-width stream-wise damage-strips with span-wise regularity*; (b) *wedged head*; (c) *corroded rough surface*; (d) *heated tail*, referring to Fig. 2. Having done a multidisciplinary analysis, a hypothesis about this new type of cavitation damage has been proposed. For details, see Refs. [3,4]. The main features together with the proposed mechanism are briefly introduced here.

The observed heated (blue and other) color zone at the tails of damaged areas indicates a temperature of 250°C − 600°C (termed as 'bluing' in heat-treatment) is encountered. The only hydrodynamic mechanism involved in a Francis turbine capable of generating temperatures at or above this range is cavitation. Metallurgical analysis [3,4] also explains that corrosion appearing on the damaged surface (martensitic stainless steel) is only a consequence of cavitation attack. The narrow and shallow attributions of damage strips suggest that the damage is not caused by large cavitating structures in the main flow directly striking on the guide vane surface, whereas the wedged head of damage strips indicates that this type of cavitation damage is likely relating to the turbulent spots generated during boundary layer transition to turbulence that are also featured by wedge head.

For nuclei to cavitate in boundary layer, long enough negative pressure drop generated in the boundary-layer is essential. The process of laminar streak breakdown into turbulent spots may provide an ideal flow structure for creating such negative pressure drop lasting long enough for nuclei to cavitate if the freestream pressure there is also low enough (but not necessarily down to the vapor pressure). Estimation on the span-wise wave-length (spacing) of laminar streak (i.e., Klebanoff wave) is approximately equivalent to the observed span-wise spacing of the damage strips (0.1 *m*), which is also supportive of the hypothesis that the cavitation inception is triggered by boundary-layer turbulence-production. Thus the damaged (roughened) spots in turn trigger subsequent cavitation (damage) immediately downstream [3,4]. This dynamic behavior progresses stream-wise, resulting in such a horizontal damage strip with a wedged head and heated tail.

The turbulence in free-stream is one of the key factors for triggering cavitation inception in boundary layer since it alters boundary-layer instabilities (e.g., the growth of K-mode etc.) through receptivity mechanism. For details of receptivity mechanism, readers are referred to [5–7]. Span-wise distortions (modulations) can be induced by various free-stream disturbances. For example, small low-frequency three-dimensional perturbations in the free stream can produce significant distortion within the boundary layer, leading to alternating span-wise thickening and thinning [6]. Steady disturbances (e.g., artificial roughness, vortices, etc.) can also cause a similar type of span-wise modulation. These distortions are all in the form of elongated streaks named as Klebanoff mode or K-mode [8–10]. For extremely large turbines, the scale effect makes the free-stream turbulence level of prototype turbine much higher than model turbine (i.e., Reynolds number is usually higher by the order of 10^2). The large turbines are thus more susceptible to this type of cavitation inception developed in the boundary-layer through the receptivity mechanism. Detailed similarity analysis is given in Ref. [3].

For turbines in the left-power plant, the flow in the guide-vane passages was subject to a high level of free-stream turbulence, owing to a structure named as 'guide-plate' equipped in the spiral case prior to the entrance of the stay-vane passage. This device was mainly for reducing the unit size. As an evidence of high free-stream turbulence generated by this device, the premature damage of the 'guide-plate' (a piece torn off) accompanying by severe pressure-fluctuation and machine-vibration was reported after commissioning. In addition, the units were operating at low head

---

[1] Corresponding author.

Contributed by Fluids Engineering Division of ASME for publication in the Journal of Fluids Engineering. Manuscript received October 25, 2010; final manuscript received May 5, 2011; published online June 15, 2011. Assoc. Editor: Edward M. Bennett.

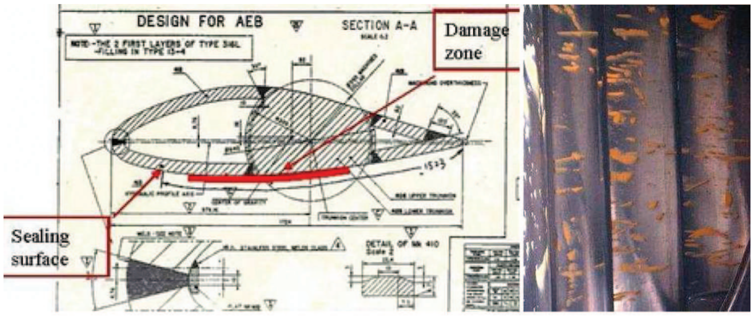

Fig. 1 Damages on the surface of guide vane: (*a*) position; (*b*) pattern

conditions ($61-72\ m$) in the initial stage of operation [11]. Under such conditions, the reduced inlet circulation made the lower surface of guide vane more vulnerable to cavitation. This type of cavitation damage has been identified from all the turbines in the left plant which are developed by different leading manufactures. Therefore, it is not an isolated technical problem but a fundamental challenge to fluid science. A thorough investigation will benefit not only the power industry but also our scientific knowledge in general.

In this paper as the first step of such a thorough investigation, numerical studies on the influences of the addition of 'guide-plate' on the free-stream turbulence level (in particular the low-frequency gust type) are reported. CFD has been performed to obtain the main flow features in the whole turbine passage with more detailed analysis on the free-stream pressure-fluctuations near the surface of the guide vanes. These calculations have been performed in parallel on the high-performance computers at the Cavitation Research Group of Warwick University.

2 Physical Model and Computational Method

2.1 Prototype Turbine. The specifications of the investigated turbine are: runner diameter $D = 9.8\ m$, rated power 710 *MW*, max efficiency guaranteed 96.26%, rated speed 75 *rpm*, and rated head 80.6 *m*. The average operating head ($H = 67\ m$) during the period that the damage occurred (i.e., Year: 2005–2006) is used for the simulations in this paper. The turbine consists of a spiral case, a runner of 15 blades and an elbow draft tube. It has 24 stay vanes and 24 guide vanes. The cross section of the Three Gorges plant together with the 'guide-plate' is shown in Fig. 3.

According to the model tests [11], the range of $280-410\ MW$ has been found as the main unstable zone, presenting all types of unsteady flows (particularly the vortex rope in the draft tube). Numerical simulations have been performed on some typical operation points within full load range for the initial period. Two representative cases are presented in this paper: One with guide vane opening of 16° (315 *MW*) is within the "unstable operation zone"; the other with guide vane opening of 35° (540 *MW*) is within the so-called "quasi-stable operation zone."

2.2 Geometry and Grid. Our numerical simulation investigates the effect of 'guide-plate' (including its supporting plates) on the free-stream turbulence in the entire flow passage of the turbine (in particular near the damage surface of the guide vanes). Three physical models are employed: case 1 without the 'guide-plate' and the supporting plates; case 2 with the 'guide-plate' only and case 3 with the 'guide-plate' and the supporting plates (total 14 pieces installed evenly for supporting the 'guide-plate'). The axial cross-sections of these three cases are shown in Fig. 4(*b*). Other geometrical dimensions remain the same for comparability.

Unstructured meshes have been employed for this calculation owning to the complex shape of the turbine. The flow is considered to be incompressible. The whole calculation domain is divided into five components (spiral case, stay vanes, guide vanes, runner and draft tube), referring to Fig. 4(*a*). For each component, different computational grids have been generated manually according to the flow patterns and details sought. Firstly, the grid independence has been investigated. In order to investigate the delicate structure of vortices inside the spiral case (around the 'guide-plate'), a further refinement of the mesh around the 'guide-plate' for case 2 and 3 has been complemented. For these two cases, the grid numbers of other components have also been increased to balance mesh distribution throughout the whole flow field. For case 1, the final mesh of the whole turbine passage is about 2600000 elements which is also verified by other numerical

Fig. 2 Damages features: (*a*) wedged head; (*b*) corroded rough surface; (*c*) heated area

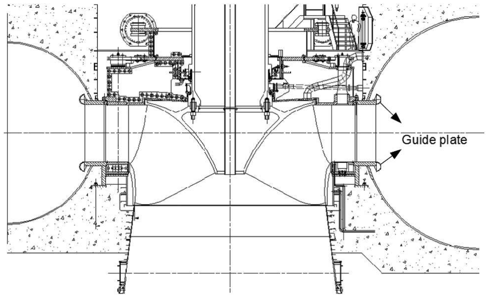

Fig. 3 The cross section of investigated turbine with 'guide-plate' structure equipped in the spiral case

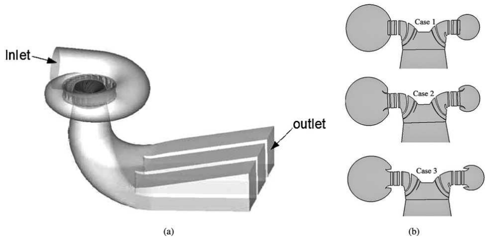

Fig. 4 (*a*) Calculated turbine model; (*b*) Axial cross-sections of three models

studies (e.g., [12,13]) for the Three Gorges turbine. Among them are 300000 elements in the stay vane, 500000–550,000 elements in the guide vanes (subject to operation conditions), 220000 elements in the runner and 430000 elements in the draft tube. However, for case 2 and 3, we have added 500000 more elements in the spiral case. Further fining of mesh size has been tested showing no improvement in the observed vortex structure but increasing calculation time.

2.3 Numerical Method. The renormalization group (RNG) $\kappa-\varepsilon$ turbulence model has been employed to close the governing equations [14]. A second order fully implicit scheme is applied for time discretization, central difference for the diffusion term and second order upwind scheme for the convective term. The SIMPLEC algorithm is used for the discretized equations. The slide mesh model is used to get time-accurate solutions of the strong rotor-stator interactions (i.e., runner-guide vanes and runner-draft tube). The total pressure and the turbulence condition have been set at the inlet of the spiral case from preliminary steady calculations. The static pressure condition has been set at the outlet of draft tube. All simulations have been performed by using a commercial CFD software Fluent.

The momentum equation is

$$\rho\frac{\partial\overline{u_i}}{\partial t}+\rho\overline{u_j}\frac{\partial\overline{u_i}}{\partial x_j}=\rho F_i-\frac{\partial\bar{p}}{\partial x_i}+\mu\frac{\partial^2\overline{u_i}}{\partial x_j\partial x_j}-\rho\frac{\partial}{\partial x_j}\left(\overline{u_i'u_j'}\right) \tag{1}$$

Here, $-\rho\overline{u_i'u_j'}$ is the Reynolds stress of turbulent flow,

$$-\rho\overline{u_i'u_j'}=\mu_t\left(\frac{\partial\overline{u_i}}{\partial x_j}+\frac{\partial\overline{u_j}}{\partial x_i}\right)-\frac{2}{3}\left(\rho k+\mu_t\frac{\partial\overline{u_i}}{\partial x_i}\right)\delta_{ij}, \tag{2}$$

$\bar{p}$ is the averaged pressure; ρ is the fluid density; and F is the body force acting on the unit volume fluid.

The equations based on RNG turbulence model are:

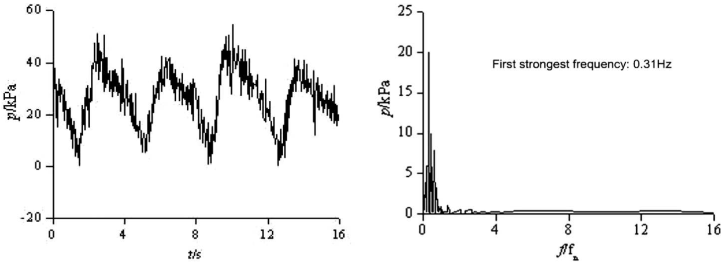

(a)

(b)

Fig. 5 (*a*) Pressure fluctuations against time; (*b*) Pressure fluctuations against frequency with opening of 16°

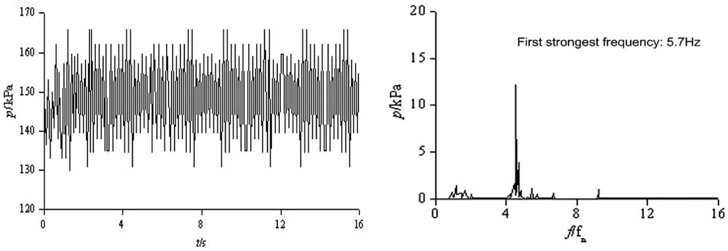

(a)

(b)

Fig. 6 (*a*) Pressure fluctuations against time; (*b*) Pressure fluctuations against frequency with opening of 35°

$$\rho \frac{Dk}{Dt} = \frac{\partial}{\partial x_j}\left(\alpha_k \mu_{eff} \frac{\partial k}{\partial x_j}\right) + 2\mu_t \overline{S_{ij}} \frac{\partial \overline{u_i}}{\partial \overline{x_j}} - \rho\varepsilon \tag{3}$$

$$\rho \frac{D\varepsilon}{Dt} = \frac{\partial}{\partial x_j}\left(\alpha_\varepsilon \mu_{eff} \frac{\partial \varepsilon}{\partial x_j}\right) + 2C_{1\varepsilon} \frac{\varepsilon}{k} v_t \overline{S_{ij}} \frac{\partial \overline{u_i}}{\partial \overline{x_j}} - C_{2\varepsilon}\rho \frac{\varepsilon^2}{k} - R \tag{4}$$

Here, the strain tensor components:

$$\overline{S_{ij}} = \left(\frac{\partial \overline{u_i}}{\partial \overline{x_j}} + \frac{\partial \overline{u_j}}{\partial \overline{x_i}}\right);$$

the effective viscosity $\mu_{eff} = \mu_t + \mu$, where the eddy viscosity is $\mu_t = C_\mu(k^2/\varepsilon)$, and μ is the molecular viscosity of fluid; and the additional term $R = \left[C_\mu \eta^3(1-\eta/\eta_0)/1+\beta\eta^3\right](\varepsilon^2/k)$ with $\eta = S(k/\varepsilon)$. The coefficients above are evaluated as

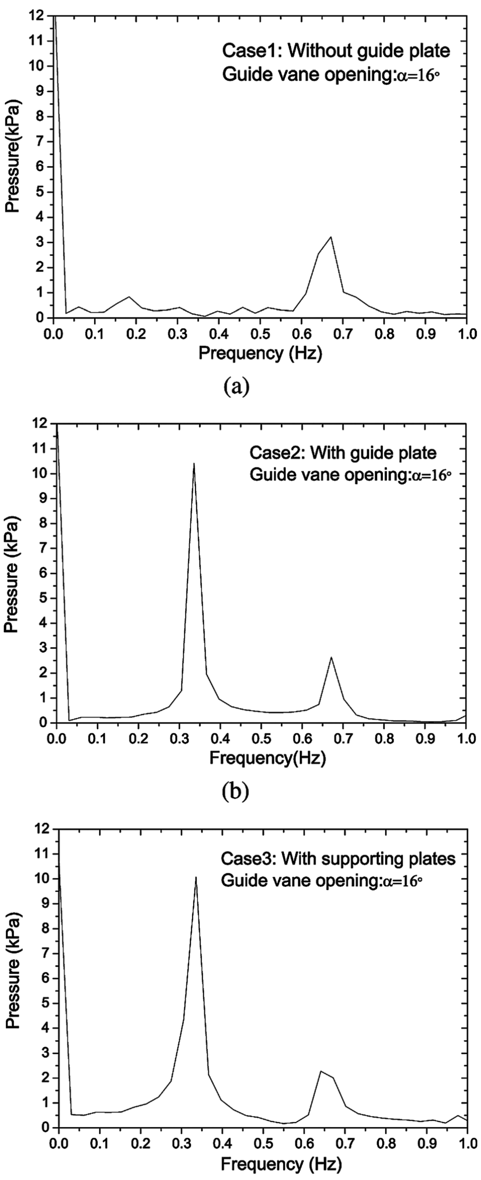

(a)

(b)

(c)

Fig. 7 FFT results in the draft tube with the opening of 16°: (*a*) case 1; (*b*) case 2; (*c*) case 3

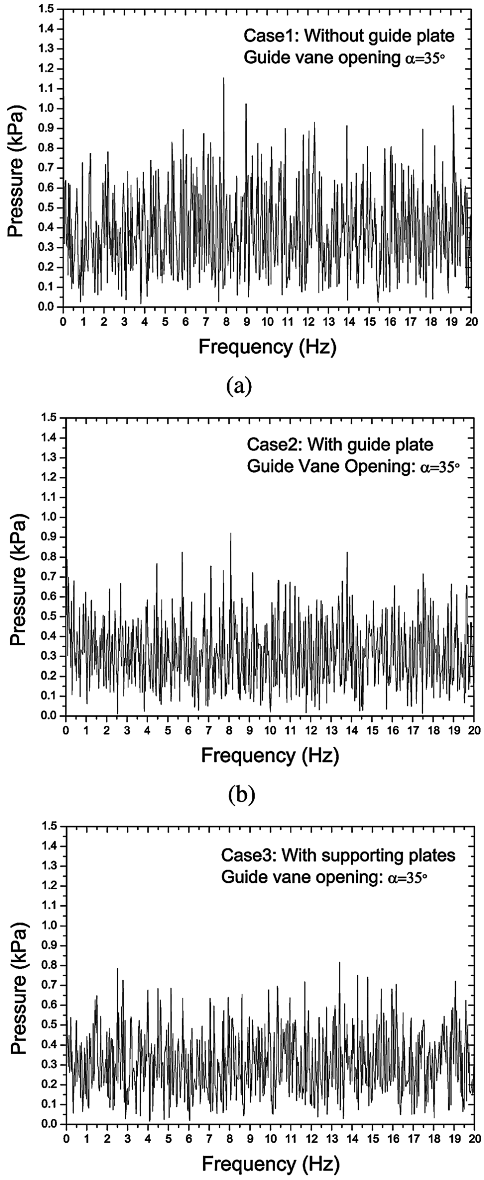

(a)

(b)

(c)

Fig. 8 FFT results in the draft tube with the opening of 35°: (*a*) case 1; (*b*) case 2; (*c*) case 3

$\eta_0 = 4.38, C_\mu = 0.0845, \beta = 0.012, C_{1\varepsilon} = 1.42, C_{2\varepsilon} = 1.68, \alpha_k = 1.0, \alpha_\varepsilon = 0.769$.

The governing equations are discretized as a set of algebraic equations by the finite volume method in spatial domain at each time step. The time steps of 0.008 *s* and 0.004 *s* corresponding to 1/100 and 1/200 of runner rotation are adopted for simulations with guide vane openings of 16° and 35°, respectively. The frequency spectrum analysis of the resultant unsteady flow has been performed by using fast fourier transform (FFT) approach.

3 Investigations of Pressure Fluctuations

3.1 Measurements of Prototype Turbine. The monitoring and analysis system has been employed to measure the fluctuating pressures, cavitation noise and air entrainment etc, for studying the hydraulic instability of the turbines (equipped with 'guide-plate'). Pressure fluctuations in the draft tube are always of great concerns because they are almost the most significant unsteady sources threatening the safety of turbine operation [15,16]. A pressure transducer has been installed close to the entrance of draft tube. The range of transducer measurement is user-defined with threshold of 2.0 *MPa*. Its precision is $\pm 0.075\%$ of the set measurement range. The sampling rate is 22 *times/s* with a maximum time delay of 45 *ms*.

3.2 Locations for Pressure Calculation. For calculation verification, pressure fluctuations have been calculated at the same location in the draft tube as the pressure transducer being installed for comparing with measured results. This location is often called the recording point. The recording point used for calculating the free-stream pressure-fluctuations near the damage area locates at the middle of lower surface of the guide vanes (to be exactly, in the free-stream just outside the edge of boundary-layer). The pressure fluctuations in the flow passages of other turbine components have also been calculated for an overall understanding of the flow situation in the turbine which is not presented in this paper.

3.3 Measuring Results in Draft Tube. Figures 5 and 6 show the pressure fluctuations at the recording point in the draft tube of prototype turbine for two different operation conditions (i.e., openings 16° and 35°). The pattern of pressure fluctuations changes significantly as the opening of guide vane increases from 16° to 35°. For the opening of 16°, the extremely low-frequency component is dominated with lower (average) static pressure but higher oscillating amplitudes. Whereas, for 35°, the high frequency components are dominated with higher (average) static pressure. The first strongest frequency f_1 recorded for the opening of 16° is 0.31 *Hz*. For the opening of 35°, the 5.7 *Hz* is the strongest one.

3.4 Calculation Results in Draft Tube. The pressure fluctuations are stationary oscillations though the numerically transient trip takes quite a while to fade out. The total calculated time is 200 *s* allowing the simulations to reach the status of stationary oscillations from which the fluctuation spectra is analyzed. That is, the numerically sampling period is chosen between $146 - 180s$ for all three cases.

Figures 7 and 8 show the comparison of pressure fluctuations in the draft tube for these three cases at two operation conditions. Firstly, for the partial load (i.e., 16°), an extremely low frequency (0.336 *Hz*) with strong amplitude is distinguishingly emerged for cases 2 and 3 which is also numerically found to be transmitted throughout the whole passage, owing to its low-rate of dampness. This is highly likely owing to the addition of 'guide-plate' in the spiral case (This will be further verified by analyzing the flow pattern around the 'guide-plate' in the later part of the article). The calculated dominant low-frequency component agrees well with the measured one (0.31 *Hz*). In addition, there is a common component of 0.67 *Hz* appears for all three cases. Its amplitude in the case 1 (i.e., without the 'guide-plate') is the largest. This component having a frequency of 0.39 times of the rotation frequency (1.25 *Hz*) is often referred as Rheingans [17] pressure oscillation.

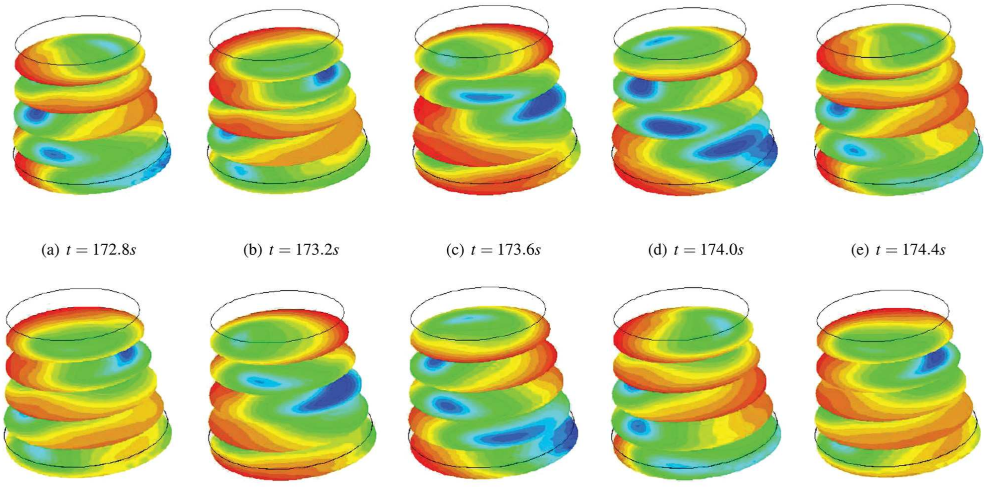
(a) $t = 172.8s$ (b) $t = 173.2s$ (c) $t = 173.6s$ (d) $t = 174.0s$ (e) $t = 174.4s$

(f) $t = 174.8s$ (g) $t = 175.2s$ (h) $t = 175.6s$ (i) $t = 176.0s$ (j) $t = 176.4s$

Fig. 9 Calculated pressure distribution against time at fixed sections in the draft tube (Case 1 with the opening of 16°)

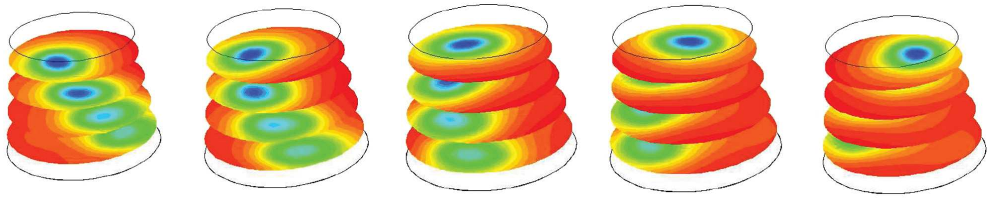

(a) $t = 172.8s$ (b) $t = 173.2s$ (c) $t = 173.6s$ (d) $t = 174.0s$ (e) $t = 174.4s$

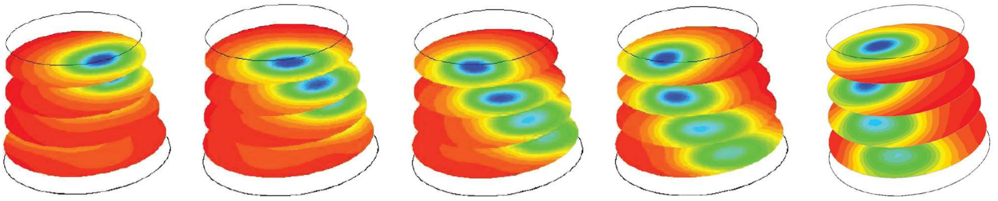

(f) $t = 174.8s$ (g) $t = 175.2s$ (h) $t = 175.6s$ (i) $t = 176.0s$ (j) $t = 176.4s$

Fig. 10 Calculated pressure distribution against time at fixed sections in the draft tube (Case 2 with the opening of 16°)

It is caused by the vortex rope in the draft tube during the partial-load operation. This component with reduced amplitudes has also been numerically captured by our simulations from other measuring points (e.g., in the spiral case or before the stay vane). However, its amplitude is far smaller compared with the component of 0.336 *Hz* caused by the 'guide-plate'. For case 1 and case 2 with the opening of 16°, the flow variations against time in the draft tube are presented in Figs. 9 and 10, showing an organized rotating vortex rope. For case 1, its period is 1.48 *s*, while for case 2, it is around 3 *s*, corresponding to frequencies of 0.67 *Hz* for case 1 and 0.33 *Hz* for case 2. It agrees well with the FFT results discussed above.

For operating at 35° which is close to the optimum condition, the calculated strongest frequency is 7.5 *Hz* which is six times of the rotation frequency (1.25 *Hz*). Most significant components having harmonic frequencies of the rotation frequency (e.g., 18.75 *Hz*, 8.75 *Hz* and 6.25 *Hz*) indicate that the rotor-stator interactions [18] are main instabilities at this operating condition. The frequency of 5.7 *Hz* has also been predicted numerically but not the strongest one. The component of 0.336 *Hz* disappears for cases 2 and 3. Hence, a question arises: why for cases 2 and 3 this 0.336 *Hz* component disappears if it is believed to be induced by the 'guide-plate' structure. In order to answer this question, we have further investigated the flow pattern around the 'guide-plate' and its influence on the whole flow field of the turbine. Some interesting findings are presented in the following part of this paper.

3.5 Pressure Fluctuations on Guide Vane. The FFT results show that the 'guide-plate' significantly increases the turbulence level in the free stream for the entire spectrum and lowers the average static pressure on the lower surface of the guide vanes as shown in Table 1. Both effects have favorable contributions to the promotion of cavitation inception within boundary layer though the local average pressure in the main flow is not below the vapor pressure. Among those increased fluctuation components the extremely low-frequency (0.336 *Hz*) component is the 1st strongest one for cases 2 and 3, but disappears for case 1. The 1st strongest component for case 1 is 18.75 *Hz*, which is the blade passing frequency (i.e., the number of blades [15] times the rotation frequency (1.25 *Hz*)). These results are shown in Fig. 11.

Figure 12 shows similar results obtained for the opening of 35° but the component of extremely low frequency (0.336 *Hz*) not appearing for cases 2 and 3. It is noticeable that the turbulence levels at low-frequency range for cases 2 and 3 are slightly decreased instead of increasing. Thus, another question arises too, i.e., why the turbulence in low-frequency range reduces for cases 2 and 3 with the opening of 35°. This will also be answered in the later part of this article.

4 Flow Pattern in Spiral Case

A new flow-structure has been identified by our numerical studies, i.e., an unsteady vortex ring around the 'guide-plate' as shown by Fig. 13. It proves the addition of 'guide-plate' inducing unstable vortices in the spiral case. These vortices change their space position and sign periodically. They act together with other unstable vortices in the turbine, forming a much longer and larger structure of vortex possessing whole flow passage of the turbine.

However, for the opening of 16° and 35°, the detail structure of this vortex ring is very different. The vortex ring for 35° consists of many small vortices in cases of 2 and 3, like a complete ring breaking into pieces. Whereas for 16°, it is almost a complete ring. This structure difference is attributed to the difference of main flow in the spiral-case for 16° and 35° openings. The more small pieces of vortices in the ring for the opening of 35° explains

Table 1 Comparison of frequencies of pressure fluctuations on the guide vane for the opening of 16°

	Case 1	Case 2	Case 3
Static Pressure	449757 *Pa*	443283 *Pa*	436948 *Pa*
f1	18.75 *Hz*	0.336 *Hz*	0.336 *Hz*
f2	5 *Hz*	18.75 *Hz*	18.75 *Hz*
f3	0.67 *Hz*	7.5 *Hz*	7.5 *Hz*
f4	6.25 *Hz*	5 *Hz*	5 *Hz*

well the fact that the addition of 'guide-plate' makes the low-frequency components decrease and the high-frequency components increase in contrast to the case of 16° because the frequency of pressure-fluctuation varies inversely with the scale of vortex.

At the opening of 35°, owing to the operation condition close to the optimum there is no spiral vortex rope but a weak and nearly steady vortex in the draft tube as shown in Fig. 15. While operating at partial-load (i.e., 16°), the two vortex-structures (i.e., both the vortex-ring around the 'guide-plate' and the spiral vortex-rope in the draft-tube) have been connected through the vortex structures in the runner as a united and complex vortex-structure throughout the whole passage as shown in Fig. 14. Such an extremely large scale and unsteady structure is thus firstly identified from our simulations. Consequently, this structure occupying the whole system will induce this particularly low-frequency fluctuation component with a frequency (0.336 *Hz*) even lower than the vortex-rope (0.67 *Hz*) induced in the draft-tube. These low-frequency signals also transmit throughout the entire flow passage of the turbine. This structure of 'guide-plate' has now been reconstructed or removed from the turbines at the Three Gorges following the advice from Ref. [3]. And, the newly designed turbines for large hydro schemes such as WuDongDe and XiLuoDu, etc. hydro projects in China are all following these trends as well.

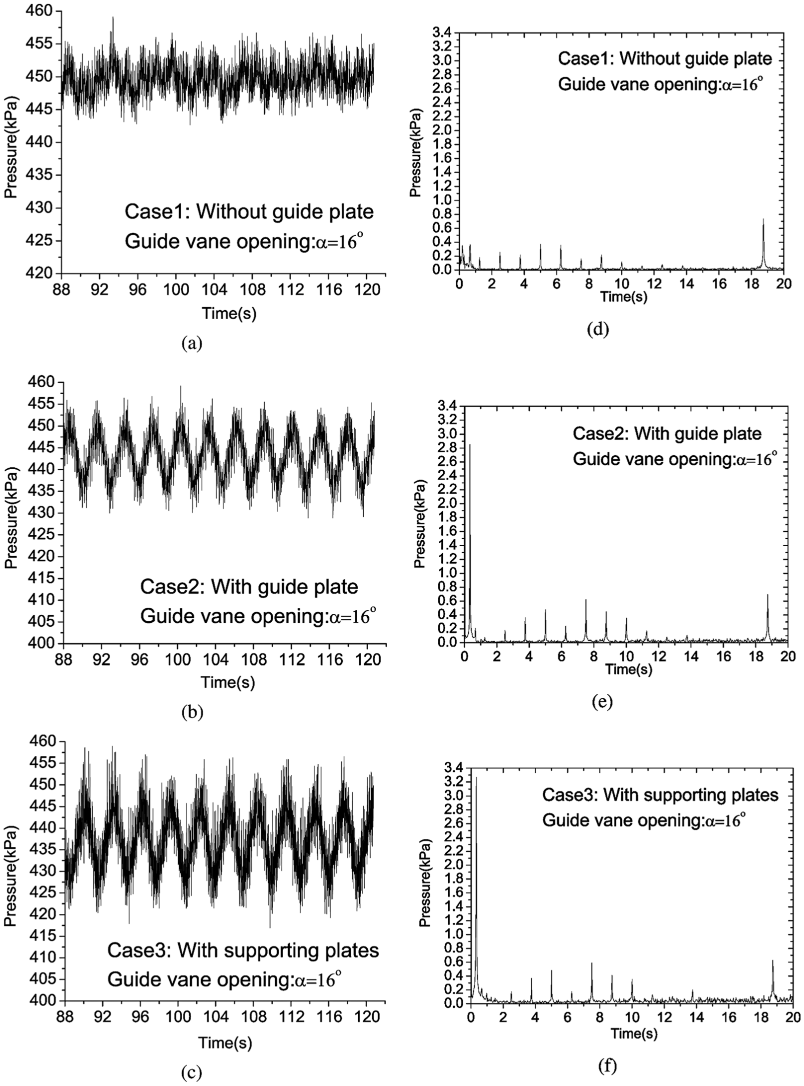

Fig. 11 (*a*)-(*c*) Pressure fluctuations against time; (*d*)-(*f*) Pressure fluctuations against frequency with opening of 16° for three cases

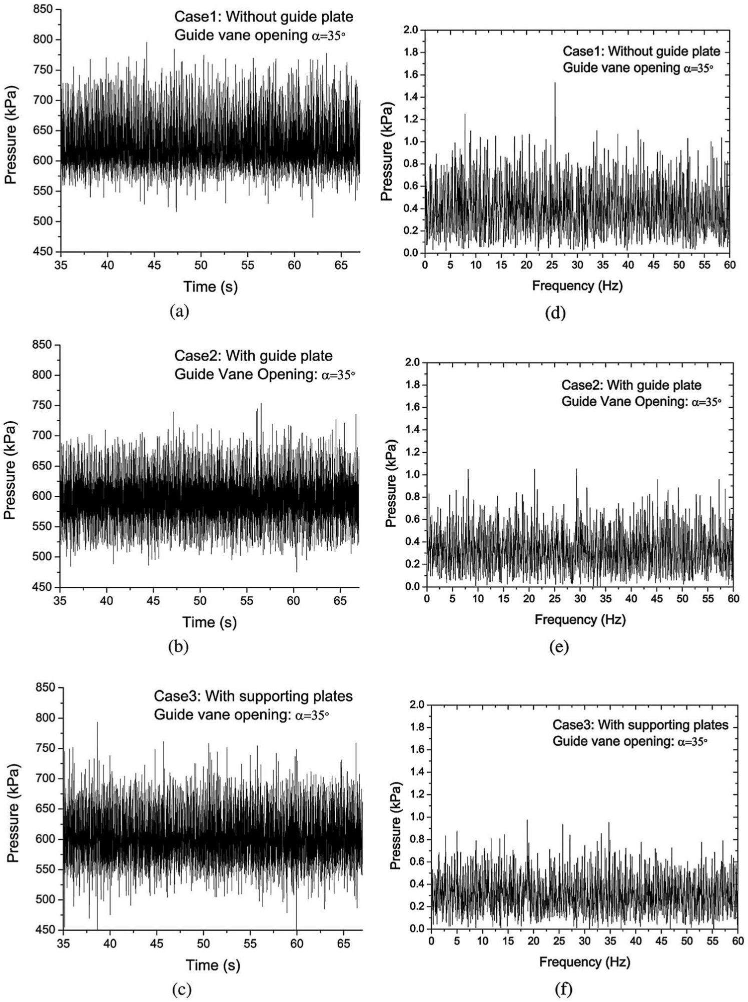

Fig. 12 (*a*)-(*c*) **Pressure fluctuations against time;** (*d*)-(*f*) **Pressure fluctuations against frequency with opening of 35° for three cases**

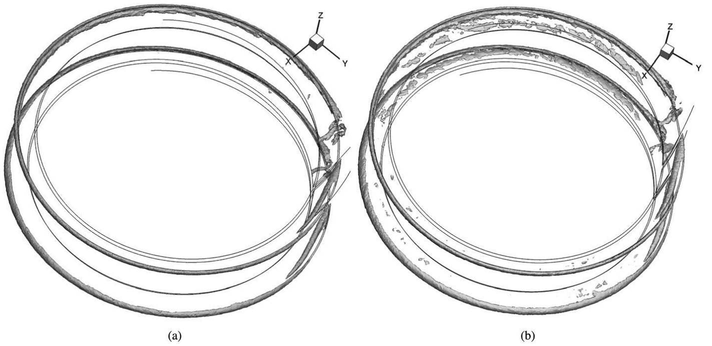

Fig. 13 The structure of vortex ring at openings of (*a*) **16° and** (*b*) **35°**

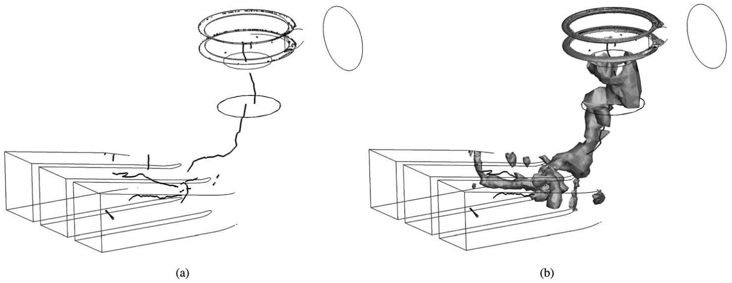

Fig. 14 (*a*) Vortex cores and (*b*) vortex pattern in the whole flow passage of turbine at openings of 16°

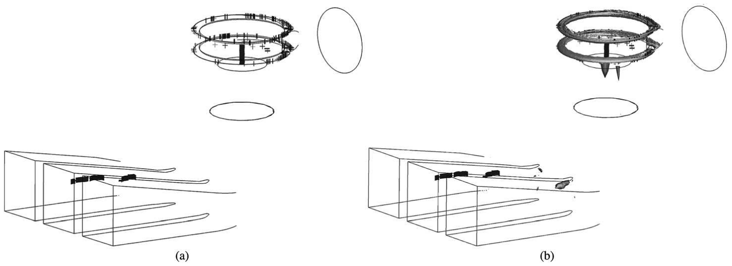

Fig. 15 (*a*) Vortex cores and (*b*) Vortex pattern in the whole flow passage of turbine at openings of 35°

5 Conclusions

(1) The studies have numerically verified the addition of the 'guide-plate' increasing the free-stream turbulence level and particularly introducing a component of extremely low-frequency pressure-fluctuation. This particular component is likely one of the sources entering the boundary-layer and promoting the growth of Klabenoff-streaks and their transition, which in turn triggers the cavitation inception in the boundary-layer of the guide vane.
(2) The 'guide-plate' also significantly lowers the average static pressure in the free-stream near the lower surface of the guide vanes, contributing to the promotion of the cavitation inception as well.
(3) The 'guide-plate' is not guiding the flow into the turbine runner smoothly but adding extremely low frequency fluctuations and preventing the flow from entering the turbine smoothly.
(4) For cases 2 and 3, a vortex-ring structure around the 'guide-plate' has been identified. Under partial-load operation conditions (e.g., 16° opening), it is a complete vortex-ring connected with other vortices throughout the whole turbine system. It is thus responsible for the extremely low-frequency (0.336 *Hz*) induced in the whole passage of turbine. It is not only responsible for the cavitation inception and damage on the guide vane but also impose a significant hydraulic instability to the system.
(5) The 'guide-plate' is harmful device, especially for partial-load operation. It is now removed from the Three Gorges turbines, and should be avoided for future design of turbines.

Acknowledgment

The financial support from the Royal Academy of Engineers (RESCM 3021), the technical and financial support from the Three Gorges authority and the PhD studentship provided jointly by the Chinese Scholarship Council (CSC) and the School of Engineering (University of Warwick) are highly appreciated.

References

[1] Escaler, X., Egusquizaa, E., Farhat, M., Avellan, F., and Coussirat, M., 2006, "Detection of Cavitation in Hydraulic Turbines," Mech. Syst. Signal Process. **20**(4), pp. 983–1007.
[2] Li, S. C., 2001, *Cavitation of Hydraulic Machinery*, Imperial College Press, London, Chap. 2.
[3] Li, S. C., 2006, "Challenge to Modern Turbine Technologies: Analysis of Damage to Guide Vane Surface of Three Gorges Turbine,'' Invited Plenary Speech at The 1st International Conference on Hydropower Technology and Key Equipment, 27–29 Oct, Beijing, pp. 96–112.
[4] Li, S. C., Liu, S. H., and Wu, Y. L., 2007, "A New Type of Cavitation Damage Triggered by Boundary-Layer Turbulent Production," Mod. Phys. Lett. B, **21**(20), pp. 1285–1296.
[5] Wu, X. and Luo, J., 2001, "Instability of Blasius Boundary Layer in the Presence of Steady Streaks," Annual Research Briefs, Centre for Turbulence Research, Stanford University, California, USA, pp. 293–304.
[6] Dryden, H. L., 1936, "Air Flow in the Boundary Layer Near a Plate," Technical Report No. 562, NACA.
[7] Bradshaw, P., 1965, "The Effect of Wind-Tunnel Screens on Nominally Two-Dimensional Boundary Layers," J. Fluid Mech. **22**, pp. 679–687.
[8] Kendall, J. M., 1985, "Experimental Study of Disturbances Produced in Pre-transitional Laminar Boundary Layer by Weak Free Stream Turbulence,'' AIAA, 18th Fluid Dynamics and Plasmadynamics and Lasers Conference, 16–18 July, Cincinnati, pp. 1685–1695.
[9] Klebanoff, P. S., 1971, "Effect of Free-Stream Turbulence on a Laminar Boundary Layer," Bull. Am. Phys. Soc., **10**(16), pp. 3659–3670.
[10] Westin, K. J., Boiko, A. V., Klingmann, B. G. B., Kozlov, V. V., and Alfredsson, P. H., 1994, "Experiments in a Boundary Layer Subjected to Free Stream Turbulence. Part I. Boundary Layer Structure and Receptivity," J. Fluid Mech. **281**, pp. 193–218.
[11] Three Gorges Power Station, 2006, "Damage of Guide-Vane Surface (Left Powerhouse): Document for the *In-Situ* Investigation Meeting,'' 12–14 March, Yi Chang, China, in Chinese.

[12] Liu, S. H., Shao, Q., Yang, J. M., Wu, Y. L., and Dai, J., 2004, "Unsteady Turbulent Simulation of Three Gorges Hydraulic Turbine and Analysis of Pressure in the Whole Passage," J. Hydroelectric Eng., **23**(5), pp. 97–101, in Chinese.
[13] Liao, C. L. and Wang, F. J., 2008, "Numerical Simulation of 3D Flow in Francis Turbine Runner with X-Type Blades," J. Hydroelectric Eng., **27**(3), pp. 141–144, in Chinese.
[14] Yakhot, V., Orszag, S. A., Thangham, S., Gatski, T. B., and Speziale, C. G., 1992, "Development of Turbulence Models for Shear Flows by a Double Expansion Technique," Phys. Fluids A., **4**(7), pp. 1510–1520.
[15] Zhang, R. K., Mao, F., Wu, J. Z., Chen, S. Y., Wu, Y. L., and Liu, S. H., 2009, "Characteristics and Control of the Draft-Tube Flow in Part-Load Francis Turbine," ASME J. Fluids Eng., **131**(2), p. 021101.
[16] Gabriel, D. C., Monica, S. I., Thi, C. V., Bernd, N., and François, A., 2007, "Experimental Study and Numerical Simulation of the FLINDT Draft Tube Rotating Vortex," ASME J. Fluids Eng., **129**, pp. 146–158.
[17] Rheingans, W. J., 1940, "Power Swings in Hydroelectric Power Plants," Trans. ASME, **62**, pp. 171–184.
[18] Wang, H. and Tsukamoto, H., 2001, "Fundamental Analysis on Rotor-Stator Interaction in a Diffuser Pump by Vortex Method," ASME J. Fluids Eng. **123**(4), pp. 737–747.

Appendix D

Brief Information of Damages

Table D.1: Brief Information of Damages [3]

	Manufacturer	Material	Commissioned	Discovered	Operation hours
11F	ALSTOM	$X3CrNiMo13-4$	27/07/04	14/10/05	10245.78h
10F	ALSTOM	$S41500$	07/04/04	27/12/05	11924.55h
9F	VGS	$GX5CrNi13-4$	11/09/05	11/12/05	2328.41h

Operating condition: upstream $135-139$ m; downstream $64-70$ m

Appendix E

Publications

1. Ting Chen and S. C. Li, “Numerical Investigation of Guide-Plate Induced Pressure Fluctuations on Guide Vanes of Three Gorges Turbines”, *Journal of Fluids Engineering*, vol. 133, no. 6, pp.1-10, June 2011.
2. Ting Chen and S. C. Li, “Guide-Plate Induced Pressure Fluctuations on Large Francis Turbines Under Partial Load”, *presentation on 9th International Conference on Hydrodynamics*, Shanghai, China, Oct. 2010.
3. Ting Chen and S. C. Li, “Numerical Studies on Streaky Pattern Caused by Boundary-Layer Transition”, *presentation on WIMRC 3rd International Cavitation Forum*, University of Warwick, UK, July 2011.

Appendix F

Honours and Awards

1. Third prize of IAHR UK Young Persons' Paper Competition (Academic section)
2. Graduate Student Travel Fund from Warwick University
3. Scholarship for PhD study from Warwick University and China Scholarship Council

Bibliography

[1] S. C. Li, “Challenge to modern turbine technologies: Analysis of damage to guide vane surface of Three Gorges turbine,” in *Plenary speech, 1st International Conference on Hydropower Technology and Key Equipment*, Beijing, 27-29 Oct. 2006.

[2] ——, “Cavitation (damage) strips with span-wise regularity on the guide vanes of three gorges turbines (phenomenon and hypothesis),” in *invited plenary paper, the 8th Int. Symposium on Cavitation*, Singapore, August 14-16 2012.

[3] ——, “Cavitation (damage) strips with span-wise regularity identified from Three Gorges turbines,” in *IEEE Canada: Electrical Power and Energy Conference*, Montreal, Canada, Oct 22-23 2009.

[4] *Damage of Guide Vane Surface (Left Powerhouse): Document for the in situ Investigation Meeting*, Three Gorges Power Station, 12-14 March 2006, Yi Chang, China.

[5] *From private files of Prof Li Shengcai, 2006.03.19.*

[6] S. C. Li, *Chap6.2 Cavitation Damage in Turbines*, S. C. Li, Ed. London: Imperial College Press, 2001, vol. 1.

[7] X. Escaler, E. Egusquizaa, M. Farhat, F. Avellan, and M. Coussirat, “Detection of cavitation in hydraulic turbines,” *Mechanical Systems and Signal Processing*, vol. 20, no. 4, pp. 983–1007, 2006.

[8] T. Jacob and J. E. Prenat, “Francis turbine surge: Discussion and data base,” in *Proc of the 18th IAHR Symposium*, Valencia, 1996, pp. 855–864.

[9] C. L. Liao and F. J. Wang, “Numerical simulation of 3D flow in francis turbine runner with X-type blades,” *J. Hydroelectric Eng.*, vol. 27, no. 3, pp. 141–144 (in Chinese), 2008.

[10] T. Chen and S. C. Li, “Numerical investigation of guide-plate induced pressure fluctuations on guide vanes of three gorges turbines,” *Journal of Fluids Engineering*, vol. 133, no. 6, pp. 1–10, 2011.

[11] Y. L. Wu, S. C. Li, S. H. Liu, and et al., *Vibration of Hydraulic Machinery*, ser. Mechanisms and Machine Science, M. Ceccarelli, Ed. Springer, 2013, vol. 11.

[12] R. K. Zhang, F. Mao, J. Z. Wu, S. Y. Chen, Y. L. Wu, and S. H. Liu, “Characteristics and control of the draft-tube flow in part-load francis turbine,” *ASME J. Fluids Eng.*, vol. 131, no. 2, pp. 1–13, 2009.

[13] S. C. Li, *Cavitation of Hydraulic Machinery*, S. C. Li, Ed. London: Imperial College Press, 2001, vol. 1.

[14] S. C. Li, S. H. Liu, and Y. L. Wu, “A new type of cavitation damage triggered by boundary-layer turbulent production,” *Modern Physics Letters B*, vol. 21, no. 20, pp. 1285–1296, 2007.

[15] S. C. Li, “Cavitation damage: Three Gorges turbines (phenomenon, implications & unknown), presentations at the Three Gorge Power Station (19 march 2006), Peking University (28 march 2006) and the National Research Institute of Hydro Power (29th march 2006).”

[16] ——, “Damage strips with span-wise regularity caused by cavitation: Observed phenomenon and envisaged mechanism,” in *SHF Conference on Cavitation and Hydraulic Machines*, Lausanne, Switzerland, 26-27 May 2011.

[17] N. Alonso-Falleiros, M. Magri, and I. G. S. Falleiros, “Intergranular corrosion in a martensitic stainless steel detected by electrochemical tests,” *Corrosion*, vol. 55, no. 8, pp. 769–778, 1999.

[18] J. W. Daily and V. E. Johnson, “Turbulence and boundary-layer effects on cavitation inception from gas nuclei,” *Trans. ASME*, vol. 78, pp. 1695–1706, 1956.

[19] V. H. Arakeri and A. Acosta, “Viscous effects in the inception of cavitation,” *ASME J. Fluids Eng.*, vol. 103, pp. 280–287, 1981.

[20] R. H. L. Saric, W. S. and E. J. Kerschen, “Boundary-layer receptivity to free-stream disturbances,” *Annu. Rev. Fluid Mech.*, vol. 34, pp. 291–319, 2002.

[21] C. B. Lee, “New feathers of CS-solitons and the formation of vortices,” *Phys. Lett.*, vol. 247, pp. 397–402, 1998.

[22] ——, “Possible universal transitional scenario in a flat plate boundary layer: measurement and visualization,” *Phys. Rev.*, vol. 62, pp. 3659–3670, 2000.

[23] C. B. Lee and J. Z. Wu, “Transition in wall-bounded flows,” *Applied Mechanics Reviews*, vol. 61, pp. 1–21, 2008.

[24] X. Wu and J. Luo, “Instability of blasius boundary layer in the presence of steady streaks,” Centre for Turbulence Research, Annual Research Briefs, 2001.

[25] P. S. Klebanoff, “Effect of free-stream turbulence on a laminar boundary layer,” *Bull. Am. Phys. Soc.*, vol. 10, no. 16, pp. 3659–3670, 1971.

[26] P. Alfredsson, M. Berggren, and D. S. Henningson, “Optimal disturbances and bypass transition in boundary layers,” *Phys. Fluids*, vol. 11, p. 134, 1999.

[27] H. L. Dryden, “Air flow in the boundary layer near a plate,” N.A.C.A., Report 562, 1936.

[28] P. Bradshaw, “The effect of wind-tunnel screens on nominally two-dimensional boundary layers,” *J. Fluid Mech*, vol. 22, pp. 679–687, 1965.

[29] J. M. Kendall, “Experimental study of disturbances produced in pre-transitional laminar boundary layer by weak free stream turbulence,” in *AIAA, 18th Fluid Dynamics and Plasmadynamics and Lasers Conference*, 16-18 July 1985, pp. 1685–1695, cincinnati.

[30] K. J. Westin, A. V. Boiko, B. G. B. Klingmann, V. V. Kozlov, and P. H. Alfredsson, “Experiments in a boundary layer subjected to free stream

turbulence. Part I: Boundary layer structure and receptivity," *J. Fluid Mech.*, vol. 281, pp. 193–218, 1994.

[31] J. H. Watmuff, "Evolution of a turbulent wedge from a streamwise streak," in *15th Australasian Fluid Mechanics Conference*, 13-17 Dec. 2004, university of Sydney, Sydney, Australia.

[32] M. Matsubara and P. H. Alfredsson, "Disturbance growth in boundary layers subjected to freestream turbulence," *J. Fluid Mech.*, vol. 430, pp. 149–168, 2001.

[33] T. K. D. Klebanoff, P. S. and L. M. Sargent, "The three-dimensional nature of boundary-layer instability," *Annu. Rev. Fluid Mech.*, vol. 12, pp. 1–34, 1962.

[34] S. C. Li, Y. J. Zhang, and F. G. Hammitt, "Investigation of low-frequency pressure fluctuation associated with venturi flow," University of Michigan, Ann Arbor, USA, Tech. Rep. Reprot No.UMICH O14571-64-I, 1983.

[35] ——, "Characteristics of cavitation bubble collapse pulses, associated pressure fluctuations and flow noise," *J. Hydraulic Res.*, vol. 24, no. 2, pp. 109–122, 1986.

[36] S. C. Li, Z. G. Zuo, S. H. Liu, Y. L. Wu, and S. Li, "Cavitation resonance," *ASME J.Fluids Eng.*, vol. 130, no. 3, p. 031302 (7 pages), 2008.

[37] P. Drtina and M. Sallaberger, "Hydraulic turbines: basic principles and state-of-the art computational fluid dynamics applications," *Proc. Instn. Mech. Engrs.*, vol. 213, pp. 85–102, 1999.

[38] H. Keck and M. Sick, “Thirty years of numerical flow simulation in hydraulic turbomachines,” *Acta Mechanica*, vol. 201, pp. 211–229, 2008.

[39] M. K. Shukla and R. Jain, “CFD analysis of 3-D flow for francis turbine,” *MIT International Journal of Mechanical Engineering*, vol. 1, no. 2, pp. 93–100, 2011.

[40] A. Ruprecht, M. Heitele, and T. Helmrich, “Numerical simulation of a complete francis turbine including unsteady rotor/stator interactions,” in *Proc 20th IAHR Symposium*, no. paper No. CFD S03, 2000.

[41] H. Versteeg and W. Malalasekera, *An introduction to computational fluid dynamics.* Springer, 2007.

[42] L. X. Zhang and Y. Guo, “Simulation of turbulent flow in a complex passage with a vibrating structure by finite element formulations,” *Modern Physics Letters B*, vol. 23, no. 2, pp. 257–260, 2009.

[43] J. Yao, Y. Yao, P. J. Mason, T. Zhang, F. Heyes, and P. Roach, “Cfd modeling of water injection flow for turbine cleaning,” *Modern Physics Letter B*, vol. 23, no. 3, pp. 341–344, 2009.

[44] B. E. Launder and D. B. Spalding, *Mathematical Models of Turbulence.* Academic Press, London, 1972.

[45] D. C. Wilcox, *Turbulence Modeling for CFD.* DCW Industries, 1998.

[46] B. J. Daly and F. H. Harlow, “Transport equations in turbulence,” *Physics of Fluids*, vol. 13, pp. 2634–2649, 1970.

[47] V. Yakhot and S. A. Orszag, "Renormalization group analysis of turbulence. I: Basic theory," *Journal of Scientific Computing*, vol. 1, pp. 3–51, 1986.

[48] Fluent Documentation v6.3.

[49] Y. Zhang and S. A. Orszag, "Two-equation RNG transport modeling of high reynolds number pipe flow," *J. Sci. Comput.*, vol. 13, no. 4, pp. 471–483, 1998.

[50] F. R. Menter, "Two-equation eddy-viscosity turbulence for engineering applications," *AIAA Journal*, vol. 32, pp. 1598–1605, 1994.

[51] J. Z. Wu, H. Y. Ma, and M. D. Zhou, *Vorticity and Vortex Dynamics*. Berlin: Springer-Verlag, 2006.

[52] R. Scardovelli and S. Zaleski, "Direct numerical simulation of free-surface and interfacial flow," *Annual Review of Fluid Mechanics*, vol. 31, pp. 567–603, 1999.

[53] P. Moin and K. Mahesh, "Direct numerical simulation: A tool in turbulence research," *Annual Review of Fluid Mechanics*, vol. 30, pp. 539–578, 1998.

[54] N. Gilbert, "Numerische simulation der transition von der laminaren in die turbulente kanalströmung," Ph.D. dissertation, Institut Förtheoretische Strömungsmechanik, Göttingen, Germany, 1988.

[55] ——, "Near-wall phenomena in transition to turbulence," in *Near-Wall Turbulence*, Hemisphere, New York, USA, 1990, pp. 7–27.

[56] R. Jacobs and P. A. Durbin, “Simulations of bypass transition,” *J. Fluid Mech.*, vol. 428, pp. 185–212, 2000.

[57] P. E. Roach and D. H. Brierley, “The influence of a turbulent freestream on zero pressure gradient transitional boundary layer development, part I: Test cases T3A and T3B,” in *Numerical Simulation of Unsteady Flows and Transition to Turbulence*, O. Pironneau, W. Rodi, I. L. Ryhming, A. M. Savill, and T. V. Truong, Eds. Cambridge University Press, Cambridge, UK, 1990, pp. 319–347.

[58] P. J. Schmid and D. S. Henningson, *Stability and Transition in Shear Flows.* Springer, New York, 2001.

[59] P. Durbin and X. Wu, “Transition beneath vortical disturbances,” *Annu. Rev. Fluid Mech.*, vol. 39, pp. 107–128, 2007.

[60] J. Deardorff, “A numerical study of three-dimensional turbulent channel flow at large reynolds numbers,” *Journal of Fluid Mechanics*, vol. 41, no. 2, pp. 453–480, 1970.

[61] J. Smagorinsky, “General circulation experiments with the primitive equations,” *Monthly Weather Review*, vol. 91, no. 3, pp. 99–164, 1963.

[62] R. O. Fox, “Large-eddy simulation tools for multiphase flows,” *Annual Review of Fluid Mechanics*, vol. 44, pp. 47–76, 2012.

[63] P. C. Schlatter, “Large-eddy simulation of transition and turbulence in wall-bounded shear flow,” Ph.D. dissertation, Swiss Federal Institute of Technology, Zurich, 2005.

[64] M. Germano, U. Piomelli, P. Moin, and W. H. Cabot, “A dynamic subgrid scale eddy viscosity model,” *Physics of Fluids*, vol. A, no. 3, pp. 1760–1765, 1991.

[65] D. You and P. Moin, “A dynamic global-coefficient subgrid-scale eddy-viscosity model for large-eddy simulation in complex geometries,” *Physics of Fluids*, vol. 19, p. 065110, 2007.

[66] W. Kim and S. Menon, “A new dynamic one-equation subgrid-scale model for large eddy simulation,” in *Proc 33rd Aerospace Sciences Meeting and Exhibit*, Reno, NV, 1995.

[67] F. Nicoud and F. Ducros, “Subgrid-scale modeling based on the square of the velocity gradient tensor,” *Flow, Turbulence and Combustion*, vol. 62, pp. 183–200, 1999.

[68] W. J. Rheingans, “Power swings in hydroelectric power plants,” *Trans. ASME*, vol. 62, pp. 171–184, 1940.

[69] A. Ruprecht, T. Helmrich, T. Aschenbrenner, and T. Scherer, “Simulation of pressure surge in a hydro power plant caused by an elbow draft tube,” in *10th International Meeting of the work group on the behaviour of hydraulic machinery under steady oscillatory condition*, Trondheim, Norway, 2001.

[70] M. Sick, P. Drfler, A. Lohmberg, and M. Casey, “Numerical simulations of vortical flows in draft tubes,” in *WCCM V*, Vienna, Austria, 2002.

[71] F. Q. Han, Y. Yu, C. X. Fang, and T. Kubota, “Dynamic behavior of helical vortex rope with dead core in bend draft tube of francis turbine,”

in *Proceedings of the 23nd IAHR Symposium on Hydraulic Machinery and Systems*, 2006.

[72] Y. Xiao, Z. Wang, and Z. Yan, “Experimental and numerical analysis of blade channel vortices in a francis turbine runner,” *Int. J. Comp. Aid. Eng. Softw.*, vol. 28, no. 2, pp. 154–171, 2010.

[73] A. Fay, “Analysis of low-frequency pulsations in francis turbine,” *Earth Env. Sci.*, vol. 12, p. 012015, 2010.

[74] L. J. Zhou and Z. W. Wang, “Investigation of draft tube surge and runner outlet flow patterns,” *Journal of Tsinghua University (Science & Technology)*, vol. 42, no. 12, pp. 29–32 (in Chinese), 2002.

[75] Z. W. Wang and L. J. Zhou, “Simulations and measurements of pressure oscillations caused by vortex ropes,” *ASME J. Fluids Eng.*, vol. 128, pp. 649–655, 2006.

[76] J. Paik, F. Sotiropoulos, and M. J. Sale, “Numerical simulation of swirling flow in complex hydro turbine draft tube using unsteady statistical turbulence models,” *Journal Hydraulic Engineering*, vol. 131, no. 6, pp. 441–456, 2005.

[77] C. Trivedi, M. J. Cervantes, B. K. Gandhi, and O. G. Dahlhaug, “Experimental and numerical studies for a high head francis turbine at several operating points,” *Journal of Fluids Engineering*, vol. 135, p. 111102, 2013.

[78] Y. J. Tang, L. P. Pan, and S. Tang, “Analysis and comparison between prototype and model of vgs unit in the left bank of three gorgess hy-

dropower plant," *Journal of China Institute of Water Resources and Hydropower Research*, vol. 5, no. 4, pp. 286–290 (in Chinese), 2007.

[79] S. H. Liu, Q. Shao, J. M. Yang, Y. L. Wu, and J. Dai, "Unsteady turbulent simulation of Three Gorges hydraulic turbine and analysis of pressure in the whole passage," *J. Hydroelectric Eng.*, vol. 23, no. 5, pp. 97–101 (in Chinese), 2004.

[80] ——, "Unsteady turbulent simulation of prototype hydraulic turbine and analysis of pressure fluctuation in draft tube," *J. Hydroelectric Eng.*, vol. 24, no. 1, pp. 74–78 (in Chinese), 2005.

[81] Y. Zhu, "Stability study of giant francis turbines," Master's thesis, Tsinghua University, 2006.

[82] C. L. Liao, "Study on hydraulic stability of large francis turbine," Ph.D. dissertation, China Agricultural University, 2008, in Chinese.

[83] Y. Xiao, Z. Wang, and Z. Yan, "Numerical analysis of unsteady flow under high-head operating conditions in francis turbine," *Int. J. Comp. Aid. Eng. Softw.*, vol. 27, no. 3, pp. 365–386, 2010.

[84] Y. X. Xiao, Z. W. Wang, Z. G. Yan, Y. Y. Luo, R. F. Xiao, G. J. Peng, and P. Xue, "Experimental and numerical analysis of pressure pulsation in francis turbine," in *ASME Fluids Engineering Division Summer Conference*, vol. 1, San Diego, CA, August 30 2008, pp. 1179–1185.

[85] A. Ruprecht, T. Helmrich, T. Aschenbrenner, and T. Scherer, "Simulation of vortex rope in a turbine draft tube," in *Proceedings of the*

Hydraulic Machinery and Systems 21st IAHR Symposium, Lausanne, September 9-12 2002.

[86] L. X. Zhang and Y. Guo, "Simulation of turbulent flow in a complex passage with a vibrating structure by finite element formulations," *Modern Physics Letters B*, vol. 23, no. 2, pp. 257–260, 2009.

[87] Y. Hu, H. Cheng, J. Hu, and X. Li, "Numerical simulation of unsteady turbulent flow through a francis turbine," *Wuhan University Journal of Natural Sciences*, vol. 16, no. 2, pp. 179–184, 2011.

[88] P. Stein, M. Sick, P. Doerfler, P. White, and A. Braune, "Numerical simulation of the cavitating draft tube vortex in a francis turbine," in *IAHR Section Hydraulic Machinery, Equipment, and Cavitation, 23rd Symposium,*, Yokohama, Japan, 2006.

[89] F. J. WANG, X. Q. LI, J. M. MA, and M. YANG, "Experimental investigation of characteristic frequency in unsteady hydraulic behaviour of a large hydraulic turbine," *Journal of Hydrodynamics*, vol. 21, no. 1, pp. 12–19, 2009.

[90] F. A. SHIRAZI and M. J. MAHJOOB, "Draft tube surge detection in francis hydroturbines using bispectrum analysis," in *Proceedings of the IEEE International Conference on Mechatronics and Automation*, no. 2077-2081, Haerbin, China, 2007.

[91] F. ARZOLA, C. AZUAJE, and Z. P. et al., "Undesired power oscillations at high load in large francis turbines: Experimental study and solution," in *Proceedings of the 23rd IAHR Symposium on Hydraulic Machinery and Systems*, Yokohama, Japan, 2006.

[92] Y. L. Zhu, H. Xiong, and D. H. Xu, "Stability analysis on ALSTOM units installed in three gorges left bank hydropower plant," in *Proceedings of the 1st International Conference on Hydropower Technology and Key Equipment.*, Beijing, China, 2006, pp. 1281–1289.

[93] H. Wang and H. Tsukamoto, "Fundamental analysis on rotor-stator interaction in a diffuser pump by vortex method," *ASME J. Fluids Eng.*, vol. 123, no. 4, pp. 737–747, 2001.

[94] R. G. Jacob and P. A. Durbin, "Shear sheltering and the continuous spectrum of the orr-sommerfeld equation," *Physics of Fluids*, vol. 10, no. 8, pp. 2006–2011, August 1998.

[95] M. Jiang, R. Machiraju, and D. Thompson, *Detection and Visualization of Vortices.* Elsevier Inc., 2005, ch. 14, pp. 295–309.

[96] F. Hussain and J. Jeong, "On the identification of a vortex," *J. Fluid Mech.*, vol. 285, pp. 69–94, 1995.

[97] V. Verma, D. Kao, and A. Pang, "Plic: bridging the gap between streamlines and lic," in *IEEE Visualization '99*, 29-29 Oct. 1999, pp. 341–351.

[98] S. Imlay, "Some computation required: Vortex visualization revisited," Tecplot, Inc., Tech. Rep., 2006.

[99] M. Sabourin, "Numerical simulation and flow analysis of an elbow diffuser," PhD thesis, cole Polytechnique Fdrale de Lausanne, Lausanne, Switzerland, 2002.

[100] V. Biela and H. Beltran, “Draft tube fins,” in *Proc of the 19th IAHR Symposium on Hydraulic Machinery and Systems*, Singapore, 1998, p. 454461.

[101] S. Pejovic, “Troubleshooting of turbine vortex core resonance and air introduction into the draft tube,” in *Proc the 21st IAHR Symposium on Hydraulic Machinery and Systems*, Lausanne, 2002, p. 511516.